MULTIVARIATE DATA ANALYSIS OF SATELLITE-DERIVED MEASUREMENTS TO DISTINGUISH NATURAL FROM MAN-MADE OIL SLICKS ON THE SEA SURFACE OF CAMPECHE BAY (GULF OF MEXICO)

Gustavo de Araújo Carvalho

Tese de Doutorado apresentada ao Programa de Pós-graduação em Engenharia Civil, COPPE, da Universidade Federal do Rio de Janeiro, como parte dos requisitos necessários à obtenção do título de Doutor em Engenharia Civil.

Orientadores: Luiz Landau
Fernando Pellon de Miranda
Peter Minnett

Rio de Janeiro
Dezembro de 2015

MULTIVARIATE DATA ANALYSIS OF SATELLITE-DERIVED MEASUREMENTS
TO DISTINGUISH NATURAL FROM MAN-MADE OIL SLICKS
ON THE SEA SURFACE OF CAMPECHE BAY (GULF OF MEXICO)

Gustavo de Araújo Carvalho

TESE SUBMETIDA AO CORPO DOCENTE DO INSTITUTO ALBERTO LUIZ COIMBRA DE PÓS-GRADUAÇÃO E PESQUISA DE ENGENHARIA (COPPE) DA UNIVERSIDADE FEDERAL DO RIO DE JANEIRO COMO PARTE DO REQUISITOS NECESSÁRIOS PARA A OBTENÇÃO DO GRAU DE DOUTOR EM CIÊNCIAS EM ENGENHARIA CIVIL

Examinada por:

Prof. Luiz Landau, D.Sc.

Prof. Fernando Pellon de Miranda, Ph.D.

Prof. Peter Minnett, Ph.D.

Prof. Nelson Francisco Favilla Ebecken, D.Sc.

Prof. Jean Louis Valentin, D.Sc.

Dra. Cristina Maria Bentz, D.Sc.

RIO DE JANEIRO, RJ - BRASIL
DEZEMBRO DE 2015

Carvalho, Gustavo de Araújo

Multivariate data analysis of satellite-derived measurements to distinguish natural from man-made oil slicks on the sea surface of Campeche Bay (Gulf of Mexico)/Gustavo de Araújo Carvalho – Rio de Janeiro: UFRJ/COPPE, 2015.

XV, 285 p.: il.; 29,7 cm.

Orientadores: Luiz Landau

Fernando Pellon de Miranda

Peter Minnett

Tese (doutorado) – UFRJ/COPPE/Programa de Engenharia Civil, 2015.

Referências Bibliográficas: p. 205-254.

1. Algoritmo. 2. Análise Exploratória de Dados. 3. Dados Multivariados 4. Análise Discriminante. 5. Análise de Componentes Principal (PCA). 6. Petróleo. 7. Manchas de Óleo (Spill). 8. Exsudação Natural (Seep). 9. Golfo do México. 10. Baía de Campeche. 11. Cantarell. 12. Oceanografia. 13. Monitoramento Ambiental. 14. Sensoriamento Remoto. 15. Satélite. 16. Radar de Abertura Sintética (SAR). 17. RADARSAT. I. Landau, Luiz *et al*. II. Universidade Federal do Rio de Janeiro, COPPE, Programa de Engenharia Civil. III. Título.

In loving memory, always forever immortal...

For everything, despite everything!

eD i-mundo Muleke Pulguento Babão
(June 1998 – August 2014)

A friend to the end.

“Muito bem eD, você eD mais.”

“Sometimes the questions are complicated, but the answers are simple!”

Dr. Seuss

“Simple things should be simple, and complex things should be possible.”

Alan Kay

“Share your knowledge. It’s a way to achieve immortality.”

The Dalai Lama

ACKNOWLEDGMENTS

It is with pleasure that I would like to register my paramount regards to:

- Dr. Minnett, who has taught me so much, scientifically- and personally-wise, not only while pursuing this degree but also during the decade of his words of wisdom.
- Dr. Paes (E.T.), from LEMOPA-UFRA, for his clever guidance of excellence during this fascinating multivariate expedition.
- Dr. Miranda for his thorough surgical text corrections, full of accurate insights.
- Dr. Landau for the opportunity, the support, and the infra structure.
- Dr. Moreira (LabSAR) for backing me up during the harsh image coding processes.
- Dra. Valério (DCC-IM-UFRJ) for making available clear enlightenments about PCA.
- Dr. Ebecken for being a very good listener and, above all, for his wise contributions.
- Dr. Valentin and Dra. Bentz for accepting the invitation to join the appraisal crew.
- UFRJ, COPPE, and PEC for the D.Sc. degree.
- PRH-ANP for the financial support.
- Pemex and MDA for the high-quality RADARSAT dataset.
- Øyvind Hammer (PAST), The University of Waikato (WEKA), Microsoft (MS Office), ESRI (ArcGIS), and Geomatica (PCI) for the software packages.
- LAMCE and LabSAR colleagues: Adriano, Beisl, Gil, Hatsue, Humberto, Mônica, Patrícia, Rosana, Sérgio, and Victor.
- Lucas and Patricia that already have room in my heart, but their assistance in text editing and in listening to my loud thoughts, surely deserve the record.
- Lívia for the sincere companion at the start of this journey. And despite the "odds", to AMA-DA AMAnDA for the lovely mid-way "evens".
- Always-good long-time comrades: Angrézinho, Dr. Cabelo, Carlinha, Catanzaro, Davi, DuppreX, Elisa, Eugênio, Dra. Gebara, Dr. Halley, Malaquias, and Roma&zap.
- Contemporary wonders from the woods: Shei-Lá, Cesar, Léu, and Will.
- A long list of other beloved folks not listed in press, yet listened in the air.
- The pure shining beauty of Bia (trix) and her conceivers: Guilherme and Sheryl.
- The everlasting inspiration received from Adir, Sandra, Magali, Morel, Eva, Merice, and Dr. Memél, as well as to the good memories from Vavá and Chico Adolfo.
- THE FOREVER OMNIPRESENT eD, THE MOST SPECIAL OF ALL PRESENTS ☺
- All Gods... For life, happiness, love, flowers, and the ocean!

Resumo da Tese apresentada à COPPE/UFRJ como parte dos requisitos necessários para a obtenção do grau de Doutor em Ciências (D.Sc.)

ANÁLISE DE DADOS MULTIVARIADOS DE MEDIÇÕES DE SATÉLITES PARA DISTINGUIR EXSUDAÇÕES NATURAIS DE DERRAMES OPERACIONAIS DE ÓLEO NA SUPERFÍCIE DO MAR NA BAÍA DE CAMPECHE (GOLFO DO MÉXICO)

Gustavo de Araújo Carvalho
Dezembro/2015

Orientadores: Luiz Landau
Fernando Pellon de Miranda
Peter Minnett

Programa: Engenharia Civil

A presente pesquisa de doutorado é uma análise exploratória com o objetivo utilizar medidas de satélite para discriminar dois tipos de manchas de óleo: exsudações naturais e derrames operacionais. O uso sensores remotos para realizar esta tarefa ainda é pouco documentado. Um conjunto de vários anos (2000-2012) de medições de radar de abertura sintética (SAR – RADARSAT) é utilizado para investigar a distribuição espaço-temporal das manchas de óleo na superfície do mar na Baía de Campeche (Golfo do México). Após o tratamento dos dados (transformação logarítmica, padronização "ranging", etc.), técnicas de análise multivariada, tais como Correlação (modo-R), Análise de Componentes Principais (ACP) e Função Discriminante, são utilizadas na elaboração de um algoritmo simples de classificação para distinguir exsudações de derrames. Esta investigação propõe uma nova interlocução entre a pesquisa geoquímica e o sensoriamento remoto para expressar diferenças geofísicas entre exsudações naturais e derrames operacionais de óleo. Nesta pesquisa, coeficientes de retroespalhamento SAR, i.e. sigma-zero (σ^o), beta-zero (β^o) e gamma-zero (γ^o), são combinados com vários atributos referentes à geometria, forma e dimensão que descrevem as manchas de óleo (conjuntamente referidas como tamanho). Os resultados indicam que a combinação dessas diversas características com as técnicas propostas é capaz de distinguir o tipo de mancha de óleo. Entretanto, o simples uso somente da informação correspondente ao tamanho das manchas também é capaz de distinguir o óleo de exsudações daquele derramado operacionalmente com precisão aceitável para uso sistemático: 70% de acuraria total.

Abstract of Thesis presented to COPPE/UFRJ as a partial fulfillment of the requirements for the degree of Doctor of Science (D.Sc.)

MULTIVARIATE DATA ANALYSIS OF SATELLITE-DERIVED MEASUREMENTS TO DISTINGUISH NATURAL FROM MAN-MADE OIL SLICKS ON THE SEA SURFACE OF CAMPECHE BAY (GULF OF MEXICO)

Gustavo de Araújo Carvalho

December/2015

Advisors: Luiz Landau

Fernando Pellon de Miranda

Peter Minnett

Department: Civil Engineering

The present D.Sc. research is an exploratory data analysis aiming to use satellite-derived measurements to discriminate between two oil slick types: naturally-occurring oil seeps and human-related oil spills. The use of satellite remote sensors for this task is still poorly documented. A multi-year dataset (2000-2012) of synthetic aperture radar (SAR – RADARSAT) is leveraged to investigate the spatio-temporal distribution of the oil slicks on the surface of the ocean in Campeche Bay (Gulf of Mexico). After a Data Treatment practice (Log Transformation, Ranging Standardization, etc.), multivariate data analysis techniques, such as Correlation (R-mode), Principal Components Analysis (PCA), and Discriminant Function, have been explored to design a simple classification algorithm to distinguish natural from man-made oil slicks. The proposed analysis promotes a novel idea bridging geochemistry and remote sensing research to express geophysical differences between seeped and spilled oil. SAR-derived backscatter coefficients, i.e. sigma-naught (σ^o), beta-naught (β^o), and gamma-naught (γ^o), are combined with various attributes referring to the geometry, shape, and dimension that describe oil slicks (referred to as size information). Results indicate that the synergy of combining these several characteristics with the application of the multivariate data analysis techniques is capable of distinguishing the oil slick type. Nevertheless, the sole, and simple use of the oil slick size information is also capable of distinguishing oil seeps from oil spills observed on the sea surface to a useful accuracy for systematic use: 70% of Overall Accuracy.

Table of Contents: **Pages**

GLOSSARY

AAD Average absolute deviation. Dispersion measure of all pixels inside oil slick polygons.

AVG Arithmetic mean. Central tendency measure of all pixels inside oil slick polygons.

AVHRR Advanced Very High Resolution Radiometer.

Beta-naught SAR backscatter coefficient (symbol: β^o) corresponding to the radar cross section (RCS – σ) normalized by the unit area in the plane of the incident radar beam (i.e. slant range direction). It is sometimes referred to as radar brightness. Because it represents the reflectivity in the direction of the incident radar beam and it is independent of the terrain slope, system design engineers generally prefer to use measures of β^o. See Section 4.3: C_1 and C_2.

Bmode Beam mode.

Brightspot Oil slick class defining oil spills from the same oilfield. See Section 2.3.2.

C_1 Radiometric-calibrated value (given in intensity or amplitude of the received radar beam) corresponding to the radar cross section (RCS – σ) normalized by the unit area: SAR backscatter coefficient. This quantitative measurement represents the SAR backscatter signature in different surface planes: sigma-naught (σ^o), beta-naught (β^o), or gamma-naught (γ^o):

$$C_1 = [\{DN^2\}+B]/A$$

where:

DN: Digital Number.

B: Constant offset (nominally set to zero for SGF products).

A: Range-dependent gain that varies upon the LUT choice (i.e. metadata files – *lutSigma.xml*, *lutBeta.xml*, or *lutGamma.xml*) to obtain a corresponding *A* to calculate σ^o, β^o, or γ^o.

C_2 Radiometric-calibrated value (expressed in decibel units – dB) corresponding to the radar cross section (RCS – σ) normalized by the unit area: SAR backscatter coefficient. This quantitative measurement represents the SAR backscatter signature in different surface planes: sigma-naught (σ^o), beta-naught (β^o), or gamma-naught (γ^o):

$$C_2 = (10*cc)*\mathrm{Log}_{10}(C_1)$$

where:

cc: Equal to 2 for the amplitude of the received radar beam and 1 for pixel values given in intensity.

C_1: Radiometric-calibrated value of σ^o, β^o, or γ^o given in intensity or amplitude, by: $C_1 = [\{DN^2\}+B]/A$

DN: Digital Number.

B: Constant offset (nominally set to zero for SGF products).

A: Range-dependent gain that varies upon the LUT choice (i.e. metadata files – *lutSigma.xml*, *lutBeta.xml*, or *lutGamma.xml*) to obtain a corresponding *A* to calculate σ^o, β^o, or γ^o.

CBOS-Data Campeche Bay Oil Slick Satellite Database. See Chapter 2.

CBOS-DScMod Campeche Bay Oil Slick Modified Database. Modified version of the Campeche Bay Oil Slick Satellite Database (i.e. CBOS-Data) used on this D.Sc. research Dissertation as the workable database. See Section 5.4.

CBOS-SatPro Campeche Bay Oil Slick Satellite Project. See Chapter 2.

CBRR	Centro Brasileiro de Recursos RADARSAT. It is nowadays called LabSAR.
CCC	Cophenetic Correlation Coefficient.
CENPES	Centro de Pesquisas Leopoldo Américo Miguez de Mello.
CFS	Correlation-Based Feature Selection.
Centroid	Represent the topological center of mass of the oil slick polygon.
Chl	Chlorophyll-a concentration.
cLAT	Latitude of the oil slick polygon centroid.
cLONG	Longitude of the oil slick polygon centroid.
Cluster	Oil slick class defining oil seeps with repeated occurrences about the same location observed on the surface of the ocean. See Section 2.3.2.
COD	Coefficient of dispersion. Dispersion measure of all pixels inside oil slick polygons.
COPPE	Instituto Alberto Luiz Coimbra de Pós-Graduação e Pesquisa de Engenharia.
COV	Coefficient of variation: ration between mean and standard deviation. Dispersion measure of all pixels inside oil slick polygons. Distinct combined *COV* sets are explored on the present D.Sc. research. See Section 5.4 (Table 5-5).
CTT	Cloud top temperature.
Damping ratio	Compares the radar return decrease from inside to outside of oil slicks.
dB	Decibel unit.
DIC	Digital image classification.
DN	Digital Number represents the grey-level brightness count assigned to each gird position (i.e. pixel) of any given SAR image – for instance, between 0 and 255 for 8-bit images. DN is an uncalibrated measure, but it can be converted to obtain radiometric-calibrated SAR backscatter coefficients: sigma-naught (σ^o), beta-naught (β^o), or gamma-naught (γ^o).
Dummy Variable	Binary-coded variable: one (1) or zero (0), thus referring to its presence (Yes) or absence (No), respectively.
EDA	Exploratory data analysis.
EOS	Earth Observing System.
ERS	European Remote-Sensing Satellites: ERS-1 and ERS-2
FFROST	Adaptive Frost Filter of the PCI Geomatics software.
Gamma-naught	SAR backscatter coefficient (symbol: γ^o) corresponding to the radar cross section (RCS – σ) normalized by the unit area in the plane orthogonal to the incident radar beam (i.e. orthogonal to the slant range direction). It is the power returned to the antenna from the area orthogonal to the radar beam. This plane is uniformly distant from the satellite and has equal brightness from near to far range on the pixel level. In being so, measurements of γ^o are usually selected for antenna calibration purposes. See Section 4.3: C_1 and C_2.
HC	Hydrocarbon compound (e.g. mineral oil or natural gas).
IOD	Illegal oil dumping. Oil observed on the sea surface for which vessels are the identified source. Also referred to as Ship Spill or ship discharge.
IOP	Inherent optical property of the water.
LabSAR	Laboratório de Sensoriamento Remoto por Radar Aplicado à Indústria do Petróleo. Previously called CBRR.
LAMCE	Laboratório de Métodos Computacionais em Engenharia.

Look alike feature	Harmless phenomena that can generate signatures in SAR imagery, which are similar to oil slicks, thus causing ambiguous interpretations and yielding false positives. These false targets range from regions of very weak wind or no wind, rain cells, atmospheric fronts, hydrodynamic effects, internal waves, long surface waves, shear zones, current boundaries, velocity bunching, eddies, upwelling zones, divergence and convergence regions, shallow water bathymetry, underwater vegetation beds, biogenic oil films, surfactants from phytoplankton blooms, grease ice, ice edge, ship's stern wake turbulence, urban runoff, operational cleaning from ships, tankers, platforms, oil rigs or FPSO units, storm water discharge, freshwater intrusion from riverine origin, to shadow zones of waves behind offshore installations, islands or land, amongst others.
LUT	Look-up-table.
MAD	Median absolute deviation. Dispersion measure of all pixels inside oil slick polygons.
MARPOL	International Convention for the Prevention of Pollution from Ships.
MDA	MacDonald Dettwiler and Associates Ltd.
MDA-GSI	MDA Geospatial Services Inc.
MDM	Mid-mean. Central tendency measure of all pixels inside oil slick polygons.
MED	Median. Central tendency measure of all pixels inside oil slick polygons.
MERIS	MEdium Resolution Imaging Spectrometer.
MetOc-Kit	Meteorological and Oceanographic Kit.
MOD	Mode. Central tendency measure of all pixels inside oil slick polygons.
MODIS	MODerate Resolution Imaging Spectroradiometer.
NOAA	National Oceanic and Atmospheric Administration.
OGEPI	Oil and gas exploration and production industry.
Oil seep	Oil floating on the sea surface that has naturally seeped on its liquid form out of the seafloor. This only considers the surface oil footprint, making no reference to the whole hydrocarbon seepage processes. This is also one of the two oil slick categories. See Section 2.3.2.
Oil slick	Indiscriminately indicates, unless otherwise specified, the sea surface footprint of oil that has seeped naturally (oil seep) or spilled after human intervention (oil spill), both on its liquid form.
Oil slick descriptor	Characteristic belonging to oil slicks (e.g. latitude, longitude, area, perimeter, etc.). Also termed as slick-feature attribute.
Oil slick type	Refers to the source of the oil observed on the sea surface: natural oil seep or man-made oil spill. Not related to the "source rock" that generates HC.
Oil spill	Oil floating on the sea surface solely attributed to man-made activities, which may include platforms, ships, or pipelines. This is also one of the two oil slick categories. See Section 2.3.2.
Orphan Seep	Oil seep not belonging to any specific Cluster class.
Orphan Spill	Oil spill not belonging to any specific Brightspot class.
PCA	Principal Components Analysis.
PEC	Programa de Engenharia Cívil.
Pemex	The Mexican oil company, i.e. Petróleos Mexicanos.
PEP	Pemex Exploración y Producción.
Per	Perimeter given in km.
Petrobras	The Brazilian oil company, i.e. Petróleo Brasileiro S.A.

QC-Standards	Comprehensive set of criteria completed to guarantee that jumbled or inconsistent information are fixed and/or removed from the CBOS-Data.
RADAR	RAdio Detection And Ranging.
RCS	Radar cross section (σ). Characterizes a reflectivity property of the reflected radar signal strength (i.e. scattering intensity) of surface targets in the direction of the radar receiver. It has a unit of m^2 and is a function of: time, position, viewing geometry, radar wavelength, and polarization (transmitted and received). The RCS normalized by the unit area (normalized-RCS) corresponds to a quantitative measure of SAR backscatter signature in different planes: sigma-naught (σ^o), beta-naught (β^o), or gamma-naught (γ^o).
RMNE	Región Marina Noreste.
RNG	Range. Dispersion measure of all pixels inside oil slick polygons.
ROI	Region of interest, more specifically, Campeche Bay.
SAR	Synthetic Aperture Radar.
SARdate	Date of the SAR overpass above the Campeche Bay region.
SARname	Name of the utilized SAR satellite.
SARtime	Time of the SAR overpass above the Campeche Bay region.
Sea-truth	Operator's interpretation of SAR images. Refers to the occurrence, or not, of oil slicks, its category (oil seep or oil spill), and class (Cluster, Brightspot, etc.). It also refers to the value of the SAR backscatter coefficients: sigma-naught (σ^o), beta-naught (β^o), or gamma-naught (γ^o).
SGF	SAR Georeferenced Fine Resolution. RADARSAT product format. This Level-1 product is usually referred to as a "path-oriented image".
Ship Spill	Oil observed on the sea surface for which vessels are the identified source. Also referred to as illegal oil damping (IOD) or ship discharge.
Sigma-naught	SAR backscatter coefficient (symbol: σ^o) corresponding to the radar cross section (RCS – σ) normalized by the unit area in the ground range plane (pixel projected onto the ground). Although its calculation depends upon the knowledge of terrain slope (not an issue on the sea surface) and the radar beam incidence angle, it is directly related to the target's reflectance per unit area (i.e. pixel projected onto the ground). For this reason, scientists frequently used σ^o measurements. See Section 4.3: C_1 and C_2.
Slick-feature attribute	Characteristics belonging to oil slicks (e.g. latitude, longitude, area, perimeter, etc.). Also termed as oil slick descriptor.
slickID	Unique identification number of each oil slick polygon.
SOI	Sphere of influence: Pemex's OGEPI related activities at Campeche Bay.
SST	Sea surface temperature.
STD	Standard deviation. Dispersion measure of pixels inside oil slick polygons.
SWH	Significant wave height.
UFRJ	Universidade Federal do Rio de Janeiro.
UPGMA	Unweighted Pair Group Method with Arithmetic Mean.
USTC	Unsupervised Semivariogram Textural Classifier algorithm.
VAR	Variance. Dispersion measure of all pixels inside oil slick polygons.
β^o	See beta-naught.
γ^o	See gamma-naught.
σ^o	See sigma-naught.

INTRODUCTION

The study accomplished during this D.Sc. research consists of investigating the sea surface signature of oil slicks in remotely sensed images – these include both natural oil seeps and man-made oil spills. Throughout the document, key concepts related to this subject are emphasized providing enough detailed information enabling any knowledgeable scientist to replicate the epistemology of the exercised methodology[1].

The standard IMRaD (Introduction, Methods, Results, and Discussion; SOLLACI & PEREIRA, 2004) writing organization structure is expanded and the text is divided in two parts. The first part has a non-IMRaD format in which four Chapters are explored to introduce the "status quo" of the context and background for the study: providing a comprehensive literature review with the contribution of others to the present investigation and introducing pertinent aspects for reaching the proposed objectives. The second part evokes another five Chapters tailoring the IMRaD. Hence, the proposed nine-Chapter structure of this D.Sc. research Dissertation is organized as described below:

Chapter 1 gives the structure of the document, introduces the nature and scope of the objectives under investigation, explaining why such effort is timely and necessary, as well as its novelty perspective. It also presents the motivations driving this study. The research rationale and structure are outlined. The justifications for the scientific effort are addressed along with the main challenges faced on the course of the present investigation and a legacy of contributions to the scientific community.

Chapter 2 provides three important matters: a description of the study area (i.e. Campeche Bay – Figure 1-1), details about Pemex's satellite-monitoring project that produced the data collection utilized herein, and a complete description of the explored multi-year dataset.

Chapter 3: gives a concise picture of the socioeconomic humankind dependence on fossil fuels. It also provides particular negative impacts (i.e. social, ecological, and economic) arising from natural and/or man-made oil releases in the environment.

[1] "The word methodology comprises two nouns: *method* and *ology*, which means a branch of knowledge; hence, methodology is a branch of knowledge that deals with the general principles or axioms of the generation of new knowledge. It refers to the rationale and the philosophical assumptions that underlie any natural, social or human science study, whether articulated or not. Simply put, methodology refers to how each of logic, reality, values and what counts as knowledge inform research." (MCGREGOR & MURNANE, 2010 – p. 2).

Chapter 4 starts with a brief introduction to classical oceanographic sampling methods mostly used previous to the introduction of satellite sensors. It further provides a concise assessment of the SAR technology focusing on the use of the two Canadian RADARSAT satellites. Unless otherwise specified, every reference throughout this manuscript to "RADARSAT imagery" refers to information from any, or both, RADARSAT satellites. Two important matters are summarized: the calculation of radiometric-calibrated SAR-derived backscatter coefficients (i.e. σ^o, β^o, and γ^o), and the three-step framework typically used to detect dark spots in SAR imagery: Digital Image Classification (DIC), Feature-Extraction, and Feature-Classification. It also discusses advantages and drawbacks of using satellite remote sensing to inspect environmental phenomena observed on the sea surface (e.g. algal blooms, oil slicks, etc.).

Chapter 5 is devoted to the methods explored during this research. It has ten Sections giving technical details about the ten Phases executed during the present investigation (Figure 1-3): Workable-Database Preparation (Green Phases: 1 to 5) and Multivariate Data Analysis Practice (Yellow Phases: 6 to 10). It starts by detailing the data verification and systematic data scanning processes. It then presents aspects about the satellite image re-processing and the calculation of new slick-feature attributes. Data treatments and data sub-divisions are also discussed. The coherent step-by-step of the data mining is addressed with explanations about the explored multivariate data analysis techniques: correlation (R-mode), Principal Components Analysis (PCA), Correlation Matrixes and Discriminant Function. The last Section explains the concepts of the classification algorithm proposed to differentiate oil seeps from oil spills.

Chapter 6 presents the results mirroring the order of the methods' Chapter. Although it is not compulsory, the reader is encouraged to read them in pairs: methods-to-results.

Chapter 7 provides the relationships among the results, thus presenting a general discussion of the observed results.

Chapter 8 outlines the concluding findings.

Chapter 9 suggests insights about recommended future work.

A vast and comprehensive list of **References** is provided.

While at the start of the manuscipt, the reader finds an all-inclusive **Glossary** that provides a list of acronyms, abbreviations, and some of the most important terms and definitions utilized on this D.Sc. research Dissertation, at the end of the manuscipt, six **Appendices** are found presenting additional material.

CHAPTER 1

RESEARCH RATIONALE

Naturally occurring fossil fuels (e.g. mineral oil, natural gas, and coal) are generated through geochemical and geological processes associated with the transformation of buried organic matter – oil and gas involve further migration of the resulting products (TISSOT & WELTE, 1984; NRCC, 2003). While oil and gas are predominantly constituted of atoms of hydrogen and carbon (such molecules are collectively known as hydrocarbon compounds – henceforth HCs), coal is mostly composed of carbon atoms (BATISTA NETO *et al.*, 2008).

Although HC is found in forms other than petrogenic-associated products (i.e. oil or gas) – pyrogenic HC (associated with the combustion of wood, oil, coal) or phytogenic HC (derived from plants) – throughout the current manuscript HC is only used to refer to petroleum[2] on its liquid form (i.e. mineral oil). Therefore, terms such as fossil fuels, HCs, mineral oil, and petroleum are interchangeably used as synonyms to oil. Even though a glossary is included as part of the document, the reader should bear in mind the following terminology:

Oil seep Oil identified on the sea surface that has naturally seeped out of the seafloor. It does not refer to the whole HC seepage process, as it only considers the surface footprint of the oil – see Section 3.2.

Oil spill Oil observed floating on the surface of the ocean that is solely attributed to man-made activities, which may include spillages from platforms, ships, pipelines, amongst others.

Oil slick In a generic sense, it indicates, unless otherwise specified, the sea surface footprint of oil that has seeped naturally (i.e. oil seep) or spilled after human intervention (i.e. oil spill).

Oil slick type Source nature of the oil slicks observed on the sea surface:
- Natural oil seep; or
- Man-made oil spill.
(It makes no reference to the "source rock" that generates HC).

[2] Etymology from the Oxford English Dictionary: Classical Latin: *petra* rock (petro: either ancient Greek *πέτρος* stone or ancient Greek *πέτρα* rock) + *oleum* oil (a variant or early form of ancient Greek *ἔλαιον*).

1.1. ENVIRONMENT, OIL SLICKS, AND SATELLITES

Every year a multitude of oil slicks are observed throughout the world's oceans. These may come from a variety of sources that range from oil terminals, refineries, ships, tankers, FPSO units (Floating Production, Storage, and Offloading), platforms, industrial plants, to natural seeps (GARCIA *et al.*, 2009; ITOPF, 2015a). Whether naturally slowly leaking, occasionally discharged in operational activities, or catastrophically released in accidents, the diffuse distribution in space and time of oil and related products makes the process of tracking and monitoring oil slicks difficult and complex to study (NRCC, 1985; HORNAFIUS *et al.*, 1999).

Oil released to the environment can result in ecosystem contamination throughout the Exclusive Economic Zones (EEZs). The proximity to shore worsens the problem and the serious social, ecological, and economic impacts occur with major negative consequences to many industry sectors such as tourism, fisheries, aquaculture, shellfish beds, etc. (JERNELOV & LINDEN, 1981b; KVENVOLDEN & COOPER, 2003). Such hazards are capable of damaging a variety of natural habitats, and cause detrimental effects that range from wild sea-life die-offs to problems to seawater desalination systems (NRCC, 2003; EOE, 2010a; 2010b).

Given the multiplicity of ecological threats caused by natural products of HC seepage and human-related oil, accurate mathematical modeling and effective surveillance systems are a pressing need – e.g. CARTHE[3]. These are essential to streamline clean-up operations at the sea surface across the EEZ and along shorelines (SAUER *et al.*, 1993; BOYD *et al.*, 2001; JAYASRI *et al.*, 2014). Likewise, there is a worldwide need for active monitoring programs to support mitigation actions, sustainable management practices, early warning systems, etc. (JOHANNESSEN *et al.*, 1997; JHA *et al.*, 2008).

The manifestations of various ocean surface processes (e.g. algal blooms, upwelling, oil slicks, etc.) may be detected using instruments on aircraft or satellites (LUSCOMBE *et al.*, 1993; JOHANNESSEN *et al.*, 2000; CARVALHO, 2002; BREKKE, 2007). In fact, there are several sensors flying on platforms in space that combine synoptic characteristics to provide valuable advantages for high-quality surveys of the Earth's surface, which, for instance, includes relevant information about the dynamics of operational, accidental, and illegal oil spills, as well as oil seeps (GOWER *et al.*, 1993; THOMPSON & MCLEOD, 2004; IVANOV *et al.*, 2002; 2004; 2005).

[3] Consortium for Advanced Research on Transport of Hydrocarbon in the Environment (CARTHE): http://carthe.org

Numerous types of passive sensors (e.g. visible sensors, as well as those in the near and thermal infrared) may be used to detect oil slicks floating on the surface of the ocean (ASANUMA *et al.*, 1986; BYFIELD, 1998; SANCHEZ *et al.*, 2003). In addition, airplanes and satellite also carry active sensors using a low-frequency pulse of electromagnetic energy that is transmitted towards a scene, or object, in which a portion of the transmitted energy reflects back (i.e. backscatters) to the source (CHAN & KOO, 2008; KUMARI, 2014). These sensors observe the strength (detection) and time delay (ranging) of the return signals – e.g. RAdio Detection And Ranging (RADAR; GUARNIERI, 2013). Currently, the most useful radar systems are Synthetic Aperture Radars (SAR)[4], which are side-looking systems operating in the microwave region of the electromagnetic spectrum (BIRK *et al.*, 1995; ALPERS, 2002; THOMPSON, 2004).

However, as some environmental phenomena can generate signatures in SAR imagery that are similar to oil slicks, this technology may yield false positives (ESPEDAL *et al.*, 1996; HOLT, 2004). The non-unique signature of oil caused by false targets can induce to ambiguous interpretations (JOHANNESSEN *et al.*, 1996). The so-called "look-alike features" range from atmospheric phenomena (e.g. regions of weak wind or no wind, rain cells, atmospheric fronts, etc.) and oceanographic features (e.g. hydrodynamic effects, internal waves, surface waves, shear zones, current boundaries, velocity bunching, eddies, upwelling zones, divergence and convergence regions, etc.), to other events such as shallow water bathymetry, underwater vegetation beds, different sea ice forms (e.g. grease ice or the ice edge), surfactants from phytoplankton blooms, and biogenic oil films. It may also include several man-made activities (e.g. ship's stern wake turbulence, urban runoff, operational cleaning from ships, storm water discharge, etc.) and natural phenomena too: freshwater intrusion from riverine origin, shadow zones of waves behind offshore installations, islands or land, amongst others.

It is useful to draw attention to the large amount of information generated by spaceborne systems, especially if compared to the limited aircraft surveillance range, the scattered ship sampling coverage, and to other data collection devices such as moored and drifting buoys (DUXBURY & DUXBURY, 1997). Hence, the use of satellite measurements to identify oil slicks directly benefits the oil and gas exploration and production industry (henceforth OGEPI), as well as a variety of societal stakeholders, which may include the general public, non-governmental organizations, environmental agencies, resource managers, governmental administrators, fishing industry, and the scientific community (ANDERSON *et al.*, 2010b; LONG, 2012).

[4] SAR Marine User's Manual: http://www.sarusersmanual.com

1.2. MOTIVATION

The Mexican oil company (i.e. Petróleos Mexicanos – Pemex[5]) has an important and well-established OGEPI operation in the Gulf of Mexico's southernmost bight where it has several platforms and oil rigs exploring and producing HCs (PEMEX, 2007). In fact, Campeche Bay (or Bay of Campeche), located off the Mexican coast (Figure 1-1), has what once was the most important petroleum province of the Western Hemisphere – the Cantarell Oil Field (CARMALT & ST. JOHN, 1986; TALWANI, 2011).

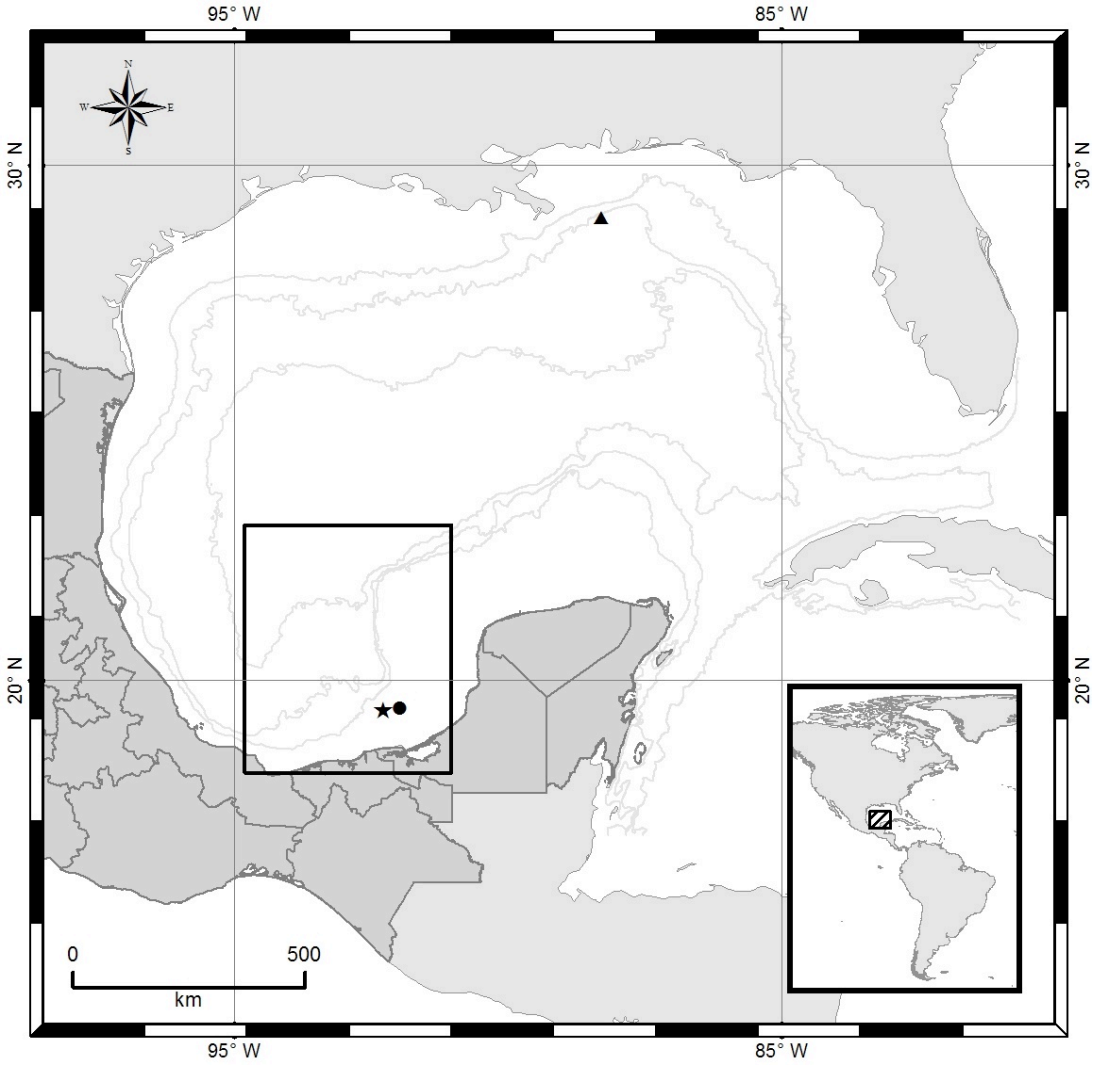

Figure 1-1: Gulf of Mexico highlighting the Campeche Bay region. The rectangle illustrates the region from which most oil slicks (98%) analyzed herein have been observed (see Section 6.1). The dot corresponds to the location of the Cantarell Oil Seep. The Ixtoc-1 and Deepwater Horizon sites are represented with a star and a triangle, respectively. Isobaths of 200m, 1000m, and 3000m are also shown. Courtesy of Adriano Vasconcelos.

[5] Pemex: http://www.pemex.com

The associated risk of operational petroleum leakage leads Pemex to be in a continuous state of alert for reducing possible negative environmental impacts on marine and coastal ecosystems (BROWN & FINGAS, 2001; SOLBERG, 2012; STAPLES & RODRIGUES, 2013). However, not all the oil observed on the surface of the ocean in this region comes from operational leaks, as oil naturally seeps in several sites throughout Campeche Bay (MIRANDA *et al.*, 2004).

The fragile and delicate coastal environment along the Mexican Gulf shoreline with its embayments, fringed by beaches, inlets, bays, river mouths, and highly sensitive mangroves, are in permanent jeopardy because of the constant occurrence of oil slicks in the Campeche Bay region (JERNELOV & LINDEN, 1981a). As a result, Pemex uses satellite measurements to monitor this region to map the oil slick occurrence, thus giving support to its decision-making processes – see Chapter 2.

Environmental and economical issues associated to natural and man-made input of HCs are a constant concern to the OGEPI (GADE *et al.*, 1996; WISMANN *et al.*, 1993). But besides the effectiveness of using satellite imagery on coastal zone management for oil contamination monitoring, a supplementary application for satellite sensors is on the recognition of the oil slick type – i.e. seeps versus spills (SENGUPTA & SAHA, 2008).

Information about the oil slick type is an improvement requirement for several purposes, for example, adequate decision support system (DSS), environmental monitoring, emergency response, proper contingency measures, legal responsibility for prosecuting the HC polluter, etc. (ENGELHARDT, 1999; MCHUGH, 2009; MERA *et al.*, 2012; 2014). Furthermore, reliable detection surveillance capable of distinguishing the oil slick type can add accuracy to oil slick's forecast systems (KULAWIAK *et al.*, 2010; OZGOKMEN *et al.*, 2014). Additionally, the knowledge of the oil slick type can enhance tridimensional mathematical models that backtrack (i.e. hindcast) oil seeps observed on the sea surface to its geographical seafloor origin (MANO *et al.*, 2011; 2014).

The oil slick type identification using satellite measurements can promote considerable scientific advances and two distinct points of view come into play:

- From the standpoint of environmental monitoring programs, one of the positive influences is the possibility of reducing ambiguities about the source of the observed oil: seeped or spilled oil. This can develop the relationship between the OGEPI and governmental agencies, thus reducing political uproar (PEMEX, 2013b).

- From an economic standpoint, the satellite synoptic view is an attractive option to distinguish the oil slick type that can lead to offshore OGEPI discoveries, bringing invaluable information for exploring active petroleum systems (BROOKS, 1990; MIRANDA *et al.*, 2001; RORIZ, 2006). Indeed, if the distinguishment of seeps and spills becomes a reality, satellite information can directly assist in the search to find new oil fields in offshore exploration frontiers, a constant goal of a crucial sector for the world's economic development (SENGUPTA & SAHA, 2008).

Inside this scope, the ability to map the surface of the ocean to distinguish seeps from spills has a couple of scientific leading purposes linked to solve two OGEPI problems: finding spills represents an environmental solution, whereas locating seeps turns out to be an economic solution as it can indicate the presence of active petroleum systems.

1.3. OBJECTIVES

Naturally-occurring oil seeps and human-related oil spills are both products of mineral oil floating on the sea surface, therefore, it is expected that their surface signatures in satellite imagery are fairly similar. It is based on this assumption that the main objective of this D.Sc. research is established:

- An exploratory data analysis (EDA) intends to distinguish natural from man-made oil slicks observed on the sea surface of Campeche Bay to a useful level of confidence for systematic use.

Specific goals are also recognized, and the present investigation aims to elucidate a twofold goal concerning oil slicks observed on the surface of the ocean in the Campeche Bay region (Figure 1-1):

- Describe their spatio-temporal distribution after disclosing important aspects related to their occurrence.
- Evaluate, by means of multivariate data analysis techniques, the capacity of distinguishing their oil slick type.

In the course of achieving the objective of this research, three scientific questions about the footprint of the oil observed on the sea surface are sought:

- Does seeped oil floating on the ocean surface have SAR backscatter signature distinctive enough to distinguish it from anthropogenically-spilled oil?
- Can the geometry, shape, and dimensions of oil slicks, as determined by digital image classification of satellite imagery, be used to distinguish seeps from spills?

- Which combination of characteristics leads to the generation of a system capable of distinguishing between seeped and spilled oil?

To address the aforementioned matters, a multi-year RADARSAT dataset (2000-2012) is leveraged to perform a data mining of selected oil slicks' characteristics, therefore, this study devises an additional goal:

- Design an innovative qualitative-quantitative classification algorithm[6] to distinguish natural from man-made oil slicks.

1.4. RESEARCH STRATEGY

For convenience, two flow diagrams are presented to facilitate the comprehension of the present D.Sc. research: Figure 1-2 shows a pictorial view of the research rationale, whereas Figure 1-3 summarizes the research structure. The former is illustrated on shades of grey and the latter is color-coded, both for clarity. Yet, specific details on the reasons for the selected strategy and the description of how they have been implemented are mustered in the length of the manuscript.

1.5. JUSTIFICATION

Along with the following two Sections (Challenges and Contributions), this Section emphasizes relevant aspects about the rationale of the present investigation. Although such information could be moved from one Section to another, the reader should bear in mind that despite all possible reasons justifying the effort to distinguish natural from man-made oil slicks, this D.Sc. research would not be possible without data.

Indeed, the exploratory nature of the investigation carried out herein is towards data analysis, and as such, it requires a comprehensive scientific-environmental dataset to reach the proposed objective. Data collections having extensive spatio-temporal resolution are imperative to be representative of the phenomena under investigation and to analyze ecological distresses (LEGENDRE & LEGENDRE, 2012). Preferably, the dataset should have good spatial coverage with enough temporal resolution to suitably reflect the environmental problem been studied.

[6] "The word *algorithm* comes to us from the name of the ninth-century Persian mathematician Abu Ja'far Mohammed ibn Mûsâ al-Khowârizmî, who wrote a treatise on mathematics entitled *Kitab al jabr w'al-muqabala*, whose title gave rise to the English word *algebra*. Informally, you can think of an algorithm as a strategy for solving a problem." (ROBERTS, 2008 – p. 8).

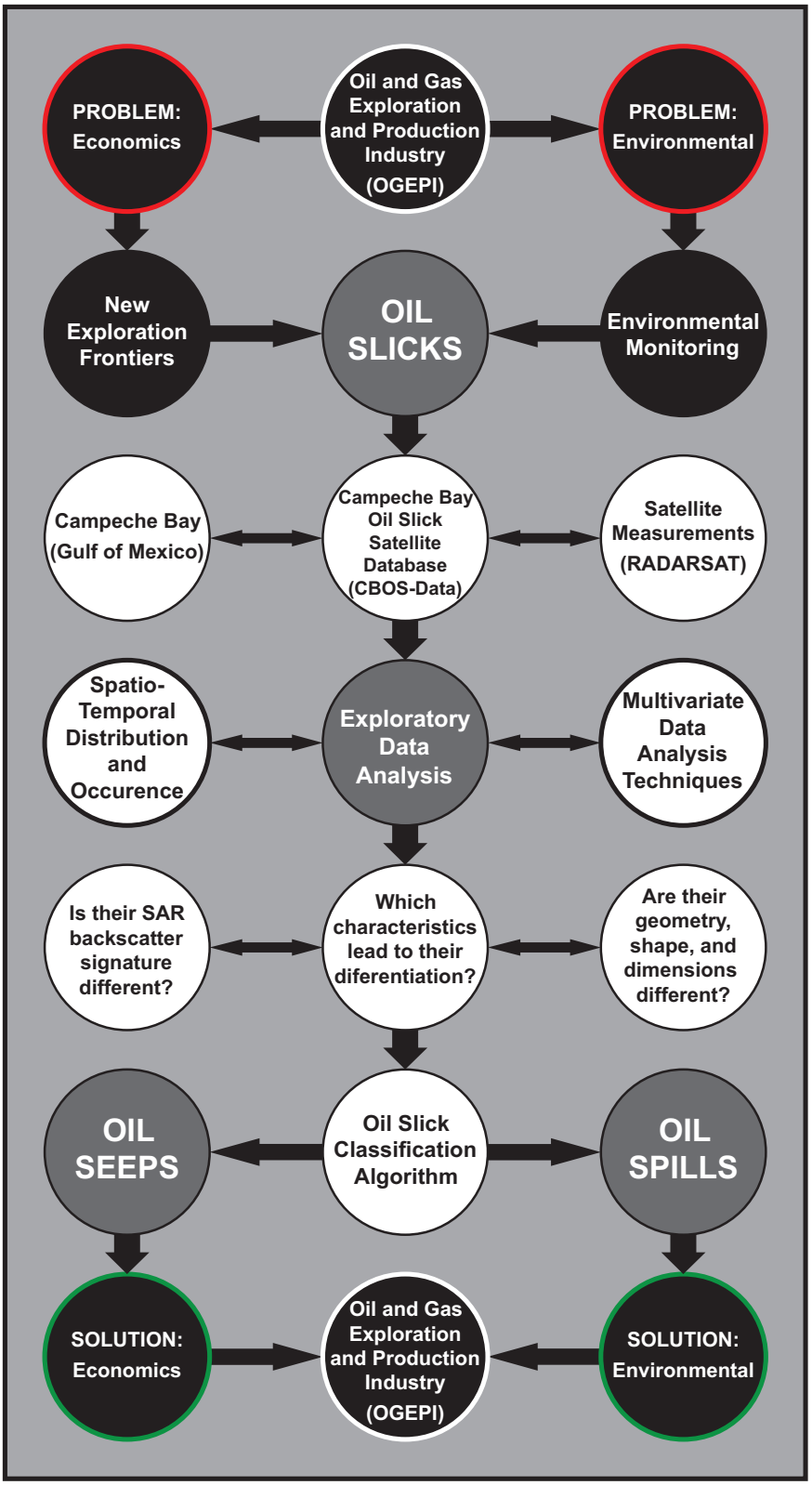

Figure 1-2: D.Sc. research rationale that uses multivariate data analysis applied to satellite-derived measurements to distinguish the type of the oil slicks (i.e. oil seeps versus oil spills) observed on the sea surface of Campeche Bay (Figure 1-1). Black circles correspond to the motivation driving this investigation (Section 1.2). Grey circles indicate the main objective and white circles represent the specific goals targeted herein (Section 1.3).

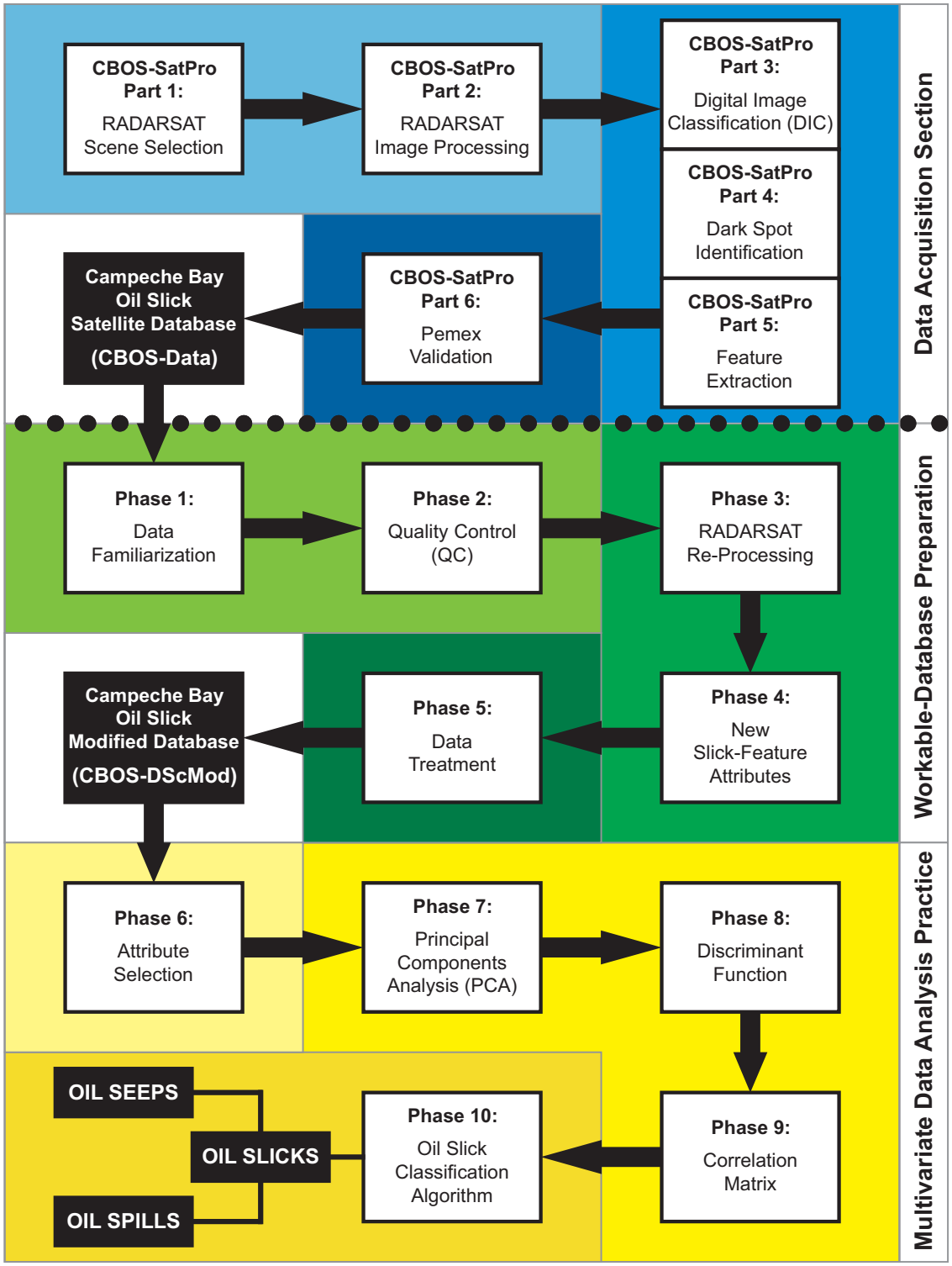

Figure 1-3: D.Sc. research structure depicting the Phases followed during this Dissertation. Dotted line represents a benchmark between the six blue Parts of the Data Acquisition section that have been accomplished during the Campeche Bay Oil Slick Satellite Project (CBOS-SatPro: between 2000 and 2012), and the two sections executed during the present investigation: Workable-Database Preparation (Green Phases: 1 to 5) and Multivariate Data Analysis Practice (Yellow Phases: 6 to 10).

More specifically, since the intention of this research is to tell apart seeps from spills using satellite imagery, a multi-year dataset imaging the surface of the ocean is a prerequisite to provide evidences for enlightening the specific goals. Indeed, the successful outcomes of the present study are only possible because of the availability of a large historical archive of oil slick sites in the Campeche Bay region. A thorough description of the Pemex monitoring project, as well as of its produced dataset used in the course of this study are presented in Chapter 2.

1.6. CHALLENGES

A broad scientific basis exists regarding the identification of oil slicks in satellite measurements (e.g. MONTALI *et al.*, 2006; TOPOUZELIS, 2008; FISCELLA *et al.*, 2010). However, even after a thorough examination of an appropriate, and vast, bibliography list (see References), the peer-reviewed, as well as the grey literature, seem to be somewhat limited concerning the differentiation of natural from man-made oil slicks. For this reason, it is good to bear in mind whilst reading this manuscript that the present analysis has a strong exploratory nature.

The differentiation between seeped and spilled oil is, in fact, not well covered (e.g. IVANOV *et al.*, 2007; SENGUPTA & SAHA, 2008; MCCAFFERY *et al.*, 2009). Instead, the major focus of the studies regarding oil slicks is to distinguish oil slicks from biogenic surface films (e.g. GADE *et al.*, 1998a; 1998b; WISMANN *et al.*, 1998) or oil slicks from look-alike features (e.g. BREKKE & SOLBERG, 2005a; 2005b). Many investigations describe manual image inspection processes or guidelines to establish automated approaches (e.g. CALABRESI *et al.*, 1999; TOPOUZELIS *et al.*, 2009; JONES, 2001). Undeniably, the exploratory data analysis performed on this investigation is intricate by nature.

Whilst the conjecture of most studies detecting oil slicks with satellite measurements tend to be short in terms of spaceborne image time series (ANDERSON *et al.*, 2010a), the present study makes use of a substantial number of oil slicks recognized in SAR imegery on the surface of the ocean in the Campeche Bay region. On the other hand, even though the dataset explored herein constitutes a noteworthy satellite resource for Pemex's environmental monitoring system, such a multi-year inventory has not been specifically acquired or compiled to accomplish an investigation as the one attained herein. As a result, challenges to reach the proposed objectives are implicit in the nature of the explored dataset that is somewhat biased towards the incidence of oil slicks related to Pemex's sphere of influence (SOI): OGEPI-related activities.

Many reasons determine the accuracy of oil slick detection algorithms, e.g. dataset, statistical approach, etc. (KUBAT *et al.*, 1998; MONTALI *et al.*, 2006). However, the success of obtaining promising results occurs when a good set of characteristics are incorporated into the automatic classifier (TOPOUZELIS, 2008). In fact, environmental analyses are based on the use of descriptors (LEGENDRE & LEGENDRE, 2012). Herein, these are also called as slick-features, attributes, or variables (i.e. items or columns of a tabular framework). The information from the descriptors is used to describe oil seeps and oil spills (i.e. transactions or tabulated lines).

Because the dataset originally explored on the present D.Sc. research (i.e. the one provided by the Pemex's environmental monitoring program) only has a handful of basic oil slick descriptors, it turns out to be humped on its physical content. Important measures describing the oil slicks' characteristics are not included and must be calculated, for instance, SAR-derived backscatter coefficients: sigma-naught (σ^o), beta-naught (β^o), and gamma-naught (γ^o). As such, the construction of a workable database is required with the calculation of new slick-feature attributes useful to describe the oil slick characteristics.

Additionally, the research completed herein differs from the other studies that have utilized the same archive of oil slicks from Campeche Bay (e.g. BEISL *et al.*, 2004; MENDOZA *et al.*, 2004a; 2004b; PEDROSO *et al.*, 2007; DA SILVA, 2008). This comes about the use of all observed oil slicks within Pemex monitoring effort use to describe the oil slick occurrence and spatio-temporal distribution, the comprehensive data filtering, the expansive data customization, as well as because of the multivariate data analysis techniques explored herein performed to differentiate oil seeps from oil spills.

1.7. CONTRIBUTIONS

Best and effective responses upon the strike of an environmental disaster come after a comprehensive scientific understanding of the complex nature of the catastrophe, e.g. oil release in the ocean (LAVROVA & KOSTIANOY, 2011; OZGOKMEN *et al.*, 2014). Based on this premise the investigation carried out herein promotes a novel idea bridging geochemistry and remote sensing research to express geophysical differences between seeped and spilled oil.

This D.Sc. research Dissertation presents experimental results of a successful attempt to discriminate oil seeps from oil spills using satellite-derive measurements. The

present D.Sc. research is a breaking edge investigation in the field of SAR imagery analysis as it positively establishes the possibilities of discriminating the oil slick type of oil slicks observed on the surface of the ocean using SAR-derived measurements from the RADARSAT satellites (CRSS, 1993; 2004; MDA, 2004; 2014). It is expected that the results of the present D.Sc. research can provide an environmental solution, as well as an economic boost while enhancing exploration programs directed at finding new oil and gas fields in offshore frontiers.

Comprehensive, but simple-to-use algorithms aref designed. Although data-specific (i.e. Pemex's satellite monitoring), its replicable format can be explored with another dataset from a different region. Along with the use of optical multispectral datasets to detect oil slicks at sea, data-mining practices are emerging to assist in the exploration for HCs (PLAZA *et al.*, 2005; SHAHEEN *et al.*, 2011; POLYCHRONIS & VASSILIA, 2013). Hence, the encouraging outcomes of the present D.Sc. research paves the way for further exercises to differentiate different targets observed in SAR imagery, for instance, oil slicks from look-alike features, also exploring classical multivariate data analysis techniques[7] as those emplyed here: Correlation (R-mode), Principal Components Analysis (PCA), Correlation Matrixes and Discriminant Function (MOITA NETO & MOITA, 1998; HAIR *et al.*, 2005; PREARO *et al.*, 2012).

In addition, as the present study uses data mining to differentiate the oil slick type, it can serve as an archetype for developing new multispectral algorithms. The study performed herein also shows that the differentiation of the oil slick type should indeed be carried out with approaches conventionally used to detect dark spots in SAR imagery, for instance, Artificial Neural Networks (ANN) – e.g. GERSHENSON (2003), ANGIULI *et al*. (2006), SHARMA *et al.* (2012), etc. Additionally, polarimetric investigations could indeed search ways to differentiate oil seeps from oil spills in SAR imagery (e.g. GAMBARDELLA *et al.*, 2007; NUNZIATA *et al.*, 2013; NUNZIATA & MIGLIACCIO, 2015).

[7] "No single family of methods can answer all questions raised in numerical ecology." (LEGENDRE & LEGENDRE, 2012 – p. 338).

CHAPTER 2

OPERATIONAL ENVIRONMENTAL MONITORING SYSTEM

Notwithstanding the concomitant oil input from both anthropogenically-spilled (i.e. petroleum leakage from OGEPI facilities associated with marine traffic of busy shipping lanes resulting in oil discharges) and naturally-occurring seepages sites varying in water depth with sizable seepage rates, what makes Campeche Bay a compelling ROI is the common presence and extensive monitoring of oil slicks observed at its sea surface. As introduced in Chapter 1, Pemex maintained a particular oil slick satellite-monitoring program from 2000 to 2012 that resulted in a comprehensive multi-year dataset, which is being explored on the present D.Sc.research. This Chapter is divided in three sections: Section 2.1 describes some peculiarities about the Campeche Bay region and its OGEPI-related activities, Section 2.2 and Section 2.3 offer, respectively, more details about the Pemex's satellite monitoring program and its resulting dataset.

2.1. STUDY AREA: CAMPECHE BAY

The region of the Caribbean off the Mexican coast, more specifically the Campeche Bay[8] (or "Gulfo de Campeche" in Spanish) is the Region of Interest (ROI) investigated herein (Figure 1-1). This region is bound by the western edge of Yucatán Peninsula and bordered by four Mexican states, namely from east to west: Yucatán, Campeche, Tabasco, and Veracruz. The local time for most of Gulf of Mexico, including the region of Campeche Bay, is minus 6 hours from the Coordinated Universal Time (UTC).

The Gulf of Mexico is approximately 1000 km meridionally (from Alabama/USA to Cancun/Mexico) and more than 1500 km zonally (from Florida/USA to Texas/USA) (Figure 1-1). Its main circulation cell is represented by the Loop Current and its oceanic rings, i.e. eddies, however, Campeche Bay is not directly influenced by such prevailing oceanographic features (VUKOVICH, 2004; 2005; 2007; MULLER-KARGER *et al.*, 2015). Two other major features influencing this region are an upwelling that brings nutrients to the surface oceanic layers of the northeastern edge of the Yucatán Peninsula and a permanent cyclonic gyre on the inner side of the Bay that promotes high phytoplankton productivity throughout the year (MERINO, 1997; GONZALEZ *et al.*, 2000).

[8] Resource Database for Gulf of Mexico Research: http://www.gulfbase.org/facts.php

A noteworthy air-sea interaction observed in the Gulf is the coupled system between its warm-water pool that acts as energy supply to tropical storms and/or hurricanes (HONG *et al.*, 2000; HU & MULLER-KARGER, 2007; NHC, 2015). In fact, Campeche Bay annually experiences intense wind conditions during the Atlantic hurricane season: boreal Summer-Fall running from June 1st through November 30th (MASTERS, 2010). The predominant wind direction in Campeche Bay, year-round, is from the east.

Environmental issues have long been observed in the Gulf of Mexico. For instance, anecdotal records, from as early as the 1650s, suggest that fish die-offs have been caused by harmful algal blooms (MAGAÑA *et al.*, 2003). However, even though such blooms still cause problems (CARVALHO *et al.*, 2010d; 2011), nowadays the major environmental concern in the Gulf of Mexico is HC contamination (PATTON *et al.*, 1981; CROUT, 2011). Petroleum commonly leaks into the Gulf due to natural causes or human-related activities, imposing a risk to the environment, shoreline inhabitants, local communities, fisheries (artisan and commercial), and to the tourism industry (MACDONALD *et al.*, 1996; GARCIA *et al.*, 2009; EOE, 2010c).

The attention of the OGEPI was brought to Campeche Bay, in the beginning of the 1960s, when a local fisherman – Rudesindo Cantarell Jiménez – reported seeing oil afloat in the region (CH, 2014). Although this phenomenon has been visually confirmed by Rudesindo, pre-Hispanic civilizations had long ago witnessed oil floating on the sea surface in the same region: *chapopotli*[9] in the Nahuatl native dialect – referred to it as "chapopotera" or "chapopote" in the language of the Spanish colonizers (QUINTERO-MARMOL *et al.*, 2005; PEMEX, 2013a). This is also referred to as asphalt, pitch, tar, or bitumen (WENDT & CYPHERS, 2008; NAEHR *et al.*, 2009). In fact, a prolific HC seepage site is found at approximately 70 km north of Ciudad del Carmen in water depths as shallow as 40 meters: the Cantarell Oil Seep (Figure 1-1 and Figure 2-1).

Over the past decades, many studies have used satellite resources to identify the oil discharge on Campeche Bay – e.g. QUINTERO-MARMOL *et al.* (2003), MENDOZA *et al.* (2004a), PEDROSO *et al.* (2007), DA SILVA (2008), etc. Such studies confirm that the most prominent oil input in area coverage, dimension, flow magnitude, and persistence is the Cantarell Oil Seep. The oil in this locality seeps intensely in visibly noticeable pulses and, once on the sea surface, usually moves to the west driven by the prevailing easterly wind (MIRANDA *et al.*, 2004).

[9] "*Petróleo crudo que brota de la tierra y es arrastado por los ríos hast alas playas del mar. En el México prehispánico se usaba como combustible y como pagamento.*" (JURADO & MONTEMAYOR, 2005 – p. 107).

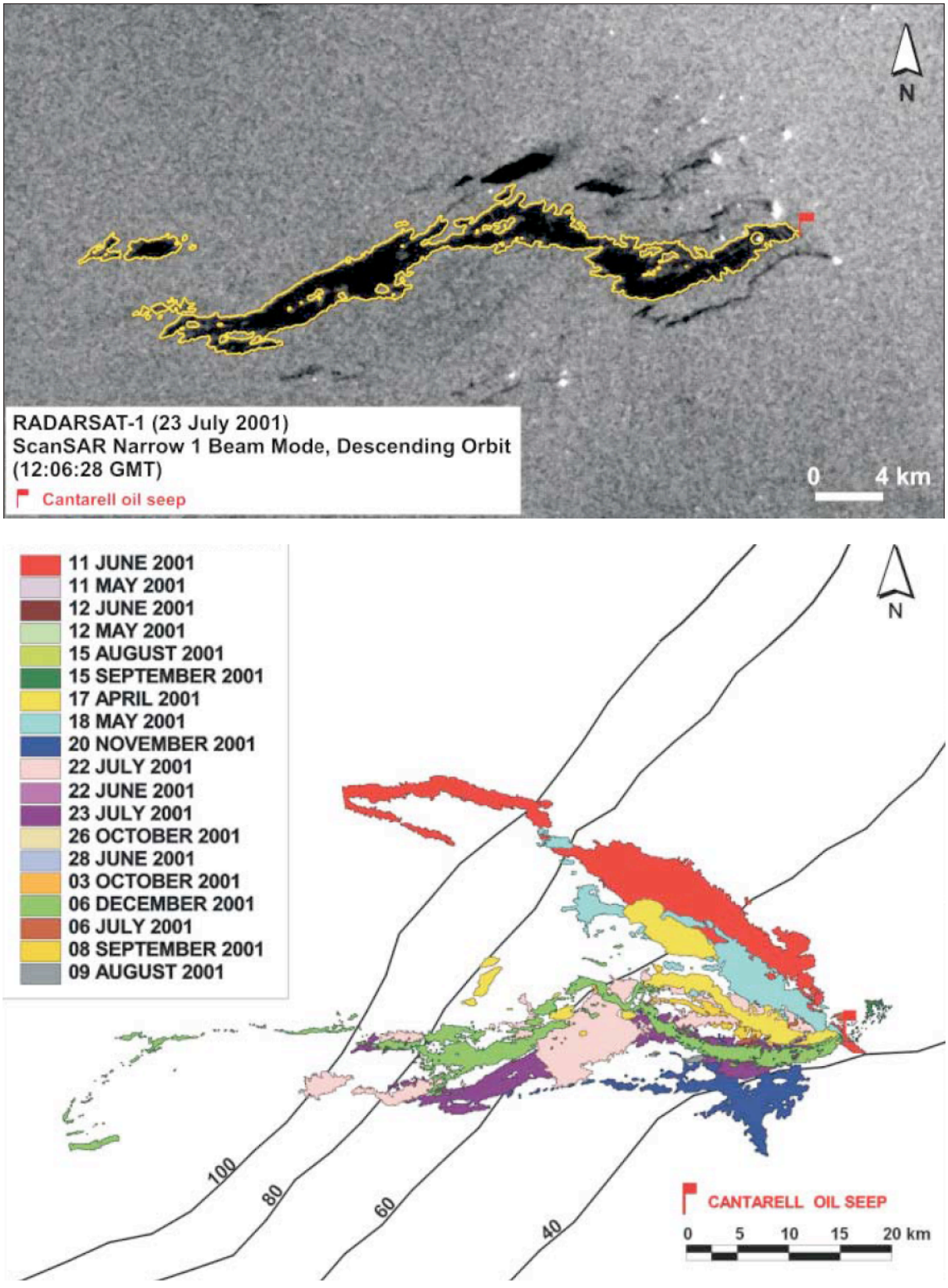

Figure 2-1: Upper panel: RADARSAT-1 scene highlighting the sea surface expression of the Cantarell Oil Seep as detected by the USTC algorithm. Other oil spills are also shown (i.e. dark zones of reduced radar backscatter). Lower panel: All surface signatures of the Cantarell Oil Seep Cluster during 2001. Source: Miranda et al. (2004). See also Figure 1-1 for the geographic location of the Cantarell Oil Seep on the Gulf of Mexico and Section 2.3.4 for the definition of Cluster.

It is very common to come across offshore sedimentary basins where oil naturally seeps to the sea surface (USGS, 2015). Indeed, about a decade after Rudesindo's revelation, Pemex started developing OGEPI activities in the Cantarell Oil Field[10] (CARMALT & ST. JOHN, 1986; VILLALÓN, 1998; PEDROSO *et al.*, 2006). The Cantarell Complex became a promising oil and gas exploration frontier, highly populated with platforms, oil rigs and pipelines; however, in recent years, its oil productivity has sharply declined (PEMEX, 2007; 2012a; TALWANI, 2011).

Since 1938, only Pemex has been allowed to exploit Mexico's oil and natural gas resources – this government-owned enterprise has constitutional consent to control OGEPI activity in Mexico. However, in 2015 its nationalized OGEPI was opened to private companies (VN, 2015). Pemex is very important to Mexico's economy and to the Federal Government, and is one of the largest Latin American oil companies (RAE, 2010). Pemex has four subsidiary companies: Pemex Exploración y Producción (PEP), Pemex Petroquímica, Pemex Gas y Petroquímica Básica and Pemex Refinación.

PEP has four petroleum administrative regions: Región Marina Noreste (RMNE), Región Norte, Región Marina Suroeste (RMSO), and Región Sur (PEMEX, 2012b). Even though the Cantarell Complex is situated at RMNE, oil spills, as well as oil seeps, occurring in this area also cause environmental impacts in the adjoining regions.

2.2. CAMPECHE BAY OIL SLICK SATELLITE PROJECT (CBOS-SATPRO)

In the search for a dynamic, reliable, and cost-effective approach to survey oil slicks in Campeche Bay, Pemex developed a plan to monitor its offshore OGEPI activities that could overcome reliance on classic and conventional oceanographic surveillance, such as direct contributions from airplane, helicopter, ship, moored, and drifting observations. These point inspections are weather-biased, restricted to daylight hours and visual inspections, thus having limited area coverage and high operational costs. In fact, given the extremely high-costs of offshore OGEPI activities, monitoring of oil slicks using satellite measurements is a well-accepted risk assessment approach in this region (e.g. BANNERMAN *et al.*, 2009; STANKIEWICZ, 2003).

[10] The Cantarell Oil Field has light oil deposits formed on a salt tectonic province in which evaporites are reported to the top of the Upper Jurassic – main source rocks are of Tithonian age (152 to 145 million years ago) – and a large anticlinal structure is associated with salt diapirs contributing to the formation of migration pathways reaching the seafloor (VILLALÓN, 1998; MIRANDA *et al.*, 2004; ALZAGA-RUIZ *et al.*, 2009; PEDROSO, 2009; TEXEIRA *et al.*, 2014).

Before the turn of the century in 2000, a technical group within PEP established an international collaboration to use SAR measurements for monitoring Campeche Bay. Having internal support from the Subdivision of Technology and Development (STDP) and Corporate Geospatial Information System (SICORI), PEP's environmental RMNE operational team approached the Canadian company RADARSAT International Inc. (RSI) and the Alberto Luiz Coimbra Institute for Graduate School and Research in Engineering (referred to as COPPE[11]) at the Federal University of Rio de Janeiro (UFRJ[12]) to elaborate a strategic oil slick environmental monitoring program. After MacDonald Dettwiler and Associates Ltd. (MDA[13]) purchased RSI (the exclusive distributor of the RADARSAT[14] satellite data), RSI was designated as MDA Geospatial Services Inc. (MDA-GSI). Both MDA-GSI and COPPE/UFRJ created the RADARSAT Resource Centre in Brazil (CBRR) to conduct such a project, among other initiatives. The CBRR is now called the Laboratory of Radar Remote Sensing Applied to the Petroleum Industry (known as LabSAR[15]). LabSAR is an associate laboratory within the Laboratory of Computational Methods in Engineering (LAMCE[16]) of the Civil Engineering Program (PEC[17]) of COPPE/UFRJ, as well as it is part of a strategic partnership with the Leopoldo Américo Miguez de Mello Research and Development Centre (referred to as CENPES[18]) within the Brazilian oil company: (Petrobras[19]).

By means of available cutting-edge imaging processing technology, jointly developed with CENPES, LabSAR researchers brought into play their multidisciplinary expertise for oil slick detection (MIRANDA *et al.*, 2004). In fact, two achievements are note:

1. The integration use of ancillary meteorological and oceanographic data from Earth Observing Systems (EOS) sensors to support the selection of SAR imagery, as well as to improve oil slick detection (MIRANDA *et al.*, 2001; BEISL *et al.*, 2001; SILVA JUNIOR *et al.*, 2003); and

2. Fully developed digital image classification (DIC) procedure exploring sea-surface radar texture and radiometry to identify oil slicks on the sea surface: USTC (Unsupervised Semivariogram Textural Classifier) (ALMEIDA-FILHO *et al.*, 2005).

[11] COPPE: http://www.coppe.ufrj.br
[12] UFRJ: http://www.ufrj.br
[13] MDA-GSI: http://gs.mdacorporation.com
[14] Canadian Space Agency: http://www.asc-csa.gc.ca/eng/satellites
[15] LabSAR: http://www.lamce.coppe.ufrj.br/secao-sensoriamento-remoto.html
[16] LAMCE: http://www.lamce.coppe.ufrj.br
[17] PEC: http://www.coc.ufrj.br
[18] CENPES: http://www.petrobras.com.br/pt/nossas-atividades/tecnologia-e-inovacao
[19] Petrobras: http://www.petrobras.br

These two encouraging outcomes that have the advantage of being low-cost compared to the high investments characterizing OGEPI activities were used as proof of concept to establish the basis for designing the environment monitoring strategy. Considering the intentions to monitor potential HC contamination in Campeche Bay, a contract was signed between PEP and MDA-GSI. This agreement aimed to use RADARSAT measurements to elucidate the origin and magnitude of the oil slicks in Campeche Bay.

As a result, a subcontract was signed between MDA-GSI and COPPE Foundation (COPPETEC[20]) for the execution the environmental monitoring project. Despite the fact that this agreement involves institutions from Mexico, Canada, and Brazil, most efforts to digitally process, interpret, and analyze the satellite imagery were conducted in the LabSAR facility at LAMCE/PEC/COPPE/UFRJ.

In the middle of 2000, a Pilot Study provided a means to design a systematic monitoring protocol for a Pre-Operational Application that took place a year later. These two years of experiments refined the oil slick detection methods within the needs and expectations of PEP's interests, making it possible to demonstrate, test, and establish a proven system capable of monitoring Pemex's SOI. After these preliminary two-years, a five-year contract (2002-2006) was employed in an operational fashion and renewable for the same period (2007-2011). At the end of the renewed contract, an additional contract assured the monitoring continuation during 2012. Supplementary short-period exploration contracts have also been signed during 2011 and 2012.

The distinct titles of this satellite-based environmental monitoring effort are listed in Table 2-1. For the sake of brevity, any reference made throughout this manuscript to this environmental monitoring project ordered by PEP is identified as the Campeche Bay Oil Slick Satellite Project – hereafter CBOS-SatPro.

This routine monitoring system has been incorporated into PEP's efforts for the assessment of potential environmental impacts and to evaluate the occurrence of oil slicks in Campeche Bay. It is mostly based on the multi-temporal inspection of SAR images of the RADARSAT satellites (MIRANDA *et al.*, 2004). Many publications are found describing this project, e.g. QUINTERO-MARMOL *et al.* (2003), MENDOZA *et al.* (2004a; 2004b), PEDROSO *et al.* (2007), among others.

[20] COPPETEC: http://www.coppetec.coppe.ufrj.br/site/

Table 2-1: Titles of the satellite-based environmental monitoring ordered by Pemex to detect oil slicks in Campeche Bay. Herein, such monitoring effort is referred to as the Campeche Bay Oil Slick Satellite Project (CBOS-SatPro).

Project (Start date)	Title (English)	Title (Spanish)
Pilot Study **(10 July 2000)**	*Local system design for detecting oil seeps and spills using images from the RADARSAT-1 satellite in the Northeast Marine Region (RMNE)*	*Diseño de un sistema local de detección de emanaciones naturales y accidentales de hidrocarburos empleando imágenes de radar del satélite RADARSAT-1, en la Región Marina Noreste (RMNE)*
Pre-Operational Application **(2001)**	*Regional program for detecting oil seeps and spills using RADARSAT-1 images on the Gulf of Mexico*	*Programa regional para la detección de emanaciones naturales y derrames de petróleo utilizando imágenes del satélite RADARSAT-1 en el Golfo de México*
Operational Contracts **(2002/2006)** **(2007/2011)**	*Oil seeps and spills monitoring using RADARSAT images in the Gulf do México*	*Monitoreo de emanaciones naturales y derrames de petróleo a través de imágenes del satélite RADARSAT en el Golfo de México*
Additional Contract **(2012)**	*Monitoring of oil seeps and spills through the use of RADARSAT -1 and RADARSAT -2 satellite images in the Gulf of Mexico in 2012*	*Monitoreo de emanaciones naturales y derrames de petróleo a través de imágenes del satélite RADARSAT-1 y RADARSAT-2 en el Golfo de México en 2012*

At the start, in 2000, only archived images of RADARSAT-1 (PARASHAR *et al.*, 1993) were explored, but programmed acquisitions were carried out in all subsequent years of the project. After RADARSAT-2 (MORENA *et al.*, 2004) was launched in 2008, measurements from both satellites were used (BANNERMAN *et al.*, 2009).

As concurrent oil seeps and oil spills occur in Campeche Bay, by ascertaining the dynamics of the observed features, PEP can define advanced management practices of decision-making strategies for environmental responses. Knowledge of the oil slick spatio-temporal distribution (i.e. origin, magnitude, displacement, behavior and fate) can be used to control and prevent deleterious impacts on the marine and coastal environment.

Another asset of the CBOS-SatPro is that PEP's initiative to characterize the oil slicks in Campeche Bay also helps to optimize environmental countermeasures avoiding financial penalties (PEMEX, 2013b). This can provide a better relationship between PEP's OGEPI operations and many societal stakeholders.

2.3. CAMPECHE BAY OIL SLICK SATELLITE DATABASE (CBOS-DATA)

The CBOS-SatPro was executed in a continuous manner for about 13 years (from 2000 to 2012) and a large amount of spaceborne SAR data was analyzed. With an average of at least one SAR scene per week, more than 700 satellite scenes were used to inspect Pemex's SOI – this includes images from both RADARSAT satellites. During this period, it was possible to observe over 14 thousand oil slicks in Campeche Bay. All information produced in the course of the CBOS-SatPro forms a comprehensive multi-year dataset of SAR measurements that is explored herein. For the purpose of the present D.Sc. research, such dataset is referred to as the Campeche Bay Oil Slick Satellite Database – hereafter CBOS-Data.

The CBOS-Data consists of the six Blue Parts of the CBOS-SatPro (Figure 1-3). As such, an important point to note is that the content of this dataset has been collected before the present investigation started. The first two parts have been performed to select and process the satellite imagery: RADARSAT Scene Selection (CBOS-SatPro Part 1: Section 2.3.1) and RADARSAT Image Processing (CBOS-SatPro Part 2: Section 2.3.2) – their schematization is portrayed on Figure 2-2.

Once the images were selected and processed, the oil slicks were identified – this is a complex process that relies on the differentiation of dark regions in SAR measurements (MACDONALD *et al.*, 1993). The final aim of the characterization of these dark regions is to tell apart targets that are oil slicks from those originating from other processes – i.e. look-alike features (HOVLAND *et al.*, 1994; JOHANNESSEN *et al.*, 1996). Specific remote sensing aspects of satellite sensors capable of detecting oil slicks are addressed in Chapter 4.

The basics of identifying dark regions in SAR imagery are often common to most oil slick detection monitoring systems (BREKKE & SOLBERG, 2005a; 2005b; SINGHA *et al.*, 2013). This is typically divided into a three-step framework: Digital Image Classification (DIC), Feature-Extraction, and Feature-Classification – Section 4.4 presents general details about these steps.

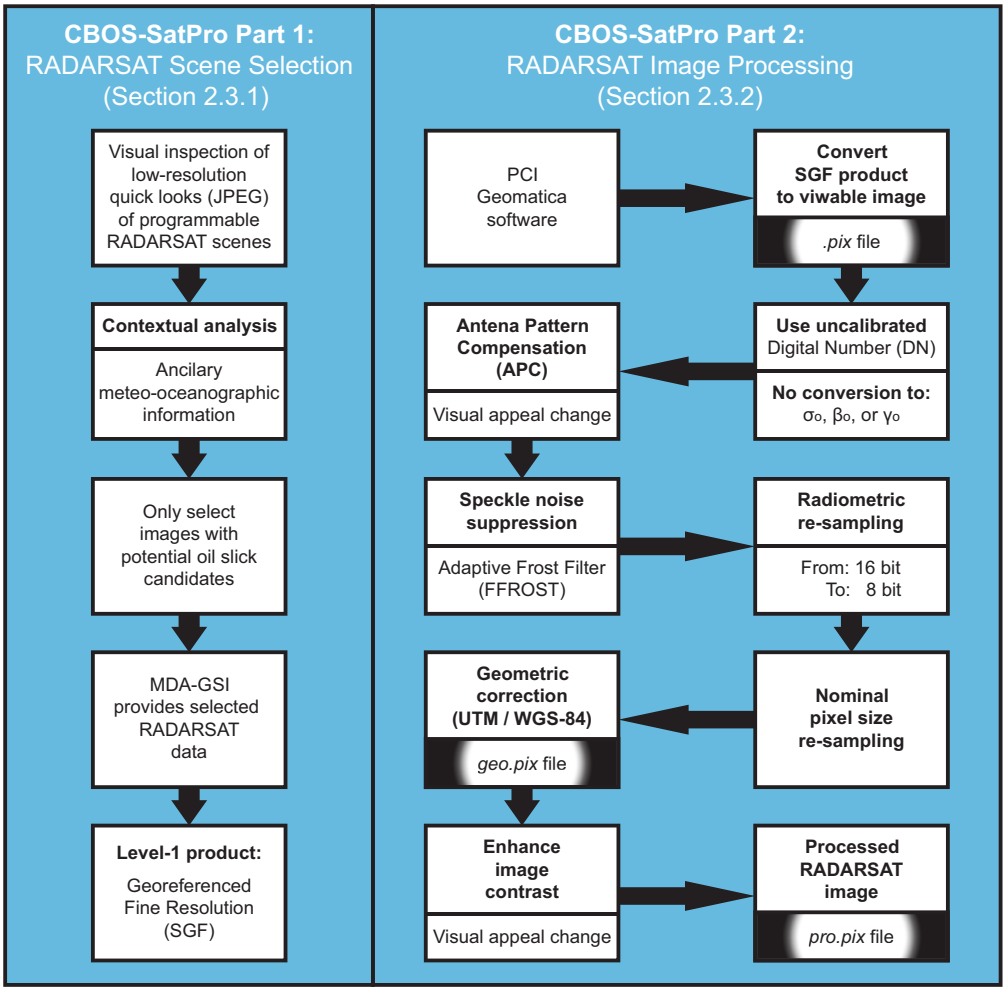

Figure 2-2: First two parts of the Data Acquisition performed during the Campeche Bay Oil Slick Satellite Project (CBOS-SatPro). See also Figure 1-3.

A noteworthy aspect about the procedures performed during of the CBOS-SatPro is that the operational processing structure completed to build the CBOS-Data has the last two steps inverted: slick-feature attributes were only calculated after the identification was completed. Essentially, this occurred because the oil slick identification was carried under the visual inspection of domain specialists that discounted look-alike features. Therefore, only targets classified as oil slicks (i.e. seeps or spills) were accounted for on the CBOS-Data.

During the CBOS-SatPro this three-step framework has been completed on a semi-automatic manner to recognize (CBOS-SatPro Part 3: Section 2.3.3), identify (CBOS-SatPro Part 4: Section 2.3.4), and characterize (CBOS-SatPro Part 5: Section 2.3.5) potential oil slicks. An additional validation (CBOS-SatPro Part 6: Section 2.3.6) took place at the end of the oil slick detection processing chain. These, which correspond to last blue Parts of the research structure flow diagram shown on Figure 1-3, are schematized on Figure 2-3.

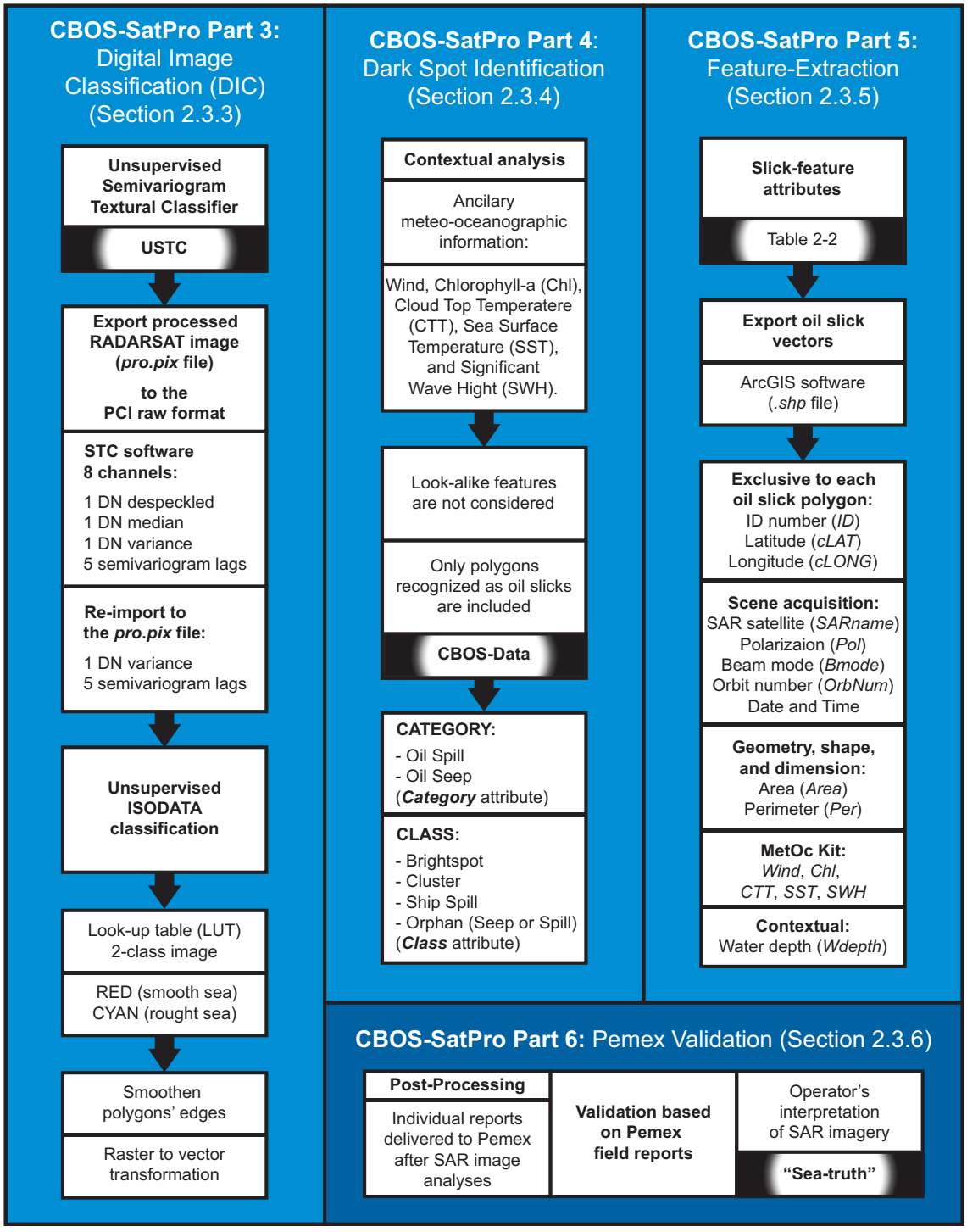

Figure 2-3: Last four parts of the Data Acquisition performed during the Campeche Bay Oil Slick Satellite Project (CBOS-SatPro). See also Figure 1-3.

In summary, the six parts of the CBOS-SatPro (Figure 2-2 and Figure 2-3) gave rise to the tabular content of the CBOS-Data. These have been executed before the start of the present investigation and correspond to the Data Acquisition Section depicted on Figure 1-3. Their description is presented below:

2.3.1. CBOS-SATPRO PART 1: RADARSAT SCENE SELECTION

Figure 2-2 schematizes the RADARSAT Scene Selection steps performed during the CBOS-SatPro, in which a careful data selection was accomplished through visual inspection of low-resolution "quick looks" (8-bit JPEG files) of scheduled RADARSAT scenes[21]. The main scene selection criterion was the presence of potential and recognizable oil slick candidates, as visually interpreted by the analyst.

This preliminary evaluation used to be performed prior to the purchase of the actual full resolution RADARSAT image, thus provided by MDA-GSI. It occurred alongside the analysis of concurrent meteo-oceanographic conditions (see Section 2.3.4) and if ancillary information was not available, the SAR image might not to be selected (BEISL *et al.*, 2001; SILVA JUNIOR *et al.*, 2003).

The ordered RADARSAT products were on the SAR Georeferenced Fine Resolution (SGF) format. Such Level-1 product is frequently referred to as a "path-oriented image" because the scene is orientated parallel to the satellite's orbit path direction (i.e. aligned with the swath geometry). Even though SGF products can be displayed as viewable images, the utilization of specific supplementary image processing software is a fundamental requirement, as described in the next Section.

2.3.2. CBOS-SATPRO PART 2: RADARSAT IMAGE PROCESSING

This Section describes the image processing chain applied to the RADARSAT images explored in the course of the CBOS-SatPro. Such procedures were performed in the order presented below – as depicted on Figure 2-2. However, they are project-specific, as the approach of different projects can be different depending upon specific goals (e.g. SOLER, 2000; SOUZA FILHO & PARADELLA, 2001; ALBUQUERQUE, 2004; PADHYE & REGE, 2015). As shown on Section 5.3, the imaging processing performed during the present D.Sc. research are not the same as those of the CBOS-SatPro.

The following ten paragraphs match the ten right-side boxes of Figure 2-2. This is intended to help the reader's comprehension of the image processing steps undergone during the CBOS-SatPro, as well as of those executed during the present D.Sc. research (see Section 5.3).

[21] As of the time this Dissertation has been competed, the quick look purchase option was no longer available.

• The complete set of the CBOS-SatPro image processing utilized functions, modules, filters, and algorithms of a specific image processing analysis tool: PCI Geomatica Software Suite. A 30-day free trial version can be fully downloaded from the PCI Geomatics webpage[22] – nevertheless, only a limited amount of very basic package functionalities are available.

• The SGF-provided products were imported to a viewable image in the PCI Database file format with the *.pix* extension (*PCIDSK*). These images are given in uncalibrated Digital Numbers (DN's) that correspond to the grey-level count assigned to each grid position (i.e. pixel) – for instance, between 0 and 255 for 8-bit images (HENDERSON & LEWIS, 1998). DN represents the amplitude of the radar return signal received by the antenna system (CHAN & KOO, 2008).

• DN values can be converted to obtain SAR-derived backscatter coefficients – i.e. sigma-naught (σ^o), beta-naught (β^o), or gamma-naught (γ^o) – in which a straightforward procedure relates DN to σ^o, β^o, or γ^o (see Section 4.3 and references therein for further details). Nevertheless, it is important to highlight that during the CBOS-SatPro this conversion was not performed and SAR images were processed and analyzed using DN's.

• A radiometric balancing (i.e. Antenna Pattern Compensation: APC) was applied to compensate for the non-uniform SAR illumination in the range direction (PCI manual). However, this procedure does not correct for the antenna beam pattern. Instead, eventual antenna-related effects are reduced with the use of a polynomial function of user-defined order: 2nd order was used in the CBOS-SatPro. In summary, the APC function only changes the image visual appeal. A multiplicative transformation is applied to each pixel: the output DN on a position *X* (*Output(X)*) is set equal to the input DN on the position *X*, minus the minimum DN of the image (*DNmin*), divided by the polynomial function (*P(X)*), minus *DNmin*, multiplied by the mean DN of the image (*DNmean*):

$$Output(X) = [(Input(X) - DNmin)/(P(X) - DNmin)] * DNmean$$

[22] PCI Geomatics: http://www.pcigeomatics.com

• High frequency noise (i.e. speckle[23]) can degrade the quality of SAR imagery. A despeckle filter is frequently implemented on a pixel-by-pixel basis as a circular symmetric user-defined exponential weighting function (PADHYE & REGE, 2015). Out of the filters designed to improve signal-to-noise-ratio, the adaptive Frost filter (*FFROST* algorithm) was selected with a 3x3 window surrounding individual pixel (FROST *et al.*, 1982; SOUZA, 2006). It has been demonstrated that this window is adequate to smooth out speckled SAR data with low levels of textural information loss and good balance in preserving image edges (ALMEIDA-FILHO *et al.*, 2005).

• When applicable, the speckle-free SAR images underwent a radiometric re-scaling correction, in which the image was re-sampled from 16 to 8 bit. This is a prerequisite to use the USTC algorithm, as portrayed in Section 2.3.3.

• An additional re-scaling correction was performed using the Image Averaging (*IIIAVG*) algorithm, in which the images were re-sampled for the nominal pixel size. This varied per beam mode (e.g. ScanSAR Narrow: from 25m to 50m).

• The PCI *OrthoEngine* module was used to geometrically correct the *.pix* file image: *geo.pix* file. Depending upon the operator's choice, the images were georeferenced using a nearest neighbor model with a 2nd-degree polynomial rectification or a RADARSAT Satellite Modeling (Radar Specific Model). Regardless of the method of choice, coordinates provided in the SGF header file were used: ground control points (GCPs) at the Earth's surface collected on the satellite GCP receiver, i.e. satellite's orbit and attitude ephemeris (RSI, 1997; 1998). Universal Transverse Mercator (UTM) at 15^{o} North with the geodetic datum World Geodetic System 1984 (WGS-84) was used to register the images.

• Histograms of the 8-bit image (0-255) were linearly stretched to enhance the contrast between low-return signal features and the return of neighboring sea clutter[24] areas. This contrast adjustment is operator-dependent and equalizes DN frequencies to a scale factor related to manually selected optimum levels of each image. As with the APC, this only changes the image visual appeal to assist interpretation.

[23] Speckle noise inherently occurs in SAR data as an intrinsic characteristic of the radiometric output. It is a multiplicative random granular noise associated with fluctuations in the pixel brightness intensity that may disrupt the visual interpretation of SAR images (HENDERSON & LEWIS, 1998; MASOOMI *et al.*, 2012).

[24] Sea clutter: textural and/or spectral signature defining (i.e. describing) the surface of the ocean from the satellite standpoint of view.

- After completing these image-processing steps (Figure 2-2), a processed image was created: *.pro.pix* file. Hence, this file is ready to be fully utilized on the three-step framework for detecting dark spots, as described in the following Sections.

2.3.3. CBOS-SATPRO PART 3: DIGITAL IMAGE CLASSIFICATION (DIC)

The DIC was performed on the *.pro.pix* files according to the schematization depicted on Figure 2-3. The USTC algorithm enhances some aspects of two sea surface domains: textural (shape and value of the circular semivariogram function) and radiometric (despeckled DN values). A peculiar aspect is that the USTC works with 8-bit data to lower computational costs. A broader discussion about the USTC algorithm and a complete description of the semivariogram function are found in MIRANDA *et al.* (2001; 2004) and ALMEIDA-FILHO *et al.* (2005). Yet, a synthesized USTC description is presented here:

- **USTC:** Unsupervised Semivariogram Textural Classifier

Because every object on the Earth's surface has its own set of textural and spectral properties, different targets have distinct signatures when detected by remote sensors. Based on this principle, the USTC algorithm identifies the fingerprint of specific targets at the sea-surface, which can be potential oil slick candidates or look-alike features, compared to the sea surface background (i.e. sea clutter). The USTC outcomes are polygons delimiting the borders of such low-backscattering features.

This deterministic digital image classifier identifies dark regions of smooth texture (and low backscatter) that present specular reflection of the incoming radar beam. The adjoining sea clutter is characterized by rough texture (and diffuse backscatter), while platforms and ships are related to a very strong return signal caused by double bounce (in the sense of a corner-cube reflector) of the transmitted radar pulse (FREEMAN, 1992).

The USTC object detection is only semi-automatic, as it requires human intervention: the shapes of interest are recognized by visual inspection of the operator, who builds a better representation of the targets observed on the SAR imagery (see USTC stages described below). Because of the USTC shaping complexity, the analyst eventually needs to regroup the polygons, frequently consisting of several parts.

MIRANDA *et al.* (2004) presents an experiment that validated the oil slick mapping capabilities of using RADARSAT imagery digitally classified with the USTC algorithm. Pemex, under the supervision of the Mexican Navy (i.e. Secretaría de Marina Armada de México – SEMAR), conducted a controlled oil spill exercise, releasing oil in the marine environment. Two separate discharges (100 and 476 liters, about 0.63 and 3 barrels, respectively) were released approximately two km apart from each other and two hours prior to the RADARSAT overpass. The accurate detection of such oil slicks (with 0.02 km^2 and 0.26 km^2, respectively) corroborates the potential of combining RADARSAT images with the USTC algorithm to monitor oil slicks observed on the sea surface. Similar controlled experiments are found in the literature using other DIC algorithms, e.g. BERN *et al.* (1993), OKAMOTO *et al.* (1994).

- **USTC 1st stage**: STC software

The processed RADARSAT images (*.pro.pix* files), delivered at the end of the RADARSAT Image Processing (CBOS-SatPro Part 2: Section 2.3.2), were exported in the PCI raw format (*.raw* file). This *.raw* file was utilized as input in the Semivariogram Textural Classifier (STC) software (MACDONALD, 1991).

The STC software requires the user to specify the number of columns and lines of each SAR image, as well as the number of semivariogram lag distances: 5 in the case of the CBOS-SatPro (RORIZ, 2006). The STC outcome has a standard STC format (*.stc* file) with 8 channels: 1 with the SAR despeckled DN values, 1 with the median DN, 1 with the DN variance, and 5 semivariogram lag distances.

Using the PCI *Imagerd* function (Read Image File), 6 channels of the *.stc* file (i.e. the variance channel and the 5 semivariogram lag distances) were imported and incorporated into the one-channel *.pro.pix* file. As a result, the *.pro.pix* file ends up with seven channels.

- **USTC 2nd stage:** Clustering

To accommodate the classification result of this clustering stage, an 8th channel is created in the *.pro.pix* file. The PCI *ISODATA* clustering algorithm (TOU & GONZALEZ, 1974) is applied to perform an unsupervised classification, in which the numbers of classes and iterations vary from case to case. A land mask was used and patches of smooth texture (representing both, oceanic surface contaminated with oil and/or look-alike features) were separated from intermediate to rough regions.

- **USTC 3rd stage:** Look-up-table (LUT)

An interactive class aggregation was performed using PCI. The previously *ISODATA* created classes are merged together, consequently forming a two-class image. For that, a LUT was created: Red class (Red: 255; Green: 0; Blue: 0) and Cyan class (Red: 0; Green: 255; Blue: 255). Such a color-scale (i.e. pseudo color table – PCT) is merely arbitrary; but as seen below, the specification of these PCT indices are useful in the description of the subsequent CBOS-SatPro Parts.

The PCT Red class is associated with regions with smooth textures (or low grey-scale DN's) that are indicative of oil slicks or look-alike features, whereas the PCT Cyan class represents the rough textures. The latter corresponds to anything else in the image: grey-scale DN's ranging between intermediate (i.e. oil-free sea surface – sea clutter) to high (i.e. double bounce of the transmitted radar pulse – ships, tankers, platforms, oil rigs, etc.).

- **USTC 4th stage:** Vectorization

The PCI Mode Filter (*FMO*), with a 3-by-3-pixel window, was applied before the vectorization process. This aimed to smooth the edges between the two PCT classes, as well as to reduce whichever classification noise may have happened.

The last USTC procedure uses the PCI *RTV* (Raster to Vector) transformation function to vectorize the raster polygons of the PCT Red class. The borders of the targets are set in a semi-automatic manner, and all vectors must be closed polygons.

2.3.4. CBOS-SATPRO PART 4: DARK SPOT IDENTIFICATION

The Dark Spot Identificatio performed during the CBOS-SatPro (Figure 2-3) places emphasis on three different aspects: visual inspection to select only oil slicks, and two data separations: into categories and classes. While category is the broadest range (i.e. oil seep or oil spill), classes are the next range in which each category has further sub-groups.

- **1st Feature-Classification Aspect:** Visual inspection

The systematic photo-interpretation started with a contextual analysis that explored what is called herein as Meteorological and Oceanographic Kit (MetOc-Kit – see Section 4.5.5). This consists of a combined broad-range of prevailing ancillary data acquired from several EOS sensors at the SAR overpass time, or as close as possible

(BEISL *et al.*, 2001; SILVA JUNIOR *et al.*, 2003). It includes the examination of value-added environmental products – i.e. meteo-oceanographic conditions such as wind (speed and direction), chlorophyll-a concentration (Chl), cloud top temperature (CTT), sea surface temperature (SST), and significant wave height (SWH).

This analysis assists the manual differentiation performed by the operator and plays a crucial role because the PCT Red class is comprised of both, indicative oil slick candidates and/or look-alike features. Therefore, the MetOc-Kit supported the operator's decision of whether the identified target was an actual oil slick or not.

As the CBOS-SatPro aimed to map oil slicks, SAR textural features that are identified as ambiguities in the SAR imagery (i.e. look-alike features) were left out of the analysis. These were not cataloged, and, in being so, from the polygons identified with the USTC analysis (CBOS-SatPro Part 3: DIC – Section 2.3.3), only the ones truly recognized by the operator as being oil slicks were included in the CBOS-Data.

- **2nd Feature-Classification Aspect:** Categorization

The selected oil slicks were manually separated into their respective oil slick type: oil seeps or oil spills. These are indexed under the *Category* attribute and are vital to the design of the qualitative-quantitative classification algorithm proposed herein – see Chapter 5.

OGEPI facilities are noticeable as brightspots on SAR imagery that are caused by the double bounce of the transmitted radar pulse (ALPERS & ESPEDAL, 2004). Depending upon the closeness of the floating oil to a specific OGEPI installation (or vessel), it was possible to associate that structure (or ship) as the source of the leaked oil – therefore classifying it as an oil spill. These are associated to passing vessels near the leaked oil (ESPEDAL & JOHANNESSEN, 2000). OGEPI facilities and ships locations were provided by PEP – see Section 2.3.6 (CBOS-SatPro Part 6: Pemex Validation).

Oil seeps were identified when there were no OGEPI facilities, ships, or other recent human activities on nearby locations associated to its location. Site repetitively is the main indicator of any oil seepage site on the surface of the ocean. Once again it is good to highlight that the term oil seep solely considers the surface oil footprint, not referring to the whole HC seepage process – see Section 3.2.

- **3rd Feature-Classification Aspect:** Classification

Each member of the two oil categories was manually classified into classes. These are represented by a site-specific criterion based on the identity of their point source on the sea surface: *Class* attribute. The following class terms are explored on the present D.Sc. research to describe the CBOS-SatPro information:

Clusters[25] A collection of oil seeps with repeated occurrences about the same geographical location on several SAR images. At least three different observations are necessary to identify a given Cluster (e.g. Figure 2-1).

Brightspots A group of oil spills from different oil rigs within the same oilfield. This nomenclature is in reference to the bright appearance of platforms and ships, on SAR imagery.

Ship Spills Ship discharges are observed in random localities and have a large variety of causes (i.e. vessels or tankers).

Orphan Seeps Oil seeps lacking site repeatability.

Orphan Spills Oil spills not belonging to any specific Brightspot.

Regarding the Cluster class nomenclature, the reader should not confuse it with anything directly related to Clustering Analyses (e.g. TOU & GONZALEZ, 1974). The number of Cluster and Brightspot classes is comparable to the number of observed seepage sites and recognized oilfields, respectively. A ship discharge – i.e. moving oil source or illegal oil dumping (IOD) – is referred herein as Ship Spills, and these form a single class unit. As Orphan Seeps are not included to any Cluster they all comprise a unit class – likewise, Orphan Spills also form a single class. The terminology "orphan" follows the nomenclature utilized by BENTZ (2006).

2.3.5. CBOS-SATPRO PART 5: FEATURE-EXTRACTION

Once the look-alike features have been removed and the oil slick polygons separated (i.e. categorized into seeps or spills and classified into its respective classes), some oil slick descriptors were calculated. Figure 2-3 schematizes the Feature-Extraction steps. The identified targets were spatially explored with the ArcGIS software, in which the

[25] Such definition implies that the oil seeped from the ocean floor ascends vertically through the water column up to the sea surface, where it is detected by SAR systems.

vectorized polygons were exported to the digital vector storage data format (*.shp* file). Each individual geospatial shapefile stores geometric locations and the associated oil slick characteristics, which were store on a tabular GIS database (Table 2-2).

Table 2-2: Slick-feature attributes (i.e. oil slick descriptors: n=19) common to most oil slicks originally present on the Campeche Bay Oil Slick Satellite Database (CBOS-Data). On the tabulated form of this dataset, lines represent oil slick polygons (objects or transactions), whereas columns correspond to oil slick descriptors (variables or items). Attributes explored in Multivariate Data Analysis Practice, shown as the Yellow Phases (6 to 10) on Figure 1-3, appear in bold – details about their use are given in Chapter 5 and Chapter 6. See also Table 5-10.

n	Attributes	Oil slick information
1	*slickID*	Polygon Identification Number
2	*SARname*	RADARSAT Satellite Name
3	*Pol*	Polarization
4	***Bmode***	**Beam mode**
5	***SARdate***	**Date**
6	***SARtime***	**Time**
7	***cLAT***	**Latitude**
8	***cLONG***	**Longitude**
9	***Category***	**Category**
10	***Class***	**Class**
11	***Area***	**Area (km^2)**
12	***Per***	**Perimeter (km)**
13	*Chl*	Chlorophyll-a Concentration (Yes or No)
14	*CTT*	Cloud Top Temperature (Yes or No)
15	*minSST*	Minimum Sea Surface Temperature (^oC)
16	*maxSST*	Maximum Sea Surface Temperature (^oC)
17	*minSWH*	Minimum Significant Wave Height (m)
18	*maxSWH*	Maximum Significant Wave Height (m)
19	*Wdepth*	Water Column Depth (m)

Some relevant information is exclusive to each oil slick polygon: identification number (*slickID*) and site location: latitude (*cLAT*) and longitude (*cLONG*). These geographical coordinates are represented by the topological center of mass of the polygon: oil slick centroid. The centroid's location was calculated with ArcGIS such that it fell inside the polygon even for oil slicks formed of multiple parts (LUSCH, 1999a).

Particular information is retrieved from the satellite scene acquisition, such as the name of the utilized SAR satellite (*SARname*) and the orientation of the transmitted and received electric field (i.e. imaging polarization – *Pol*). The imaging configuration, as defined by the swath width and ground resolution (i.e. beam mode – *Bmode*), and the date (*SARdate*) and time (*SARtime*) of the SAR overpass are also given.

Only two basic variables of geometry, shape, and dimensions were accounted for: area (*Area*) and perimeter (*Per*). These were calculated based on the identified target's vector shapefile (.*shp* file) that spatially represents each oil slick. Because most oil slicks had multiple parts, these two attributes were estimated for the individual elements and then added up. These were also computed with ArcGIS.

Considering the regional context (i.e. on the scale of the satellite image frame), some information was obtained through the examination of the ancillary meteo-oceanographic geophysical parameters (i.e. MetOc-Kit: *Chl*, *CTT*, *SST*, and *SWH* – see Section 4.5.5). When the respective EOS scenes were available, the presence, or not, of *Chl* and *CTT* were entered as discrete attributes: *Chl* and *CTT*. In addition, *SST* and *SWH* were annotated in a qualitative manner: minimum and maximum values for the SAR frame are logged (*minSST*, *maxSST*, *minSWH*, and *maxSWH*).

Another contextual attribute was provided: water column depth (*Wdepth*). This is measured in meters for the location of the oil slicks' centroid.

2.3.6. CBOS-SATPRO PART 6: PEMEX VALIDATION

On the CBOS-SatPro, the domain specialist's interpretations were taken as the reference for determining whether the oil slick was related to a seep or spill, as well as to decide their class (i.e. Cluster, Brightspot, Ship Spill, Orphan Seeps, or Orphan Spills). This type of operator-dependent analysis, as any manual inspection of satellite images, can incur errors associated with uncertainties from the interpretation of various operators (BREKKE & SOLBERG, 2005a; 2005b).

Even though a range of analysts entered information to the CBOS-Data for more than a decade, a vital post-processing occurred after each SAR image was analyzed (Figure 1-3: CBOS-SatPro Part 6). Individual reports were delivered to PEP, and on this protocol, a representative of MDA-GSI within Pemex's office validates every decision of the operators: approving, or not, whether the selected oil slicks were correctly categorized and/or classified (Figure 2-3).

This validation was mostly based on internal field reports from the environmental RMNE operational team, and, when necessary, additional direct field observations were taken. Usually, the communication practice of this validation process occurred as soon as possible after the SAR image analysis was completed.

If by any chance there was any incongruence between the SAR interpretation and the Pemex Validation, a technical debate, involving the operator analysts and the MDA-GSI representative, took place to resolve whichever difference might persist. If the operator's interpretation was found inconsistent with the field observation, the initial analysis was adjusted to match the validated result.

At the end, the final outcomes of the CBOS-Data were kept as close as possible to the actual oil slick characterization observed in the Campeche Bay region. Consequently, the operator's interpretation of the SAR images were taken as the baseline determining the occurrence, or not, of oil slicks, as well as its category (i.e. seep or spill) and class (i.e. Cluster, Brightspot, etc.).

This information is taken as a proxy of what is often termed "sea-truth". Even though such "absolute truthing" may incur errors (e.g. analyst interpretation), once the Pemex Validation was configured and reported back, it validated the CBOS-Data that became the foundation of the data mining performed on the present analysis.

CHAPTER 3

BLACK GOLD

Fossil fuels energy is enormously important in many facets of our contemporary global society. Ever since the first oil wells were explored in the second half of the 19th century, nearly all of the commerce, manufacturing and other types of businesses have been dependent upon substances derived from refining and processing crude oil or natural gas – such as gasoline (petrol), jet fuel, diesel, lubricating oil, kerosene, naphtha, paraffin, wax, asphalt, tar, bitumen, polishes, solvents, sulfur and many petrochemicals (NRCC, 2003). The byproducts list is vast and includes plastics (ethylene and propylene), rubber, fertilizers, insecticides, detergents, roofing, antifreeze, antiseptics, vitamin capsules, medicines (e.g. Aspirin), toothpaste, deodorant, shampoo, fibers (e.g. nylon and polyesters), clothes, umbrellas, surf boards, dog leashes, among many other goods of our everyday usage (NRCC, 1985; and reference therein).

In some capacity, our food, medicines, comfort, entertainment, transportation, personal devices, appliances, equipment, and machinery rely, at least partially, on fossil fuels as prime substances for production, transport, or power. Moreover, fossil fuels are part of the reasons for many political and military conflicts among nations in the world, thus reflecting in the lack of peace in some regions (GATELY, 1986; GERGES, 1993; CASCIELLO *et al.*, 2011; ORNITZ & CHAMP, 2002).

In one-way or another, most of our everyday lives are related to the OGEPI (BOESCH & RABALAIS, 1987). However, the worldwide society's dependence of this dominant non-renewable form of energy can pose an eminent risk of HC contamination (SCHOLZ *et al*., 1999).

Releases of petroleum can be acute or chronic, occur in large amounts from catastrophic accidents or slowly discharged on sporadic incidents, all of which can considerably impact the environment and be lethal to animals, plants, and entire ecosystems (NRCC, 1985). Damaging ecological impacts tend to worsen as the industrialized nations, as well as developing countries, increase the demand for fossil fuels.

3.1. WEATHERING PROCESSES

Immediately after being exposed to the environment, the composition and the characteristics of oil rapidly and continuously change over time (ITOPF, 2015b). Simultaneously occurring with changes in biological properties (such as those caused by phyto-oxidation and bacterial degradation), other processes also affect the oil during their lifetime in the environment, promoting evaporation, dissolution, emulsification, oxidation, photo-oxidation, photolysis, flocculation, sedimentation, etc. (NRCC, 2003; BATISTA NETO *et al.*, 2008). These processes alter the oil physicochemical properties and are collectively termed as weathering processes[26] (BOYD *et al.*, 2001).

Nonetheless, the most important weathering process acting over oil slicks once the oil reach the surface of the ocean is linked to the air-sea interaction: meteorological (e.g. wind, precipitation, etc.) and oceanographic (e.g. surface current circulation, waves, etc.). These environmental conditions act as natural dispersants capable of influencing superficial mixing, dispersion, spreading, advection, and drift of oil slicks.

Weathering processes also influence the oil slick detectability at sea surface with satellite data. Knowledge of meteo-oceanographic conditions of each oil slick scenario is a crucial requirement as it has a major control on the persistence and extension of such features (ESPEDAL & WAHL, 1999). Indeed, the characterization of an individual oil slick should include information on recent and past weather conditions (CALABRESI *et al.*, 1999; SINGHA *et al.*, 2013).

There are two other important aspects to consider regarding the relationship between oil and the marine environment:

1. The overall degree of negative effects is not always a function of the distance of the oil-released source; and
2. The spilled amount of oil (i.e. its volume) is not always a measure of major ecological concern.

Outsized events are not necessarily the most environmentally devastating ones. As a further matter, the size of the impact caused is also dependent on the use of chemical dispersants, oil skimming, and oil waste collection (ORNITZ & CHAMP, 2002). When systematic burning of slicks containing large amounts of oil comes into play, complicated environmental scenarios are created (EOE, 2010a, 2010c).

[26] Weathering processes cartoon:
http://www.nbcnews.com/id/37517080/ns/disaster_in_the_gulf

The nature of the liquid petroleum should not be ignored, as petroleum can vary in density, viscosity, and solubility in seawater. The mass of a given volume of oil is identified through its density, and in actual fact, the reason why oil floats on water is because it is less dense. While light oil is lost to evaporation, as it degrades more quickly, the remaining heavier fraction resists longer to weathering processes (NRCC, 1985). Light and heavy oil are classified based on American Petroleum Institute (API[27]) gravity unit (VILLALÓN, 1998; LAMMOGLIA & SOUZA FILHO, 2012). A factor to notice when dealing with oil at sea is the fluid's resistance to flow, i.e. viscosity. Fractions with higher viscosity usually weather slowly and are carried for longer distances, consequently building up thicker deposits that can persist for decades (ESSA *et al.*, 2005). Another applicable concept is solubilization – i.e. the quantity that measures the molecular dissolution of oil in water. This is directly related to toxicity levels of different oil slicks (HOSTETTLER *et al.*, 1999; NRCC, 2003).

The fate and behavior of oil slicks are influenced by specific characteristics that depend upon rate, duration, time of year, and site location. To this matter, the construction of maps with Environmental Sensitivity Index (ESI[28]) is a common practice for evaluating regions for their exposure and sensitivity to oil spillages (NOAA, 2002; ANDRADE & SZLAFSZTEIN, 2012). This ranking aims to categorize locations of main ecological, social, and economic concerns based on the spatio-temporal occurrence of animals and plants, their habits, biological and human resources, archaeological, historical, residential, recreational and cultural areas (JENSEN *et al.*, 1998; IPIECA, 2012).

3.2. NATURAL HYDROCARBON SEEPAGES AT SEA

The whole HC seepage process is typically recognized to start whenever HC migrates upwards from the source rock or from subsurface reservoirs through strata pores or fissures (CLARKE & CLEVERLY, 1991). Subsequently, just like water in freshwater springs, liquid or gaseous HC naturally ooze out of the underground (GER *et al.*, 2002; LEIFER & WILSON, 2004). If happening on the ocean, although oil and/or gas plumes are formed on the water column, it is only when oil reaches the sea surface that an oil seep can be observed with satellite measurements (MACDONALD *et al.*, 1993; 1996). As stated on preceding Chapters, the present D.Sc. research exclusively takes into consideration the footprint signature of liquid HC (i.e. mineral oil) observed on the sea surface – i.e. oil seeps (see Section 2.3.4).

[27] API measures of how heavy or light liquid petroleum is compared to water.
[28] ESI: http://oceanservice.noaa.gov/facts/esimap.html

As with rivers, the HC seepage processes do not occur everywhere in the world. Once in the water column after escaping from the seafloor, individual proportions of HCs behave differently. While the light fraction may dissolve and the heavier disperse, some of the oil that arrives at the sea surface volatize, spread away or concentrate in clumps forming an oil seep – the same are observed acting on oil that leaks from OGEPI facilities, i.e. oil spills (see Section 2.3.4).

The U.S. National Research Council (NRCC, 2003) and the Woods Hole Oceanographic Institution (WHOI, 2015) both revealed that almost half of the petroleum annually entering the world's oceans is attributed to natural seepages – see Section 3.3. Because of this large amount, it is anticipated that the resulting environmental impact should be extremely deleterious. On the other hand, most of this oil slowly seeps out of the seafloor as sporadic releases at specific locations. Because the HC seepage process usually persist over a very long period of time with low rates, they can foster a local balance in which chemosynthetic organisms, ranging between microbes to larger creatures, are able to reach an acclimation balance (NRCC, 1985).

For instance, the exposure to concentrations of HCs above background levels make possible for successive generations of organisms to adapt, even feeding on HCs, forming developed ecosystems around natural seepage sites (SPIES & DESMARIS, 1983; MONTAGNA *et al.*, 1986; 1989). Therefore, the surrounding environment and/or local communities where HC seeps out of the ground may be considered as a natural laboratory for understanding how geologically-leaked gas or liquid petroleum behave on the environment (MACDONALD *et al.*, 2010). Because these ecosystems usually host chemosynthetic communities, such locations can also assist with the comprehension of marine life's ecological response to the introduction of oil contaminants (SPIES & DAVIS, 1979; DAVIS & SPIES, 1980). Yet, HC seepage sites indicate the existence of present-day HC generation and migration; therefore, they are important features to be considered in OGEPI exploration studies in offshore sedimentary basis (CLARKE & CLEVERLY, 1991; ABRAMS, 1996).

Several strategic OGEPI fields are concentrated alongside oil seepage locations (GARCIA *et al.*, 2009; CSBPD; 2015). Around these areas, it is not rare for naturally released oil to be mistakenly attributed to man-made oil spills from platforms, oil rigs, ships, tankers or pipelines – the opposite also holds true (PEMEX, 2013b). OGEPI members and societal stakeholders are continuous looking forward to reducing ambiguous reports regarding oil spillage and/or oil seepage (SENGUPTA & SAHA, 2008). This has motivated the development of more accurate detection techniques for

responsive systems that can support *in situ* data collection (e.g. BENTZ *et al.*, 2007a; 2007b; 2007c; 2012; SHCHERBAK *et al.*, 2008; DASSENAKIS *et al.*, 2012).

Usually, when oil is observed on the sea surface within the same area and is captured by satellite imaging in different scenes during several years, there is a strong indication of a persistent source on a nearby location (MACDONALD *et al.*, 2002). However, this repetitiveness may not always occur as vents comprising a seepage complex can get blocked because of environmental or geologic factors (SENGUPTA & SAHA, 2008). The petroleum reservoirs from where the oil may be seeping may not be directly beneath the observed site on the sea surface (TRASHER *et al.*, 1996). In fact, if an oil seep occurring at deep waters is observed on the sea surface, its origin at the seafloor may be situated tenths of kilometers away (MIRANDA *et al.*, 1998).

Geologists and geophysicists are aware that wherever oil on the sea surface is identified as coming from an oil seepage site, instead of an OGEPI installation, it is an indication of the existence of active oil migration routes signifying possible HC active source rocks in the vicinity (STANKIEWICZ, 2003; LEIFER *et al.*, 2006; 2010; USGS, 2015). As pointed out in Chapter 2, OGEPI activity in Campeche Bay originated from the discovery of the Cantarell Oil Seep. Perhaps, remarkable achievements in discovering new HC accumulation areas may be possible if satellite measurements are distinguish oil seeps from oil spills (ESSA *et al.*, 2005).

It is reasonable to assume that if a system capable of recognizing the oil slick type becomes available (i.e. seeps are distinguishable from spills), data assimilation in mathematical models for forecasting or hindcasting oil trajectories based on numerical simulations of ocean currents will potentially be more accurate (OLASCOAGA *et al.*, 2008; DIETRICH *et al.*, 2012; OLITA *et al.*, 2012). This is indeed one of the objectives of the present D.Sc. research: design an innovative classification algorithm to distinguish natural from man-made oil slicks using satellite-derived measurements.

3.3. OIL AND GAS EXPLORATION AND PRODUCTION INDUSTRY (OGEPI)

OGEPI activities are site-specific but their locations vary temporally and geographically. At sea, most activities occur close enough to the shoreline to cause inevitable damages to sensitive coastal habitats if oil is released during extraction, transportation, refining, storage, distribution, or consumption (NRCC, 1985). Operational, accidental, illicit, or intentional releases are diffuse, varying in frequency, location, and intensity.

HCs leakages are notorious for causing toxic effects ranging between the cellular level to individual organisms (NOAA, 2013). Even a small amount of oil can cover a wide area of several hundred meters (MIRANDA *et al.*, 2004). Indeed, oil spills can contaminate coastal marine environments and cause serious threats to entire communities, populations, and ecosystems (NRCC, 2003).

Anthropogenic oil releases to the marine environment are frequently related to accidents with oil rigs or ships, pipeline rupture, deliberate oil-contaminated ballast and oily water discharge, disposal of what is termed as produced-water, oil-bearing cuttings from drilling process, underwater blowouts, etc. (BENTZ & MIRANDA, 2001a; 2001b; GARCIA *et al.*, 2009; NEUPARTH *et al.*, 2012). Because of continuing OGEPI activity, HC releases into the environment are most likely to persist. Historically, major HC-related disasters (e.g. Ixtoc-1, Exxon Valdez, Deepwater Horizon, etc.) draw attention and raise the awareness of the public surfacing political, economic, ecological, and scientific concerns (LEIFER *et al.*, 2012). Over time, this perception tends to transform local and international policies, hence reducing the frequency of accidents.

In 1979, the Campeche Bay experienced the blowout of an exploratory oil well, in which oil from the Ixtoc-1 platform, operated by Pemex, leaked into the Gulf of Mexico waters for more than 9 months (NOAA, 1980; 1981). The Ixtoc-1 disaster is ranked as one of the world's largest unintentional and peacetime oil spill event in history (JERNELOV & LINDEN, 1981a; JERNELOV, 2010). It still calls the attention of the media[29] and of the scientific community as tar mats observed more than 30 years later[30] have been related to it.

An incident that attracted wide publicity because of severe ecological consequences occurred in 1989, when the oil tanker Exxon Valdez grounded on the coast of Alaska caused a major and destructive oil spill (MONSON *et al.* 2000; EOE, 2010d). Patches of the Exxon Valdez oil were reported a decade later (HOSTETTLER *et al.*, 1999).

Another example of oil persistence in the environment is shown by ESSA *et al.* (2005): the collision of two super tankers 17 km offshore the United Arab Emirates in 1994. Photos taken nine years later show the longevity of the spilled oil even after rigorous beach clean-up procedures were applied.

[29] Ixtoc disaster:
http://www.harteresearchinstitute.org/ixtoc-i-and-oil-spill-resources

[30] Ixtoc Expedition 30 years later:
http://ixtoc1expedition.blogspot.com.br

A recent catastrophe that caused enormous environmental damage occurred in 2010. The explosion and sinking of the Deepwater Horizon[31] drilling oil rig, owned by Transocean Ltd. (leased by BP, former British Petroleum), occurred less than 100 km southeast of the Mississippi River in the northern Gulf of Mexico: Macondo Prospect (EOE, 2010c; MACDONALD, 2010). This was accompanied by an oil well rupture at the seafloor that leaked for about 4 months (INNMAN *et al.*, 2010; DEL FRATE *et al.*, 2011).

The Office of Response and Restoration within the Emergency Response Division of the National Oceanic and Atmospheric Administration's (NOAA) maintains a website[32] that presents a myriad of oil spillages since the mid-1950s. It includes scientific articles, news, photos, and site location of the most significant worldwide oil incidents. Other similar sources are also found in the World Wide Web – e.g. a summary of the OGEPI operations in the Gulf of Mexico Outer Continental Shelf region[33].

Notwithstanding the numerous accidental oil spill episodes, it was after armored divisions of the elite Iraqi Republican Guard of the dictator Saddam Hussein invaded Kuwait, with subsequent USA-led coalition's military offensive campaign to expel Iraqi forces out of Kuwait, that the world saw an unprecedented amount of oil and combustion products been intentionally released to air, land, and water (READMAN *et al.*, 1992). One of the major consequences of the "Gulf War" (1990-1991) was the considerable quantity of crude oil that reached the coasts of Kuwait, Bahrain, Qatar, United Arab Emirates, Oman, but mostly on Saudi Arabia (JONES *et al.*, 1998). The exact volume of strategic wartime petroleum purposefully dumped by Iraqi forces on the Persian Gulf is difficult to determine but it is recognized as the largest oil spillage disaster ever reported (MPB, 1993).

Many essential components ensuring compliance of safety standard protocols have been agreed upon precautionary marine protection legislation (OGC, 2015). Several actions have been taken to reduce environmental problems, ranging from coastal patrol vessels, stringent environmental planning, enhanced contingency strategies, rigorous regulations limiting operational spillage, new tanker design with partitioned compartments or double hulls, etc. (IMO, 2010; IPIECA, 2015). Requirements for

[31] NASA Earth Observatory:
http://earthobservatory.nasa.gov/Features/OilSlick/

[32] NOAA Emergency Response Division:
http://incidentnews.noaa.gov

[33] Bureau of Ocean Energy Management, Regulation and Enforcement (BOEMRE): http://www.boemre.gov

ballast-water exchange when well out to sea, as well as strict law enforcement against tank-washing discharges, lengthen the list of international regulations to reduce oil impact in coastal regions. A procedure only allowing very small oil quantities (15 parts per million) to be released at sea have been established: International Convention for the Prevention of Pollution from Ships, 1973 as modified by the Protocol of 1978 (MARPOL 73/78). However, this is deceptively achieved by mixing oil with water (i.e. bilge water), as the flow of oily water discharged at sea is not regulated (EPA, 2008).

Despite the OGEPI's policies to reduce accidents, ineffective safety inspection practices, malfunctioning equipment, aging installations and offloading operations can cause environmental danger to nearby locations (NRCC, 1985; 2003). Another hazard can emerge from increased supertanker traffic and broadening of major shipping routes (ESSA *et al.*, 2005). Together with extensive pipelines and conscious, but negligent and/or illegal, sludge discarding from OGEPI installations and/or ships, these can all bring risks to locations far from major OGEPI fields with reduced or no means to react to oil contamination. Additional oil input to the sea comes from the human consumption activities. These mostly occur on land and are carried to the marine environment via urban runoff, wastewater, and rivers. Two-stroke boat engines, recreational and non-tanker vessels are also significant sources.

Accordingly to NRCC (2003), the outcome of HCs released into the marine environment can be separated into three different input types: production processes, routine transportation, and consumption. Nonetheless, a non-anthropogenic input type is the oil naturally coming from oil seeps. It is important to have an overall estimate of the fossil fuel input. Yet, drawing an accurate assessment is somewhat complex.

For instance, in 1975, the U.S. National Research Council has estimated that an annual average of 6,100,000 metric tons (~1,785 millions of gallons) of HCs were released to the world's oceans. However, a decade later, in 1985, the same agency estimated a worldwide volume of about 3,200,000 metric tons (~935 millions of gallons), and in their latest report, in 2003, the total load dropped to 1,300,000 metric tons (~380 millions of gallons). Rather than an actual reduction, these long-term changes are attributed to better measurement technologies and better estimation techniques. Using their latest global estimates, 3% are recognized as coming from the production processes, 12% from routine transportation, and 37% from human consumption activity; the remaining 48% is related to natural HC seepage sources (NRCC, 1985; 2003).

CHAPTER 4

SATELLITE REMOTE SENSING

The basis of remote sensing techniques lies in the acquisition of data (e.g. radiance) about a target (e.g. ocean surface) without direct contact, thus having the collector (e.g. satellite sensor) located at a certain distance of the observed target[34]. In Earth Sciences, the remote sensing of the environment is usually performed with the assistance of mechanical devices onboard aerial platforms such as helicopters, airplanes, or satellites. The so-called remote sensors measure and record the electromagnetic energy that is emitted, reflected or scattered from different targets (LUSCH, 1999b; CLARK & RILEE, 2010). For instance, in the Oceanography field this could easily be pictured as an oil slick detected with sensors onboard satellites (SOUZA, 2009).

In fact, regarding the subjects particularly related to the lithosphere, biosphere, cryosphere, hydrosphere, and atmosphere, satellite remote sensing measurements are a valuable way of effectively documenting conditions over large areas, regions short of *in situ* observations or inaccessible locations (NOVO, 1998). The use of satellite sensors to monitor marine ecosystems is especially useful when dealing with recurring phenomena that normally occur on the sea surface (GADE & ALPERS, 1999).

4.1. BEFORE THE SATELLITE ERA

For much of the last century, the bulk of the oceanographic investigations were conducted with direct field sampling methods[35]. Although this way of data collection is still largely used on environmental monitoring, traditional oceanographic surveys involving direct field sampling are time-consuming and ship-time for deployment and recovery operations have high operational costs (PRANDLE, 2000). Two different reference viewpoints frames – Eulerian (i.e. moorings that are fixed in space) and Lagrangian (i.e. drifting buoys that follow a tagged fluid parcel in time) – are extensively used to study ocean processes (PICKARD & EMERY, 1996).

[34] Remote Sensing Tutorial:
http://www.crisp.nus.edu.sg/~research/tutorial/rsmain.htm

[35] Portal NOAA CoastWatch:
http://coastwatch.noaa.gov

Most monitoring programs that solely rely on field sampling have a spatial and temporal bias. The weather is a major adversity for classical oceanographic surveillance systems, in which favorable conditions are frequently required for data collection (BROWN *et al.*, 1997). *In situ* sampling efforts establish discrete and non-uniform coverage with data stations that are not so often revisited. Visual observations from boats, helicopters and airplanes are limited to daily observations and mostly dependent on visual inspection capabilities. This sparse coverage creates considerable data gaps that may prevent some conclusions to be drawn (SCHOFIELD & GLENN, 2004).

The inadequacy of acquiring *in situ* measurements on large areas constrains the use of such methods in many cases and the ability to locate and track surface ocean features incurs a considerable amount of work (DICKEY, 1991). This may inhibit the complete observation of several phenomena (e.g. oil slicks, oceanic front, eddies, phytoplankton blooms, offshore outflow of river plumes, etc.) and, as a result, many questions regarding such processes have long remained unanswered (DIETRICH *et al.*, 1980).

After the inception of spaceborne sensors, about forty years ago (LUSCH, 1999b), a myriad of high-quality ocean-related studies has been accomplished (e.g. ROBINSON & MITCHELSON, 1983; DENMAN & ABBOTT, 1994; SMYTH *et al.*, 2003; YODER & KENNELLY, 2006). However, even though satellites can provide a synoptic view of numerous problems and many ocean features, they are not capable of replacing field sampling, especially in circumstances requiring the study of depth-dependent processes (STEWART, 2008). Nevertheless, if conventional ground sampling techniques and satellite measurements are employed complementary, supplementary, and supportively, several advances can be made in the management of surveillance systems, early detection, environmental monitoring, law enforcement and oceanographic science (GOWER, 2004; MCHUGH, 2009; TUFTE *et al.*, 2004; DASSENAKIS *et al.*, 2012).

4.2. BASIC CONCEPTS OF SYNTHETIC APERTURE RADAR (SAR)

Many efforts of using SAR sensors are described showing a wide range of oceanographic applications, for example, flood mapping, underwater bottom topography, ship traffic monitoring, oil slicks reconnaissance, etc. (BIRK *et al.*, 1995; ROKOSH, 2000; VAN DER SANDEN, 2004). This Section offers to the reader a summary of SAR theoretical concepts in language accessible to non-oceanographers, as well as a didactic discussion on the advances in using SAR for environmental monitoring focused on detecting oil slicks.

Radars are ranging instruments, i.e. account for the time elapsed between the transmission of the signal and the reception of the returned signal (MCCANDLESS & JACKSON, 2004; DPI, 2015). SAR is an active microwave-imaging sensor with its own illumination source that measures the strength and time delay of the returning signal (STEWART & LARSON, 2000). SAR measurements are independent of weather conditions and can be operated during days and nights. Images created by SAR systems are anisotropic, i.e. have different ground resolutions along (azimuth direction) and across (range direction) the flight path (MARTIN, 2004; TRIVERO & BIAMINO, 2010). BUONO *et al.* (2015) present an extensive review of single-, co-, partially-, and full-polarimetric SAR capabilities to detect oil slicks on the surface of the ocean.

The high dielectric constant[36] of water causes microwave radar beams not to penetrate in the sea surface (LUSCH, 1999c; HOLT, 2004). In association to that, it is well known that oil films on the sea surface increase the top layer viscosity, which cause the surface roughness of the water to decrease (NRCC, 2003). Smooth seas drastically reduce the return signal, i.e. electromagnetic backscattering energy that characterizes the Bragg scattering mechanism (HOVLAND *et al.*, 1994; TRIVERO *et al.*, 1998). Active microwave radars (e.g. SAR) can detect changes in surface tension, and, as a matter of fact, many investigations have focused on studying dark zones observed (i.e. areas of reduced radar backscatter) in high-resolution SAR imagery (e.g. CALABRESI *et al.*, 1999; SOLBERG *et al.*, 1999; LIU *et al.*, 2011).

Unfortunately, and in principle, oil is not the only factor capable of smoothing the sea surface, i.e. dampening out capillary waves and/or suppressing short gravity waves that are only a few centimeters in length (MARTIN, 2004). SAR's ability to detect surfactants is strongly limited by several environmental conditions (e.g. low wind, upwelling zones, etc.) that also modulate the surface roughness (STAPLES & HODGINS, 1998). In addition, SAR detects the surface manifestation of some man-made activities (e.g. ship wake, etc.) that cause the same type of response as oil (MCHUGH, 2009). Just like oil slicks, look-alike features also appear darker than surrounding water and this is caused by the lower microwave backscattering response of such sea surface features (TRIVERO *et al.*, 1998; DIGIACOMO & HOLT, 2001).

While the different dark features observed on SAR images are either oil slick candidates or look-alike features, some of these ambiguities are not necessarily difficult to distinguish from actual oil slicks, for instance, particular shape characteristics,

[36] Dielectric constant is the ratio between any substance permittivity to the free space permittivity and influences the incident radar beam reflection, abosortion, and dissipation (ONSTOTT & SHUCHMAN, 2004).

distinct environmental configurations, or certain occurring weather-depend phenomena (ESPEDAL, 1998; 1999). However, the differentiation between oil slicks and look-alike features is not always straightforwardly achieved, as flawless models to identify oil slicks are yet to be created (BREKKE & SOLBERG, 2005b). Recent studies have investigated the polarimetric approaches to detect oil slicks in SAR images (MIGLIACCIO *et al.*, 2007; 2009a; 2009b; 2011a; 2011b; 2012).

Phenomenon that may cause other targets to be confused with the actual response of oil slicks on SAR imagery are not addressed on the present D.Sc. research. Look-alike features have not been taken into consideration during the CBOS-SatPro, as they were filtered out of the CBOS-Data by experienced domain analysts (see Chapter 2).

An aspect to highlight while detecting oil slicks using SAR measurements is that the knowledge of the wind speed is very important (CHRISTIANSEN *et al.*, 2006). In low wind conditions (< 2-3 m/s), oil slicks are not well distinguished from smoothened ambient water, because little to no microwave energy is backscattered and dark regions are formed all around in oil-free areas (BERN *et al.*, 1993). In the lack of backscattered energy reaching the SAR antenna that occur in the absence of wind, it is often impossible to detect oil slicks. In other situations, under moderate wind speed (approximately between 3 and 8 m/s) oil slicks appear darker in contrast with the background radar signal of the surrounding water (STAPLES & HODGINS, 1998). At high wind speed situations (> 8 m/s) oil slicks are spread away, dispersing or mixing into the upper ocean and the resulting clutter makes its detection difficult (ALPERS & HUHNERFUSS, 1989).

Despite the fairly narrow “ideal” wind speed range suggested in the literature to enable oil detection on the sea surface, the nature of the oil and its thickness also play important roles in the dampening of capillary waves on the ocean surface in SAR imagery (ESPEDAL *et al.*, 1998). Perhaps, in eventual cases, oil slicks may be detected at wind speed up to 12 to 14 m/s (DIGIACOMO *et al.*, 2004; LITOVCHENKO *et al.*, 1999). However, wind measurements are not considered on the research presented herein.

Despite the advantages in imaging the world’s oceans surface for oil slick detection (e.g. weather-independent, day-and-night coverage and a marine science toolset that detect fine-scale texture of the sea surface), most SAR instruments present particular limitations if compare to other meteo-oceanographic satellite sensors: cannot measure true colors, restricted area coverage, long site-repeat intervals, and its relative high operational costs that demand-specific collections. The concomitant use of SAR and

Earth Observing System (EOS) can, to some extent, increase the spatio-temporal coverage of environmental monitoring surveys for detecting oil slicks (e.g. SIPELGAS & UIBOUPIN, 2007; HU *et al.*, 2009). To this end, it is desirable to explore other sensors for detecting oil slicks, some of which are discussed in Section 4.6.

A number of satellite missions with SAR sensors are have been put in orbit over the past decades providing commercial operational services, for example, COnstellation of small Satellites for the Mediterranean basin Observation (COSMO-SkyMed[37]), Environmental Satellite (Envisat[38]), European Remote Sensing Satellite (ERS[39]), Japanese Earth Resources Satellite (JERS[40]), Phased Array type L-band Synthetic Aperture Radar (PALSAR[41]), Radar Imaging Satellite (RISAT[42]), TerraSAR[43], amongst others[44]. The present D.Sc. research explores the Canadian RADSARSAT satellites: RADARSAT-1[45] and RADARSAT-2[46] satellites (CRSS, 1993; 2004; MDA, 2004; 2014).

The RADARSAT SGF products explored during the CBOS-SatPro (see Chapter 2) are generated with standard ground coordinate pixel dimensions of either 12.5m (for operational beam modes of Standard, Wide, Extended Low and Extended High) or 6.25m (for Fine beam). The Standard beam mode swath width is 100 km wide, while the one related to the Wide beam mode covers. Typical spatial resolutions are of the order of 25 m – i.e. twice the pixel size (RSI, 1997; 1998). For the ScanSAR Narrow and Wide beam modes, the nominal spatial resolution is, respectively, 50 m and 100 m (Table 4-1 and Figure 4-1).

While all RADARSAT-1 beam modes only transmit and receive horizontally polarized signals (HH), most RADARSAT-2 beam modes are able to generate a few single polarimetric image products: linear parallel polarization (HH or VV) or linear cross-polarization (HV or VH). Some RADARSAT-2 beam modes can generate dual parallel and cross-polarizations (HH+HV or VV+VH) or even a full quad-polarized image can be selected (HH, VV, HV, VH) (ALI *et al.*, 2004a; 2004b; VAN DER SANDEN, 2004; NRCAN, 2014).

[37] COSMOS-SkyMed: http://www.cosmo-skymed.it/en/index.htm
[38] Envisat: https://earth.esa.int/web/guest/missions/esa-operational-eo-missions/envisat
[39] ERS: https://earth.esa.int/web/guest/missions/esa-operational-eo-missions/ers/satellite
[40] JERS: http://global.jaxa.jp/projects/sat/jers1/index.html
[41] PALSAR: http://www.alos-restec.jp/en/staticpages/index.php/aboutalos-palsar
[42] RISAT: http://www.isro.gov.in/Spacecraft/risat-1
[43] TerraSAR: http://www.geo-airbusds.com/terrasar-x/
[44] Earth Observation Portal: https://directory.eoportal.org/web/eoportal/satellite-missions
[45] http://gs.mdacorporation.com/SatelliteData/Radarsat1/Radarsat1.aspx
[46] http://gs.mdacorporation.com/SatelliteData/Radarsat2/Radarsat2.aspx

Table 4-1: RADARSAT-2 technical specifications. The radiometric depth of all RADARSAT beam modes is 16-bit. From: FOX *et al*. (2004).

Beam Modes	Nominal Swath Width (km)	Spatial Ground Resolution (m) **	Approximate Incident Angles
Ultra-Fine	20x20	3x3	30°x40°
Multi-Look Fine	50x50	8x8	30°x50°
Fine	50x50	8x8	37°x49°
Standard	100x100	25x26	20°x49°
Wide	150x150	30x26	20°x45°
ScanSAR Narrow *	300x300	50x50	20°x46°
ScanSAR Wide *	500x500	100x100	20°x49°
Extended Low	170x170	40x26	10°x23°
Extended High	50x50	18x26	50°x60°
Fine Quad-Pol	25x25	9x8	20°x41°
Standard Quad-Pol	25x25	25x8	20°x41°

* 8-bit in RADARSAT-1.

** Range x Azimuth.

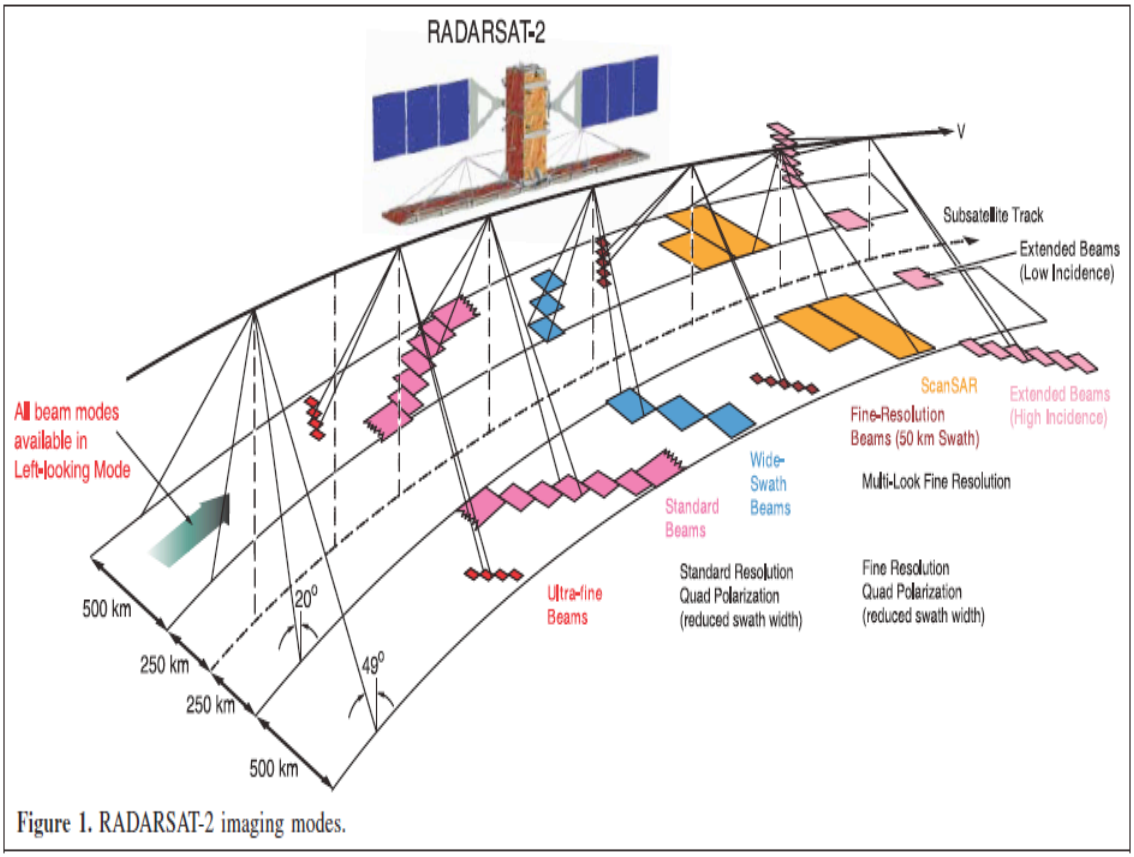

Figure 4-1: RADARSAT-2 imaging modes. From: FOX *et al.* (2004).

4.3. RADARSAT RADIOMETRIC-CALIBRATED IMAGE PRODUCTS

The image format of the RADARSAT products varies between satellites. While RADARSAT-1 images are stored in the standard CEOS format (Committee on Earth Observation Satellites), RADARSAT-2 images have a specific data file structure based on GeoTIFF imagery and encoded eXtensible Markup Language (*.xml* file) that includes the SGF file (*product.xml*) and metadata files (i.e. *lutSigma.xml*, *lutBeta.xml*, and *lutGamma.xml*).

Metadata of the data files from both RADARSAT satellites have an additional table containing the incidence angle of the radar beam in the range direction. As shown on Section 5.4, this table is used to derive an incidence angle image product to give the satellite standpoint of view per pixel for individual oil slicks. Other supplementary support files are also delivered together with the RADARSAT imagery, e.g. design schema templates. The naming convention of the RADARSAT product files provided by MDA-GSI is shown on Table 4-2 (GILL, 2010).

Table 4-2: Nomenclature of the RADARSAT products:

RS2_OK1111_PK2222_DK3333_Bmode_YYYYMMDD_HHMSS_PP_PTY.zip		
RS2	Satellite Name	Radarsat-2
OK1111	Order Key	
PK2222	Product Key	
DK3333	Delivery Key	
Bmode	Beam Mode	e.g. SCNA, SCNB, WDE1, WDE2 or EXL1.
YYYYMMDD	Acquisition Date	Year (YYYY), Month (MM), and Day (DD)
HHMMSS	Acquisition Start Time	Hour (HH), Minute (MM), and Second (SS)
PP	Polarization	e.g. VV – transmits and receives vertically.
PTY	Product Type	SGF – SAR Georeferenced Fine

The SGF RADARSAT-2 products have three output scaling look-up-tables (LUTs) supplied (i.e. metadata files) to calculate radiometric-calibrated SAR measurements, whereby the uncalibrated grey-level count (i.e. Digital Number – DN) is directly related to SAR-derived backscatter coefficients – i.e. sigma-naught (σ^o), beta-naught (β^o), and gamma-naught (γ^o) (MDA, 2011). The SGF RADARSAT-1 CEOS format only provides a single LUT: β^o (THOMPSON & MCLEOD, 2004).

SAR-derived backscatter coefficients represent the average radar reflectivity of the target normalized by the unit area, i.e. normalized radar cross section[47] (RCS: σ) (RSI, 1997; 1998). Quantitative measures of σ^o, β^o, and γ^o correspond to the SAR backscatter signature in different surface plane areas (AIRBUS, 2014b; EL-DARYMLI *et al.*, 2014; THAKUR, 2014; ASF, 2015), as explained (Table 4-3) and illustrated (Figure 4-2) below.

Table 4-3: SAR backscatter coefficients that correspond to the SAR backscatter signature in different surface planes. These quantities are explored on this research.

Sigma-naught (σ^o)	Normalized-RCS in the ground horizontal range plane. Sometimes referred to as scattering coefficient. Measure frequently adopted as the radar signal backscatter strength. Although its calculation depends upon the knowledge of terrain slope (not an issue on the sea surface) and the radar beam incidence angle, it is directly related to the target's reflectance per unit area (i.e. pixel projected onto the ground). For this reason, scientists frequently use σ^o measurements.
Beta-naught (β^o)	Normalized-RCS in the radar's line-of-sight (i.e. slant range). Sometimes referred to as radar brightness (or reflectivity) coefficient. Because it represents the reflectivity in the direction of the incident radar beam and is independent of the terrain slope, system design engineers generally prefer to use measures of β^o.
Gamma-naught (γ^o)	Normalized-RCS in the plane orthogonal to the slant range direction. It is the power returned to the antenna from the area orthogonal to the radar beam. This plane is uniformly distant from the satellite and has equal brightness from near to far range on the pixel level. In being so, measurements of γ^o are usually selected for antenna calibration purposes.

Even though DN values are enough for qualitative usage, such as the monitoring implementation of the CBOS-SatPro that maps sea surface oil slicks, the use of DN is not meaningful when comparing SAR images. For this reason, DN values are not recommended to cross-compare time series of SAR images (FREEMAN, 1992; EL-DARYMLI *et al.*, 2014). Conversely, radiometric-calibrated SAR measurements (i.e. σ^o, β^o, or γ^o) are essential for quantitative analyses, as their use permits the comparison of data acquired from the same sensor with different dates and beam modes, as well as the evaluation of data acquired with various sensors (ESA, 2014).

[47] RCS characterizes a reflectivity property of the reflected radar signal strength (i.e. scattering intensity) of any surface target (e.g. oil slick) in the direction of the radar receiver (i.e. antenna). It has a unit of m^2 and is a function of sensor parameters (e.g. viewing geometry, radar wavelength, transmitted and received polarization, etc.), target's properties (e.g. time, position dielectric constant, roughness, geometry, etc.), as well as of the terrain slope, etc. (HOLECZ *et al*., 1993).

As explained in Chapter 2, RADARSAT images utilized during the CBOS-SatPro have been analyzed in DN. However, as a time series with a substantial number of SAR images is compared in the present investigation, the use of radiometric-calibrated SAR measurements is recommended (FREEMAN, 1992; EL-DARYMLI *et al.*, 2014; ESA, 2014). As such, a re-processing of the RADARSAT images was required, as described in Section 5.3.

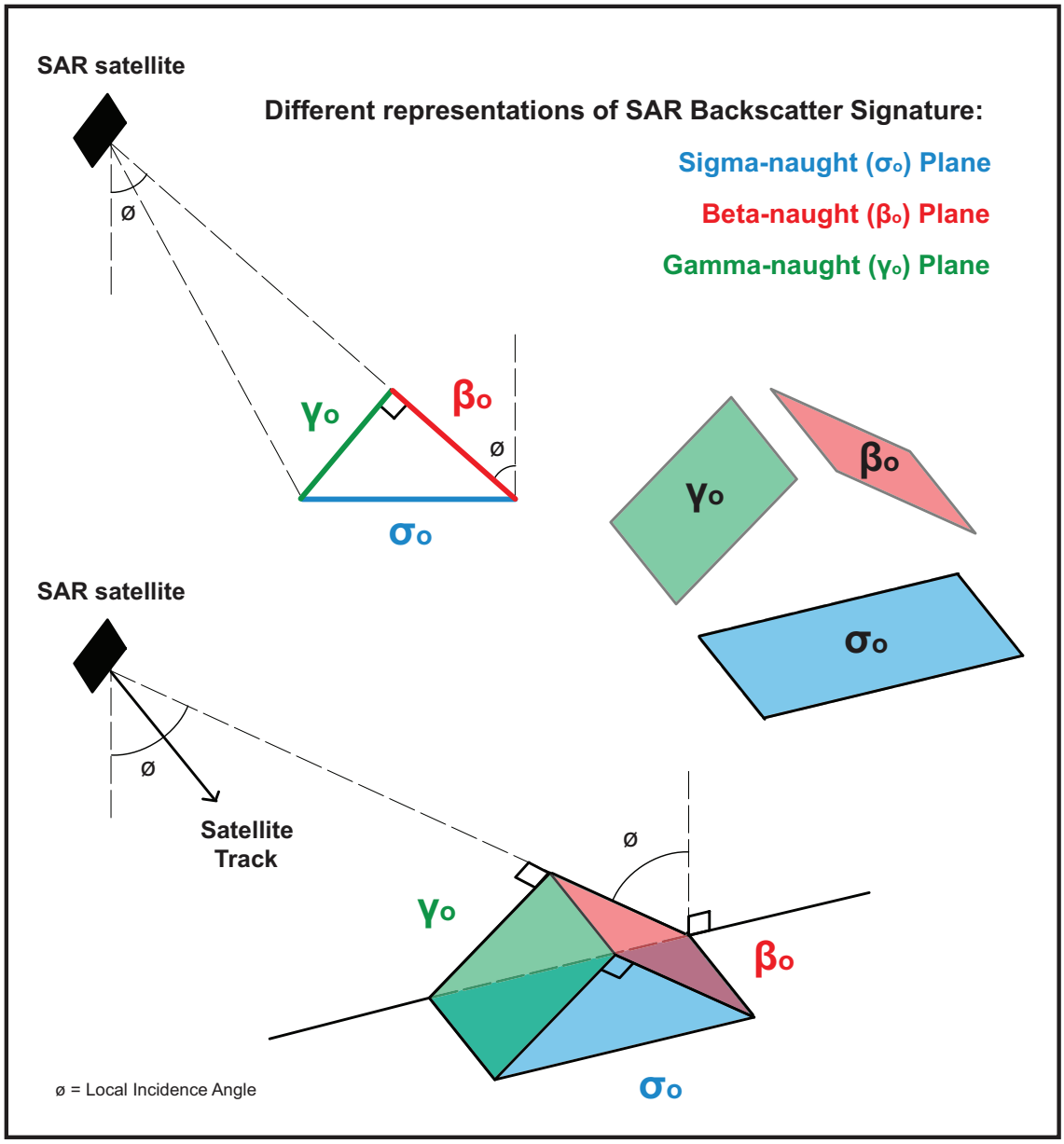

Figure 4-2: Conceptual diagrams representing the relationship among the SAR-derived backscatter coefficients, which are considered quantitative measures of SAR backscatter signature in different surface planes: sigma-naught (σ^o), beta-naught (β^o), and gamma-naught (γ^o). Modified from: AIRBUS (2014b) and EL-DARYMLI *et al.* (2014).

The conversion of uncalibrated SGF DN values to radiometric-calibrated SAR-derived backscatter coefficients (i.e. σ^o, β^o, or γ^o) is achieved according to the following expression:

$$C_1 = [\{DN^2\}+B]/A$$

While the constant offset (*B*) is nominally set to zero for SGF products, the gain value (*A*) varies for each pixel in the range direction (MDA, 2011). Although the process to calculate σ^o, β^o, or γ^o is exactly the same, C_1 depends upon the LUT choice (i.e. metadata files: *lutSigma.xml*, *lutBeta.xml*, and *lutGamma.xml*) to obtain the corresponding range-dependent gain values. These LUTs have only one gain listed for each pixel in the range direction.

C_1 is given in linear values of amplitude (*Amp*), or intensity (*Int*), of the radar return signal received by the antenna system – their relationship is given by: $Int=Amp^2$. Therefore, if a log transformation is applied to C_1, a dimensionless physical quantity representing power is obtained (MDA, 2011). This is calculated as follows:

$$C_2 = (10*cc)*\text{Log}_{10}(C_1)$$

where *cc* is equal to 1 for the intensity of the received radar beam and 2 for pixel values given in amplitude. Regardless of the input being amplitude or intensity, C_2 is expressed in decibel units (dB).

In essence, the evaluation of σ^o, β^o, and γ^o is similar among SAR sensors with different specifications[48], but their calculations vary somewhat from sensor to sensor; even different RADARSAT products, i.e. Single Look Complex (SLC), have specific calculations (LAUR *et al.*, 1998; SHEPHERD, 2000; MDA, 2011; AIRBUS, 2014a; 2014b; IYYAPPAN *et al.*, 2014; THAKUR, 2014). It is also important to distinguish between the radiometric-calibrated SAR measurements explored herein (i.e. σ^o, β^o, and γ^o) and other SAR calibration methods[49], for example, in-lab (e.g. chirp parameters), in-orbit (e.g. lifetime instruments and parameters or gain changes), or external (e.g. corner-cube reflector or geometric) (FREEMAN, 1992; FOX *et al.*, 2003; JAYASRI, 2014; PADHYE & REGE, 2015).

[48] TerraSAR-X Documentation:
http://www.geo-airbusds.com/en/228-terrasar-x-technical-documents

[49] SAR Calibration Workshop Proceedings:
https://earth.esa.int/documents/10174/1597298/SAR26.pdf

4.4. Dark Spot Detection in SAR Imagery

Most oil slick detection monitoring systems follow a three-step framework: Digital Image Classification (DIC), Feature-Extraction, and Feature-Classification (BREKKE & SOLBERG, 2005b; GAMBARDELLA *et al.*, 2010; SINGHA *et al.*, 2013). While Figure 4-3 graphically represents such framework, this Section individually describes each step. These steps are applied in tandem on SAR images, and can be fully either automated, semi-automatic or manually operated. As pointed out in Chapter 2, the last two steps have been inverted during the CBOS-SatPro and the slick-feature attributes are only calculated once the oil slicks are identified.

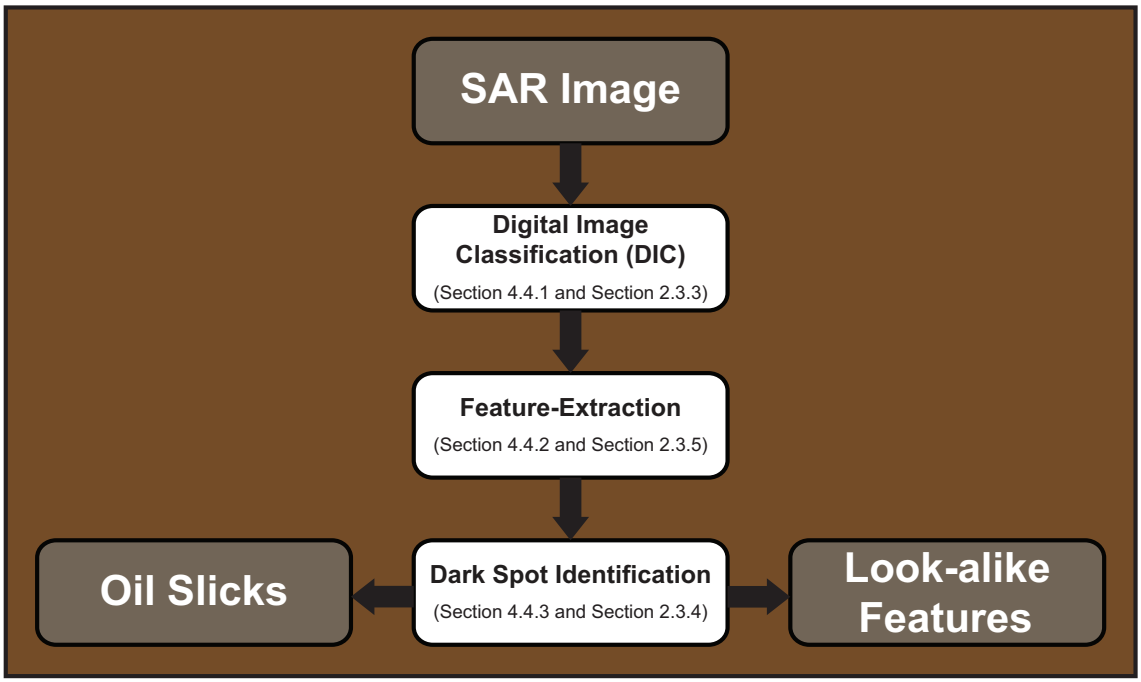

Figure 4-3: Typical three-step framework used to indentify dark spots in SAR imagery. During the Campeche Bay Oil Slick Satellite Project (CBOS-SatPro) the last two steps were inverted: slick-feature attributes were only calculated upon the identification of oil slicks (see Chapter 2). Adapted from BREKKE & SOLBERG (2005b).

4.4.1. Digital Image Classification (DIC)

The course of identifying oil slicks starts with the SAR imagery been digitally classified. During the DIC, the image can be submitted to different procedures (e.g. deterministic or statistic classification) that take into account some aspects of one, or two, sea surface domains: radiometric and textural. This aims to discriminate regions with smooth texture (i.e. low backscattering) from the rough sea surface background (i.e. with diffuse backscattering). The former has a darker visual appeal than the latter.

Even though this defines two types of polygons (i.e. potential oil slick candidates and look-alike features), at this stage there is not much certainty of which is which. Such polygons are only identifying the presence, and its limits (i.e. borders), of dark spots in the SAR image that are indicative of low backscatter response. Therefore, it is essential to stress that every representative target, which may include oil slicks and look-alike features, are flagged. As the polygons with smooth texture regions can be yielded by several processes (HOVLAND *et al.*, 1994; JOHANNESSEN *et al.*, 1996; HOLT, 2004; SENGUPTA & SAHA, 2008), the recognition of these targets is indeed the purpose of the next two steps of the framework – explained in the next two Sections.

Several studies have described a wide variety of image classification techniques: e.g. user-defined or automatic adaptive threshold (MARONE *et al.,* 1998; SOLBERG *et al.*, 1999; SHU *et al.,* 2010; GANTA et al., 2002), hysteresis threshold (CANNY, 1986; KANAA *et al.*, 2003), Laplace or difference of Gaussian (CHANGE *et al.,* 1996; HEN *et al.,* 1994), wavelets (WU & LIU, 2003), local variation of wave spectra (MERCIER *et al.*, 2003), mathematical morphology (GASULL *et al.,* 2002), fuzzy clustering (BARNI *et al.,* 1995; FISCELLA *et al.*, 2000), Artificial Neural Networks (ANN) (CALABRESI *et al.*, 1999; DEL FRATE *et al.*, 2000; TOPOUZELIS *et al.*, 2007; SINGHA *et al.*, 2013), among many others.

In the case of the CBOS-SatPro, the oil slicks observed in Campeche Bay and logged on the CBOS-Data have been identified and classified after the use of the USTC algorithm (ALMEIDA-FILHO *et al.*, 2005)**.** The USTC discriminates regions with different backscattering based on the sea-surface radar textural (circular semivariogram function shape and value) and radiometric (despeckled DN values signatures). This classifier is described in Section 2.3.1 and further discussed in MIRANDA *et al.* (2001; 2004). In addition, several studies are found demonstrating the successful USTC applications in identifying oil slicks – e.g. BEISL *et al.* (2001), BENTZ & MIRANDA (2001a; 2001b), RODRÍGUEZ *et al.* (2007).

4.4.2. FEATURE-EXTRACTION

Once the polygons are identified, several slick-feature attributes can be computed to characterize each polygon, taking into account the information of the pixels within the oil slick's limits (MONTALI *et al.*, 2006; TOPOUZELIS, 2008). Each oil slick is then characterized either from the point of view of the satellite scene (e.g. incidence angle, satellite beam mode, etc.), aspects related to the SAR-derived backscatter coefficient

(i.e. σ^o, β^o, or γ^o), textural information (e.g. contrast), geometry, shape, and dimensions variables (e.g. area, perimeter, etc.), and contextual descriptors (e.g. latitude, longitude, bathymetry, etc.) features. Appropriate guidelines to acquire such descriptors are a leading requirement for the success of any classification algorithm (KUBAT *et al.*, 1998; BREKKE & SOLBERG, 2005b).

Depending upon the line-of-attack of the investigation been executed, a range of suitable slick-feature attributes arise to help the definition of criteria to discriminate oil spills from look-alike features. However, as there is not a systematic Feature-Extraction procedure, qualitative and quantitative statistical features are arbitrarily selected on each of them – e.g. while COCOCCIONI *et al.* (2009) used 7 slick-features, PISANO (2011) and TOPOUZELIS *et al.* (2007) used 10, CALABRESI *et al.* (1999), SOLBERG *et al.* (1999) and DEL FRATE *et al.* (2000) used 11, FISCELLA *et al.* (2000; 2010) and SINGHA *et al.* (2013) used, respectively, 12, 13 and 14, and BENTZ (2006) evaluated 40 different slick-features.

Some investigations describe the most common features, such as TOPOUZELIS *et al.* (2009) and TOPOUZELIS & PSYLLOS (2012) that combine 25 of them: they used a genetic classification algorithm and discovered that best results occurred with 10 slick-features. While the handful of slick-feature attributes calculated during the CBOS-SatPro are shown on Table 2-2, a comprehensive list of slick-feature attributes explored on the present D.Sc. research is presented in Chapter 5.

4.4.3. DARK SPOT IDENTIFICATION

Oil slicks and look-alike features are classified based on descriptors – i.e. extracted slick-feature attributes that characterize the polygons (i.e. identified targets). Hence, it is in the Feature-Classification step that oil slicks are differentiated from other targets capable of producing dark features in the SAR image which cause misidentification issues on the analysis and interpretation for oil detection purposes (HOVLAND *et al.*, 1994; JOHANNESSEN *et al.*, 1996; HOLT, 2004; SENGUPTA & SAHA, 2008).

Once the polygons are classified (i.e. identified as oil slicks), they are stored in a geographical information system (GIS) to promote the spatial visualization of the oil slicks (IVANOV & ZATYAGALOVA, 2008; LITOVCHENKO & IVANOV, 2008; MOROVIC & IVANOV, 2011). This initiative can help with the identification of patterns (or trends[50]) recognizable in the form of maps. On a tabular framework, each data entry

[50] Physical Geography: http://www.physicalgeography.net

is sorted out in different events, in which the lines of this database represent individualized oil slick polygons (i.e. objects or transactions) and the columns correspond to the information used to characterize each oil slick polygon (i.e. variables or items). Chapter 5 provides more information about ways to explore this type of tabulated information.

A conversion from raster to vector polygons occurs after detecting such regions. Alternatively, individual shapes that have contiguous pixels are grouped and then individualized as polygons based on their SAR backscatter – this characterizes a segmentation procedure.

Some environmental monitoring programs include on their database not only the oil slick information, but also the look-alike feature attributes (e.g. BENTZ, 2006). This intends to build a dataset capable of training classification algorithms to flag – i.e. identify, and thus eliminate – features producing similar signatures in SAR imagery to actual oil slicks (BREKKE & SOLBERG, 2005b).

Several ways to perform Feature-Classification are found in the peer-reviewed literature (e.g. CALABRESI *et al.*, 1999; SOLBERG *et al.*, 1999; DEL FRATE *et al.*, 2000; FISCELLA *et al.*, 2000; 2010; SINGHA *et al.*, 2013). On the CBOS-SatPro, oil slicks are manually identified by the careful interpretation of operators.

4.5. SATELLITE SENSORS IN SUPPORT FOR OIL SLICK DETECTION

This Section includes numerous aspects of a broad range of prevailing ancillary meteo-oceanographic geophysical parameters used in support of oil detection. Despite the individual limitations presented by each specific satellite system listed on this Section, the complex approach of using combined spaceborne measurements from various Earth Observing System (EOS) sensors with different resolutions makes it possible to reduce the effects of their individual drawbacks (e.g. RORIZ, 2006).

4.5.1. VISIBLE/NEAR INFRARED (VIS/NIR)

Exactly because of the long site-revisiting interval of SAR satellites, the use of additional satellite information with shorter revisit interval becomes an interesting and advantageous strategy to monitor oil slicks on the sea surface (e.g. SIPELGAS & UIBOUPIN, 2007). It is true that for environmental studies inspecting high temporal variability processes (e.g. algal blooms, oil slicks, etc.), SAR images may be inadequate depending on the scope of the monitoring program (e.g. BENTZ *et al.*,

2004). However, different from SAR imagery, the optimal use of visible/near infrared sensors (VIS/NIR) for detecting and monitoring oil-contaminated areas are still under evaluation (e.g. HU *et al.*, 2009; CHEN & HU, 2014).

VIS/NIR that include ocean color sensors, have nearly daily coverage of most regions on the globe. Nowadays, MODerate Resolution Imaging Spectroradiometer (MODIS; SALOMONSON *et al.*, 1989; ESAIAS *et al.*, 1998), MEdium Resolution Imaging Spectrometer (MERIS) and Visible Infrared Imager Radiometer Suite (VIIRS) are the most utilized VIS/NIR sensors capable of providing a cost-effective supplementary tool for environmental monitoring. Other sensors, such as the proof-of-concept Coastal Zone Color Scanner (CZCS; HOVIS *et al.*, 1980; EVANS & GORDON, 1994) that flew from 1978 to 1986, and the more recently deceased (1997-2010) Sea-viewing Wide Field-of-view Sensor (SeaWIFS; HOOKER *et al.*, 1992; HOOKER & MCCLAIN, 2000; MCCLAIN *et al.*, 2004) are the heritage ocean color sensors of the National Aeronautics and Space Administration (NASA).

One of the main characteristics of VIS/NIR sensors is the determination of a proxy of chlorophyll-a on the sea surface. Chlorophyll-a maps can recognize regions with phytoplankton activity and biological growth (GONZALEZ *et al.*, 2000; GONZALEZ-SILVERA *et al.*, 2004). The knowledge of productive areas are relevant for the oil slick detection processes as algal blooms on the sea surface can change the surface roughness of the sea, thus misleading the search for oil in SAR images (BENTZ *et al.*, 2003; 2004; 2005).

MODIS acquires data in 36 spectral bands and images the Earth's surface every 1 to 2 days (ANDERSON *et al.*, 2003). Two distinct EOS mission satellites have the MODIS instrument onboard: Aqua (EOS PM-1) and Terra (EOS AM-1). Of particular interest whilst using the MODIS instrument is the relationship between the concomitant acquisition of biological (e.g. Chlorophyll-a) and physical (e.g. Sea Surface Temperature) variables that occurs with a large geophysical parameter library. This sensor measures various inherent optical properties (IOPs) of the water (CARDER *et al.*, 1999) in nine different spectral wavelengths (λ = 412, 443, 488, 531, 551, 667, 678, 748 and 869 nm) ranging from particulate backscatter ($b_{bp(\lambda)}$), total scatter ($b_{(\lambda)}$), phytoplankton absorption ($a_{ph(\lambda)}$), absorption of detritus and CDOM[51] ($a_{dg(\lambda)}$), and total absorption ($a_{(\lambda)}$). MODIS also provides standard products such as water-leaving radiance ($L_{w(\lambda)}$), normalized water-leaving radiance ($nL_{w(\lambda)}$), remote sensing reflectance

[51] CDOM: Colored Dissolved Organic Matter.

($R_{rs(\lambda)}$), downwelling diffuse attenuation coefficient (K_{490}) and fluorescence line height (FLH).

It is important to highlight that oil slicks can be differed from actual seawater by some characteristics (e.g. higher refractive index, higher absorption coefficient and higher viscosity) that can influence the backscattered and reflected signals, hence providing means for their recognition if using VIS/NIR (BULGARELLI & DJAVIDNIA, 2012). In being so, the various MODIS-retrieved variables (i.e. Chl, IOPs and standard products) have indeed the potential for detecting oil slicks (e.g. SIPELGAS & UIBOUPIN, 2007; HU *et al.*, 2009; CHEN & HU, 2014).

Even though VIS/NIR detect the reflected electromagnetic energy from sunlight, there are situations in which the detection method applied to study oil slicks on the sea surface using these sensors are similar to SAR principles (HU *et al.*, 2003). These occur because at certain viewing angles, more specifically at sunglint conditions, the light reflected back to the sensor produces smoothed-like regions such as those observed in SAR imagery (ADAMO *et al.*, 2006; 2007).

In the absence of sunglint, the Lw can reflect the property of pure seawater areas, as well as oily regions. The difference between the L_w of clear water and the L_w of oil-contaminated regions can provide useful information that can be possibly used for oil slick identification (BULGARELLI & DJAVIDNIA, 2012). The R_{rs} at 547 nm and 531 nm are pointed out to be influenced by the particulate organic carbon and diffuse attenuation coefficient of oil slicks (INNMAN *et al.*, 2010).

Additionally, as different oil slicks present different colorations (BONN, 2009), the spectral reflectance variation depends upon the oil chemical composition. ADAMO *et al.* (2005; 2007) propose the use of MODIS band 2 (841-876 nm) and MERIS band 13 (855-875 nm) as the most sensitive bands (i.e. wavelengths) for extracting the spectral properties of oil slicks.

Nevertheless, some limiting characteristics of using optical bands for environmental monitoring should be pointed out. They are restricted by the need for solar illumination and the requirement for cloud-free skies. As a result, VIS/NIR sensors only produce meaningful measurements in the daytime. This is relevant because SAR images can be acquired regardless of illumination, but SAR images acquired at night will not have correspondent VIS/NIR data.

In addition, most VIS/NIR images have a coarse ground resolution of about 1 km at nadir point. However, there are VIS/NIR imagers that acquire measurements with a spatial resolution of approximately 250-300 meters (e.g. MODIS, MERIS), which is practical for oil slick detection in the marine environment (GOWER *et al.*, 2006).

4.5.2. THERMAL INFRARED (TIR)

Sensors working at the thermal infrared (TIR) portion of the electromagnetic spectrum – also referred to as imaging radiometers – are suitable for retrieving Sea Surface Temperature (SST) measurements. The oceanographic interpretation of SST maps offers important information about ocean circulation pattern, for example, upwelling zones, oceanic front, eddies, river plumes, urban runoff, wastewater, etc.

The most common sensor that retrieves SST information is the five channel Advanced Very High Resolution Radiometer (AVHRR) installed onboard a series of NOAA satellites. Another one is the Imager on the Geostationary Operational Environmental Satellite (GOES).

A relevant issue to point out whilst using TIR measurements is the SST difference between day and night observations, typically caused by diurnal heating and cooling after nightfall. To avoid possible biases between day and night SST measurements, CARVALHO *et al.* (2002; 2003a; 2003b) suggest splitting the SST dataset into daytime and nighttime.

Furthermore, even a very thin cloud cover can interfere with the accuracy of SST measurements. Because TIR cannot see the ocean surface in the presence of clouds, another TIR application widely used is the location of clouds. The Cloud Top Temperature (CTT) gives an idea of atmospheric fronts or heavy rain cells. These atmospheric phenomena may be present at the time of SAR acquisition influencing on the sea surface roughness, consequently causing misinterpretation on the oil slick detection.

Depending upon the seawater composition, the absorption of sunlight can vary across the sea surface, what can change the energy re-emission in thermal radiation (MARTIN, 2004). Perhaps, the chemical composition of oil slicks can influence on SST retrievals. Changes in emissivity are the possible cause for thick oil slicks appearing hotter and oil slicks with intermediate oil thickness appearing cooler in TIR images (FINGAS & BROWN, 2000). Indeed, ESSA *et al.* (2005) present satellite images displaying oil slicks having lower SST than the surrounding clear water surface.

On the other hand, thin oil slicks can reach a thermal equilibrium with the surrounding water preventing temperature differences to be noticed (YING *et al.*, 2009). While studying TIR imagery from the Deepwater Horizon incident, INNMAN *et al.* (2010) did not find thick oil slicks capable of causing SST differences.

4.5.3. MICROWAVE ALTIMETER

Wave patterns and the sea state conditions are also important factors for oil slick detection (PEDROSO *et al.*, 2007). In calm seas, the radar backscatter signal can better define an oil slick, if compared to rough sea conditions. Two satellite missions acquire good-quality Significant Wave Height (SWH) measurements: TOPEX/POSEIDON and Jason. Strong gradients found on SWH determinations can result in sudden changes in local incidence angle values, affecting the SAR sea surface response (RORIZ, 2006).

SWH are useful parameters in SAR interpretations, but not strictly applicable for the present investigation. Satellite altimeters provide measurements only along the sub-satellite track, which limits its usefulness while detecting oil slicks, as it requires oil slicks to be directly beneath the satellite nadir to fulfill the prerequisite for matching SAR measurements with the altimeter data. Chapter 5 presents more information about the match-up analysis performed on the present D.Sc. research.

4.5.4. MICROWAVE SCATTEROMETER

The magnitude of the wind blowing over the ocean is a vital parameter for oil slick detection (FALLAH & STARK, 1976). While the deceased QuikSCAT satellite used to carry aboard the SeaWinds instrument, the EUMETSAT METOP satellites carry the Advanced Scatterometer (ASCAT). Both sensors are all-weather microwave measurements capable of providing near-surface data for the retrieval of wind information.

Because of the spatial resolution of 25 km owned by this type of instrument, its measurements may not be adequate for match-up analyses as the one performed on the present investigation (see Chapter 5). However, wind vector retrievals from SAR measurements may produce relevant information acquired at the moment of the oil slick SAR image acquisition.

4.5.5. METEOROLOGICAL AND OCEANOGRAPHIC KIT (METOC-KIT)

As certain meteorological and oceanographic phenomena (e.g. low wind, upwelling zones, etc.) express the same signature on SAR images as oil slicks (JOHANNESSEN *et al.*, 1996), satellite ancillary measurements can shed light on the differentiation of targets that are actual oil spills from false targets (ESPEDAL *et al.*, 1996; HOLT, 2004). Within this perspective, the synergy of combining several sensors providing data in accordance with such recognizable environmental features can assist with the interpretation of dark spots present in SAR images.

As a result, improvements to OGEPI activities and to environmental monitoring can both be achieved. SIPELGAS & UIBOUPIN (2007) discuss possible ways to distinguish oil spills from false targets in SAR imagery off the coast of Estonia in the Gulf of Finland. They use Chl and SST images from MODIS, as well as wind data from the High Resolution Limited Area Model (HILRAM) to rule out the look-alike features. As for the Cantarell Complex region, BEISL *et al.* (2001) and SILVA JUNIOR *et al.* (2003) have both previously demonstrated the operational effectiveness of using meteo-oceanographic satellite information in support to SAR imagery interpretation.

In fact, some retrieved products (e.g. wind, Chl, CTT, SST and SWH) acquired from distinct EOS sensors (e.g. QuikSCAT, MODIS, AVHRR and TOPEX/POSEIDON) are essential to aid in the selection and interpretation of SAR images (FINGAS & BROWN, 1997; BREKKE & SOLBERG, 2005a). To this extent, this collection of relevant meteo-oceanographic ancillary information have been explored during the CBOS-SatPro in support to the analyses of SAR images, as well as to provide environmental and weather conditions at the closest time of the observed oil slicks scenarios. Herein, this set of prevailing information is referred to as MetOc-Kit.

4.6. SATELLITE OCEANOGRAPHY

After introducing the spaceborne measurements acquired with EOS sensors, the reader finds on this Section a general review of several remote sensing practical applications that leverage such sensors.

Spaceborne sensors have long proved to be suitable for large-scale observation of Earth's ecosystems (NOVO, 1998). Remotely sensed data can, above all, be valuable to detect, map, monitor and track oil before it reaches sensitive areas and becomes a problem for animal and plant life. It has already been shown that remote sensors are a valuable source of information to study ocean dynamics and monitoring trends in

ecological processes (JOHANNESSEN *et al.*, 2000). Satellite oceanography lies on global coverage. The vast amount of data produced by satellites provides the capability of studying daily to periodic variability of large-scale phenomena with seasonal and decadal temporal variability (GREGG & CONKRIGHT, 2001; 2002; MCCLAIN *et al.*, 2004; 2006). For instance, there are satellites (e.g. AVHRR/NOAA, GOES) capable of assisting studies requiring a finer time-scale resolution, such as tracking ocean currents or atmospheric circulation processes (BREAKER *et al.*, 2000).

Indeed, the synoptic view provided by satellites offers the possibility to enhance monitoring strategies and is capable of benefiting many societal stakeholders (DIGIACOMO *et al.*, 2004; INNMAN *et al.*, 2010). Sensors varying in physical nature (i.e. visible, infrared and microwave systems) have largely been explored and their use covers wide applications (KOSTIANOY *et al.*, 2006). As a matter of fact, near-real-time surveillance provides successful services to trim down timelines to locate features at the ocean surface such as oil slicks, shear current, upwelling, algal blooms, urban runoff, wastewater, etc. (e.g. JOLLIFF *et al.*, 2003; SMYTH *et al.*, 2003; SOUZA, 2005; Takahashi and Kawamura, 2005; CARVALHO *et al.*, 2007; 2008; 2010a; 2010b; 2010c).

Nowadays, it is common to come across investigations using space technologies to study oceanographic phenomena. For instance, CARVALHO *et al.* (2002; 2003a; 2003b) study the wind influence on Cabo Frio upwelling (23ºS/42ºW), in which the wind has been acquired with QuikSCAT and the SST data with the AVHRR/NOAA. These authors define a simple upwelling index that uses the area having SSTs ≤ 18°C and the SST difference between the upwelling core temperature and the surrounding water (≥ 18°C). SSTs of 18°C are about the warmer temperature of the South Atlantic Central Water (SACW; CAMPOS *et al.*, 1995; SILVEIRA *et al.*, 2000), which is the water mass upwelling in the Cabo Frio region. Significant Spearman correlation observed between their simple upwelling index and wind data confirm that the upwelling intensity is considerably influenced by the wind speed (>10m/s) and by the component parallel to the shoreline 12h to 24h before each scenario.

Harmful algal blooms (HABs) are a major human health concern around the world's ocean (KUSEK *et al.*, 1999). On the Gulf of Mexico, along the west Florida coast, most investigations aiming to study the well know Florida Red Tide focus on *in situ* sampling of laboratory experiments (e.g. MILLIE *et al.*, 1997; MCLEROY-ETHERIDGE & ROESLER, 1999; SCHOFIELD *et al.*, 1999). However, CARVALHO *et al.* (2010d; 2011) survey this phenomenon performing a long-term pixel-by-pixel analysis (2002-

2006) using MODIS images. They introduce a satellite-based algorithm for the identification of the main toxic alga, i.e. *Karenia brevis*, and compared it with two other methods – i.e. CANNIZZARO *et al.* (2008) and STUMPF *et al.* (2003). Near-coincident *in situ* samples provide the number of cells per liter (FWRI, 2002). After an optimization procedure considering the optical characteristics of each method, the capabilities of their algorithm and Cannizzaro's technique are combined into a new hybrid algorithm capable of enhancing the detection of such HABs.

Successful joint analyses are reported using several remote-sensing resources with different resolution and coverage. This confirms the complexity of performing multi-satellite assessment of biological and hydrodynamic surface oceanic features. For example, SHCHERBAK *et al.* (2008) combine various EOS sensors with quasi-concurrent measurements (i.e. MODIS from both Terra and Aqua satellites, AVHRR/NOAA, Meteosat-8, QuikSCAT, TOPEX/Poseidon, Jason-1, Envisat ASAR/MERIS and ERS-2) to study the oceanographic dynamics along the Russian coast of the Sea of Azov and Black Sea. With an extensive campaign, exploring more than 1100 images, eddies, coastal runoff outflow as well as anthropogenic and biogenic oil are monitored, in which their summary map products consistently depict the relationship between the coastal circulation and the pollutants' evolution, transport and drift.

Besides ecological phenomena, satellites play a vital importance in monitoring the worlds' oceans as they are extensively used to locate oil slicks on the sea surface (FINGAS & BROWN, 1997; 2000; BREKKE & SOLBERG, 2005b). Previous studies have shown that satellite measurements are effective in detecting oil slicks. While STRINGER *et al.* (1989) visually interpret AVHRR/NOAA imagery of the Exxon Valdez accident, ESPEDAL & JOHANNESSEN (2000) present a SAR image from the ERS-1 satellite illustrating the signatures of different surface features connected to offshore OGEPI facilities on the British and Norwegian sectors of the North Sea that could be oil related. Likewise, ADAMO *et al.* (2007) use SAR alongside MODIS and MERIS imagery to explore the temporal resolution of the ocean color sensors in detecting oil slicks.

Undeniably, the use of SAR imagery can, to some extent, present the position of oil slicks by tracking its displacement (CLARK, 1993). Such ability is a valuable mechanism for oil spill response efforts. Numerous implementations of operational satellite-based surveillance for oil spill detection monitor different areas of world's oceans (e.g. North Sea, Norwegian Sea, and Baltic Sea), in which trained operators

process and interpret satellite images searching for oil signatures (e.g. TUFTE *et al.*, 2004; PEDERSEN *et al.* 1996; WAHL *et al.*, 1996).

Yet, oil slicks do not have a particular or individual signature in satellite imagery. As a result, specific ways to discriminate between oil slicks and ambiguous signatures are the focus of many investigations. For example, ESPEDAL & JOHANNESSEN (2000) discuss a Norwegian research effort of the Nansen Environmental and Remote Sensing Center (NERSC) to discriminate man-made oil spills from look-alike features. The main steps of the NERSC supervised discrimination algorithm, which have been tested with 124 oil slicks, are briefly summarized below:

1. SAR processing consisting of normalization, 16 to 8 bit pixel re-scaling, re-sampling to 100 m pixels and calibration;

2. Digital analysis that identifies the source and calculates some relevant parameters such as texture, gradients, geometry, shape, and dimensions;

3. Contextual analysis that provides the location of platforms/oil rigs and the repeated location of oil seepage sites, in which images are plotted and incorporated on a database with local wind and its history, rain cells, SST, Chl, grease ice, and bottom topography. Ancillary data that are used to rule out look-alike features;

4. Modeling analysis accounting previous environmental conditions used to characterize the behavior of doubtful dark spots; and

5. Concluding reports listing SAR backscatter signatures classified as operational oil spills or look-alike features are issued.

The spatial and temporal distributions of oil slicks are widely inspected using SAR, but, even though surveys exploring the synoptic view of a multi-satellite analysis are infrequent, it is not rare to find them in the peer-reviewed literature (BREKKE & SOLBERG, 2005b). Conversely, the use of the satellites for distinguishing natural oil seeps from man-made oil spills is still poorly documented.

While SAR measurements provide a specific type of data (e.g. sea surface roughness) and the visible imagery obtains other sort of information (e.g. Chl, $L_{w(\lambda)}$, $R_{rs(\lambda)}$, IOPs), equivalent information can be extracted from both sensors (e.g. coast line). Even though the combined use of SAR and visible measurements is a subject requiring further investigation, IOANNIDIS & VASSILAKI (2008) summarize three ways to integrate measurements from both sensors for high-quality mapping products:

1. In sequence: One sensor's output serves as input for processing the other. Monitoring systems that do not use other sort of data can benefit from SAR data being used to improve the visible information, or vice-versa;

2. In parallel: Measurements of both sensors are processed separately, yet, having their products' effectiveness superimposed basically for presentation purposes; and

3. Auxiliary: The output of one sensor is used as complementary information for the other in cases when it is not possible to extract some information from one sensor, or when there are gaps or incomplete acquisition (e.g. data fusion).

A multi-satellite oil slick detection example is shown by BULGARELLI & DJAVIDNIA (2012) that analyze MODIS images from the Deepwater Horizon drilling oil rig accident off the coast of Louisiana, Gulf of Mexico. Their analysis inspects the optical properties of the water outside the sunglint zone. They demonstrate that it is possible to spectrally discriminate between the water likely to be contaminated with oil and the surrounding water with different Chl values. They suggest that oil slicks are not misinterpreted with atmospheric processes if using their proposed uniform atmospheric correction other than the SeaWiFS Data Analysis System (SeaDAS) default module.

ADAMO *et al.* (2005) suggest an interesting methodology using VIS/NIR satellite-imaging sensors applied to several oil spill cases on the North Atlantic Ocean and on the Mediterranean Sea. These authors support the usage of ocean color imagery for tracking the oil spill evolution over time. They explore high-resolution (250 m) optical measurements from MODIS (both onboard TERRA and AQUA) centered at 859 nm (band 2), acquired a few hours from SAR measurements from the ERS-2 satellite. In fact, their methodology just holds true if the inspected site is affected by sunglint. The sunglint effect is affected by dampening of short wavelength waves that decrease the sunlight reaching the sensor after reflection from the sea surface.

MODIS's capability to detect natural oil seeps in the open ocean is also shown by HU *et al.* (2009). For oil slick mapping, the roughness of the sea surface is used, as revealed by the sun-glitter pattern, rather than exploring the optical properties of the water (ADAMO *et al.*, 2006; 2007). An approximately 30% overestimation of MODIS oil slick coverage was observed in the NW Gulf of Mexico. Because of MODIS's coarse ground resolution if compared to SAR measurements (i.e. 250 m against 25 m), some pixels at the oil slick edge may be a mixture of oil-contaminated and non-oily water. These authors suggest a more systematic assessment for the global seepage rate

evaluation using MODIS imagery since its nearly daily coverage (cloud cover permitting) could surely assist on the identification of new oil seeps.

MARGHANY *et al.* (2009) indicate the possibility of using a multi-fractal characterization of different sea surface features observed in two RADARSAT-1 images: Wide (W1) and Standard (S2) beam modes. They propose a modified fractal box count approach to construct maps of fractal dimension (FD) to discriminate oil spills from other targets. Both images present good discrimination between different textures and pixels corresponding to oil spills, which exhibit lower fractal values ($1.48 > FD > 2.0$) than non-related oil patches: look-alike feature ($2.4 > FD > 3.0$), shear current ($3.7 > FD > 3.9$), low wind ($1.57 > FD > 2.5$), and ship ($2.4 > FD > 4.0$). Lower standard deviation errors are found for W1 mode possibly because of the preferable steeper incidence angles for oil slick detection that maximizes the ocean surface signal and provides a better backscattering contrast.

Similarly, SILVA *et al.* (2013) suggest using FD of transect lines to detect oil slicks on another RADARSAT-1 beam mode image: ScanSAR Narrow 1 (SCNA). Their proposed technique is based on the dynamic behavior of a spring-mass system-like, in which the spring geometry is associated with the sea surface roughness and the spring is configured from transect lines. Zonally and meridionally transects extract the SAR-signal (grey level) from each feature. Three types of external forces acting on the springs are considered: horizontal force, vertical force, and couple moment. They conclude that the utilized dynamic fractal approach, originally introduced by BEVILACQUA *et al.* (2008), is capable of discriminating among different targets: oil slick, low wind, oil rig, and sea clutter.

CHAPTER 5

METHODS

The motivations of the present D.Sc. research provide developing solutions to two problems of OGEPI-related activities: the first one copes with environmental monitoring and the second one concerns in finding new oil exploration frontiers. The objectives proposed herein are established based on three gaps of the peer-reviewed literature: 1) Describe the spatio-temporal distribution and occurrence of oil slicks; 2) Utilize classical multivariate data analysis techniques for studying oil slicks; and 3) Discriminate oil seeps from oil spills using satellite measurements.

The scientific questions under investigation are closely related to the existence of a specific monitoring of oil slicks under Pemex's SOI using RADARSAT imagery (i.e. CBOS-SatPro). The design of the proposed qualitative-quantitative classification algorithm benefits from the data choice: a large historical archive of oil slick information in the Campeche Bay region (i.e. CBOS-Data).

While Figure 5-1 outlines the aforesaid, further considerations about the structure of the present D.Sc. research are portrayed on Figure 1-2 (rationale) and Figure 1-3 (structure). This Chapter provides information about the methods employed through the course of this investigation and it has a formal spirit of a wide-ranging tutorial to enable knowledgeable scientists not only to understand, but to replicate straightforwardly, every step performed herein on any equivalent dataset.

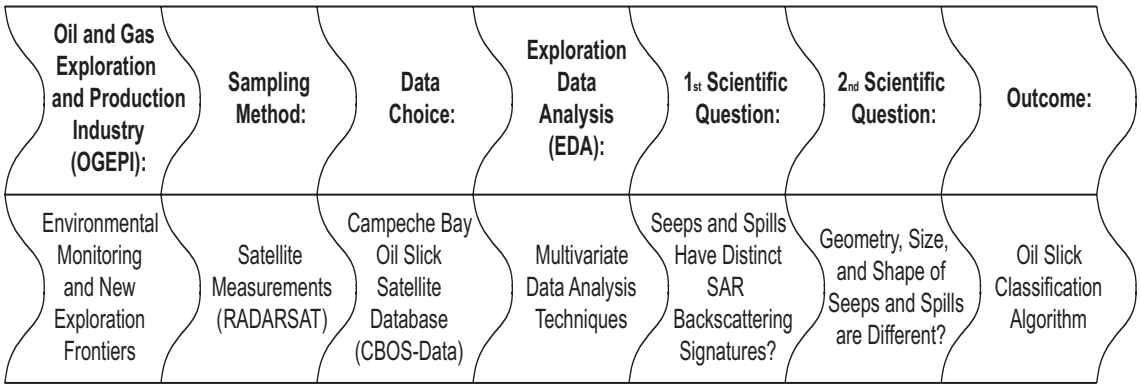

Figure 5-1: Synoptic representation picturing the mainframe of the present D.Sc. research. Expanded details facilitating the comprehensiveness while reading this D.Sc. Dissertation are found on Figure 1-2 and Figure 1-3.

Data Acquisition: CBOS-SatPro Parts 1 to 6 (Blue Section: Figure 1-3)

The CBOS-Data has come out after the execution of the six blue Parts of the CBOS-SatPro (Figure 1-3). However, the data acquisition has not been accomplished during the present D.Sc. research, instead, it mostly occurred before 2012 at the LabSAR facility (LAMCE/PEC/COPPE/UFRJ) – see Chapter 2 for extended details. Notwithstanding that, these Parts are extremely relevant for the comprehensiveness of the present study. Their summary is presented below:

CBOS SatPro Part 1	**RADARSAT Scene Selection**: Scene selection occurs with the analysis of concurrent meteo-oceanographic conditions. See Section 2.3.1.
CBOS SatPro Part 2	**RADARSAT Image Processing**: Processed images (*.pro.pix*) are given in uncalibrated Digital Numbers (DN's). See Section 2.3.2.
CBOS SatPro Part 3	**Digital Image Classification (DIC)**: The USTC algorithm is utilized to recognize smooth texture regions (i.e. low backscattering) in SAR imagery. Such dark regions delimit the borders of polygons representing potential oil slick candidates and/or look-alike features. See Section 2.3.3.
CBOS SatPro Part 4	**Dark Spot Identification:** Identified polygons are manually inspected to exclude look-alike features. Recognized oil slicks are grouped (i.e. oil seeps or oil spills) and divided in classes (based on its point source). See Section 2.3.4.
CBOS SatPro Part 5	**Feature-Extraction**: Compute, list, and tabulate slick-feature attributes that describe the oil slicks – whilst lines of this tabular framework represent oil slick polygons (or transactions), columns are their attributes (or items). Oil slick vectors are stored on a spatial GIS database. See Section 2.3.5.
CBOS SatPro Part 6	**Pemex Validation**: The operators' interpretations is sent to Pemex representatives that validates the SAR image analysis as the baseline (i.e. a proxy of what is often termed as "sea-truth") indicating the actual occurrence, or not, of oil slicks. See Section 2.3.6.

The scientific effort performed on the present D.Sc. research started upon the CBOS-Data availability. The structure of the ten Phases of the present D.Sc. dissertation is divided in two main color-coded sections. While the former represents the Workable-Database Preparation (Green Phases: 1 to 5), the latter encompasses a Multivariate Data Analysis Practice (Yellow Phases: 6 to 10), as portrayed on Figure 1-3.

The following sections present a thorough explanation about the methods performed on such Phases; but first, however, their succinct descriptions are outlined. It is worth pointing out that the results sections mirror the methods ones, thus, one may read them in pairs – i.e. methods-to-results sections. However, this is not mandatory and common continuous reading is also feasible.

Workable-Database Preparation: Phases 1 to 5 (Green Section: Figure 1-3)

Phase 1 **Data Familiarization:** Organize and carefully inspect the CBOS-Data for inconsistent data entries. Describe the spatio-temporal distribution related to the oil slicks' occurrence. See Section 5.1.

Phase 2 **Quality Control (QC):** Define QC-Standards to guarantee that the CBOS-Data meet some effective criteria and conditions to reach the objectives of the present D.Sc. research. See Section 5.2.

Phase 3 **RADARSAT Re-Processing:** The RADARSAT-2 images are processed to provide the SAR backscatter signature: sigma-naught (σ^o), beta-naught (β^o), and gamma-naught (γ^o). See Section 5.3.

Phase 4 **New Slick-feature Attributes:** Calculate new slick-feature attributes, thus customizing the CBOS-Data into the actual workable dataset: Campeche Bay Oil Slick Modified Database (CBOS-DScMod). See Section 5.4.

Phase 5 **Data Treatment:** Set the CBOS-DScMod dimensionally homogeneous: Negative Values Scaling, Log_{10} Transformation, Ranging Standardization, and Dummy Variables. See Section 5.5.

Multivariate Data Analysis Practice: Phases 6 to 10 (Yellow Section: Figure 1-3)

Phase 6 **Attribute Selection:** The association among the CBOS-DScMod attributes is explored to reduce the number of variables to those that can better assist in distinguishing spills from seeps. See Section 5.6.

Phase 7 **Principal Components Analysis (PCA):** Select meaningful Principal Components (PC's). See Section 5.7.

Phase 8 **Discriminant Function:** Discriminate Analyses use the original variables values and the selected PC's. See Section 5.8.

Phase 9 **Correlation Matrix:** Verify the inter-variable correlation among all variables and selected PC's. See Section 5.9.

Phase 10 **Oil Slick Classification Algorithm:** Use Discriminant Functions to design the qualitative-quantitative algorithm to differentiate oil spills from oil seeps. See Section 5.10.

5.1. PHASE 1: DATA FAMILIARIZATION

This Section describes the first of two pre-processing data verification Phases (Figure 1-3), in which a careful inspection has been carried out to find eventual discrepancies that may have happened whilst data entries were logged onto the CBOS-Data (i.e. oil slick information: Table 2-2). The earlier any inconsistency is discovered, the smaller the chance an error is propagated throughout the processing chain. Whenever possible, eventual irregularities were fixed; otherwise, the uncovered mistake was taken out from the analysis: remove respective polygon (line or transaction). This is a "data cleaning" process as it removes noise and resolves incomplete data issues.

This organizes and prepares the information within the CBOS-Data. Recapitulating Chapter 2 that fully described the CBOS-Data, this dataset has been compiled for over a decade by a considerable number of analysts that have entered information of more than 14 thousand oil slicks observed in Campeche Bay coming from 766 RADARSAT scenes. To this extent, it was necessary to spend a great amount of time sorting out the available information for the purposes of the environmental analysis attained herein. Also, the format in which the information was stored added challenge to the usage of the CBOS-Data, as different file formats were provided:

.xls	Microsoft Excel
.doc	Microsoft Word
.pdf	Adobe Reader
.txt	Text Editor
.shp	ArcGIS vector
.jpg	Image display
.tif	Image display
.pix	PCI Database file format
.xml	SGF product

Imperatively, besides searching and organizing the CBOS-Data content, this meticulous, labor-intensive Data Familiarization Phase provides a comprehensive description of the information produced during the CBOS-SatPro. Because of its large spatio-temporal range, with information acquired between 2000 and 2012, the description of the CBOS-Data reveals important aspects related to the oil slicks' occurrence in the Campeche Bay region. Indeed, the first of the two objectives proposed on the present D.Sc. research is revealed by the outcomes of such practice. The findings of the present Phase are shown on Section 6.1.

5.2. PHASE 2: QUALITY CONTROL (QC)

A systematic Quality Control (QC) is performed on this Section, the second pre-processing data verification Phase (Figure 1-3). The QC bridges the rationale and structure of this D.Sc. research (Section 1.4) with the organized basic oil slick descriptors that came out of the preceding Phase. Once again, recalling that the CBOS-Data has not been put together to reach the goals of the present D.Sc. research. Instead, it was supposed to support Pemex's decision-making processes by identifying oil slicks on the surface of the ocean in the Campeche Bay region.

In spite of that, the CBOS-Data must meet certain effective criteria – these are referred to as "QC-Standards" – to guarantee the quality of circumstances to cope with the objective of the present D.Sc. research (Section 1.3). The extent of the QC actions is dependent upon the familiarization processes, and in being so, the QC-Standards are established after the accomplishment of the Data Familiarization practice. Accordingly, such conditions are presented in Section 6.2.

5.3. PHASE 3: RADARSAT RE-PROCESSING

This Section presents details about the first of two image-processing Phases performed during this research (Figure 1-3). It describes the satellite image processing practices accomplished to reach the proposed objectives. Although it involves the same RADARSAT images explored during the CBOS-SatPro, only scenes containing oil slick polygons that have passed the QC-Standards (Section 6.2) are considered.

A threefold difference is evident from the image processing steps performed on the CBOS-SatPro Part 2 (RADARSAT Image Processing: Section 2.3.2 – Figure 2-2):

1. The PCI *.pix* files (i.e. DN images) were converted to radiometric-calibrated image products: σ^o, β^o, and γ^o – see Table 4-3;
2. The two operations to make the image visually appealing were not performed: APC (Antenna Pattern Compensation) and image contrast enhancement; and
3. No radiometric re-scaling was performed and images have been processed and analyzed with their original radiometric depths (see Table 4-1).

While the former allows quantitative cross-comparison of images acquired in different dates, the application of the 2nd would invalidate such assessment (FREEMAN, 1992; THOMPSON & MCLEOD, 2004; EL-DARYMLI *et al.*, 2014; ESA, 2014). The latter is a requirement of the USTC algorithm (see Section 2.3.3), not employed herein.

Besides these differences, the image processing steps carried out herein correspond to the ones performed during the CBOS-SatPro, following the same order depicted on Figure 2-2. During the initial process that imports the provided-SGF Level-1 products to the viewable image in the PCI *.pix* format, the radiometric-calibrated SAR-derived backscatter coefficients (i.e. σ^o, β^o, and γ^o) were already calculated following the conversions presented in Section 4.3 (i.e. C_1 and C_2 given in amplitude and dB, respectively). Subsequently, the adaptive Frost filter with 3x3 window was applied (see Table 5-1) and followed by a nominal pixel re-sample. Then, the RADARSAT Satellite Modeling (Radar Specific Model) was used to georeference the images.

Because of the exploratory nature of the present D.Sc. research, various radiometric-calibrated image products are investigated: Table 5-1. These include several forms of SAR backscatter signature (i.e. σ^o, β^o, and γ^o) given with the amplitude of the received radar beam (C_1) and in dB units (C_2), both with and without the application of the Frost filter. An additional image product was crested to give the incidence angles – i.e. satellite standpoint of view per pixel (see SAR scene attribute *INC.ang* in Section 5.4). The image product with the incidence angle was derived from the provided-SGF table containing the radar beam incidence angles in the range direction (Section 4.3). The reader should remember the acronyms provided on Table 5-1 as they are extensively used throughout the manuscript.

Table 5-1: Radiometric-calibrated image products (n=13) explored on the present D.Sc. research: incidence angle (*INC.ang*) and the various forms of SAR backscatter signature using sigma-naught (σ^o), beta-naught (β^o), and gamma-naught (γ^o).

Image Products §	***FFROST*** *	σ^o	β^o	γ^o
C_1 in Amplitude	Without	*SIG.amp*	*BET.amp*	*GAM.amp*
	With	*SIG.amp.FF*	*BET.amp.FF*	*GAM.amp.FF*
C_2 in dB	Without	*SIG.dB*	*BET.dB*	*GAM.dB*
	With	*SIG.dB.FF*	*BET.dB.FF*	*GAM.dB.FF*
Incidence angle (*INC.ang*)				

§ See Section 4.3 for further details: Table 4-3 and Figure 4-2.

* Frost filter (FROST *et al.*, 1982).

$C_1 = [\{DN^2\}+B]/A$

$C_2 = (10*cc)*Log_{10}(C_1)$

where:

DN: Digital Number.

C_1: Radiometric-calibrated values of σ^o, β^o, or γ^o given in amplitude.

C_2: Radiometric-calibrated values of σ^o, β^o, or γ^o expressed in dB.

A: Range-dependent gain: *lutSigma.xml*, *lutBeta.xml*, or *lutGamma.xml*.

B: Constant offset (nominally set to zero for SGF products).

cc: Equal to 2 for the amplitude of the received radar beam.

5.4. PHASE 4: NEW SLICK-FEATURE ATTRIBUTES

The second, and last image-processing Phase performed during the present D.Sc. research (Figure 1-3) shows the calculation of new slick-feature attributes. These attributes are calculated to describe the oil slicks that have passed the QC-Standards established on Phase 2 (Quality Control: Section 6.2) using information retrieved from the satellite scenes processed on Phase 3 (RADARSAT Re-Processing: Section 6.3). Two main reasons explain why new slick-features are evoked:

1. Because the CBOS-Data is short of characteristics describing the observed oil slicks (see Table 2-2); and
2. To guarantee the excellence of the proposed qualitative-quantitative classification algorithm described in Section 5.10.

Although some of the new attributes explored herein are derived from the pre-existing basic oil slick descriptors shown on Table 2-2, others are bridged from elemental characteristics found in the peer-reviewed literature (Section 4.4.2). However, it is essential to emphasize that all slick-feature attributes suggested by the literature have been proposed to differentiate oil slicks from look-alike features (e.g. PISANO, 2011; SINGHA *et al.*, 2013), and not to distinguish oil seeps from oil spills as intended herein. Additionally, because of the exploratory nature of the present D.Sc. research, a particular set of basic statistical characteristics (LANE *at al.*, 2015) is experimentally used as new attributes to describe the characteristics of individual oil seeps and oil spills.

The new slick-feature attributes are included as new columns (or items) in the tabular framework of the CBOS-Data. Consequently, such practice builds-up a synergistic multivariate data library describing the individual oil slick polygons in the hyperspace (i.e. transactions or tabulated lines). This customized tabular dataset is used on this D.Sc. research Dissertation as the workable database explored in the further Phases to pave the way for the subsequent data mining. As such, from this point onwards, this analysis makes use of the modified version of the CBOS-Data that is referred to as the Campeche Bay Oil Slick Modified Database – hereafter CBOS-DScMod.

Four major types of attributes are considered, taking into account contextual information, satellite scene descriptors, geometry, shape, and dimension characteristic of individual oil slicks (i.e. size information), and SAR backscatter signature. A series of acronyms is provided throughout this Section that the reader should pay close attention as these are explored on the remaining of the manuscript.

The typical values and histograms of these attributes are provided in Section 6.4. Three questions need to be answered before plotting a histogram: 1) What is the number of bins? 2) What are the starting and ending points? 3) What is the bin width? Although the answers for theses questions affect the histogram shape, there is no ideal histogram binning selection method to provide correct answers. Herein, the number of bins was selected after experimenting with different methods (WAND, 1997; HAMMER, 2015b). The "Rice Rule" has been used (LANE *et al.*, 2015), in which the number of bins is equal to two times the cubic root of the number of observations that is 4,916 oil slicks, as for the QC-Standards outcome presented in Phase 2 (Section 6.2). This rule answers the first question: 34 bins. The minimum and maximum values of each attribute were initially applied as starting and ending points. The bin width was calculated by subtracting the starting from the ending point, then dividing the result by 34. However, the starting and ending points were optimized based on visual analysis of the resulted histogram shapes. This optimization was repeated several times to accommodate the outliers flagged on this visual analysis. This manual adjustment let the final number of intervals used in the histograms equals to 36 bins.

The calculation of the proposed new attributes is straightforward.

- **1st Attribute Type:** Contextual Information

The *Category* attribute informs the oil slick type of each polygon as visually interpreted by domain analysts: oil seep or oil spill. Likewise, the *Class* attributes classify its respective class. Two other relevant contextual attributes provide the geographical location of each polygon: latitude (*cLAT*) and longitude (*cLONG*) of the oil slick's centroid. A pair of satellite overpass attributes (i.e. *SARtime* and *SARdate*) also contributes with valuable information about the observed oil slick: while the former provides the time the oil slick has been imaged, the latter provides its observation date. Table 5-2 presents the contextual descriptors (n=6) explored on the present D.Sc. research; nonetheless, it is good to draw attention to the fact that these attributes are expanded and replaced after undergoing a set of Data Treatments in the Section 5.5.

- **2nd Attribute Type:** SAR Scene Descriptors

Of the existing CBOS-Data attributes (Table 2-2) related to the satellite scene, only the one representing the imaging configurations defined by the swath width and ground resolution of each oil slick polygon is kept – i.e. beam mode (*Bmode*). An additional SAR scene attribute is retrieved from the incidence angle image product (Table 5-1: *INC.ang*) to provide the acquisition geometry of the radar beam for each pixel within

the oil slick polygons. As shown below, when the SAR backscatter signature attributes are introduced, different basic statistical characteristics are also calculated for the *INC.ang* attribute. Table 5-3 presents the SAR scene descriptors (n=37) explored on the present D.Sc. research; however, it is good to emphasize that the *Bmode* attribute is expanded and replaced after a set of Data Treatments that occur in the Section 5.5.

Table 5-2: Oil slick characteristics explored on the present D.Sc. research: 1st Attribute Type (Contextual Information; n=6). These attributes are expanded and replaced after undergoing a set of Data Treatments proposed in Section 5.5 – see Table 5-10.

1st Attribute Type: Contextual Information § *			
1 2	***Category*** ***Class***		Oil Slick Type
3 4	***cLAT*** ***cLONG***	Latitude (°N) Longitude (°W)	Spatial Location
5 6	***SARtime*** ***SARdate***	Overpass Time Overpass Date	Temporal Location

§ Attributes originally present on the CBOS-Data – see Table 2-2.

* Attributes expanded and replaced in Section 5.5 – see Table 5-10.

Table 5-3: Oil slick characteristics explored on the present D.Sc. research: 2nd Attribute Type (SAR Scene Descriptors; n=37). These attributes undergo a set of Data Treatments proposed in Section 5.5 – see Table 5-10.

2nd Attribute Type: SAR Scene Descriptor		
1	***Bmode*** § *	Beam mode
2-37 **	***INC.ang***	Incidence angle of the radar beam

§ Attribute originally present on the CBOS-Data – see Table 2-2.

* Attribute expanded and replaced in Section 5.5 – see Table 5-10.

** Includes the 36 statistical measures calculated for the 4th Attribute Type.

- **3rd Attribute Type:** Geometry, Shape, and Dimension – Size Information

The two basic attributes of geometry, shape, and dimensions present in the CBOS-Data content (Table 2-2) are included in the CBOS-DScMod: area (*Area*) and perimeter (*Per*). Based on these two simple attributes, seven intricate ratios are derived:

The first measure evoked herein is the area to perimeter ratio (km):

$$AtoP = Area/Per$$

FISCELLA *et al.* (2010) suggest using the perimeter to area ratio (km^{-1}):

$$PtoA = Per/Area$$

Complementary, FISCELLA *et al.* (2010) and SINGHA *et al.* (2013) recommend using a dimensionless normalized perimeter to area ratio:

$$PtoA.nor = Per/[(2*(\mathrm{Pi}*Area))\hat{}(1/2)]$$

While small *PtoA.nor* values are usually related to simple geometry, larger values come from oil slicks with more complex geometries (CALABRESI *et al.*, 1999).

A dimensionless complexity measure is given by SOLBERG *et al.* (1999), such that:

$$COMPLEX.ind = (Per^2)/Area$$

In addition, BENTZ (2006) uses another dimensionless descriptor to illustrate how compact (i.e. close to a circle) is a sea-surface observed feature:

$$COMPACT.ind = (4*\mathrm{Pi}*Area)/(Per^2)$$

Two other indices have been utilized by PISANO (2011) to describe the oil slicks' characteristics, two of which are given by:

$$SHAPE.ind = [0.25*Per]/[Area\hat{}(1/2)]$$

$$FRAC.ind = [2*\ln(0.25*Per)]/[\ln(Area)]$$

The former has a unit of km^{-1}, whereas the latter is a dimensionless quantity. These two indices yield values close to the unit for regular polygons (i.e. circular or square); and larger numbers represent form irregularity (MCGARIGAL & MARKS, 1994).

An additional attribute is provided: the total number of pixels inside each oil slick polygon (*LEN*). Table 5-4 summarizes the attributes of geometry, shape, and dimension (n=10) explored herein.

- **4th Attribute Type**: SAR Backscatter Signature

The match-up of remote sensing and near-coincident *in situ* measurements is customarily completed to disclose the relationship between the satellite information and what is observed on a specific time and location. The analysis performed herein uses different measures to describe the backscatter radar signal strength of individual oil slicks (i.e. σ^o, β^o, and γ^o – see Table 4-3 and Figure 4-2) that are matched to the outcomes of the oil slick mapping executed during the CBOS-SatPro. Accordingly, the SAR backscatter signatures are compared with the sea-truthing introduced in Chapter 2 that represents the operator's interpretation defining the oil slick's categories and classes.

Table 5-4: Oil slick characteristics explored on the present D.Sc. research: 3rd Attribute Type (n=10). These attributes describe the attributes of Geometry, Shape, and Dimension (i.e. Size Information) of the oil slick polygons.

3rd Attribute Type: Geometry, Shape, and Dimension				
1	***LEN***	Number of pixels inside the oil slick polygon.		
2	***Area*** §	km^2		
3	***Per*** §	km	Perimeter	
4	***AtoP***	km	*Area* to *Per* ratio	*Area*/*Per*
5	***PtoA***	km^{-1}	*Per* to *Area* ratio	*Per*/Area
6	***PtoA*.nor**	*	Normalized *PtoA*	*Per*/[(2*(Pi**Area*))^(1/2)]
7	***COMPLEX.ind***	*	Complexity Index	(Per^2)/*Area*
8	***COMPACT.ind***	*	Compact Index	(4*Pi**Area*)/(Per^2)
9	***SHAPE.ind***	km^{-1}	Shape Index	[0.25**Per*]/[*Area*^(1/2)]
10	***FRAC.ind***	*	Fractal Index	[2*ln(0.25.**Per*)]/[ln(*Area*)]

§ Attributes originally present on the CBOS-Data – see Table 2-2.

* Dimensionless quantity.

The pairing of *in situ* measurements with collocated remote sensing data is usually achieved by comparing field observation with the pixel matching the sampling location (i.e. pixel-by-pixel evaluation) or with a multi-pixel box (i.e. 3x3, 5x5, etc.) centered at this location (BAILEY & WERDELL, 2006; CARVALHO, 2008). However, as the investigation performed herein analyses sea surface features (i.e. oil slicks), the centroid value (or centered box) may not be representative of the textural and/or radiometric information of the entire polygon (HU *et al.*, 2000).

Based on this reasoning, the present D.Sc. research uses information from all pixels within the individual polygons. As described below, different basic statistical measures are experimentally used to characterize the SAR backscatter signature of each oil slick observed during the CBOS-SatPro. These measures are separately calculated for the 13 radiometric-calibrated image products: *SIG.amp*, *SIG.amp.FF*, *SIG.dB*, *SIG.dB.FF*, *BET.amp*, *BET.amp.FF*, *BET.dB*, *BET.dB.FF*, *GAM.amp*, *GAM.amp.FF*, *GAM.dB*, *GAM.dB.FF*, and *INC.ang* (Table 5-1).

Firstly, as suggested by BENTZ (2006) and SINGHA *et al.* (2013), an arithmetic mean (*AVG*) of all pixels inside individual polygons is computed for each radiometric-calibrated image product. In the same way, three other numerical measures are given to represent the central tendency of the oil slick's SAR backscatter signature: the

median (*MED*), the mode (*MOD*), and the mid-mean (*MDM*[52]). These are used as different indicative ways to express a location parameter for the distribution center.

To analyze the spread of the SAR backscatter signature of the pixel values within an oil slick, six ways are explored as statistical measures of dispersion: standard deviation (*STD*), coefficient of dispersion (*COD*[53]), variance (*VAR*), total range (*RNG*), average absolute deviation (*AAD*[54]), and median absolute deviation (*MAD*[55]).

To evaluate the relative relationship between the dispersion of the pixel values around the central tendency value of the pixels within an oil slick polygon, a dimensionless quantity comes into play: the coefficient of variation (*COV*). Originally, this measure involves the ratio between *STD* and *AVG*, and is useful to compare the degree of variation of data with different units and different meanings. Because distinct forms of dispersion and central tendency measures are explored, *COV* is adapted to match other pair-values. As such, six *COV* sets are given combining different basic statistical characteristics, for instance, *STD*/*AVG*, *STD*/*MED*, *STD*/*MOD*, and *STD*/*MDM*, and so on.

SINGHA *et al.* (2013) and SOLBERG & VOLDEN (1997) refer to *COV* as power-to-mean ratio. While SOLBERG *et al.* (1999) describe such relationship as a measure of oil slick's homogeneity, for BENTZ (2006) this depicts the oil slick's heterogeneity. Although different authors recommend exploring *COV*, it is imperative to emphasize that oil slicks with different spatial structures (i.e. having a completely different pixel configuration) can have identical average or median values and the same standard deviation. Therefore, it might happen that the *COV* does not contribute much in target differentiation (MIRANDA, 1990).

Besides the abovementioned statistical measures (i.e. central tendency, dispersion, *COV*, etc.), minimum (*MIN*) and maximum (*MAX*) values of the pixels inside each polygon are also used as supplementary quantities to describe the oil slicks' radiometric-calibrated image products (Tables 5.1 and 5-5).

---

[52] *MDM* trims 25% at both ends to calculate the mean of the values between the 2nd and 3rd interquartiles.

[53] *COD* is calculated by subtracting the 1st interquartile from the 3rd interquartile, then dividing by the sum of these two interquartiles: (IQR3-IQR1)/(IQR3+IQR1)

[54] *AAD* corresponds to the mean of the absolute difference of each value minus the mean.

[55] *MAD* represents the median of the absolute difference of each value minus the median.

The information from the area surrounding the oil slicks also plays an essential role in the oil slick identification process, i.e. classification between oil slick and look-alike feature (e.g. SOLBERG *et al.*, 1999; FISCELLA *et al.*, 2000; 2010). Some authors evoke the term “damping ratio”, making reference to the radar return decrease from the inside to the outside of the oil slicks (HOLT, 2004). Nonetheless, no information from the background oil-free surface around the oil slicks has been taken into consideration in the experiments conducted herein and the objectives of the present study are solely attained using information from the inside of polygons delimiting oil seeps and oil spills. The decision of not using damping ratio variables has been made to evaluate a simpler as possible range of variables that only accounts for information within the oil slicks polygons’ limits.

Table 5-5 presents the pool of SAR backscatter signature descriptors (i.e. basic statistical measures: n=432) explored to describe the characteristics of the pixels inside the oil slicks as a function of radiometric-calibrated image products (Table 5-1). As shown on Section 5.5, these attributes undergo a set of Data Treatments.

- **Attribute Types:** Summary

The collection of slick-feature attributes used on the present D.Sc. research to describe the oil slicks observed during the CBOS-SatPro accounts for four major types of oil slick characteristics: contextual (Table 5-2: n=6), satellite scene (Table 5-3: n=37), geometry, shape, and dimension (Table 5-4: n=10), and SAR backscatter signature (Table 5-5: n=432). Although 485 different descriptors have been introduced so far, the number of attributes is expanded as some of them are replaced after undergoing a set of Data Treatments on the next Section.

5.5. PHASE 5: DATA TREATMENT

This is the last Phase of the Workable-Database Preparation (Figure 1-3) and this Section addresses three matters involving the oil slick characteristics of the CBOS-DScMod proposed in the previous Phase:

1. Statistical methods of data comparison;
2. Slick-features with different units; and
3. Attributes with qualitative values.

Table 5-5: Oil slick characteristics explored on the present D.Sc. research: 4th Attribute Type (SAR Backscatter Signature; n=432 †). These attributes describe the basic statistical characteristics of all pixels inside the oil slick polygons.

4th Attribute Type: SAR Backscatter Signature				n=**36**x12=432 §
Basic statistical measures				n=**12**x12=144 §
1	1-12	***AVG***	Average	Central Tendency (n=4)
2	13-24	***MED***	Median	
3	25-36	***MOD***	Mode	
4	37-48	***MDM***	Mid-Mean	
5	49-60	***STD***	Standard Deviation	Dispersion (n=6)
6	61-72	***COD***	Coefficient of Dispersion	
7	73-84	***VAR***	Variance	
8	85-96	***RNG***	Total Range	
9	97-108	***AAD***	Average Absolute Deviation	
10	109-120	***MAD***	Median Absolute Deviation	
11	121-132	***MIN*** †	Minimum	
12	133-144	***MAX***	Maximum	
COV = Coefficient of Variation				n=**24**x12=288 §
13	145-156	***COV.STD/AVG*** *		**1st combined COV set** *STD* divided by Central Tendency (n=4)
14	157-168	***COV.STD/MED***		
15	169-180	***COV.STDMOD***		
16	181-192	***COV.STD/MDM***		
17	192-204	***COV.COD/AVG***		**2nd combined COV set** *COD* divided by Central Tendency (n=4)
18	205-216	***COV.COD/MED***		
19	217-228	***COV.COD/MOD***		
20	229-240	***COV.COD/MDM***		
21	241-252	***COV.VAR/AVG***		**3rd combined COV set** *VAR* divided by Central Tendency (n=4)
22	253-264	***COV.VAR/MED***		
23	265-276	***COV.VAR/MOD***		
24	277-288	***COV.VAR/MDM***		
25	289-300	***COV.RNG/AVG***		**4th combined COV set** *RNG* divided by Central Tendency (n=4)
26	301-312	***COV.RNG/MED***		
27	313-324	***COV.RNG/MOD***		
28	325-336	***COV.RNG/MDM***		
29	337-348	***COV.AAD/AVG***		**5th combined COV set** *AAD* divided by Central Tendency (n=4)
30	349-360	***COV.AAD/MED***		
31	361-372	***COV.AAD/MOD***		
32	373-384	***COV.AAD/MDM***		
33	385-396	***COV.MAD/AVG***		**6th combined COV set** *MAD* divided by Central Tendency (n=4)
34	397-408	***COV.MAD/MED***		
35	409-420	***COV.MAD/MOD***		
36	421-432	***COV.MAD/MDM***		

§ Separately calculated for the 12 different forms of σ^o, β^o, and γ^o (Table 5-1): *SIG.amp*, *SIG.amp.FF*, *SIG.dB*, *SIG.dB.FF*, *BET.amp*, *BET.amp.FF*, *BET.dB*, *BET.dB.FF*, *GAM.amp*, *GAM.amp.FF*, *GAM.dB*, *GAM.dB.FF*.

† See Negative Values Scaling in Section 6.5 that eliminates 9 MIN variables.

* Original COV ratio.

The 1st matter refers to subsequent data mining – e.g. Phase 8 (Discriminant Function: Section 5.8) – that assumes normal distribution of the data. While the 2nd matter refers to most slick-features within the CBOS-DScMod, the 3rd one concerns only to some contextual variables (e.g. *Category*, *Class*, etc.) and a SAR scene descriptor (*Bmode*). LEGENDRE & LEGENDRE (2012) define "coding" as the process in which a data value is converted into another data value. Different coding ways are found in the literature to overcome the three aforementioned matters (VALENTIN, 2012). In preparation for the Multivariate Data Analysis Practices, shown as the Yellow Phases (6 to 10) on Figure 1-3, specific Data Treatments (i.e. coding) are applied in sequence to the oil slick characteristics within the CBOS-DScMod.

The CBOS-DScMod has both numeric values (i.e. quantitative or metric variables – e.g. *Area*, *FRAC.ind*, *SIG.amp.AVG*, etc.) and non-numeric values (i.e. qualitative or non-metric variables – e.g. *Class*, *Bmode*, etc.). A conspicuous aspect about the Data Treatment performed on the present Phase is that, after its application, all oil slick characteristics assume discrete (i.e. integer) or continuous (i.e. float) numerical metric values, and no categorical variables are passed to further Phases.

- **1st Data Treatment:** Log_{10} Transformation

Several non-linear transformations can be applied to quantitative attributes to bring non-symmetric distributions (e.g. Figure 6-19, Figure 6-20, Figure 6-21, Figure 6-22, and Figure 6-23) to, or at least close to, a normal distribution pattern (i.e. Gaussian bell-shape). Various forms of transformation have been explored on this study: square, cubic, and fourth root, as well as natural (napierian) and base 10 (Log_{10}) logarithms (LEGENDRE & LEGENDRE, 2012; VALENTIN, 2012; LANE *et al.*, 2015).

Although such transformations can be independently applied to each attribute, for consistency, during this investigation all-numeric variables have uniformly undergone the same transformation (column-wise). The visual analysis of histograms showed that Log_{10} had best results to stabilize the data, to decrease the effect of outliers, and to reduce the skewness of most attributes. An exception is *FRAC.ind* with its negative to positive range (Table 6-13) that was transformed with a cubic root.

- **2nd Data Treatment:** Negative Values Scaling

Because logarithm functions can not be applied to negative values, the pixels inside the oil slicks were inspected before the Log_{10} transformation. This mostly relates to the SAR Backscatter Signature (Table 5-5: 4th Attribute Type), as the other Attribute Types are all positive (except *FRAC.ind*). Oil slick measurements given in dB are negative

and also undergone this linear scaling action. Eventually, oil slicks that for some reasons[56] had negative amplitude pixel values also undertook the Negative Values Scaling Data Treatment, which consists of subtracting the minimum negative pixel value within the oil slick (*negPIXmin*) from each pixel inside this oil slick (*PIX*) and adding one to it:

$$PIXpos = [PIX-(negPIXmin))+1]$$

where *PIXpos* is the new positive pixel value. This type of coding is usually called "translation" (SNEATH & SOKAL, 1973). It simply adds two constants to each pixel inside particular oil slicks: *negPIXmin* and 1. The pixel with the minimum negative value becomes equal to 1: *PIX*=*negPIXmin* gives *PIXpos*=1. Although this additional Data Treatment changes the values of the pixels inside some oil slicks, the relationship among pixel values within individual oil slicks is preserved, therefore, this additional Data Treatment does not cause any deleterious impact to the analysis performed herein, which compares the relationship among pixel values (SNEATH & SOKAL, 1973; LANE *et al.*, 2015).

- **3rd Data Treatment:** Ranging Standardization

While some of the quantitative attributes within the CBOS-DScMod are dimensionless (e.g. dB), others have incompatible units (e.g. km, km^2, decimal degree, etc.). To compare the oil slick characteristics in the subsequent data mining, the same common scale is recommended (MOITA NETO & MOITA, 1998; LEGENDRE & LEGENDRE, 2012; VALENTIN, 2012). Of the various available methods, there is no dearth of standardization. However, MILLIGAN & COOPER (1988), who investigated different approaches to standardize variables, advocated that, depending upon the utilized statistics (e.g. Clustering Analyses), Ranging is more effective than other methods (e.g. z-score).

As such, after applying the two-abovementioned Data Treatments (i.e. Negative Values Scaling and Log_{10} Transformation) the Ranging scaling procedure has been uniformly applied (column-wise) to all-numeric variables within the CBOS-DScMod. The Ranging Standardization, besides bounding the magnitude of the attributes to values between zero (0) and one (1), also equalizes the variability of the attributes to a common scale (SNEATH & SOKAL, 1973):

$$Xranged = [X-Xmin]/[Xmax-Xmin]$$

[56] For instance: speckle noise, range-dependent gain calculation imprecision, open *.shp* files causing information not belonging to the oil slick to be accounted for, etc.

where *Xranged* is the new Ranged value, *X* is the actual attribute value for a particular oil slick, *Xmin* is the minimum value of for this attribute among all oil slicks, and *Xmax* is the maximum value of such attribute. For instance, if taking the *SIG.amp.AVG* value of one oil slick: subtract the minimum *AVG* for this radiometric-calibrated image product of all 4,916 oil slicks, and then the result is divided by the maximum *AVG* of all 4,916 oil slicks minus the minimum *AVG* of all 4,916 oil slicks. The *Xranged* variables assume non-negative values, and only one oil slick with *Xranged*=0 and another one with *Xranged*=1, respectively when *X*=*Xmin* and when *X*=*Xmax*. Exceptions may occur if there is more than one oil slick with the same *Xmin* or *Xmax* values.

- **4th Data Treatment:** Dummy Variables

Certain slick-feature attributes within the CBOS-DScMod are converted to a specific indicator type: "Dummy Variable" (LEGENDRE & LEGENDRE, 2012). These include the qualitative attributes (i.e. string variables: *Category*, *Class*, and *Bmode*) and the quantitative spatio-temporal variables (i.e. *SARtime*, *SARdate*, *cLAT*, and *cLONG*). For convenience, the Dummy Variables explored herein have values of one (1) or zero (0), thus referring to its presence (Yes) or absence (No), respectively. The usage of this type of binary-coded variable has two explanations:

1. An attempt to decompose complex variabilities (i.e. hidden knowledge) into more useful information; and
2. To allow the application of multivariate data analysis techniques that assume the variables are quantitative descriptors.

Explanations of how the oil slick characteristics have been expanded and converted into Dummy Variables are given below:

An easy way to understand Dummy Variables is, for instance, demonstrated with the *SARtime* attribute. From this, one new Dummy Variable is created: *DoN* (day or night) that corresponds to the oil slicks imaged during the daytime or at nighttime, thus matching the RADARSAT orbit direction: descending and ascending overpasses above the Campeche Bay region (Table 6-2: UTC). In this case, the oil slicks observed during the day (descending passes) have the *DoN* variable equal to 1, and those imaged at night (ascending passes) have the *DoN* variable equal to 0. Table 5-6 presents an example to illustrate the conversion of the *SARtime* attribute into *DoN*.

Table 5-6: Example of a new numeric Dummy Variable (*DoN*: Day or Night) included in the Campeche Bay Oil Slick Modified Database (CBOS-DScMod) to replace one contextual attribute: *SARtime*. See also Table 5-2.

Contextual Attribute	New Dummy Variable (n=1)	Numeric Dummy Values Example	
		Oil slick image during the day	Oil slick image at night
SARtime	*DoN*	**1**	**0**

The *SARdate* attribute is broken down regarding eleven distinct date elements. The first two are the actual day of year (*DoY*) and month (*MON*) when the oil slick has been observed. Once these are retrieved, they undergo the Ranging Standardization.

Another date element considers the boreal seasons that is represented by four Dummy Variables: *WNT*, *SPG*, *SMM*, and *FLL*, respectively for Winter (J/F/M), Spring (A/M/J), Summer (J/A/S), and Fall (O/N/D). If an oil slick has been imaged during the boreal Winter it has the *WNT* variable equal to 1, and the other dummy season variables equal to 0; and so on for *SPG*, *SMM*, and *FLL*. Similarly, another date element set corresponds to the five analyzed years: if an oil slick has been observed in the year 2008, a Dummy Variable equal to 1 was assigned for that observation and the other dummy year variables were set to 0 for that oil slick; and so on for *2009*, *2010*, *2011*, and *2012*. Table 5-7 presents a few dates to demonstrate the conversion of the *SARdate* attribute into Dummy Variables.

From the qualitative *Category* attribute two new Dummy Variables are created: *oSPILL* and *oSEEP* for the observations that are identified as oil spills and oil seeps, respectively. Likewise, from the qualitative *Class* attribute, nine new Dummy Variables come into play: six to classify oil spills (*BGT*, *BGT-1*, *BGT-2*, *BGT-3*, *SHP*, and *orphSP*) and three to describe oil seeps (*CANT*, *CLUS*, and *orphSE*). Because three specific Brightspots registered a large number of oil spills (Table 6-12), they have been separated into: *BGT-1*, *BGT-2*, and *BGT-3*. Some examples of the new Dummy Variables created from the *Category* and *Class* attributes are illustrated in Table 5-8.

The only qualitative SAR scene descriptor to undergo a Dummy Variable conversion is the *Bmode* that is split in four: *SCNA*, *SCNB*, *WDE1*, and *WDE2* (Table 5-9). These, respectively, represent the RADARSAT-2 beam modes that imaged the oil slicks within the CBOS-DScMod: ScanSAR Narrow 1, ScanSAR Narrow 2, Wide 1, and Wide 2.

Table 5-7: Example of eleven new numeric Dummy Variables (*DoY*, *MON*, *WNT*, *SPG*, *SMM*, *FLL*, *2008*, *2009*, *2010*, *2011*, and *2012*) included in the Campeche Bay Oil Slick Modified Database (CBOS-DScMod) to replace one contextual attribute: *SARdate*. See also Table 5-2.

Contextual Attribute	New Dummy Variables (n=11)			Numeric Dummy Values Examples			
				12 June 2009	10 January 2010	3 August 2008 **	31 December 2012 **
SARdate	*1.*	***DoY*** § *	Day of Year	**163**	**10**	**216**	**366**
	2.	***MON*** § *	Months	**6**	**1**	**8**	**12**
	3.	***WNT***	Winter	**0**	**1**	**0**	**0**
	4.	***SPG***	Spring	**1**	**0**	**0**	**0**
	5.	***SMM***	Summer	**0**	**0**	**1**	**0**
	6.	***FLL***	Fall	**0**	**0**	**0**	**1**
	7.	***2008*** **		**0**	**0**	**1**	**0**
	8.	***2009***		**1**	**0**	**0**	**0**
	9.	***2010***		**0**	**1**	**0**	**0**
	10.	***2011***		**0**	**0**	**0**	**0**
	11.	***2012*** **		**0**	**0**	**0**	**1**

§ Not Dummy Variable: require Log_{10} Transformation and Ranging Standardization.

* *DoY* (from 1 to 366 **) and *MON* (from 1 to 12).

** Leap years.

Table 5-8: Example of eleven numeric Dummy Variables (*oSPILL*, *oSEEP*, *BGT*, *BGT-1*, *BGT-2*, *BGT-3*, *SHP*, *orphP*, *CANT*, *CLUS*, and *orphSE*) included in the Campeche Bay Oil Slick Modified Database (CBOS-DScMod) to replace two qualitative contextual attributes: *Category* and *Class*. See also Table 5-2.

Contextual Attribute	New Dummy Variables (n=11)			Numeric Dummy Values Examples			
				Cantarell Oil Seep	Orphan Seep	Orphan Spill	Ship Spill
Category	1.	***oSPILL***	Oil spills	**0**	**0**	**1**	**1**
	2.	***oSEEP***	Oil seeps	**1**	**1**	**0**	**0**
Class	3.	***BGT***	Brightspots	**0**	**0**	**0**	**0**
	4.	***BGT-1***	Bright-1	**0**	**0**	**0**	**0**
	5.	***BGT-2***	Bright-2	**0**	**0**	**0**	**0**
	6.	***BGT-3***	Bright-3	**0**	**0**	**0**	**0**
	7.	***SHP***	Ship Spills	**0**	**0**	**0**	**1**
	8.	***orphSP***	Orphan Spills	**0**	**0**	**1**	**0**
	9.	***CANT***	Cantarell Oil Seep	**1**	**0**	**0**	**0**
	10.	***CLUS***	Other Clusters	**0**	**0**	**0**	**0**
	11.	***orphSE***	Orphan Seeps	**0**	**1**	**0**	**0**

Table 5-9: Example of four new numeric Dummy Variables (*SCNA*, *SCNB*, *WDE1*, and *WDE2*) included in the Campeche Bay Oil Slick Modified Database (CBOS-DScMod) to replace one SAR scene attribute: *Bmode*. See also Table 5-3.

SAR Scene Attribute	New Dummy Variable (n=4)	Numeric Dummy Values Examples			
		Oil slick imaged with ScanSAR Narrow 1	Oil slick imaged with ScanSAR Narrow 2	Oil slick imaged with Wide 1	Oil slick Imaged with Wide 2
Bmode	*1* ***SCNA***	**1**	**0**	**0**	**0**
	2 ***SCNB***	**0**	**1**	**0**	**0**
	3 ***WDE1***	**0**	**0**	**1**	**0**
	4 ***WDE2***	**0**	**0**	**0**	**1**

A more complicated Dummy Variable retrieval process comes from the two contextual oil slick characteristics of spatio-location: latitude (*cLAT*) and longitude (*cLONG*). From these, six new variables are created: three for latitude and three for longitude. This occurs once the Log_{10} Transformation has been applied to both, which have been converted to decimal degrees during Phase 1 (Data Familiarization: Section 6.1). These six new variables are based on visual inspection of the latitude and longitude Log-Transformed histograms (Figure 6-24) that have a bimodal distribution frequency.

In the latitude domain, two new Dummy Variables correspond to two regions of oil slick occurrence (Figure 6-24 top panel: *RG1.LAT* and *RG2.LAT*); idem for the longitude domain (Figure 6-24 bottom panel: *RG1.LONG* and *RG2.LONG*). The creation processes are the same for both domains: the trough between the two peaks of each histogram sets the limits between the two regions. While oil slicks on the left side of the trough belong to Region-1 (*RG1*=1 and *RG2*=0), oil slicks on the right side (including those from the trough) belong to Region-2 (*RG1*=0 and *RG2*=1).

Here it is where it gets intricate: the other two new variables that come into play (*PKD.LAT* and *PKD.LONG*) are not binary-coded Dummy Variables; instead, they have undergone an unusual Data Treatment, yet, identical for the two domains. The retrieval of the so-called peak distance (*PKD*) is achieved by calculating the absolute difference between the values of individual oil slicks to the peak (i.e. bivariate mode) of its respective region. This is independently calculated per region: oil slicks within Region-1 (*RG1*=1) have the peak distance calculated in relation to the mode of this region, whereas oil slicks from Region-2 (*RG2*=1) use the mode of its region. After the peak distance calculation, the Ranging Standardization is separately applied to the two regions per domains. This means that, differently from all variables that have undergone the Ranging Standardization, *PKD.LAT* and *PKD.LONG* have each two zeros (0) and two ones (1), one for each region.

- **Data Treatment:** Summary

The CBOS-DScMod, which was initially introduced in Phase 4 (New Slick-Feature Attributes: Section 5.4) with 485 different oil slick descriptors, has been further refined during the present Phase and now accounts for 511 variables: 485-7+33. The Data Treatments performed herein are illustrated on Figure 5-2 and summarized below:

1. The values of all pixels inside the oil slicks are positive (e.g. dB) due to the application of the Negative Values Scaling. This occurred before the Log_{10} Transformation and was followed by the Ranging Standardization;

2. The frequency of distribution of all variables has been brought to, or at least close to, a Gaussian distribution: Log_{10} Transformation;

3. All qualitative variables are coded with values lying between 0 and 1 after the Ranging Standardization; and

4. The 7 qualitative attributes (e.g. *Category*, *Class*, *Bmode*, etc.) have been replaced by 33 new Dummy Variables (binary-coded to 1 or 0). These are presented in Table 5-10.

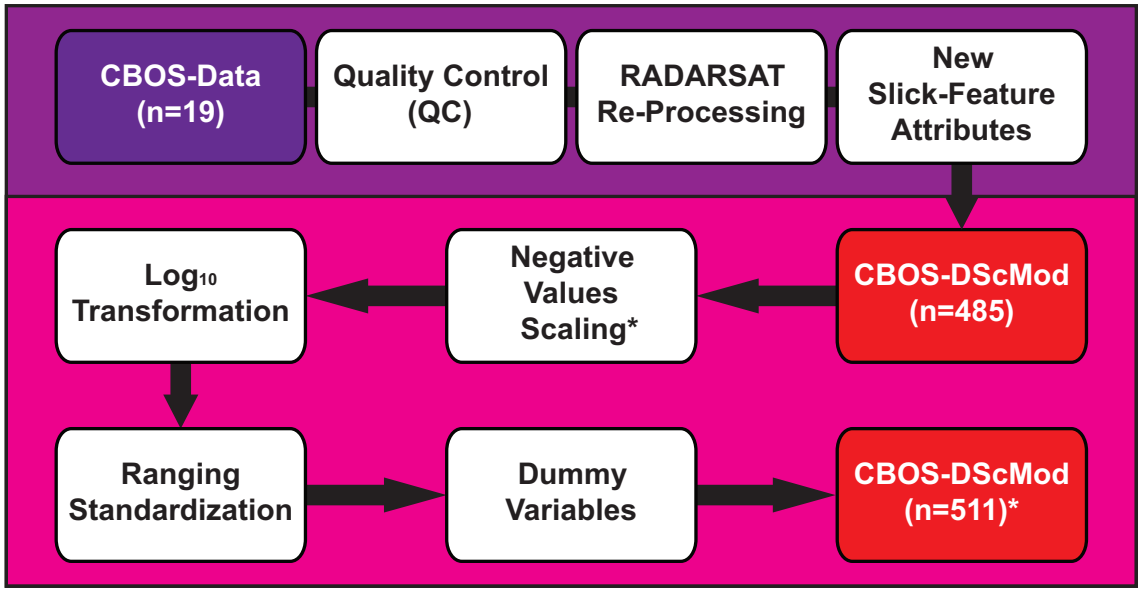

Figure 5-2: Sequence of Data Treatments applied to the attributes of the Campeche Bay Oil Slick Modified Database (CBOS-DScMod). *An important observation should be made about the Negative Values Scaling: 9 *MIN* variables were eliminated, leaving the CBOS-DScMod with 502 variables (as shown on Section 6.5), instead of 511.

Table 5-10: Summary of the thirty-three new numeric Dummy Variables (binary-coded to 1 or 0) used to describe oil slick characteristics. These are included in the tabular framework of the Campeche Bay Oil Slick Modified Database (CBOS-DScMod) to replace seven qualitative attributes.

Replaced: Old Attributes		Included: New Dummy Variables			
1	*Category* (Table 5-8) ¥	1	1	***oSPILL***	Oil Spill
		2	2	***oSEEP***	Oil Seep
2	*Class* (Table 5-8) ¥	3	1	***BGT***	Brightspot
		4	2	***BGT-1***	Bright-1
		5	3	***BGT-2***	Bright-2
		6	4	***BGT-3***	Bright-3
		7	5	***SHP***	Ship Spills
		8	6	***orphSP***	Orphan Spill
		9	7	***CANT***	Cantarell
		10	8	***CLUS***	Clusters
		11	9	***orphSE***	Orphan Seep
3	Latitude (*cLAT*) ¥	12	1	***RG1.LAT***	Region-1
		13	2	***RG2.LAT***	Region-2
		14	3	***PKD.LAT****	Peak Distance
4	Longitude (*cLONG*) ¥	15	1	***RG1.LONG***	Region-1
		16	2	***RG2.LONG***	Region-2
		17	3	***PKD.LONG****	Peak Distance
5	*SARtime* (Table 5-6) ¥	18	1	***DoN***	Day (1) or Night (0)
6	*SARdate* (Table 5-7) ¥	19	1	***DoY****	Day of Year
		20	2	***WNT***	Winter J/F/M
		21	3	***SPG***	Spring A/M/J
		22	4	***SMM***	Summer J/A/S
		23	5	***FLL***	Fall O/N/D
		24	6	***2008***	Analyzed Years
		25	7	***2009***	
		26	8	***2011***	
		27	9	***2010***	
		28	10	***2012***	
		29	11	***MON****	Month
7	Beam Modes (*Bmode*) (Table5-9) ¥¥	30	1	***SCNA***	ScanSAR Narrow 1
		31	2	***SCNB***	ScanSAR Narrow 2
		32	3	***WDE1***	Wide 1
		33	4	***WDE2***	Wide 2

¥ Table 5-2: 1st Attribute Type (Contextual information).

¥¥ Table 5-3: 2nd Attribute Type (SAR scene descriptor).

* Not Dummy Variable: requires Log10 Transformation and Ranging Standardization (Figure 5-2).

5.6. PHASE 6: ATTRIBUTE SELECTION

This is the first Phase of the Multivariate Data Analysis Practice (Figure 1-3). This Section discusses an imperative step in the numerical analysis of the CBOS-DScMod: the choice of more relevant descriptors among the several attributes (n=511) proposed in Phase 4 (New Slick-Feature Attributes: Sections 5.4 and 6.4) and further refined in Phase 5 (Data Treatment: Sections 5.5 and 6.5). Attribute selection (also termed as feature selection[57]) deals with the complex matter of reducing dimensionality.

In most instances of numerical ecology assessments, space reduction helps the elucidation of the problem solution, as well as may improve the performance of classification algorithms (HALL, 1999; LEGENDRE & LEGENDRE, 2012). An aspect of notice is that the sample size is not affected: 4,916 oil slicks, as established in Phase 2 (Quality Control: Section 6.2).

Independent attributes (i.e. lower degree of dependence from one variable to another) reduce the messiness of the subsequent data mining, as the use of correlated variables does not fulfill a particular pre-requisite of the Discriminant Analysis performed on Phase 8 (Section 5.8). That this assumption be satisfied (i.e. variables not correlated with each other, or the least correlated as possible) is fundamental to give robustness to the Discriminant Function results.

The analyses explored herein evaluate the relevance of the attributes to eliminate redundant or irrelevant variables to the classification (prediction) processes (JAIN & ZONGKER, 1997). The attributes within the CBOS-DScMod are clustered to select more representative variables, in order to reduce the variable-hyperspace dimension. It is expected that the attribute selection processes explored herein incurred without loss of information. Accordingly, the multivariate data analysis techniques that are explored to distinguish the oil slick type are not only performed with 502 attributes, as previously proposed (Figure 5-2). Instead, they are also developed with what is called herein as "original sets" and "optimal subsets" of selected variables.

As the choice of the attribute selection method strongly influences in the variable subset, two distinct attribute selection approaches are explored mostly based on their simplicity: UPGMA (Unweighted Pair Group Method with Arithmetic Mean) and CFS (Correlation-Based Feature Selection).

[57] GUYON & ELISSEEFF (2003 – p. 1157) list the feature selection objectives: "improving the prediction performance of the predictors, providing faster and more cost-effective predictors, and providing a better understanding of the underlying process that generated the data."

- **UPGMA:** Unweighted Pair Group Method with Arithmetic Mean

Clustering analyses identify objects (or descriptors) that are similar enough to be grouped together, and/or recognize differences among objects (or descriptors) to form such groups (SNEATH & SOKAL, 1973). There are two viewpoints about clustering data: Q-mode and R-mode (VALENTIN, 2012). While the former reveals the degree of association among objects (i.e. transactions or lines of a tabular framework), the latter measures resemblance between variables (i.e. items or table columns). These are sometimes referred to as "single instances" as they uncover the relationship among the objects (variables) based on the variables (objects). As the CBOS-DScMod objects are oil slicks and its variables are the oil slick descriptors, the analysis proposed in this first attribute selection method is in the R-mode.

Of the metrics available to quantify the dependence among variables (e.g. single linkage, weighted clustering, etc.), the Unweighted Pair Group Method with Arithmetic Mean (UPGMA) has been selected. This sequential, agglomerative, hierarchical, non-overlapping (SNEATH & SOKAL, 1973) strategy is also referred to as Unweighted Arithmetic Average Clustering (LEGENDRE & LEGENDRE, 2012).

The UPGMA choice was based on its clustering criteria: it uses an equally-weighted pair wise group relationship among variables and, as the method's name suggests, groups are formed based on mean resemblance: a variable is attributed to a specific group that has the larger mean resemblance with all other variables of that same group (VALENTIN, 2012). The utilized resemblance measure (similarity) was the Pearson's r correlation coefficient, following LEGENDRE & LEGENDRE (2012): quantitative physical, or environmental descriptors neither ordered nor monotonically related.

A free scientific data analysis software package (PAleontological STatistics: PAST[58] version 2.17c) has been utilized to implement the UPGMA (HAMMER *et al.*, 2001). Rooted-tree dendrograms (i.e. diagrams of relationships) with a bootstrapping of 100 replicates help to find hierarchical relationships (i.e. affinity) among variables. PAST lists in a separate table the order the variables appear in the dendrograms.

As there is a large subjectivity while interpretation dendrograms to decide the threshold (i.e. cut-off level) to form groups (e.g. KELLEY *et al.*, 1996), associated to the exploratory nature of the present D.Sc. research, two values have been arbitrarily selected to assess the robustness of the groups that were formed. These are simple to

[58] PAST: http://folk.uio.no/ohammer/past/

incorporate but are user-defined values. Their choice aimed to guarantee replicability, as different cut-offs gives different groups of variables.

The first threshold uses the Cophenetic Correlation Coefficient (CCC[59]), a metric commonly used to quantify the deformation degree of the dendrogram, i.e. Pearson's r correlation between the distance matrixes: actual and predicted (FARRIS, 1969; SARÇILI *et al.*, 2013; SILVA & DIAS, 2013). Nevertheless, herein, the CCC value is subjectively used as a cut-off to specify the clusters. Its value is automatically calculated in PAST and varies depending upon dataset. The second threshold is simply to use a fixed similarity value of 0.5 (i.e. Pearson's r correlation coefficient).

These thresholds are used to draw horizontal lines (i.e. phenon lines) across the dendrograms: when such lines cross a branch ("edge" or vertical line), a group is formed (SOKAL & ROHLF, 1962; NCSS, 2015). One should note that the attribute selection occurs twice for each UPGMA implementation, one for each phenon line: CCC and 0.5 thresholds.

The order the variables are plotted is not relevant other than forming groups. In addition, the number of groups and the number of members in each group (i.e. cluster size; SNEATH & SOKAL, 1973) are not relevant while reducing the CBOS-DScMod variables dimensionality. This is because the exploratory nature of this research focuses on designing the simplest possible classification algorithm to distinguish natural from man-made oil slicks, regardless of which and how many variables are used. Therefore, from each group of similar variables, only one variable is selected. Correlation imposes complicatedness on subsequent data mining, e.g. Phase 8 (Discriminant Function: Section 5.8).

Variable were selected giving preference to an arbitrary user-defined strategy based on the simplicity of their meanings and on their calculation form: simple variables are preferred over complicated ones: basic variables in lieu of ratios (e.g. *Area* versus *AtoP*), C_1 (amplitude) rather than C_2 (dB), SAR backscatter signature without Frost filter than with Frost, and central tendency is preferable to dispersion metrics. The variables choice followed the order shown on Table 5-1 (σ^o, β^o, or γ^o), as well as the order the information is shown on Tables 5-2 to 5-5 (e.g. *AVG*, *MED*, *MOD*, and *MDM, etc.*).

[59] CCC also determines the classification and clustering efficiency: clusters are considered useful with values of about 0.75 or 0.8 (VALENTIN, 2012; NCSS, 2015).

- **CFS:** Correlation-Based Feature Selection

The second method to evaluate the redundancy and irrelevancy of the CBOS-DScMod variables (n=502) is the Correlation-Based Feature Selection – CFS (HALL & SMITH, 1997; 1999; BOUCKAERT *et al*., 2008). The scientific machine learning open source package utilized to implement CFS subset evaluation was the Waikato Environment for Knowledge Analysis: WEKA[60] version 3.6.12.

Two reasons are given for using the CFS: application simplicity and its fully automated processes, as compared to the semi-automatic UPGMA implementation manner, which has two user-defined steps: variable selection strategy and thresholds to find clusters (and therefore, variables). The CFS attribute selection characteristics also justify its choice as it is based on a heuristic variable selection strategy. The worth of various attributes subsets (i.e. groups of selected variables) is evaluated to choose attributes with low inter-correlation but highly correlated to the categories been distinguished (HALL, 1999). In essence, a "merit" is calculated as a measure of the usefulness of the selected optimal subset of attributes. This is based on the redundancy among all variables and the predictability of individual variables to distinguish spills and seeps. As such, several possible combinations of attributes are searched to find the variables that best classify (i.e. predict) the two pre-determined categories: oil seeps or oil spills.

The WEKA attribute selection tool has two separate parts the user needs to specify: evaluation function and search algorithm. The former is the actual method by which the subsets of attributes are evaluated: CFS (*CfsSubsetEval*). The purpose of the latter is to improve the evaluation function and of the available suite of search algorithms, the best-first searching strategy (*BestFirst*) has been selected to navigate through the attribute subsets (WILT *et al.*, 2010). This is one of the most commonly used search algorithms: it searches the space of attributes that has a size of 2^d (in which "d" is the number of attributes) by greedy hill-climbing augmented (AHA & BANKERT, 1994).

WEKA default settings were used for all options of the attribute evaluator and search method – except that the backward sequential selection (*BSS*) was used instead of the default forward sequential selection (*FSS*), as it searched more subsets. Best first *BSS* starts with a full set of attributes and backward search (remove) those that its removal maximizes the search results, i.e. lower correlation among variables and higher correlation to the distinguished category (TETKO *et al.*, 2008).

[60] WEKA: http://www.cs.waikato.ac.nz/ml/weka/

- **Attribute Selection:** Summary

The two methods utilized to select the attributes' optimal subsets, i.e. UPGMA (CCC and 0.5) and CFS (n=33), to be explored in the subsequent data mining were performed in different original sets of data (n=11), as shown on Figure 5-3 – these are collectively referred to as data sub-divisions (n=44). It is expected that the particularly fruitful attribute-wise evaluations disclose hidden complexities into useful information capable to distinguish oil spills from oil seeps. As such, the reader should bear in mind that the information presented on Figure 5-3 is extremely relevant for the comprehension of the rest of the manuscript, this includes, for instance, the order the subsequent data mining is explored.

Firstly, a complete exploration of the full remote sensing library content of the CBOS-DScMod was evaluated: all variables proposed in Section 5.4 and Section 5.5 (n=502). Subsequently, an investigation was completed with all SAR backscatter signature variables (Table 5-1 and Table 5-5: σ^o, β^o, or γ^o) with (n=433)[63‡] and without (n=423)[61‡] the geometry, shape, and dimension attributes. To determine the associated uncertainties of using different sets of attributes to differentiate the oil slick type, several attribute selection investigations were completed in parallel to explore each of the three SAR backscatter coefficients (σ^o, β^o, and γ^o) with (n=151) and without (n=141) the attributes of geometry, shape, and dimension. The geometry, shape, and dimension attributes were also analyzed in a separate mode.

Although literature suggests not using images given in Digital Numbers (DN's) to compare SAR images (FREEMAN, 1992; THOMPSON & MCLEOD, 2004; EL-DARYMLI *et al.*, 2014), an assessment has explored DN's. DN images were processed in the same way as explained in Phase 3 (RADARSAT Re-Processing: Section 5.3), except that there was no calculation of radiometric-calibrated SAR-derived backscatter coefficients, and Frost filter and APC (Antenna Pattern Compensation) were applied following the procedures depicted on Figure 2-2 – see also Section 2.3.2. DN signatures have been expressed by the same set of basic statistical characteristics calculated for the pixels inside the oil slicks experimentally used to describe SAR backscatter signature (Table 5-5: 4th Attribute Type): *AVG*, *MED*, *MOD*, *MDM*, *STD*, *COD*, *VAR*, *RNG*, *AAD*, *MAD*, six *COV* sets, and *MAX* (n=35)[62]. The Data Treatment processes proposed in Phase 5 (Section 5.5) have also been performed (Figure 5-2).

[61‡] 9 *MIN* variables were eliminated by the Negative Values Scaling (Section 6.5).
[62] The *MIN* variable was eliminated by the Negative Values Scaling (Section 6.5).

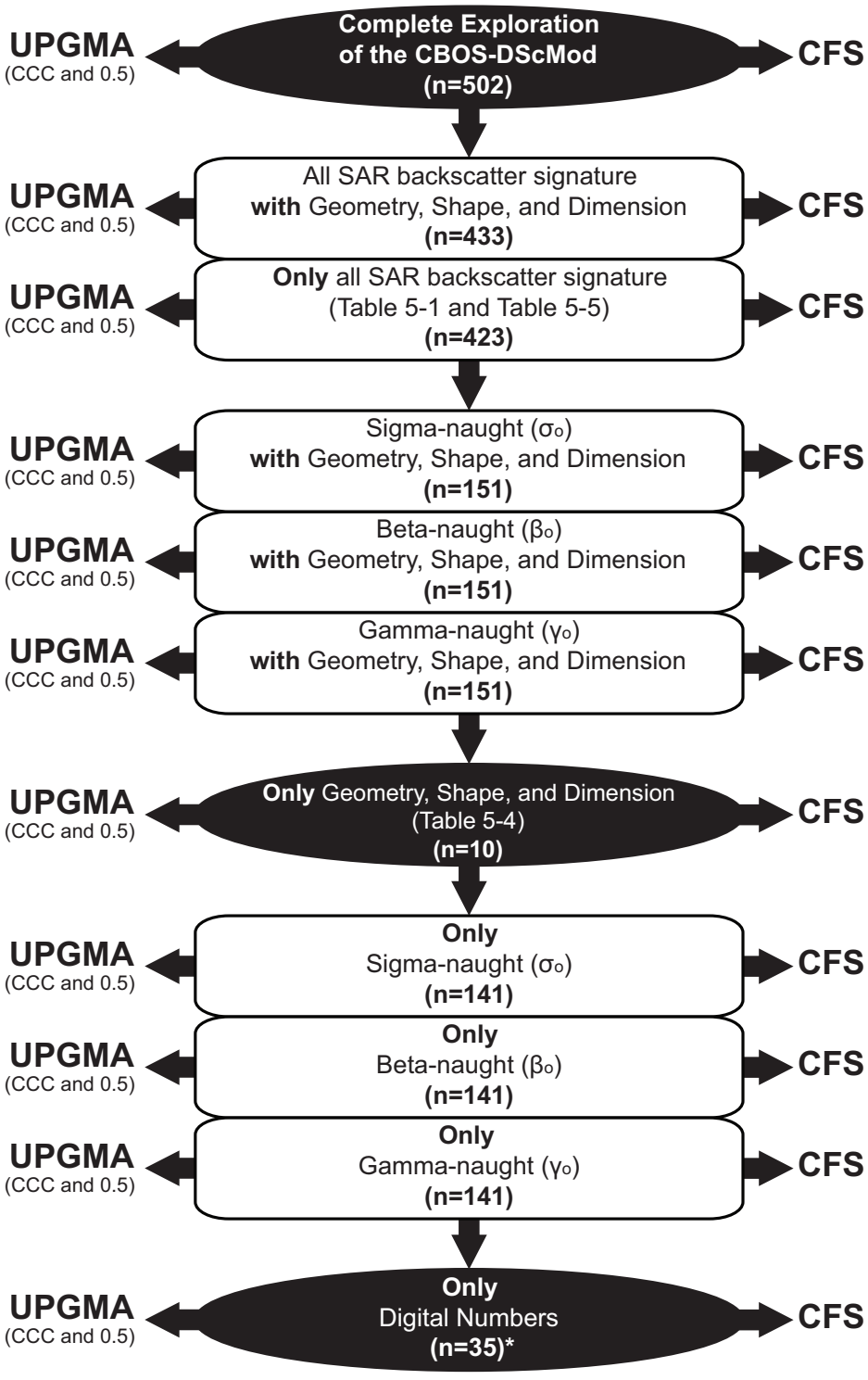

Figure 5-3: Forty-four data sub-divisions that have undergone two attribute selection methods: UPGMA (Unweighted Pair Group Method with Arithmetic Mean) and CFS (Correlation-Based Feature Selection). The UPGMA implementation performed herein employs two user-defined thresholds to form groups on the dendrogram analysis: CCC (Cophenetic Correlation Coefficient) and 0.5 (fixed similarity value). The CFS automatically provides the selected variables. These define the eleven original sets (shown on the middle column) and the thirty-three optimal subsets of selected variables within the Campeche Bay Oil Slick Modified Database (CBOS-MODD). *Digital Numbers (DN's) were only explored in separate.

5.7. PHASE 7: PRINCIPAL COMPONENTS ANALYSIS (PCA)

The same software package (PAST) utilized to implement the UPGMA was used to run the Principal Components Analysis (PCA) – however, with a more resent version: 3.06 (HAMMER *et al*., 2001). The PCA was applied to the forty-four data sub-divisions proposed in the preceding Phase (Figure 5-3). For instance, complete exploration (n=502), all SAR backscatter signature with (n=433) and without (n=423) the geometry, shape, and dimension variables, only sigma-naught (n=141), only beta-naught (n=141), only gamma-naught (n=141), etc.

The application of the PCA has a twofold justification:

- Reduce dimensionality in the attributes domain with the least possible loss of information, similarly to the implementations of the Attribute Selection practice (Phase 6: Section 5.6). Reduction of the variable-hyperspace dimension usually helps on the interpretation of large multivariate datasets (HALL, 1999; LEGENDRE & LEGENDRE, 2012), which is indeed the case of the CBOS-DScMod (Tables 5-1 to 5.5). PCA identifies uncorrelated hypothetical variables, called "Principal Components" (PC's) axes, that concentrate, as much as possible, the variance of the analyzed multi-dimensional dataset.

- Assure the absolute fulfillment of the pre-requisite of Discriminant Analyses (Phase 8: Section 5.8) to avoid multi-collinearity among the explored variables. It is true that the Attribute Selection practice (Phase 6: Section 5.6) has already selected less correlated variables, but residual correlation might still be present. The use of PC's is supported because the PC's axes are orthogonal to each other – i.e. linearly independent related (SHLENS, 2005; VALENTIN, 2012).

PCA has long been utilized as an ordination-like technique[63], e.g. RAO (1964). It is frequently credited to be introduced by PEARSON (1901) and perhaps, nowadays, it is probably the most used exploratory data analysis technique (ABDI & WILLIAMS, 2010; DE LEEUW, 2011; 2013). While the "Ordination" term was proposed by GOODWALL (1954), "Principal Component" was introduced by HOTELLING (1933).

[63] Ordination Methods - An overview: http://ordination.okstate.edu/overview.htm

Fundamentally, PCA's calculate the amount of variance (i.e. eigenvalues) per individual PC axis (i.e. eigenvectors). Geometrically, successive rigid orthogonal rotations are completed only of the axes system in the multi-dimensional space, in which each PC accounts for as much of the variability as possible, and subsequent PC's concentrate less and less of the remaining variance. The success of PCA's can, to some extent, be determined by the percentages of variance per PC, and ideally, it is expected that most of the variance is concentrated on fewer PC's as possible (ALEXANDER, 2008; LEGENDRE & LEGENDRE, 2012).

A multivariate dataset with i^{th} variables involves a i^{th}-dimensional hyperspace, in which one PC is assigned per variable. If compared to the commonly used 2D space, a hyperspace is very hard to picture, specially as the number of variables increases, e.g. original set of the complete exploration of the CBOS-DScMod (Figure 5-3: n=502). However, PCA is a powerful tool to deal with i^{th}-dimension problems (SMITH, 2002).

As the quantitative attributes within the CBOS-DScMod have different meanings, and different units, eigenvalues and eigenvectors have been computed with a correlation matrix (i.e. normalized variance-covariance) with the Singular Value Decomposition (SVD) algorithm (RICHARDSON, 2009). As such, all variables are automatically standardized in PAST, i.e. divided by their standard deviations (HAMMER, 2015a).

The PCA assigns transformed values ("scores") corresponding to each observation (i.e. oil slicks: n=4,916) on the new coordinate system. Once eigenvalues, PC's, scores, and their loadings are computed, the PC's concentrating the most part of the variance can be selected. Different ad hoc rules[64] are found in the literature to indicate the most relevant PC's (e.g. CATTELL, 1966; ALEXANDER, 2008). Informally, these rules aim to answer the following question: "How many PC's one should consider?"

Eigenvalues are conveniently expressed in percentages of variance, and as the sum of all PC's variances, i.e. amount of total variance of the data. The practice of selecting the meaningful PC's that concentrate the larger fraction of the total variance represents pitfalls to the subsequent data mining: noise can be included (i.e. overestimation) or some information can be lost (i.e. underestimation) (HAIR *et al.*, 2005). It is very helpful, while deciding the number of dimensions of the new reduced variable space, to order the eigenvalues from the degree of variance they concentrate per PC: highest to lowest. Even though some guidelines are available (e.g. PERES-NETO *et al.*, 2003;

[64] How many PC's to keep?
https://rip94550.wordpress.com/2008/02/11/pca-fa-example-2-jolliffe-discussion-3/

2005; LEDESMA & VALERO-MORA, 2007), there is no "rule of thumb" to determine the best "stopping rule" method to proceed with PC-selection.

A widely used cut-off to decide the number of PC's to account for is proposed by JOLLIFFE (2002). In essence, the Jolliffe Cut selects the PC's that have eigenvalues greater than the average of all eigenvalues. Another frequently used cut-off visually analyses what is called scree plot (i.e. eigenvalues on a decreasing order plotted versus increasing PC's axes), in which the PC-selection occurs on the "Elbow" (or "Knee") where the curve flattens (ABDI & WILLIAMS, 2010). These two cut-offs have been initially investigated herein; however, the Jolliffe Cut showed to be too "loose" as it considers too many PC's, and a somewhat skeptical action was taken while performing the Knee Test due to its subjective nature (MUTSVANGWA & DOUGLAS, 2007; ALEXANDER, 2008). As such, two other cut-offs have been explored and implemented to select meaningful PC's (HAIR *et al*., 2005).

The first one also analyzes the scree plot, but the PC-selection occurs based on the random model curve of expected eigenvalues (i.e. "broken stick"). The broken stick is also plotted on the scree plot and PC's falling below this curve (i.e. to its right side) are not considered (CATTELL, 1966; JACKSON, 1993). This cut-off strategy has a peculiar particularity to select PC's: if the broken stick curve crosses the bootstrapping[65] eigenvalue error bars (i.e. is inside the 95% confidence interval), this PC is also not considered (LEGENDRE & LEGENDRE, 2012; HAMMER, 2015a). Herein, this is simply referred to as "Scree Plot". The second selected PC cut-off was a simpler and direct method based on the so-called Kaiser-Guttman criterion that discards any PC after a specific lower bound: eigenvalue of 1 (KAISER, 1961; HAIR *et al*., 2005). Herein, this is referred to as "Kaiser Criterion".

Once the PC-selection process was completed, the loadings expressing the relationship between variables (rows) and PC's (columns) were considered. Loadings plots were investigated to verify the importance (i.e. meaning) of the original variables on each selected PC. This aimed to determine if there were variables with higher weight (i.e. loadings) influencing each PC from a statistical point of view. Bootstrapping error bars in the PAST coefficient mode were plotted per variable, and those having bars not crossing the abscissa are deemed to influence the PC (HAMMER, 2015a).

[65] PERES-NETO *et al.* (2003) suggest using one thousand row-wise bootstrapping replicates to give the confidence interval of 95% for the eigenvalues. However, only 500 replicates were applied herein as some PCA's were taken more than 10 hours to run.

The PCA's applied during this D.Sc. research aim to identify patterns within the variables included in the CBOS-DScMod. Once the meaningful PC's were selected, the score values were subjected to the Discriminant Analysis (Phase 8: Section 5.8). As with the Attribute Selection (Phase 6: Section 5.6), the PCA is an extremely important practice in the design of the classification algorithm to distinguish oil spills from oil seeps.

5.8. PHASE 8: DISCRIMINANT FUNCTION

A leading information shall be clear about Discriminant Analyses: it differ from Clustering Analyses, as it is not meant to determine to which group each object belongs to (VALENTIN, 2012). A preceding condition to perform Discriminant Analyses is that every object is required to be sorted (i.e. labeled) into a known group – have a membership of that specific group. Frequently, when there is no previous knowledge about the relationship between groups and objects, a Clustering Analysis (for instance, K-means) is accomplished to provide the grouping information. However, the present D.Sc. research is fortunate, as the content of the CBOS-Data has been made available – see Section 1.5 (Justification) and Chapter 2 (Operational Environmental Monitoring System) – thus giving rise to the full remote sensing library content of the CBOS-DScMod.

A Discriminant Analysis is a multivariate technique that is usually accomplished to interpret *a priori* known groups of objects previously identified, thus having a twofold intent: to discriminate "old" objects and to classify "new" objects (HAIR *et al*., 2005). At first, the data is separated – i.e. discriminated. This is considered the exploratory part of the Discriminant Analysis as it searches for characteristics (i.e. original attributes or selected PC's) capable of separating the objects (i.e. oil slicks: n=4,916) of a particular population (i.e. CBOS-DScMod) into two or more groups (i.e. oil spills or oil seeps). Afterwards, new objects can be allocated to one of these groups – i.e. classification.

The group information sorting the objects is used to assess the discriminant accuracy (PUS, 2015). In another words, the exploratory part of Discriminant Analyses mainly consist in finding a mathematical function that arranges the objects among the reported groups. This is based on a linear combination of the selected characteristics seeking the highest discriminating power, thus minimizing the probability of miss discrimination. PAST (version 2.17c – the same one used on the UPGMA implementation; HAMMER *et al.*, 2001) was used to calculate this linear combination that is called "Discriminant Function", which is given by:

$$DF(X) = (w_1X_1 + w_2X_2 + w_3X_3 + ... + w_nX_n) - C_{off}$$

where:
DF(X) is the dependent variable (i.e. Discriminate Function).
X_n is the independent variable (i.e. attribute value).
w_n is the weight of each independent variable.
C_{off} is the constant offset.

The discriminant process starts by drawing a proper straight line across the two datasets (i.e. spills and seeps), as such it maximizes the differences between these two groups and minimize the distances within the member of these groups (LOHNINGER, 1999). It then, plots the projection of each oil slick along this line to construct a histogram. The Hotelling's t^2 (counterpart of the Student's t-test – i.e. the square of the t-test) is used as a metric to test whether there is equality on their means, thus examining how different they are; a *p* value of significance is provided (HAMMER, 2015a; 2015b). This represents the first intent of the Discriminant Analysis: discriminate the objects. The second intent (to classify new objects) can be achieved by means of *DF(X)* presented above.

In summary, the Discriminant Analysis executed herein uses information previously measured (i.e. CBOS-DScMod variables) to tell apart the two possible oil slick types of oil slick samples. While the dependent variable is the category information (i.e. seep or spill), each analyzed sample is a member of only one of the two categories at a time: simple binary discrimination. As such, the Discriminant Functions are utilized on the design of the classification algorithm to distinguish natural from man-made oil slicks.

During the present D.Sc. research, a number of Discriminant Functions were tested using as input various data sources following the structure of Figure 5-3 – forty-four data sub-divisions, i.e. eleven original sets and their respective thrirty-three optimal subsets: UPGMA (CCC and Fixed) and CFS. However, these were doubled, as two sets were actually tested: the first set is represented by the original values of variables (prior to the PCA: Table 6-31), and the second set is represented by the scores of the PC's that were selected on the PCA's (Table 6-33).

The accuracy of the Discriminant Functions is assessed via Confusion Matrixes, which are simple 2-by-2-tables where one can quantify misclassification chances by using a cross validation estimate (SNEATH & SOKAL, 1973; MAIMON & ROKACH, 2010). These are addressed in deeper details on Phase 10 (Oil Slick Classification Algorithm: Section 5.10).

5.9. PHASE 9: CORRELATION MATRIX

Correlations matrixes aim to verify eventual residual inter-variable correlation that might still be present even after the thorough Attribute Selection and PCA practices. These matrixes are provided to determine the relationship among all original values of the CBOS-MODD variables (no PCA applied: Table 6-31), as well as among the scores of the selected PC's (with PCA applied: Table 6-33). The parametric Pearson's r correlation coefficient are given along with the p(uncorrelated).

5.10. PHASE 10: OIL SLICK CLASSIFICATION ALGORITHM

The design of classification algorithms implies a deeper interpretation of the information provided on Table 5-11, that illustrates adapted matrixes following the design proposed by CARVALHO *et al*. (2010; 2011). Usually, only the Overall Accuracy is reported, but CARVALHO (2008) has demonstrated that this yields a gap on the quality of the provided information, which can mislead the user (ALBERG *et al.*, 2004; THERIAULT *et al.*, 2006). As a result, various metrics come into play to report the effectiveness of the Discriminant Functions.

The information on Table 5-11 assists in answering the question: "What is the cost of incorrect discrimination?" One should not only look into the Overall Accuracy (i.e. the diagonal of the Confusion Matrix), but a full line- and column-wise inspection of the Matrix: Sensitivity-Specificity balance and a trade-off between the Positive and Negative Predictive Values. The former is obtained by looking into the Matrix lines, whereas the latter is achieved exploring the columns.

Steadiness is searched among line and column information of Table 5-11. This is because the lines give the reference frame of the information of what it is previously known (i.e. spills and seeps): how many of the known oil slick samples are correctly (or incorrectly) identified? Conversely, the columns reference frame changes to: how many oil slick samples identified by the algorithm are correctly (or incorrectly) identified? While the first question (about lines) measures the success of identifying know samples, the second question (about columns) provide a metric of the success of the algorithm to identify oil slick samples.

One should be aware that the nomenclature of the various metrics utilized herein, as presented on Table 5-11, can vary (e.g. LEE *et al.*, 2009; NUSSMEIER *et al.*, 2010). For instance, Producer's Accuracy (Sensitivity or Specificity), User's Accuracy (Positive or Negative Predictive Values), Commission Error instead of False Negative or False

Positive, and Omission Error rather than Inverse of the Positive Predictive Value or Inverse of the Negative Predictive Value. However, any misunderstanding is clearly explained with a careful inspection of Table 5-11, especially because of its wide-open character.

To better obtain useful information of the capabilities shown herein to differentiate spills from seeps, the reader should get acquainted with Table 5-11. It is crucial for the full comprehension of the proposed algorithms that these metrics are understood. A methodical step-by-step discussion is given in the form of a brief tutorial, thus intended to assist those not very used to these metrics (CARVALHO, 2008).

Table 5-11: Confusion Matrixes utilized to assess the Discriminant Function accuracy. Adapted from CARVALHO *et al*. (2010; 2011). Given as percentages (¥) and as frequency of occurrence (§).

¥	Algorithm Outcome Seeps	Algorithm Outcome Spills	
Actual Seeps	Positive Predictive Value	Invert Neg Predictive Value	
Actual Spills	Invert Pos Predictive Value	Negative Predictive Value	
	100%	100%	

¥	Algorithm Outcome Seeps	Algorithm Outcome Spills	
Actual Seeps	A*100 [A+C]	B*100 [B+D]	
Actual Spills	C*100 [A+C]	D*100 [B+D]	
	100%	100%	

¥	Algorithm Outcome Seeps	Algorithm Outcome Spills	
Actual Seeps	Sensitivity	False Negative	100%
Actual Spills	False Positive	Specificity	100%

¥	Algorithm Outcome Seeps	Algorithm Outcome Spills	
Actual Seeps	A*100 [A+B]	B*100 [A+B]	100%
Actual Spills	C*100 [C+D]	D*100 [C+D]	100%

§	Algorithm Outcome Seeps	Algorithm Outcome Spills	
Actual Seeps	GOOD Seeps	BAD Seeps	ALL Actual Seeps
Actual Spills	BAD Spills	GOOD Spills	ALL Actual Spills
	ALL Algorithm Seeps	ALL Algorithm Spills	ALL Slicks
			OVERALL Accuracy

§	Algorithm Outcome Seeps	Algorithm Outcome Spills	
Actual Seeps	A	B	A+B
Actual Spills	C	D	C+D
	A+C	B+D	A+B+C+D
			OVERALL Accuracy

As a starting point, one should answer the following set of four questions focusing on the lines of Table 5-11: true condition These are frequently referred to as Producer's Accuracy (*PA*) and Commission Error (*CE*).

Q1-PA-CE: How many known oil seep samples are correctly identified? This is the Sensitivity: A, also given by (A*100)/[A+B].

Q2-PA-CE: How many known oil spill samples are correctly identified? This is the Specificity: D, also given by (D*100)/[C+D].

Q3-PA-CE: How many known oil seep samples are misidentified? These are the False Negative cases (B, also given by (B*100)/[A+B]), which are coupled with Sensitivity.

Q4-PA-CE: How many known oil spill samples are misidentified? These are the cases of False Positive (C, also given by (C*100)/[C+D]), which are linked to Specificity.

The second set of four questions are given to interpret the columns of Table 5-11: predicted condition. These converge to what is usually called as User's Accuracy (*UA*) and Omission Error (*OE*).

Q1-UA-OE: How many oil seeps identified by the Function are indeed known oil seeps? This is the Positive Predictive Value: A, also given by (A*100)/[A+C].

Q2-UA-OE: How many oil spills identified by the Function are indeed known oil spills? This is the Negative Predictive Value: D, also given by (D*100)/[B+D].

Q3-UA-OE: Of samples identified by the Function as oil seeps, how many are oil spills*?* This is the Inverse of the Positive Predictive Value: C, also given by (C*100)/[A+C].

Q4-UA-OE: Of samples identified by the Function as oil spills, how many are oil seeps? This is the Inverse of the Negative Predictive Value: B, also given by (B*100)/[B+D].

CHAPTER 6

RESULTS

The results of the present D.Sc. research are shown mirroring the organization structure of Chapter 5. In being so, a suggestion for the reader is to refer to the following results' sections right after reading its corresponding methods one, on a one-to-one relation: methods-to-results sections. However, customary continuous reading is also feasible.

6.1. PHASE 1: DATA FAMILIARIZATION

This Section presents the findings of the first pre-processing data verification Phase (described in Section 5.1) that aims to search and organize the CBOS-Data content, guaranteeing that jumbled information is fixed and/or removed (Table 2-2): polygon identification (*slickID*), geographical coordinates (*cLAT* and *cLONG*), category (*Category*), class (*Class*), date (*SARdate*), time (*SARtime*), satellite name (*SARname*), beam mode (*Bmode*), polarization (*Pol*), area (*Area*), perimeter (*Per*), water column depth (*Wdepth*), and the MetOc-kit, which include chlorophyll-a concentration (*Chl*), cloud top temperature (*CTT*), sea surface temperature (*minSST* and *maxSST*), and significant wave height (*minSWH* and *maxSWH*). This Section is also focused on describing the oil slicks' spatio-temporal distribution after revealing important aspects related to their occurrence in the Campeche Bay region. It is based on this descriptive analysis that the QC-Standards are defined – see Phase 2 (Section 6.2). A specific color-code is instituted and followed in the course of the current Section.

- **CBOS-Data Attributes:** General Description

There are gaps on the unique oil slick polygon identification (*slickID* attribute). These were mostly caused by the Pemex Validation (CBOS-SatPro Part 6: Section 2.3.6) that occasionally re-grouped some polygons and disqualified others. Another point to note about the *slickIDs'* sequential numbering is that sometimes some oil slicks are not logged in the order they have occurred. This is because the satellite imagery is not always ordered, processed, or analyzed in chronological order. Despite the eventual numbering gaps, 14,210 oil slicks have been observed and had their information entered on the CBOS-Data.

The start of the CBOS-SatPro dates from 10 July 2000 (Pilot Study: Table 2-1), but its first data entry (*SARdate* attribute) is from 15 April 1997 (Table 6-1). Archived images (n=5) having oil slicks (n=33) identified between 1997 and 1999 are included from the inspection of previous considerations (i.e. proof of concept) to design the CBOS-SatPro (see Section 2.2). While RADARSAT-1 images were utilized during the entire CBOS-SatPro, RADARSAT-2 imagery only started to be acquired upon its launch in 2008 (BANNERMAN *et al.*, 2009). The last images used are from December/2012.

Table 6-1: Date range of the RADARSAT scenes explored during the Campeche Bay Oil Slick Satellite Project (CBOS-SatPro).

Date Range	From			To		
RADARSAT-1	15	April	1997	14	December	2012
RADARSAT-2	13	March	2008	15	December	2012

The satellite overpass time (*SARtime* attribute) reveals the lag differences between the SAR scene and EOS sensors (MetOc-kit). Several mistakes appear logged on the CBOS-Data but were corrected mostly by switching UTC and local time columns. The RADARSAT overpasses above Campeche Bay are presented in Table 6-2.

Table 6-2: Overpass flight time of both RADARSAT satellites above Campeche Bay. Orbit direction is also shown.

Orbit	Local Time		UTC
Descending	5am-7am	Early morning	(11am-1pm)
Ascending	5pm-7pm	Late afternoon	(11pm-1am)

The exact location of the oil slicks is of vital relevance. While verifying the geographical coordinates (*cLAT* and *cLONG* attributes), several oil slicks were found with latitude values > 90 degrees. Essentially, the latitude and longitude columns were switched and have all been corrected. The latitude of the oil slicks' centroids ranges from 18.2^{o}N to 26.5^{o}N and the longitude varies between 85.6^{o}W to 95.6^{o}W. However, most oil slicks (~98%) are observed below 23.0^{o}N and from 91.0^{o}W to 95.0^{o}W (Figure 1-1).

- ***Category* Attribute:** Frequency and Area Coverage

The number of oil slicks per category is somewhat unevenly distributed (Figure 6-1). Of the 14,210 oil slicks observed in the Campeche Bay region during the CBOS-SatPro, there are more oil slicks identified as oil spills (n=8,008; 56.3%) than oil seeps (n=6,202; 43.7%). If taking into consideration the overall surface area coverage of all oil slicks this pattern is inverted (Figure 6-2), and oil seeps (31,447 km^2; 67.4%) occupy more than twice the area covered by oil spills (15,246 km^2; 32.6%).

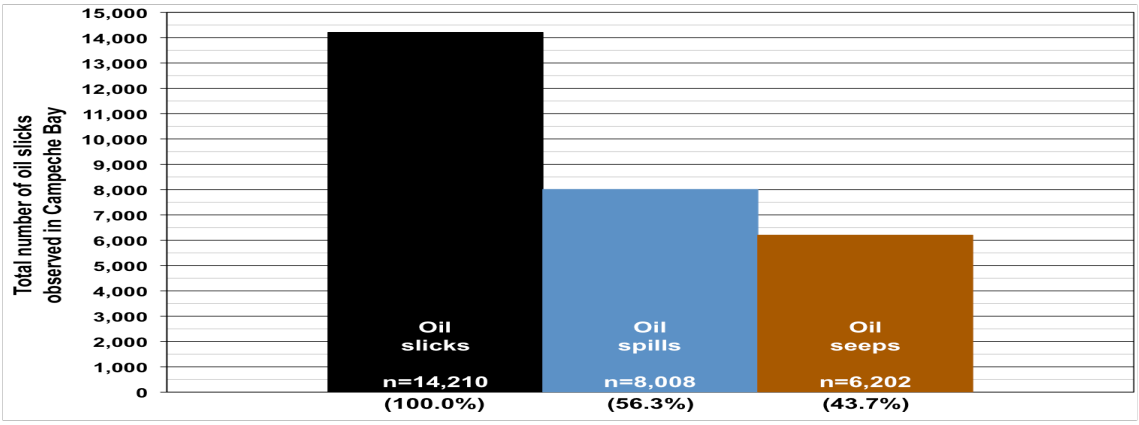

Figure 6-1: Frequency per *Category* attribute: oil slicks (black) observed during the Campeche Bay Oil Slick Satellite Project (CBOS-SatPro) imaged with both RADARSAT satellites – oil spills (blue) and oil seeps (brown). Refer to Figure 6-11 for equivalent information from each of the two RADARSAT satellites.

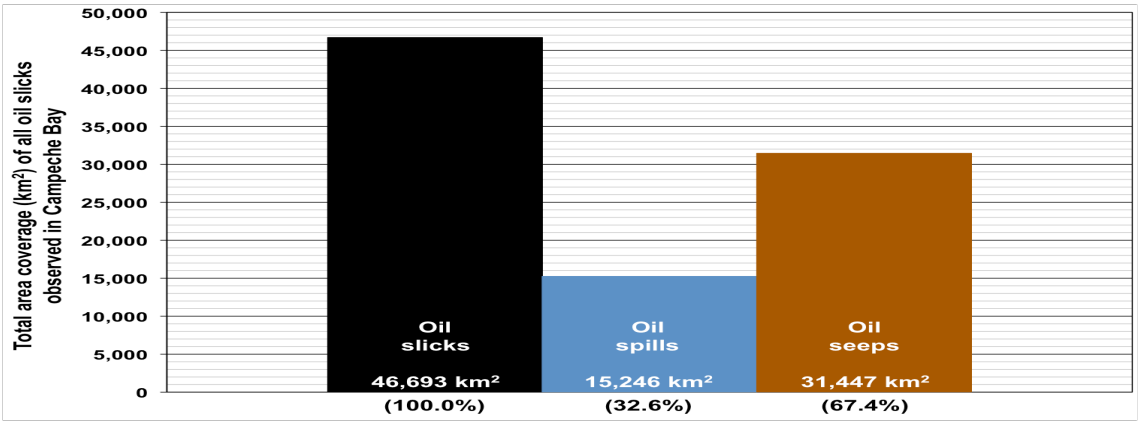

Figure 6-2: Overall surface area coverage per *Category* attribute: oil slicks (black) observed during the Campeche Bay Oil Slick Satellite Project (CBOS-SatPro) imaged with both RADARSAT satellites – oil spills (blue) and oil seeps (brown). Refer to Figure 6-12 or equivalent information from each of the two RADARSAT satellites.

- ***Class* Attribute:** Frequency and Area Coverage

Figure 6-3 shows the number of observation within each of the 71 recognized Brightspots (i.e. groups of oil spills from individual OGEPI facilities belonging to the same oilfield). While 12 Brightspots only have one oil spill observation, one has 528, other 701, and another tops 1,674 oil slick observations.

Figure 6-4 shows that 89 Clusters (i.e. collection of oil seeps observed about the same location, e.g. Figure 2-1) have been identified in the Campeche Bay region. Of these, two have as low as 3 oil seeps (i.e. the minimum number of observations necessary to identify a Cluster), one has 215 different occurrences, and the Cantarell Oil Seep Cluster spots out with 653 oil seep observations.

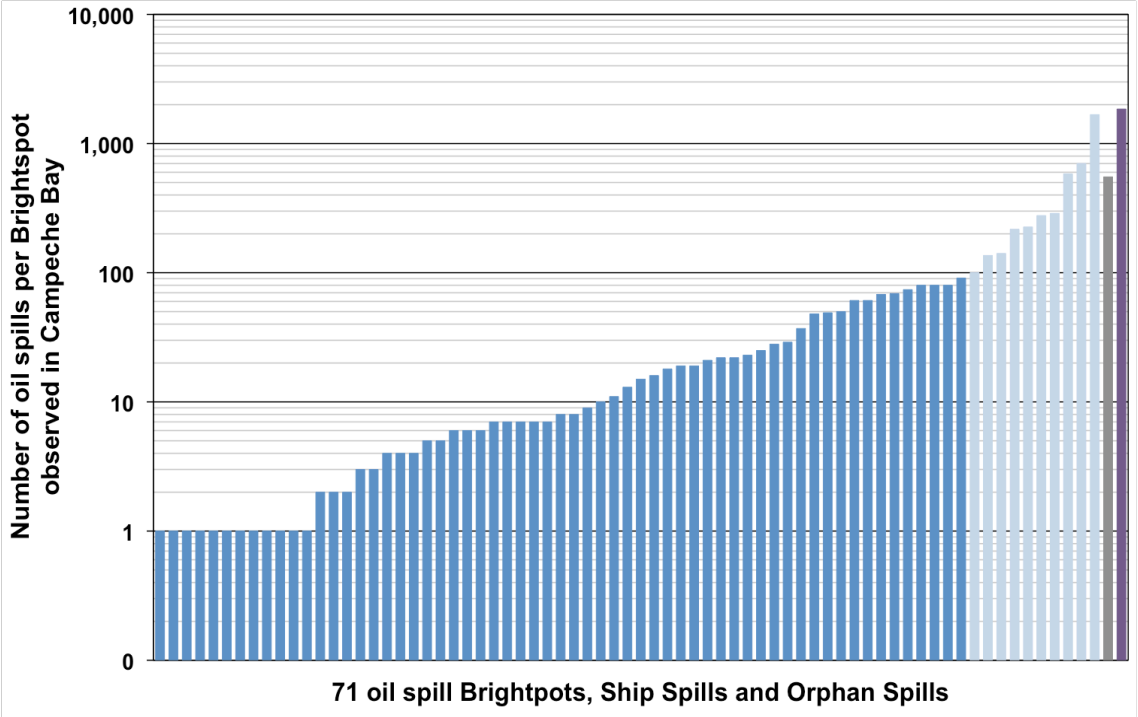

Figure 6-3: Frequency of oil spills per Brightspot imaged with both RADARSAT satellites. Of the 71 recognized Brightspots, there are 61 with ≤ 99 different oil spill observations (shown in darker blue) and 10 that have ≥ 100 oil spills each (indicated in light blue). Ship Spills and Orphan Spills appear in grey and purple, respectively.

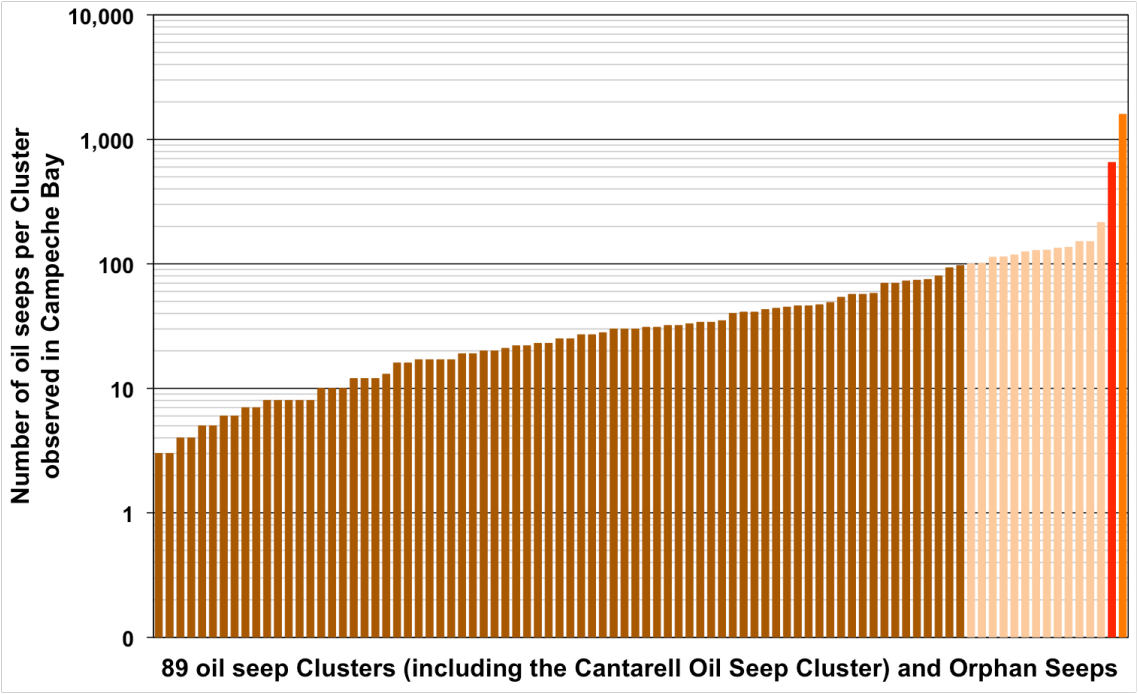

Figure 6-4: Frequency of oil seeps per Cluster imaged with both RADARSAT satellites. There are 89 identified Clusters: 75 with ≤ 99 different oil seep observations (indicated in darker brown), 13 that have ≥ 100 oil seeps each (shown in light brown), and the Cantarell Oil Seep Cluster (shown in red). Orphan Seeps appear in orange.

An aspect of note whilst considering the oil classes is that Brightspots and Clusters, respectively, color-coded presented on Figure 6-3 and Figure 6-4 are divided in groups related to the number of different observations. The 71 recognized Brightspots are divided in 61 with ≤ 99 oil spills each (n=1,263) and 10 with ≥ 100 oil spills each (n=4,342) – Figure 6-3. The 89 identified Clusters have 75 with ≤ 99 oil seeps each (n=2,242), 13 Clusters with ≥ 100 oil seeps each (n=1,715), and the Cantarell Oil Seep Cluster (n=653) – Figure 6-4.

- **Oil Slicks per Class:** Total Frequency

Figure 6-5 (left side) depicts the frequency of oil spills per class. The majority of oil spills are grouped to one of the 71 identified Brightspots (n=5,605; 70.0%). Orphan Spills represent 23.1% (n=1,851) and Ship Spills are as low as 6.9% (n=552) of the oil spills.

Figure 6-5 (right side) also depicts the frequency of oil seeps per class. Most oil seeps belong to the 89 identified Clusters (n=3,957; 63.8%). The Cantarell Oil Seep Cluster is a major exception (n=653; 10.5%), as its signature is present in most RADARSAT scenes (n=766) analyzed during the CBOS-SatPro: 85%. The remaining 25.7% (n=1,592) oil seeps are Orphan Seeps.

- **Oil Slicks per Class:** Total Area Coverage

Figure 6-6 (left side) shows the area (km^2) of oil spills per class. The 61 Brightspots with ≤ 99 different oil spill observations (5,690 km^2; 37.3%) and the 10 Brightspots that have ≥ 100 different oil spill observations (5,434 km^2; 35.6%) cover about the same surface area. While these 71 Brightspots sum 72.9% (11,124 km^2), Orphan Spills correspond to 21.2% (3,228 km^2) of the total area of the observed oil spills. Ships Spills covered about 894 km^2 (5.9%), in which seldom ship discharges came from the same moving oil source. However, some ships have 8-10 different observations, and two vessels catch the attention with 22 and 65 oil slick features.

Figure 6-6 (right side) shows the area (km^2) of oil seeps per class. While the 75 Clusters with ≤ 99 different oil seep observations cover 3,779 km^2 (12.0%), the 13 Clusters with ≥ 100 different oil seep observations cover 5,168 km^2 (16.4%). These 88 Clusters sum 8,947 km^2 (28.4%), whereas Orphan Seeps are responsible for only 2,757 km^2 (8.8%). The Cantarell Oil Seep (see Figure 2-1) itself has an exceptional larger area coverage corresponding to 62.8% (19,743 km^2) of the total area of the observed oil seeps within the CBOS-Data.

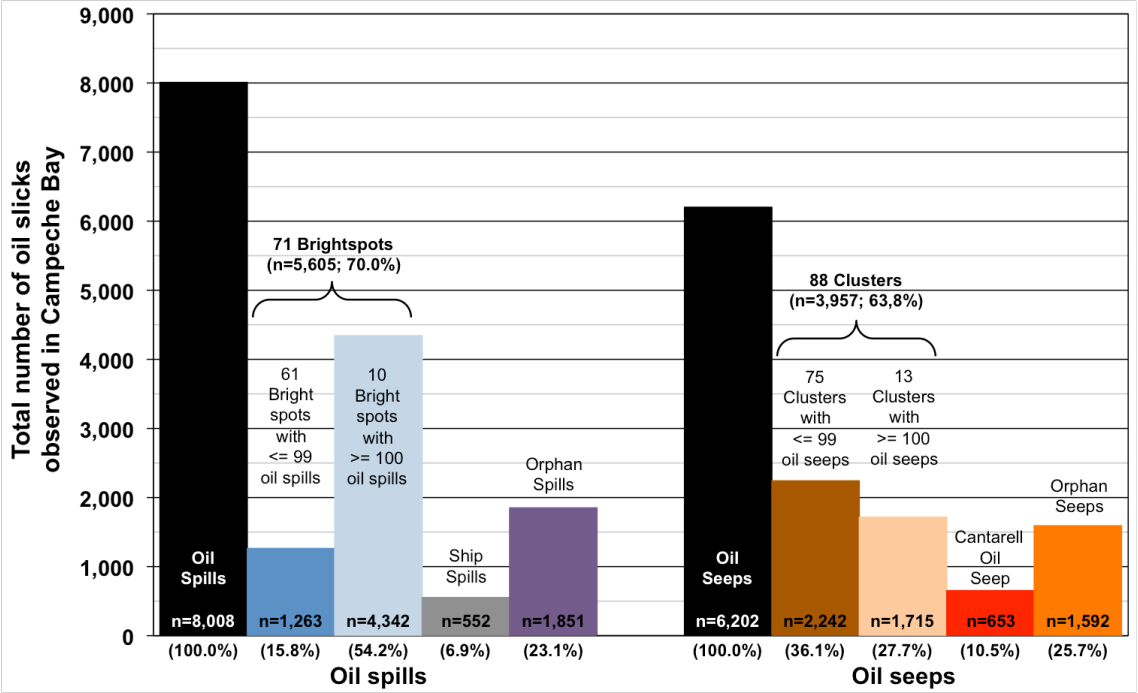

Figure 6-5: Frequency per Class attribute: oil slicks (black) logged on the Campeche Bay Oil Slick Satellite Database (CBOS-Data) imaged with both RADARSAT satellites: oil spills (cold colors; left side) and oil seeps (warm colors; right side).

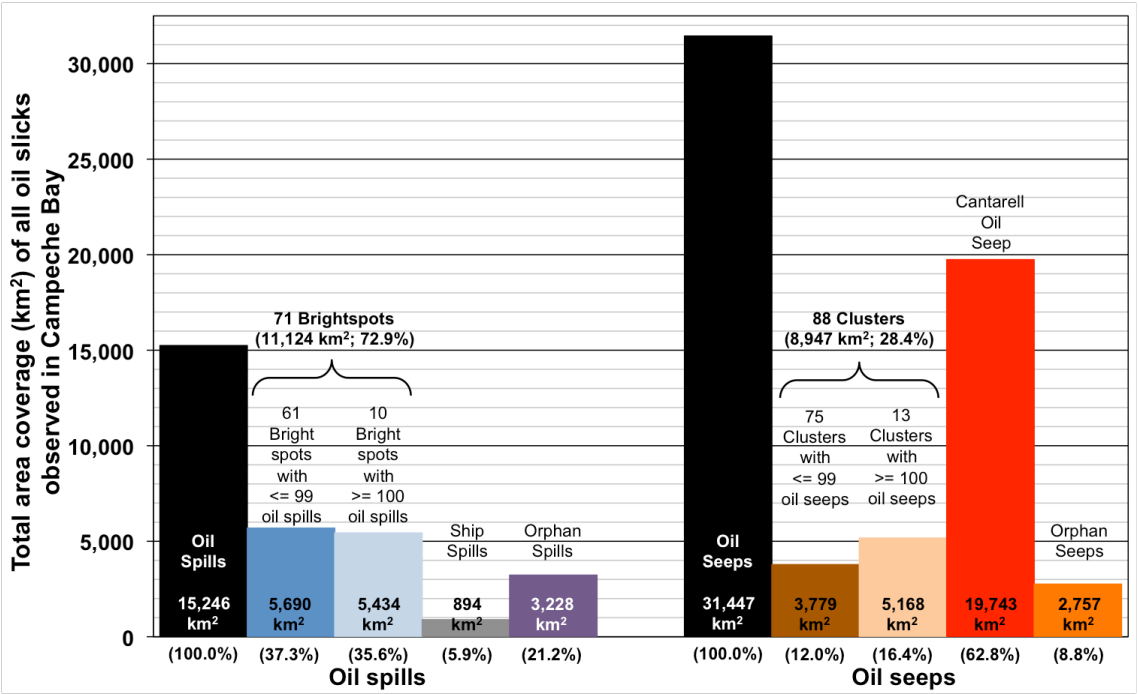

Figure 6-6: Total surface area coverage per Class attribute: oil slicks (black) logged on the Campeche Bay Oil Slick Satellite Database (CBOS-Data) imaged with both RADARSAT satellites: oil spills (cold colors; left side) and oil seeps (warm colors; right side).

- **Occurrence of all oil slicks:** Overall Frequency

Figure 6-7 portrays the percentage of frequency per class among the 14,210 oil slicks observed during the CBOS-SatPro. Interesting to note is that whilst the 10 Brightspots with ≥ 100 oil spill observations represent about one third of the entire dataset (n=4,342; 30.5%), the 61 Brightspots with ≤ 99 oil spill observations correspond to a much smaller fraction (n=1,263; 8.9%) of the identified oil slicks. A different pattern is noticeable among the oil seep classes, in which the 13 Clusters with ≥ 100 oil seep observations represent a little more than one tenth of the entire dataset (n=1,715; 12.1%) and the 75 Clusters with ≤ 99 oil seep observations correspond to a quite similar portion (n=2,242; 15.8%).

Orphan Spills (n=1,851; 13.0%) and Orphan Seeps (n=1,592; 11.2%) also have comparable proportions. The least frequent are the Cantarell Oil Seep that records 4.6% (n=653) of the oil slicks observed in Campeche Bay, followed by Ship Spills that only occur in 3.9% (n=552) of times (Figure 6-7).

- **Occurrence of all oil slicks:** Overall Area Coverage

It is evident from Figure 6-8 that most of the 46,693 km^2 covered by all oil slicks observed in Campeche Bay comes from the Cantarell Oil Seep (19,743 km^2; 42.3%), what contrasts with its small frequency (see Figure 6-7). An interesting characteristic about the oil slicks observed in the Campeche Bay region is that if the massive contribution of the Cantarell Oil Seep is disregarded, from the remaining overall area (26,950, km^2) the oil spills' influence (15,246 km^2; 56.6%) is larger than of the oil seeps (11,704 km^2; 43.4%).

Figure 6-8 also illustrates that even though the 10 Brightspots with ≥ 100 oil spill observations (5,434 km^2; 11.6%) occur more frequently (see Figure 6-7) than the 61 Brightspots with ≤ 99 oil spill observations (5,690 km^2; 12.2%), they both cover about the same area. An equivalent areal representativeness is showed by the 13 Clusters with ≥ 100 oil seep observations (5,168 km^2; 11.1%).

Likewise, the 75 Clusters with ≤ 99 oil seep observations (3,779 km^2; 8.1%), Orphan Spills (3,228 km^2; 6.9%), and Orphan Seeps (2,757 km^2; 5.9%) also cover somewhat similar areas. Ships spills only cover 1.9% (894 km^2) of the area of all oil slicks observed during the CBOS-SatPro (Figure 6-8).

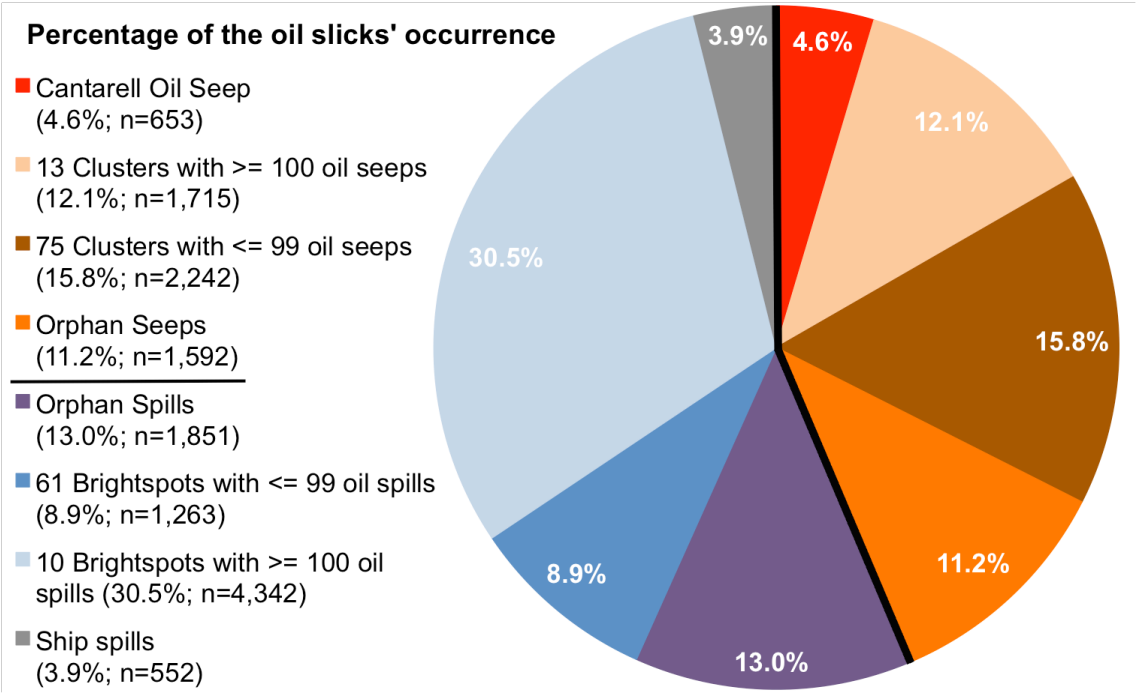

Figure 6-7: Percentage of the overall frequency of occurrence of all oil slicks (n=14,210) shown per *Class* attribute imaged with both RADARSAT satellites: oil spill (cold colors: n=8,008; 56.3%) and oil seep (warm colors: n=6,202; 43.7%). These include Orphan Seeps, Orphan Spills, and Ship Spills.

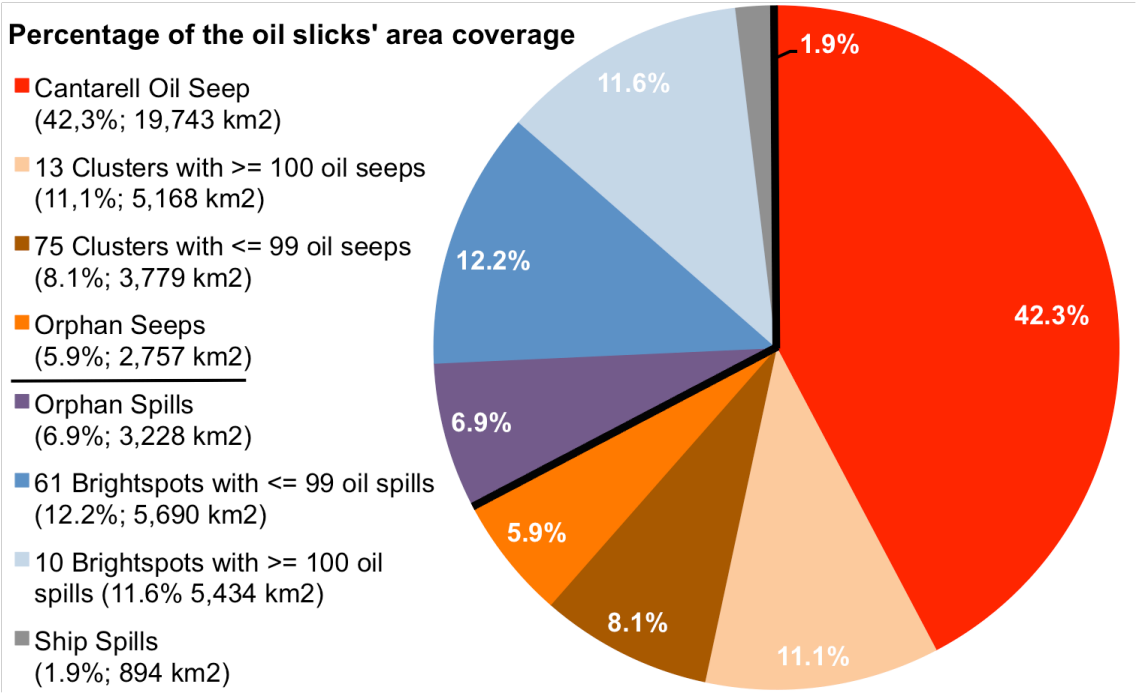

Figure 6-8: Percentage of the overall area coverage of occurrence of all oil slicks (46,693 km^2) shown per *Class* attribute imaged with both RADARSAT satellites: oil spill (cold colors: 15,246 km^2; 32.6%) and oil seep (warm colors: 31,447 km^2; 67.4%). These include Orphan Seeps, Orphan Spills, and Ship Spills.

- **RADARSAT Satellites:** *SARname*

Because measurements from RADARSAT-1 have been explored for longer than those of RADARSAT-2 (Table 6-1), there are more RADARSAT-1 scenes (n=482; 63%) compared to RADARSAT-2 scenes (n=284; 37%) – see Table 6-3. Because of this reason, more oil slicks are imaged with RADARSAT-1 (Figure 6-9: n=8,896; 62.6%) than with RADARSAT-2 (Figure 6-10: n=5,314; 37.4%).

Table 6-3 illustrates the regular SAR image acquisition during the Operational Contracts that usually provided on average at least one RADARSAT scene per week. This table also shows the RADARSAT-1 acquisition (2009-2010) gap that occurred because the onboard tape recorder was not functioning properly and only direct downlink data were available (Figure 6-9). An unexplained slight increase in oil slick frequency occurred from 2005 to 2008. The excessive number of oil slicks observed in the last two years (2011-2012) reflects the larger amount of satellite scenes (Figure 6-9 and Figure 6-10) utilized due to supplementary short-period exploration contracts.

Table 6-3: RADARSAT scenes per year and annual number of oil slicks imaged during the Campeche Bay Oil Slick Satellite Project (CBOS-SatPro).

Year	RADARSAT-1 Scenes		RADARSAT-2 Scenes		Both RADARSAT Scenes		Oil Slick Frequency	
* **97/99**	5	1.0%	-	-	**5**	**0.7%**	33	0.2%
2000	9	1.8%	-	-	**9**	**1.2%**	99	0.7%
2001	23	4.8%	-	-	**23**	**3.0%**	303	2.1%
** **2002**	51	10.6%	-	-	**51**	**6.7%**	866	6.1%
2003	53	11.0%	-	-	**53**	**6.9%**	860	6.1%
2004	51	10.6%	-	-	**51**	**6.7%**	876	6.2%
2005	58	12.0%	-	-	**58**	**7.6%**	1,097	7.7%
2006	57	12.0%	-	-	**57**	**7.4%**	1,018	7.2%
2007	61	12.7%	-	-	**61**	**8.0%**	1,063	7.5%
*** **2008**	10	2.0%	59	20.8%	**69**	**9.0%**	1,261	8.9%
2009	-	-	39	13.7%	**39**	**5.1%**	887	6.2%
2010	-	-	60	21.1%	**60**	**7.8%**	826	5.8%
2011	62	12.8%	62	21.8%	**124**	**16.1%**	2,619	18.4%
2012	42	8.7%	64	22.6%	**106**	**13.8%**	2,402	16.9%
Total	**482**	**100.0%**	**284**	**100.0%**	**766**	**100.0%**	**14.210**	**100.0%**

* Inspection of previous considerations about the utilized methodology: proof of concept with archived images (see Section 2.2).

** Start of Operational Contracts (Table 2-1).

*** Start of RADARSAT-2 acquisition (Table 6-1).

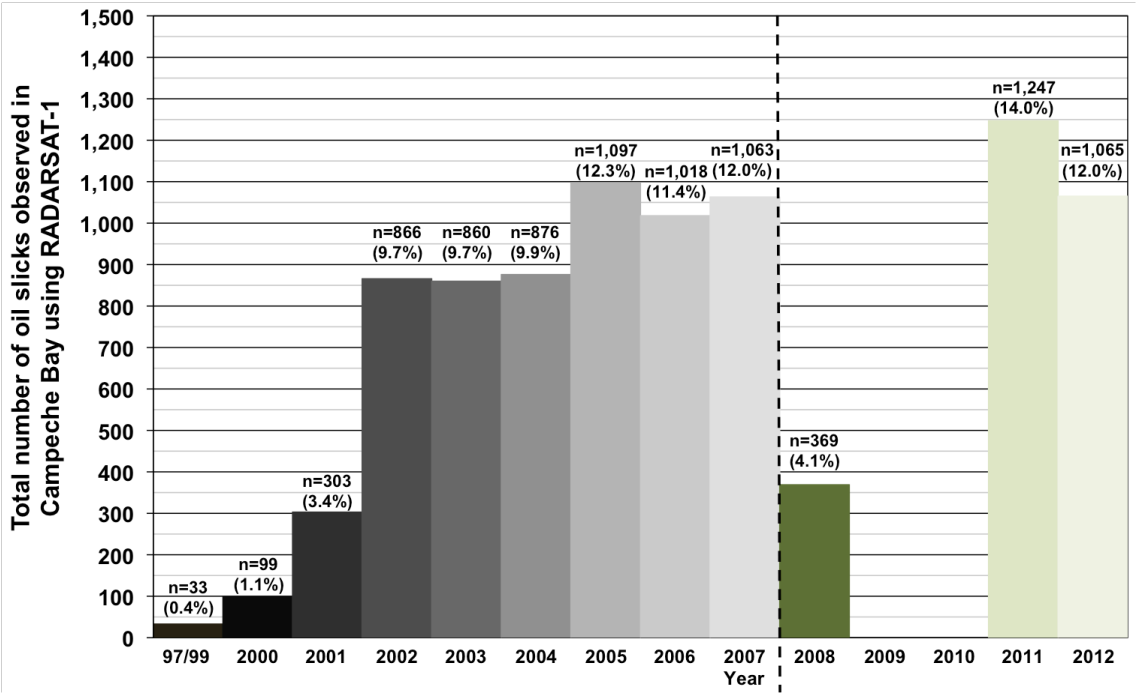

Figure 6-9: Annual distribution of oil slicks imaged with RADARSAT-1 imagery (n=8,896). Dashed line represents the start of the RADARSAT-2 acquisition.

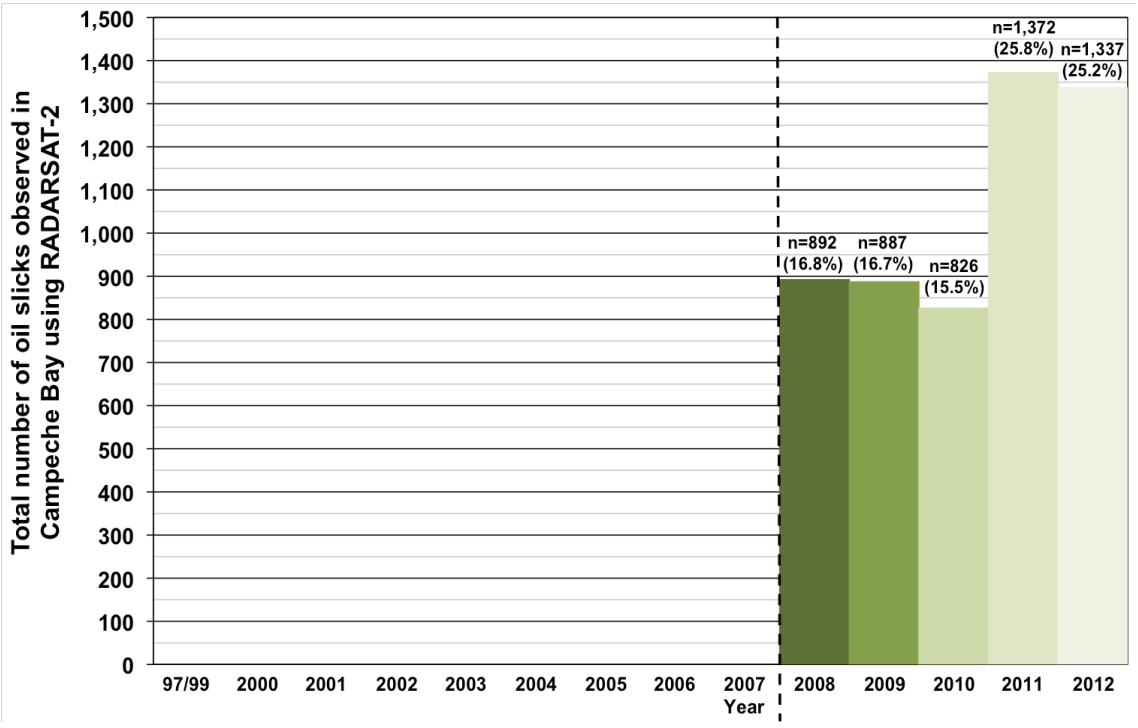

Figure 6-10: Annual distribution of oil slicks imaged with RADARSAT-2 imagery (n=5,314). Dashed line represents the start of the RADARSAT-2 acquisition.

Considering the seasonal occurrence of oil slicks throughout the CBOS-SatPro, there is an approximately even distribution among the Winter (J/F/M: 23.0%), Spring (A/M/J: 31.4%), Summer (J/A/S: 24.0%), and Fall (O/N/D: 21.6%). However, a predominant incidence of oil slicks during the boreal Spring months is observed – this season have the two first months preceding and the last one within the Atlantic hurricane season: June 1st through November 30th (MASTERS, 2010). Figure 6-11 and Figure 6-12 portray, respectively, the frequency distribution and the total surface area coverage of oil slicks per category imaged with each of the two RADARSAT satellites. As expected, these are, respectively, similar to Figure 6-1 and Figure 6-2.

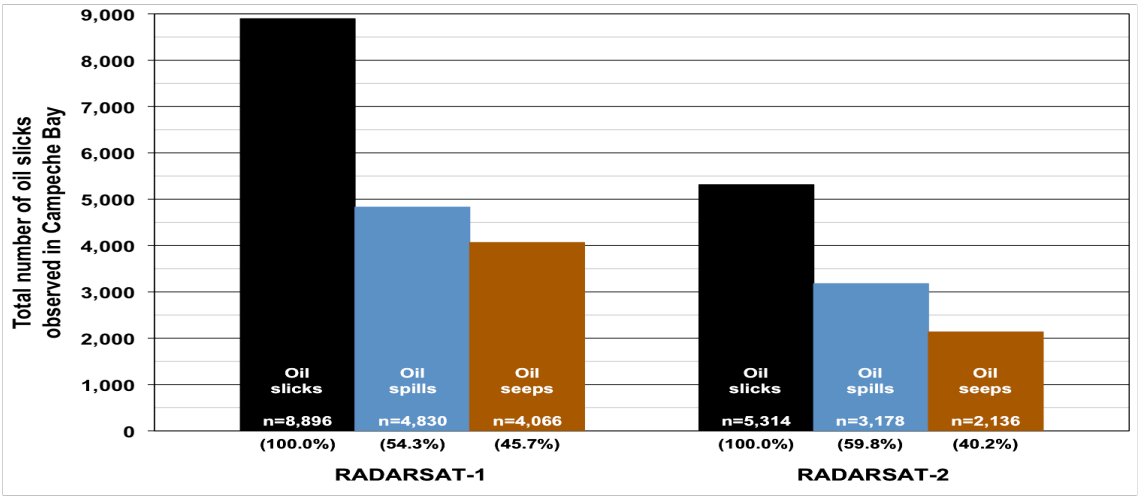

Figure 6-11: Frequency per *Category* attribute: oil slicks (black) as imaged with each of the two RADARSAT satellites during the Campeche Bay Oil Slick Satellite Project (CBOS-SatPro) – oil spills (blue) and oil seeps (brown). Refer to Figure 6-1 for equivalent information from both RADARSAT satellites together.

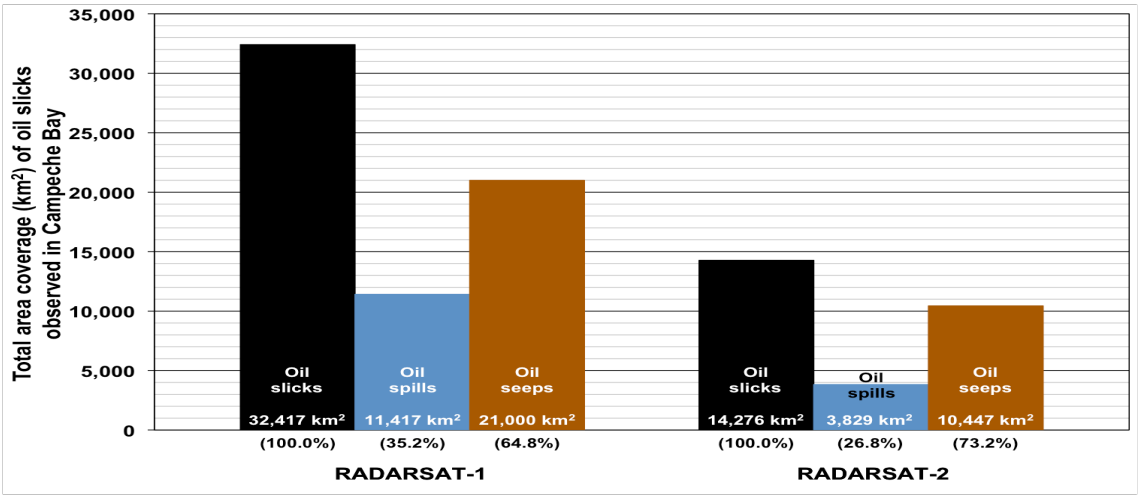

Figure 6-12: Total surface area coverage per *Category* attribute: oil slicks (black) as imaged with each of the two RADARSAT satellites during the Campeche Bay Oil Slick Satellite Project (CBOS-SatPro) – oil spills (blue) and oil seeps (brown). Refer to Figure 6-2 for equivalent information from both RADARSAT satellites together.

- **Beam Mode:** *Bmode*

About 91% (n=12,892) of the oil slicks observed during the CBOS-SatPro have been imaged with the two ScanSAR Narrow modes: ScanSAR Narrow 1 (SCNA; n=8,777) and ScanSAR Narrow 2 (SCNB; n=4,115), as portrayed in Table 6-4. In fact, their imaging characteristics (e.g. incidence angle and ground resolution) are the most appropriate RADARSAT beam modes to monitor the sea surface after detecting oil slicks (NRCAN, 2014). The remaining 10% are divided such that the two Wide modes sum 8% (WDE1: n=847; and WDE2: n=287) and Extended Low represents 1,3% (EXL1; n=177). Only 7 oil slicks have been imaged with one ScanSAR Wide (SCW).

Table 6-4: Oil slick distribution per beam mode and per RADARSAT satellite.

RADARSAT Beam Modes		Oil Slicks		RADARSAT-1		RADARSAT-2	
SCNA	ScanSAR Narrow 1	**8,777**	**(61.7%)**	5,888	(66.2%)	2,889	(54.3%)
SCNB	ScanSAR Narrow 2	**4,115**	**(29.0%)**	2,134	(24.0%)	1,981	(37.3%)
WDE1	Wide 1	**847**	**(6.0%)**	462	(5.2%)	385	(7.3%)
WDE2	Wide 2	**287**	**(2.0%)**	271	(3.0%)	16	(0.3%)
EXL1	Extended Low 1	**177**	**(1.1%)**	134	(1.5%)	43	(0.8%)
SCW	ScanSAR Wide	**7**	**(~0.1%)**	7	(0.1%)	0	
Total		**14,210**	**(100%)**	**8,896**	**(100%)**	**5,314**	**(100%)**

- **Polarization:** *Pol*

While all RADARSAT-1 products are HH-polarized, most RADARSAT-2 beams utilized on the CBOS-SatPro are VV-polarized (n=276; 97%). VV is indeed the most suitable polarization for oil slick detection on the sea surface (VAN DER SANDEN, 2004).

- **Geometric Attributes:** Area and Perimeter

A remarkable characteristic about the occurrence of oil spills and oil seeps in the Campeche Bay region is their size distribution. Most oil slicks (Table 6-5: n=9,398; 66.1%) have, what is considered herein, "small" surface area coverage (i.e. < 1 km^2). This corresponds to more than 2/3 of the observed oil spills (Table 6-6: n=6,196; 77.4%) and to approximately half of the oil seeps (Table 6-7: n=3,202; 51.7%).

Of the 14,210 oil slicks of the CBOS-Data, only 5.2% (Table 6-5: n=734) have, what is considered herein, "large" surface area coverage (i.e. ≥ 10 km^2). Among these, there are only 63 observations with major surface area coverage (i.e. ≥ 100 km^2): 15 oil spills (Table 6-6) and 48 oil seeps (Table 6-7). The frequency of oil slicks' size per category is illustrated on Figure 6-13 and Figure 6-14, respectively, per satellite.

Table 6-5: Total number of **oil slicks** per area and per RADARSAT satellite.

Surface Area Coverage	Oil Slicks	RADARSAT-1	RADARSAT-2
Only oil slicks < 0.5 km^2	**7,088 (49.9%)**	4,004 (45.0%)	3,084 (58.0%)
0.5 ≤ oil slicks < 1 km^2	**2,310 (16.2%)**	1,549 (17.5%)	761 (14.3%)
1 ≤ oil slicks < 2 km^2	**1,845 (13.0%)**	1,276 (14.3%)	569 (10.7%)
2 ≤ oil slicks < 3 km^2	**794 (5.6%)**	559 (6.3%)	235 (4.4%)
3 ≤ oil slicks < 4 km^2	**471 (3.3%)**	332 (3.7%)	139 (2.6%)
4 ≤ oil slicks < 5 km^2	**300 (2.1%)**	223 (2.5%)	77 (1.4%)
5 ≤ oil slicks < 6 km^2	**217 (1.5%)**	143 (1.6%)	74 (1.4%)
6 ≤ oil slicks < 7 km^2	**160 (1.1%)**	113 (1.3%)	47 (0.9%)
7 ≤ oil slicks < 8 km^2	**108 (0.8%)**	75 (0.8%)	33 (0.6%)
8 ≤ oil slicks < 9 km^2	**104 (0.7%)**	79 (0.9%)	25 (0.5%)
9 ≤ oil slicks < 10 km^2	**79 (0.6%)**	56 (0.6%)	23 (0.5%)
10 ≤ oil slicks < 100 km^2	**671 (4.7%)**	443 (5.0%)	228 (4.3%)
Only oil slicks ≥ 100 km^2	**63 (0.5%)**	44 (0.5%)	19 (0.4%)
All oil slicks	**14,210 (100%)**	**8,896 (100%)**	**5,314 (100%)**

Table 6-6: Total number of **oil spills** per area and per RADARSAT satellite.

Surface Area Coverage	Oil Spills	RADARSAT-1	RADARSAT-2
Only oil spills < 0.5 km^2	**5,031 (62.8%)**	2,719 (56.3%)	2,312 (72.8%)
0.5 ≤ oil spills < 1 km^2	**1,165 (14.6%)**	785 (16.2%)	380 (12.0%)
1 ≤ oil spills < 2 km^2	**774 (9.7%)**	544 (11.3%)	230 (7.2%)
2 ≤ oil spills < 3 km^2	**300 (3.7%)**	226 (4.7%)	74 (2.3%)
3 ≤ oil spills < 4 km^2	**170 (2.1%)**	131 (2.7%)	39 (1.2%)
4 ≤ oil spills < 5 km^2	**99 (1.2%)**	76 (1.6%)	23 (0.7%)
5 ≤ oil spills < 6 km^2	**79 (1.0%)**	61 (1.3%)	18 (0.6%)
6 ≤ oil spills < 7 km^2	**64 (0.8%)**	45 (0.9%)	19 (0.6%)
7 ≤ oil spills < 8 km^2	**30 (0.4%)**	26 (0.5%)	4 (0.1%)
8 ≤ oil spills < 9 km^2	**46 (0.6%)**	37 (0.8%)	9 (0.3%)
9 ≤ oil spills < 10 km^2	**34 (0.4%)**	24 (0.5%)	10 (0.3%)
10 ≤ oil spills < 100 km^2	**201 (2.5%)**	144 (3.0%)	57 (1.8%)
Only oil spills ≥ 100 km^2	**15 (0.2%)**	12 (0.2%)	3 (0.1%)
All oil spills	**8,008 (100%)**	**4,830 (100%)**	**3,178 (100%)**

Table 6-7: Total number of **oil seeps** per area and per RADARSAT satellite.

Surface Area Coverage	Oil Seeps	RADARSAT-1	RADARSAT-2
Only oil seeps < 0.5 km^2	**2,057 (33.2%)**	1,285 (31.6%)	772 (36.2%)
0.5 ≤ oil seeps < 1 km^2	**1,145 (18.5%)**	764 (18.8%)	381 (17.8%)
1 ≤ oil seeps < 2 km^2	**1,071 (17.3%)**	732 (18.0%)	339 (15.8%)
2 ≤ oil seeps < 3 km^2	**494 (8.0%)**	333 (8.2%)	161 (7.5%)
3 ≤ oil seeps < 4 km^2	**301 (4.9%)**	201 (4.9%)	100 (4.7%)
4 ≤ oil seeps < 5 km^2	**201 (3.2%)**	147 (3.6%)	54 (2.5%)
5 ≤ oil seeps < 6 km^2	**138 (2.2%)**	82 (2.0%)	56 (2.6%)
6 ≤ oil seeps < 7 km^2	**96 (1.2%)**	68 (1.7%)	28 (1.3%)
7 ≤ oil seeps < 8 km^2	**78 (1.5%)**	49 (1.2%)	29 (1.4%)
8 ≤ oil seeps < 9 km^2	**58 (0.9%)**	42 (1.0%)	16 (0.8%)
9 ≤ oil seeps < 10 km^2	**45 (0.7%)**	32 (0.8%)	13 (0.6%)
10 ≤ oil seeps < 100 km^2	**470 (7.6%)**	299 (7.4%)	171 (8.0%)
Only oil seeps ≥ 100 km^2	**48 (0.8%)**	32 (0.8%)	16 (0.8%)
All oil seeps	**6,202 (100%)**	**4,066 (100%)**	**2,136 (100%)**

It is important to note that the oil slick size distribution explored throughout this Section is merely an arbitrary choice. The values selected to be shown on Table 6-5, Table 6-6, and Table 6-7 are only used to illustrate the size disparity of the oil slicks observed in the Campeche Bay region during the CBOS-SatPro.

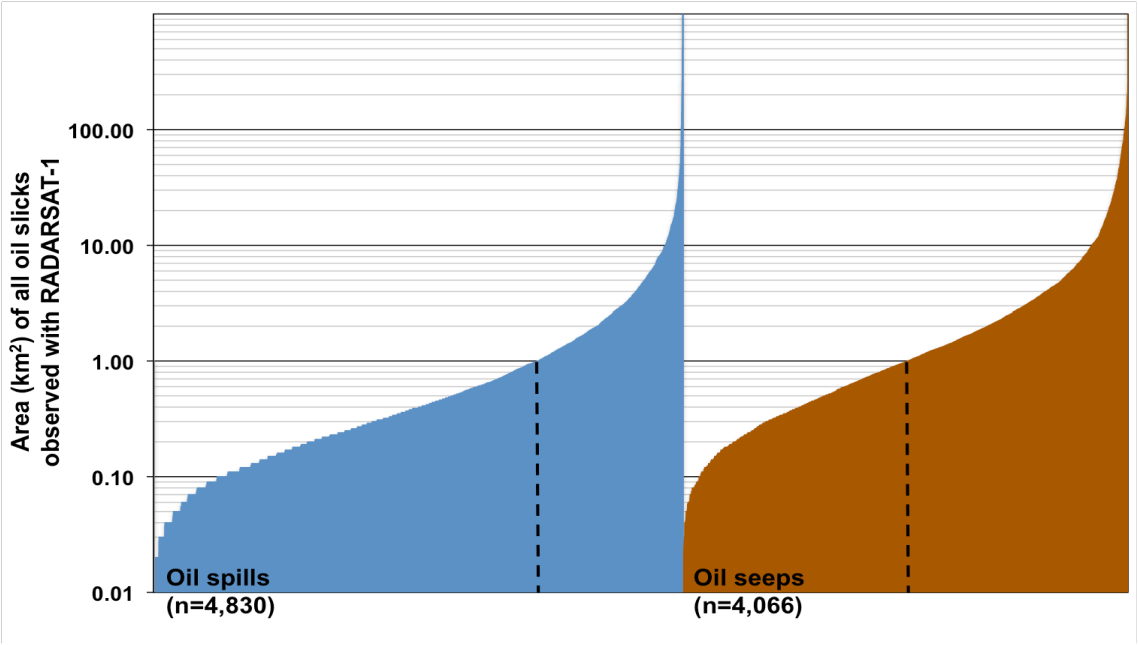

Figure 6-13: Frequency of oil slicks' area (km^2) imaged with RADARSAT-1 (n=8,896): oil spills (blue) and oil seeps (brown). Dashed lines correspond to oil slicks with areas of 1 km^2.

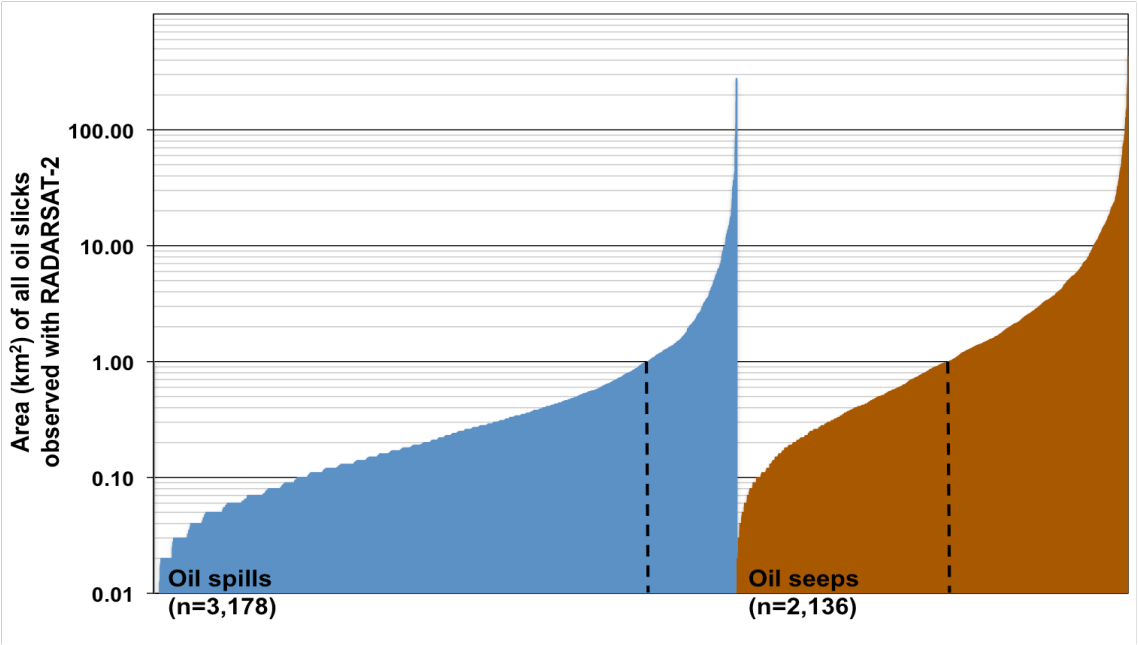

Figure 6-14: Frequency of oil slicks' area (km^2) imaged with RADARSAT-2 (n=5,314): oil spills (blue) and oil seeps (brown). Dashed lines correspond to oil slicks with areas of 1 km^2.

Table 6-8 shows the size distribution of the 20 largest areas among all oil slicks, in which major outliers occur on both categories: the Cantarell Oil Seep is the most representative with another specific Brightspot. The median and average oil slick sizes among all oil slicks within the CBOS-Data are, respectively: 0.5 km^2 and 3.3 km^2. This table also shows the average size per class and per category (oil spills: 1.9 km^2; and oil seep: 5.1 km^2). A remarkable aspect is that, if the Cantarell Oil Seep contribution is not considered, the average oil seep size drops considerably: 2.1 km^2. However, the average size of all oil slicks only falls to 3.0 km^2.

Table 6-8: Area (km^2) of the oil slicks within the Campeche Bay Oil Slick Satellite Database (CBOS-Data) imaged with both RADARSAT satellites.

		Oil Slicks	Oil Spills	Oil Seeps ****
Largest Areas (km^2)	1st	1,789.0	994.1 *	1,789.0
	2nd	994.1 *	533.5 *	495.8
	3rd	533.5 *	500.8 *	436.2
	4th	500.8 *	277.5	294.5
	5th	495.8	267.0 **	261.6
	6th	436.1	264.8 *	254.9
	7th	294.5	214.6 *	254.6
	8th	277.5	190.6 *	243.8
	9th	267.0 **	174.9	231.0
	10th	264.8 *	168.3 *	209.7
	11th	261.6	139.7 *	207.4
	12th	254.9	111.2	203.9
	13th	254.6	108.0	198.1
	14th	243.8	107.5	196.2
	15th	231.0	101.4	189.5
	16th	214.6 *	96.6	176.2
	17th	209.7	88.4	163.0
	18th	207.4	86.8 ***	159.5
	19th	203.9	80.8 ***	156.3
	20th	198.1	78.1	154.7
	Minimum	**0.01**	**0.01**	**0.01**
	Median	**0.5**	**0.3**	**0.9**
	Average	**3.3 (3.0 §)**	**1.9 (1.5 ¥)**	**5.1 (2.1 §)**
61 Brightspots ≤ 99 oil spills (Without *)			**4.5 (2.2 ¥)**	
10 Brightspots ≥ 100 oil spills			**1.3**	
Ship Spills			**1.6**	
Orphan Spills			**1.7**	
75 Clusters ≤ 99 oil seeps				**1.7**
13 Clusters ≥ 100 oil seeps				**3.0**
Cantarell Oil Seep				**30.2**
Orphan Seep				**1.7**

* Same Brightspot (One of the 61's with ≤ 99 oil spill observations).
** Ship Spill.
*** Orphan Spills.
**** Cantarell Oil Seep (Except the underlined that is from another Cluster).
§ Not considering the influence of the Cantarell Oil Seep.
¥ Not considering the influence of the Brightspot *.

Taking into account the perimeter attribute (*Per*), the minimum and maximum values for all oil slicks are: 0.2 km and 5,093.2 km. Table 6-9 shows the 5 largest perimeters; the second largest perimeters are also much smaller than the largest ones for both categories. The average and median oil slick perimeters are, 35.3 km and 10.7 km, respectively.

Table 6-9: Perimeter (km) information about the oil slicks separated for oil spills (blue) and oil seeps (brown) imaged with both RADARSAT satellites.

		Oil Slicks	Oil Spills *	Oil Seeps ***
Largest Perimeters (m)	1st	5,093.2	5,093.2	3,536.7
	2nd	3,536.7	2,086.9	2,826.8
	3rd	2,826.8	2,084.8 **	2,660.6 ***
	4th	2,660.6 ***	1,895.4	2,605.3
	5th	2,086.9	1,521.2	2,484.8
Minimum		0.2	0.2	0.2
Median		35.3	18.8	56.6
Average		10.7	6.8	19.9

* Same Brightspot (From the 61's with ≤ 99 oil spill observations).
** Largest Ship Spill.
*** Largest Orphan Spills.
**** Cantarell Oil Seep.

The relationship between area and perimeter is displayed on Figure 6-15 per category.

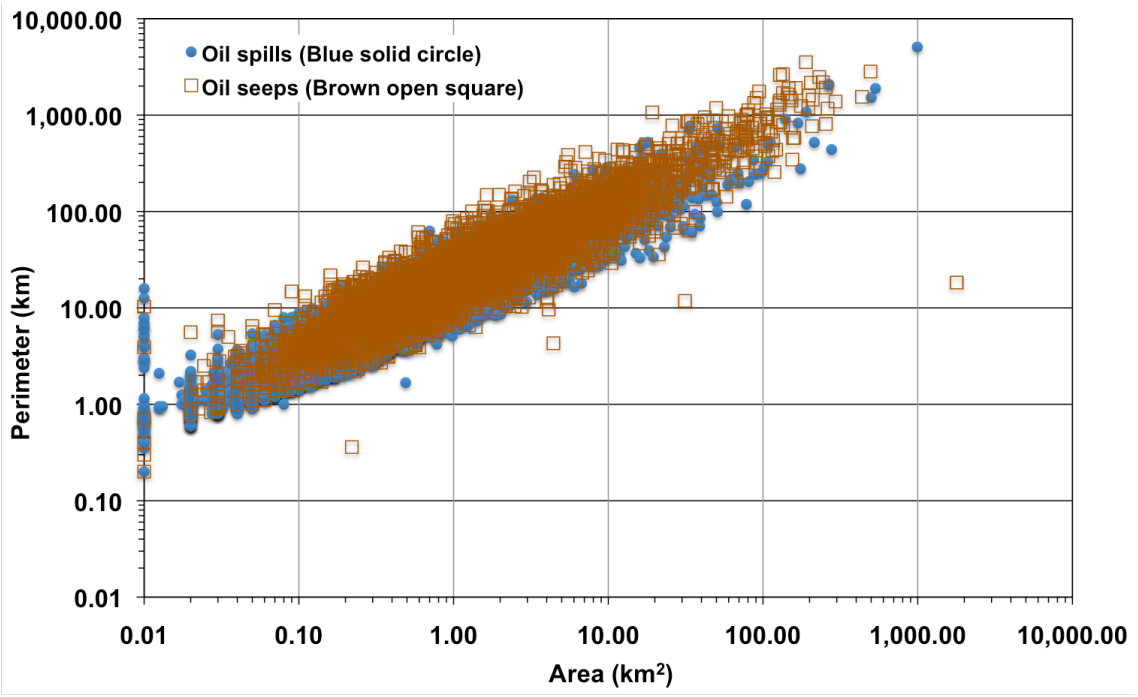

Figure 6-15: Scatterplot (log scaled) with the relationship between area (km^2) and perimeter (km) for all oil spills (blue solid circles) and oil seeps (brown open squares).

- **Contextual Attribute:** Water Depth (*Wdepth*)

The water column depth attribute (*Wdepth*) is not provided for all CBOS-Data entries (Table 6-10), being only given for 40% (n=5,669) of the observed oil slicks. These have been logged only for about 7.5 years (between January 2002 and September 2009) and their average and median values are, respectively, 484 m and 59 m.

Table 6-10: Water column depth (m) of the oil slicks (n=5,669) imaged with both RADARSAT satellites: oil spills (blue) and oil seeps (brown).

Water Column Depth (m)	Oil Slicks	Oil Spills	Oil Seeps
Shallower	2	2	20
Deeper	3,966	2,500	3,966
Average	**484**	73	1,296
Median	**59**	50	1,500
Number of Records	**5,669**	3,764 (**66.4%**)	1,905 (**33.6%**)

Figure 6-16 revels that the vast majority of oil spills (96%) occurs in shallower regions (< 100 m) and most oil seeps (63%) are observed in deep waters (> 1000 m). The water depth of the region where the oil slicks were imaged does not have any relation with their area and perimeter, as illustrated on Figure 6-17 and Figure 6-18, which show oil slicks of various sizes occurring at the same water depths.

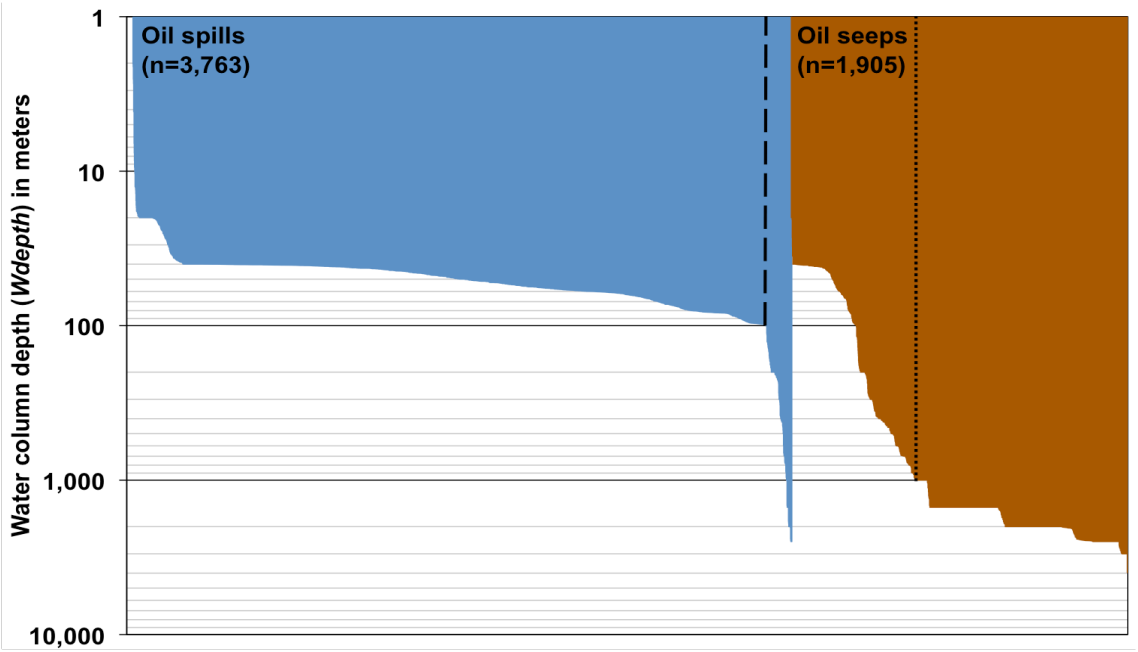

Figure 6-16: Water column depth (m) of the oil slicks observed on the sea surface in the Campeche Bay region: oil spills (blue) and oil seeps (brown). These have only been logged for 40% (n=5,669) of the oil slicks within the Campeche Bay Oil Slick Satellite Database (CBOS-Data). Dashed and dotted lines indicate 100 m and 1000 m depths, respectively.

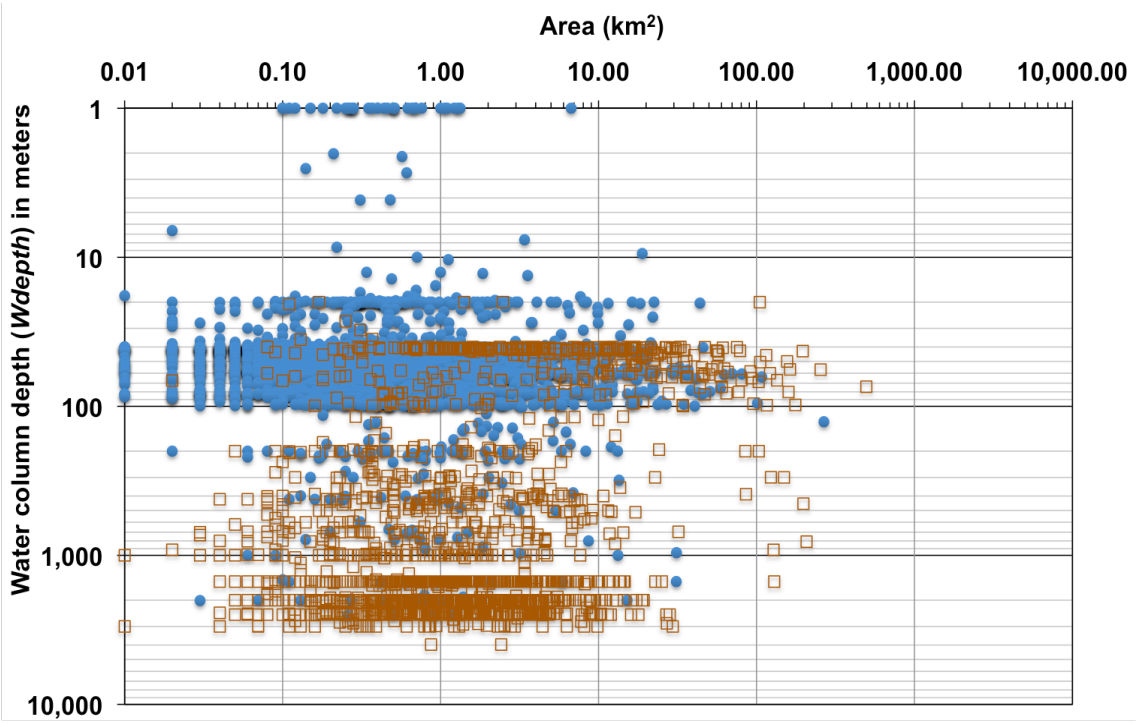

Figure 6-17: Area (km^2) versus water column depth (m): oil spills (blue solid circle) and oil seeps (brown open square).

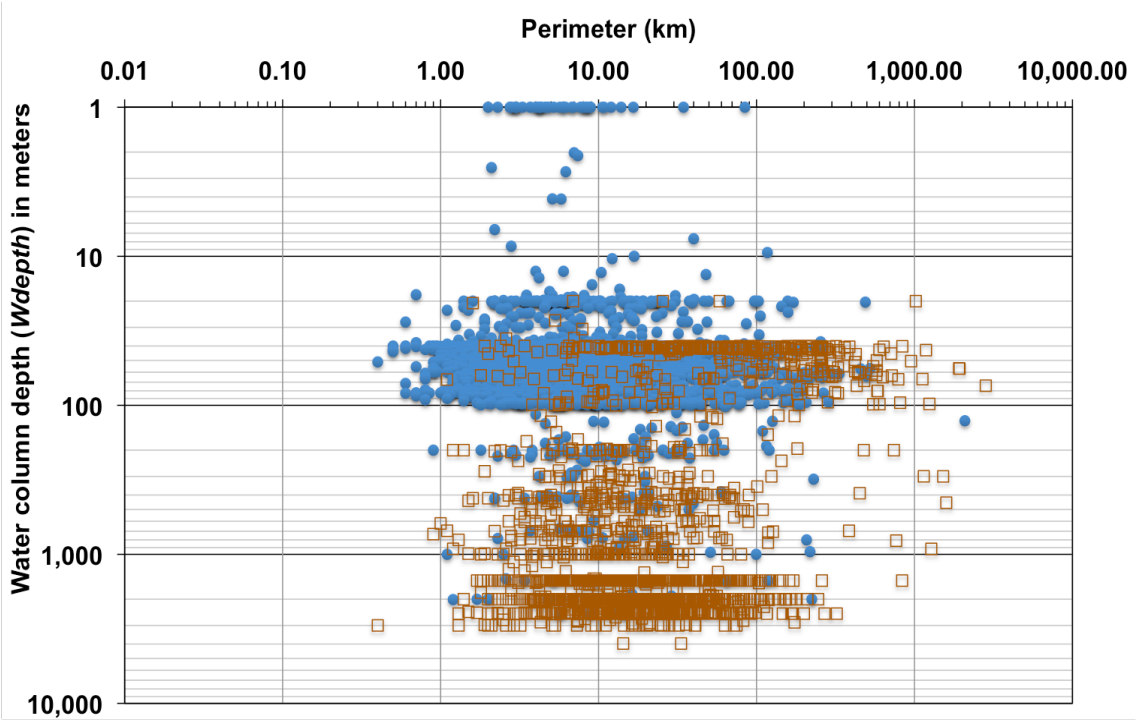

Figure 6-18: Perimeter (km) versus water column depth (m): oil spills (blue solid circle) and oil seeps (brown open square).

- **MetOc-Kit:** *Chl*, *CTT*, *minSST*, *maxSST*, *minSWH*, and *maxSWH*

Unfortunately, there is not much to consider about the MetOc-Kit attributes logged on the CBOS-Data. This is mostly because they were inappropriately logged for the purposes of the analysis intended herein: they were not retrieved at the oil slicks' location. *Chl* and *CTT* are discrete attributes that only indicate the presence (or absence) of the chlorophyll-a concentration value and cold clouds (i.e. with temperatures below 40^{o}C). *SST* and *SWH* were logged as minimum and maximum values within the satellite frame, i.e. not in the position of the oil slick.

In addition, they were not logged in a continuous manner, i.e. they have been intermittently entered on the CBOS-Data. And even though these attributes started being registered at the CBOS-SatPro start, *SWH* is only registered until November 2008, and *SST*, *Chl*, and *CTT* span to September 2009.

- **Publication:** Scientific Meeting and Journal Submission

While preliminary results of this Phase have been orally presented on the XVII Brazilian Remote Sensing Symposium (SBSR[66] – on April 2015 in João Pessoa-PB/Brazil: CARVALHO *et al.*, 2015a), the complete set of results have been submitted to a special issue (Long-Term Satellite Data and Applications) of the Canadian Journal of Remote Sensing (CJRS): CARVALHO *et al.* (2015b) – see Appendix 1. The results of the Data Familiarization practice fully elucidate the first proposed specific goal of the present D.Sc. research: the use of RADARSAT measurements to describe the occurrence and spatio-temporal distribution of the oil slicks observed on the surface of the ocean in the Campeche Bay region. Further discussion matters about the Data Familiarization are found on Chapter 7.

6.2. PHASE 2: QUALITY CONTROL (QC)

The findings of the second pre-processing data verification Phase (described in Section 5.2) are presented on this Section. After analyzing the various aspects related to the information within the CBOS-Data – as disclosed in the Data Familiarization (Phase 1: Section 6.1) – it is possible to define certain QC-Standards. These, which are specified to give consistency to the scene selection utilized in the present investigation, are described below:

[66] SBSR: http://www.dsr.inpe.br/sbsr2015/files/p0217.pdf

- **1st QC-Standard:** *SARname* and *Pol* attributes

The two RADARSAT satellites have quite similar technical specifications – yet, they are not exactly the same (CRSS, 1993; 2004; MDA, 2004; 2014). For instance, two main differences are highlighted regarding the CBOS-SatPro imagery:

1. As showed in Table 6-4, most oil slicks observed during the CBOS-SatPro have been imaged with SCNA and SCNB (n=12,892; 91%). These beam modes are the RADARSAT modes suitable to image the sea surface, and therefore to detect oil slicks (NRCAN, 2014). However, their radiometric depths are different (Table 4-1): RADARSAT-1 (8-bit) and RADARSAT-2 (16-bit); and
2. Whereas RADARSAT-1 is HH-polarized (n=482; 100%), most RADARSAT-2 explored in the CBOS-SatPro are VV-polarized (n=276; 97%). In fact, of these two RADARSAT polarizations, VV is the most suitable to detect oil slicks due to enhanced backscattering contrast compared to sea clutter (WISMANN *et al.*, 1998; GIRARD-ARDHUIN *et al.*, 2003; VAN DER SANDEN, 2004).

As a result, it is based on these specifications aspects that the *SARname* and *Pol* attributes are used to establish a primary QC-Standard. Accordingly, images from the earlier RADARSAT (i.e. 8-bit HH-polarized) are not explored during the further Phases of the present D.Sc. research because of its characteristics that differ from the ones from the more sophisticated and useful RADARSAT-2 imagery: 16-bit, VV-polarized.

- **2nd QC-Standard:** MetOc-Kit and *Wdeth* attributes

A secondary QC-Standard leaves out of the present analysis some of the original attributes within the CBOS-Data (Table 2-2): the water column depth attribute (*Wdepth*) and the MetOc-Kit information that include chlorophyll-a concentration (*Chl*), cloud top temperature (*CTT*), sea surface temperature (*minSST* and *maxSST*), and significant wave height (*minSWH* and *maxSWH*) are not considered herein. This decision is based on the fact that such attributes are not provided for the bulk of the oil slicks observed during the CBOS-SatPro (see Section 6.1).

- **3rd QC-Standard:** Missing Data

Additionally, some RADARSAT images were not available, nor were some polygons identifying certain oil slicks. This structures a further QC-Standard, in which the actual existence of the satellite scene and its companion information (i.e. oil slick polygon) defined the exclusion of some information out of the present analysis.

- **QC-Standard:** Summary

The establishment of the three QC-Standards constitutes the basis to filter the information within the CBOS-Data. As a result, from this point onwards only RADARSAT-2 scenes (16-bit, VV-polarized: n=277) and its imaged oil slicks (n=4,916) are explored alongside the following CBOS-Data attributes (Table 2-2): geographical coordinates (*cLAT* and *cLONG*), category (*Category*), class (*Class*), date (*SARdate*), time (*SARtime*), beam mode (*Bmode*), area (*Area*), and perimeter (*Per*).

These conditions strengthen and give consistency to the calculation of the SAR backscatter signature (i.e. σ^o, β^o, and γ^o expressed in amplitude (C_1) and in dB units (C_2) – Table 5-1), as described in the Phase 4 (New Slick-Feature Attributes: Section 5.4). As such, with the establishment of the QC-Standards, an appropriate plan is devised for the data usage during the present D.Sc. research. A synoptic summary of this plan is pictured on Figure 1-2 and Figure 1-3, and fully explained in Chapter 5.

- **QC-Standard:** Data Reduction

A consequence of applying the QC-Standards is a decrease in spatio-temporal coverage of the observed oil slicks. Two data reductions are observed, one in the number of satellite images and another in the frequency distribution of oil slicks. These are related to the fact that RADARSAT-2 imagery started to be acquired in March of 2008, rather than in 1997 as for RADARSAT-1 (Table 6-1).

The data reduction rate caused by using only the 16-bit, VV-polarized RADARSAT-2 images is shown in Table 6-11. This information is presented in relation to the entire content of the CBOS-Data (i.e. oil slicks imaged with both RADARSAT satellites) and considering only the RADARSAT-2 images utilized during the CBOS-SatPro.

Table 6-11: Data reduction caused by the three QC-Standards.

QC-Standards	**After**	**Before**	
Data Reduction	**RADARSAT-2** (16-bit, VV-polarized)	Both RADARSAT	Only all RADARSAT-2
SAR Scenes	**277**	766 (63.8%)	284 (2.5%)
Oil Spills	**2,895**	8,008 (63.8%)	3,178 (8.9%)
Oil Seeps	**2,021**	6,202 (67.4%)	2,136 (5.4%)
Oil Slicks	**4,916**	14,210 (65.4%)	5,314 (7.5%)

6.3. PHASE 3: RADARSAT RE-PROCESSING

The first image-processing Phase, described in Section 5.3, accounts for the re-processing of the imagery that passed the QC-Standards: 277 RADARSAT-2 scenes (Table 6-11: 16-bit, VV-polarized). Each scene processed includes the georeferenced *.tif* files of 13 image products: *SIG.amp*, *SIG.amp.FF*, *SIG.dB*, *SIG.dB.FF*, *BET.amp*, *BET.amp.FF*, *BET.dB*, *BET.dB.FF*, *GAM.amp*, *GAM.amp.FF*, *GAM.dB*, *GAM.dB.FF*, and *INC.ang* (Table 5-1), as well as their corresponding PCI *.pix* files.

These have been processed using a personal computer (Sony Vaio with 700 GB of disk space) running Windows 8.1 Pro. The operational system of such machine is 64 bit and its processor is an Intel Core i-7 2.9 GHz with 6 GB of RAM memory. Such image processing procedures have been completed using PCI Geomatica version 2014, exclusively using in-house EASI command codes (i.e. batch scripting) of the FOCUS Data Viewer.

The size of each processed scene is about 27 GB, and together, the 277 scenes occupy almost 7.5 TB on disk. Due to storage limitation, external hard drives were used (two LaCie 4 TB d2 Professional Thunderbolt Series HDD 7200 RPM with USB3 connection) and it took about 10 days to process the 277 scenes, as the average processing time per scene was 55 min. When the computer hard disk was used instead, the timescale to process each image was reduced to about half: 25 min.

6.4. PHASE 4: NEW SLICK-FEATURE ATTRIBUTES

This Section quantifies the products of the second image-processing Phase described in Section 5.4, which considers the calculation of new slick-feature attributes. These attributes pertain to four major types of oil slick characteristics: contextual information (Table 5-2), satellite scene descriptors (Table 5-3), attributes describing the geometry, shape, and dimension of the oil slicks (Table 5-4), as well as those characterizing the SAR backscatter signature (Table 5-5). The typical value (represented by a set of basic qualitative-quantitative statistics: minimum, maximum, average, and standard deviation) of some of attribute within the CBOS-DScMod is presented herein.

The oil slick frequency, per category and per class, discussed on this Section follows the explanation of Section 2.3.4 (CBOS-SatPro Part 4: Dark Spot Identification). Herein, the same color-code instituted in Section 6.1 is followed; however, different from Section 6.1 (Figure 6-3 and Figure 6-4), all documented Clusters and Brightspots are respectively grouped to form two single classes; exceptions are discussed below.

The 2,021 oil seeps are classified in three distinct classes, i.e. Cantarell Oil Seep Cluster (n=238), all other Clusters (n=1,200), and Orphan Seeps (n=583). Because of its exceptionally large superficial area coverage, the signature from the Cantarell Oil Seep is analyzed separately. The 2,895 oil spills have six classes: all recognized Brightspots (n=1,050), Bright-1 (n=575), Bright-2 (n=276), Bright-3 (n=255), Ship Spills (n=159), and Orphan Spills (n=580). As three particular Brightspots stand out in the number of oil spills from the platforms belonging to these oilfields (n=1,106), their signatures are also separated as stand alone classes: Bright 1 to 3 (see Table 5-8).

The frequency of oil slicks per *Category* and *Class* attributes is presented in Table 6-12 that also presents the range of the two contextual descriptors of spatial location: latitude (*cLAT*) and longitude (*cLONG*). The two contextual descriptors of temporal location explored in the CBOS-DScMod (i.e. *SARdate* and *SARtime*) spans about the same distribution of all entries within the CBOS-Data (Table 6-1 and Table 6-2).

Table 6-12: Frequency, per category and per class, of the oil slicks within the Campeche Bay Oil Slick Modified Database (CBOS-DScMod) and their respective latitude (*cLAT*) and longitude (*cLONG*) range. See also Table 5-2 and Table 5-8.

Category and Class	n	% *		Latitude (°N) **	Longitude (°W) **
Oil Spills	**2,895**	**58.9**		**18.274 26.366**	**85.614 94.814**
Brightspots	**1,050**	**36.3**	**21.4**	18.460 26.366	91.123 94.814
Bright-1	**575**	**19.9**	**11.7**	19.227 19.500	92.004 92.385
Bright-2	**276**	**9.5**	**5.6**	19.451 19.641	92.030 92.265
Bright-3	**255**	**8.8**	**5.2**	19.120 19.435	92.031 92.436
Ship Spills	**159**	**5.5**	**3.2**	18.502 20.999	90.819 94.492
Orphan Spills	**580**	**20.0**	**11.8**	18.274 25.318	85.614 94.098
Oil Seeps	**2,021**	**41.1**		**18.525 26.561**	**87.305 95.609**
Cantarell	**238**	**11.8**	**4.8**	19.133 19.832	91.915 93.118
Clusters	**1200**	**59.4**	**24.4**	18.734 24.304	91.531 94.748
Orphan Seeps	**583**	**28.8**	**11.9**	18.525 26.561	87.305 95.609
Oil Slicks	**4,916**	**100.0**		**18.274 26.561**	**85.614 95.609**

* Percentages calculated per category, per class, and overall.
** Range: minimum and maximum values.

Table 6-13 presents the typical values, per oil slick category, describing the geometry, shape, and dimension attributes of the oil slicks within the CBOS-DScMod (Table 5-4: 3rd Attribute Type). Such characteristics are presented per oil slick class in Appendix 2.

Table 6-13: Typical values (i.e. basic qualitative-quantitative statistics: minimum, maximum, average, and standard deviation) describing the geometry, shape, and dimension characteristics (Table 5-4: 3rd Attribute Type) of the oil slicks within the Campeche Bay Oil Slick Modified Database (CBOS-DScMod).

Oil Slicks (n=4,916)	Minimum	Maximum	Average	Standard Deviation	Sum (km^2)
LEN *	3.0	823,850.0	**4,567.7**	25,725.9	
Area **(km^2)**	0.0025	436.1525	**2.7129**	14.2145	13,336.6
Per **(km)**	0.2	2,484.8	**33.9**	116.1	
AtoP **(km)**	0.0033	0.6582	**0.0482**	0.0355	
PtoA **(km^{-1})**	1.5193	300.0000	**27.9943**	16.4569	
PtoA.nor **	0.8463	46.1191	**5.5458**	4.2786	
COMPLEX.ind **	9.0	26,728.3	**616.5**	1,611.7	
COMPACT.ind **	0.0005	1.3963	**0.0848**	0.0982	
SHAPE.ind **(km^{-1})**	0.75	40.87	**4.91**	3.79	
FRAC.ind **	-2,353.2	426,242.8	**647.4**	15,270.7	
Oil Spills (n=2,895)	**Minimum**	**Maximum**	**Average**	**Standard Deviation**	**Sum (km^2)**
LEN *	3.0	443,948.0	**2,002.6**	12,427.9	
Area **(km^2)**	0.0025	277.4900	**1.2421**	7.7306	3,595.8
Per **(km)**	0.2	772.3	**15.5**	39.6	
AtoP **(km)**	0.0033	0.6582	**0.0445**	0.0366	
PtoA **(km^{-1})**	1.5193	300.0000	**30.2178**	16.7603	
PtoA.nor **	1.1283	37.5652	**4.3875**	2.7407	
COMPLEX.ind **	16.0	17,732.9	**336.3**	712.8	
COMPACT.ind **	0.0007	0.7855	**0.1074**	0.1071	
SHAPE.ind **(km^{-1})**	1.00	33.29	**3.89**	2.43	
FRAC.ind **	-487.9	395,511.4	**375.8**	11,726.4	
Oil Seeps (n=2,021)	**Minimum**	**Maximum**	**Average**	**Standard Deviation**	**Sum (km^2)**
LEN *	13.0	823,850.0	**8,242.0**	36,960.8	
Area **(km^2)**	0.0100	436.1525	**4.8198**	19.9617	9,740.9
Per **(km)**	0.3	2,484.8	**60.2**	171.4	
AtoP **(km)**	0.0036	0.3978	**0.0535**	0.0333	
PtoA **(km^{-1})**	2.5139	280.0000	**24.8093**	15.4690	
PtoA.nor **	0.8463	46.1191	**7.2051**	5.3947	
COMPLEX.ind **	9.0	26,728.3	**1,017.9**	2,306.3	
COMPACT.ind **	0.0005	1.3963	**0.0525**	0.0724	
SHAPE.ind **(km^{-1})**	0.75	40.87	**6.39**	4.78	
FRAC.ind **	-2,353.2	426,242.8	**1,036.4**	19,239.0	

* Number of pixels inside the oil slicks.

** Dimensionless quantity.

The new slick-feature attributes referring to the geometry, shape, and dimension of the oil slicks (Table 5-4: 3rd Attribute Type) have been retrieved with in-house Python codes. Likewise, those involving basic statistical measures – i.e. *INC.ang* and SAR backscatter signature (Table 5-5: 4th Attribute Type) – were also retrieved with Python, but using batch ArcGIS scripting functions. The calculation of *INC.ang* and the attributes of the 4th type were retrieved by matching the individual oil slick polygons with the 13 radiometric-calibrated image products: *SIG.amp*, *SIG.amp.FF*, *SIG.dB*, *SIG.dB.FF*, *BET.amp*, *BET.amp.FF*, *BET.dB*, *BET.dB.FF*, *GAM.amp*, *GAM.amp.FF*, *GAM.dB*, *GAM.dB.FF*, and *INC.ang* (Table 5-1).

The *AVG* attribute (i.e. arithmetic mean of all pixels inside individual oil slick polygons) is shown to describe the SAR backscatter signature of the CBOS-DScMod oil slicks: Table 6-14 (sigma-naught: σ^o), Table 6-15 (beta-naught: β^o), and Table 6-16 (gamma-naught: γ^o).

Table 6-14: Typical values (i.e. basic qualitative-quantitative statistics: minimum, maximum, average, and standard deviation) of the average (*AVG*: arithmetic mean of all pixels inside individual oil slick polygons) SAR backscatter signature (**Sigma-naught: σ^o**) of the oil slicks within the CBOS-DScMod. These values correspond to incidence angles ranging from 19.5° to 46.6°. See also Table 5-1 and Table 5-5.

Sigma-naught (σ^o)	***SIG.amp.AVG***	***SIG.amp.FF.AVG***	***SIG.dB.AVG***	***SIG.dB.FF.AVG***
Oil Slicks (n=4,916)	**Amplitude without Frost**	**Amplitude with Frost**	**Decibels without Frost**	**Decibels with Frost**
Minimum	0.000907	0.000995	-62.195921	9.552999
Maximum	0.660908	0.635781	-8.801640	62.054795
Average	**0.027028**	**0.029074**	**-40.873467**	**41.020277**
Standard Deviation	0.045919	0.048927	10.705655	10.564339
Oil Spills (n=2,895)	**Amplitude without Frost**	**Amplitude with Frost**	**Decibels without Frost**	**Decibels with Frost**
Minimum	0.001060	0.001135	-61.211937	11.133664
Maximum	0.660908	0.635781	-9.089579	61.200692
Average	**0.025685**	**0.027619**	**-41.490243**	**41.656948**
Standard Deviation	0.048334	0.051418	10.556650	10.423009
Oil Seeps (n=2,021)	**Amplitude without Frost**	**Amplitude with Frost**	**Decibels without Frost**	**Decibels with Frost**
Minimum	0.000907	0.000995	-62.195921	9.552999
Maximum	0.447408	0.474392	-8.801640	62.054795
Average	**0.028953**	**0.031158**	**-39.989960**	**40.108272**
Standard Deviation	0.042155	0.045051	10.857283	10.700323

Table 6-15: Typical values (i.e. basic qualitative-quantitative statistics: minimum, maximum, average, and standard deviation) of the average (*AVG:* arithmetic mean of all pixels inside individual oil slick polygons) SAR backscatter signature (**Beta-naught: β^o**) of the oil slicks within the CBOS-DScMod. These values correspond to incidence angles ranging from 19.5° to 46.6°. See also Table 5-1 and Table 5-5.

Beta-naught (β^o)	***BET.amp.AVG***	***BET.amp.FF.AVG***	***BET.dB.AVG***	***BET.dB.FF.AVG***
Oil Slicks (n=4,916)	**Amplitude without Frost**	**Amplitude with Frost**	**Decibels without Frost**	**Decibels with Frost**
Minimum	0.001282	0.001407	-59.187699	5.101585
Maximum	1.882817	1.811290	0.216535	59.053293
Average	**0.065618**	**0.070543**	**-35.404322**	**35.631894**
Standard Deviation	0.129032	0.137584	12.284491	12.040587
Oil Spills (n=2,895)	**Amplitude without Frost**	**Amplitude with Frost**	**Decibels without Frost**	**Decibels with Frost**
Minimum	0.001493	0.001598	-58.418408	5.101585
Maximum	1.882817	1.811290	0.216535	58.403050
Average	**0.061845**	**0.066466**	**-36.258413**	**36.507780**
Standard Deviation	0.136405	0.145210	12.165771	11.916276
Oil Seeps (n=2,021)	**Amplitude without Frost**	**Amplitude with Frost**	**Decibels without Frost**	**Decibels with Frost**
Minimum	0.001282	0.001407	-59.187699	5.267341
Maximum	1.254385	1.329995	0.059730	59.053293
Average	**0.071022**	**0.076383**	**-34.180872**	**34.377222**
Standard Deviation	0.117491	0.125662	12.353100	12.109488

Regardless of oil slick category, the typical values of σ^o, β^o, and γ^o shown on Tables 6-14, 6-15, and 6-16 have been derived with incidence angles ranging from 19.5° to 46.6°. Although an analysis comparing incidence angle is out of the scope of this research, it is conspicuous how typical SAR backscatter signature values (i.e. *AVG* attribute) change with incidence angles varying between ≥19.5° and <28.5°, ≥28.5° and <37.5°, and ≥37.5° and ≤46.6°, as presented in Appendix 3. Another interesting evaluation, not performed during the present D.Sc. research, is a compilation of typical σ^o, β^o, and γ^o values varying with wind field measurements locally obtained from *in situ* equipments or from satellite data at the same time, or close enough, of the oil slick observation (CLARO, 2007; RODRIGUES, 2011; RODRIGUES *et al.*, 2013).

Table 6-16: Typical values (i.e. basic qualitative-quantitative statistics: minimum, maximum, average, and standard deviation) of the average (*AVG*: arithmetic mean of all pixels inside individual oil slick polygons) SAR backscatter signature (**Gamma-naught:** γ^{o}) of the oil slicks within the CBOS-DScMod. These values correspond to incidence angles ranging from 19.5° to 46.6°. See also Table 5-1 and Table 5-5.

Gamma-naught (γ^{o})	*GAM.amp.AVG*	*GAM.amp.FF.AVG*	*GAM.dB.AVG*	*GAM.dB.FF.AVG*
Oil Slicks (n=4,916)	**Amplitude without Frost**	**Amplitude with Frost**	**Decibels without Frost**	**Decibels with Frost**
Minimum	0.001282	0.001407	-59.183525	9.016371
Maximum	0.705821	0.682226	-8.194344	59.193962
Average	**0.030161**	**0.032452**	**-39.234321**	**39.392071**
Standard Deviation	0.049123	0.052329	10.106872	9.963671
Oil Spills (n=2,895)	**Amplitude without Frost**	**Amplitude with Frost**	**Decibels without Frost**	**Decibels with Frost**
Minimum	0.001467	0.001571	-59.162005	10.757918
Maximum	0.705821	0.682226	-8.547585	58.769908
Average	**0.028796**	**0.030973**	**-39.738457**	**39.916931**
Standard Deviation	0.051720	0.055008	9.904402	9.768760
Oil Seeps (n=2,021)	**Amplitude without Frost**	**Amplitude with Frost**	**Decibels without Frost**	**Decibels with Frost**
Minimum	0.001282	0.001407	-59.183525	9.016371
Maximum	0.479105	0.508002	-8.194344	59.193962
Average	**0.032117**	**0.034571**	**-38.512166**	**38.640229**
Standard Deviation	0.045084	0.048168	10.349790	10.191845

Typical values for the original *COV* attribute (Table 5-5: *COV.STD/AVG*) that describes the relative dispersion of the pixel values around the central tendency inside the oil slick are presented in Table 6-17 for the 13 radiometric-calibrated image products of the oil slicks within the CBOS-DScMod. While low *COV* indicates low variability, high COV values denote high variability within the pixels of individual oil slicks, for instance: 0.1 means that the *STD* is equal to 10% of the *AVG*.

Histograms with the frequency distribution of some of the attributes within the CBOS-DScMod is shown on Figure 6-19, Figure 6-20, Figure 6-21, Figure 6-22, and Figure 6-23. These histograms are helpful to examine the statistical distribution of such attributes, as well as they assist on the characterization of the oil slicks observed in Campeche Bay.

Table 6-17: Typical values (i.e. basic qualitative-quantitative statistics: minimum, maximum, average, and standard deviation) characterizing the Coefficient of Variation (*COV*: ratio between *STD* and *AVG* attributes) of the oil slicks within the Campeche Bay Oil Slick Modified Database (CBOS-DScMod). These values correspond to incidence angles ranging from 19.5° to 46.6°. See also Table 5-5.

Oil Slicks: *COV.STD/AVG*		**Minimum**	**Maximum**	**Average**	**Standard Deviation**
Incidence Angle	*INC.ang*	0.000024	0.083812	**0.002118**	0.004341
Sigma-naugh (σ°) *	*SIG.amp*	0.197564	16.407197	**0.813826**	0.748304
	SIG.amp.FF	0.172066	15.281376	**0.636604**	0.742414
	SIG.dB	-1.111435	-0.056387	**-0.176553**	0.078373
	SIG.dB.FF	0.030392	0.640210	**0.124347**	0.060784
Gamma-naugh (γ°) *	*BET.amp*	0.197471	16.373387	**0.813620**	0.745226
	BET.amp.FF	0.172094	15.058628	**0.636383**	0.738978
	BET.dB	-50.074967	101.814973	**-0.215557**	1.728912
	BET.dB.FF	0.032990	1.137100	**0.159431**	0.106188
Beta-naugh (β°) *	*GAM.amp*	0.197592	16.444979	**0.813965**	0.750020
	GAM.amp.FF	0.172044	15.513617	**0.636758**	0.744536
	GAM.dB	-1.184094	-0.058703	**-0.183557**	0.080929
	GAM.dB.FF	0.032022	0.662951	**0.129200**	0.062331
Oil Spills: *COV.STD/AVG*		**Minimum**	**Maximum**	**Average**	**Standard Deviation**
Incidence Angle	*INC.ang*	0.000024	0.031398	**0.001186**	0.001940
Sigma-naugh (σ°) *	*SIG.amp*	0.197564	13.369330	**0.823675**	0.774880
	SIG.amp.FF	0.172066	14.082050	**0.647057**	0.759865
	SIG.dB	-1.111435	-0.056387	**-0.176553**	0.078373
	SIG.dB.FF	0.030392	0.640210	**0.119729**	0.059213
Gamma-naugh (γ°) *	*BET.amp*	0.197471	13.363505	**0.823582**	0.774613
	BET.amp.FF	0.172094	14.082496	**0.646959**	0.759597
	BET.dB	-50.074967	101.814973	**-0.215557**	1.728912
	BET.dB.FF	0.032990	1.137100	**0.151352**	0.103104
Beta-naugh (β°) *	*GAM.amp*	0.197592	13.375513	**0.823716**	0.775017
	GAM.amp.FF	0.172044	14.081563	**0.647102**	0.760004
	GAM.dB	-1.184094	-0.058703	**-0.179359**	0.083345
	GAM.dB.FF	0.032022	0.662951	**0.124737**	0.060957
Oil Seeps: *COV.STD/AVG*		**Minimum**	**Maximum**	**Average**	**Standard Deviation**
Incidence Angle	*INC.ang*	0.000053	0.083812	**0.003453**	0.006118
Sigma-naugh (σ°) *	*SIG.amp*	0.472796	16.407197	**0.799717**	0.708450
	SIG.amp.FF	0.263220	15.281376	**0.621630**	0.716595
	SIG.dB	-1.111435	-0.056387	**-0.176553**	0.078373
	SIG.dB.FF	0.046627	0.448954	**0.130963**	0.062387
Gamma-naugh (γ°) *	*BET.amp*	0.472687	16.373387	**0.799349**	0.700929
	BET.amp.FF	0.263093	15.058628	**0.621232**	0.708309
	BET.dB	-50.074967	101.814973	**-0.215557**	1.728912
	BET.dB.FF	0.049864	0.670910	**0.171002**	0.109448
Beta-naugh (β°) *	*GAM.amp*	0.472803	16.444979	**0.799997**	0.712644
	GAM.amp.FF	0.263246	15.513617	**0.621940**	0.721729
	GAM.dB	-0.722302	-0.086892	**-0.189571**	0.076958
	GAM.dB.FF	0.048900	0.467745	**0.135594**	0.063721

* Amplitude and decibels with and without the Frost filter (FROST *et al.*, 1982).

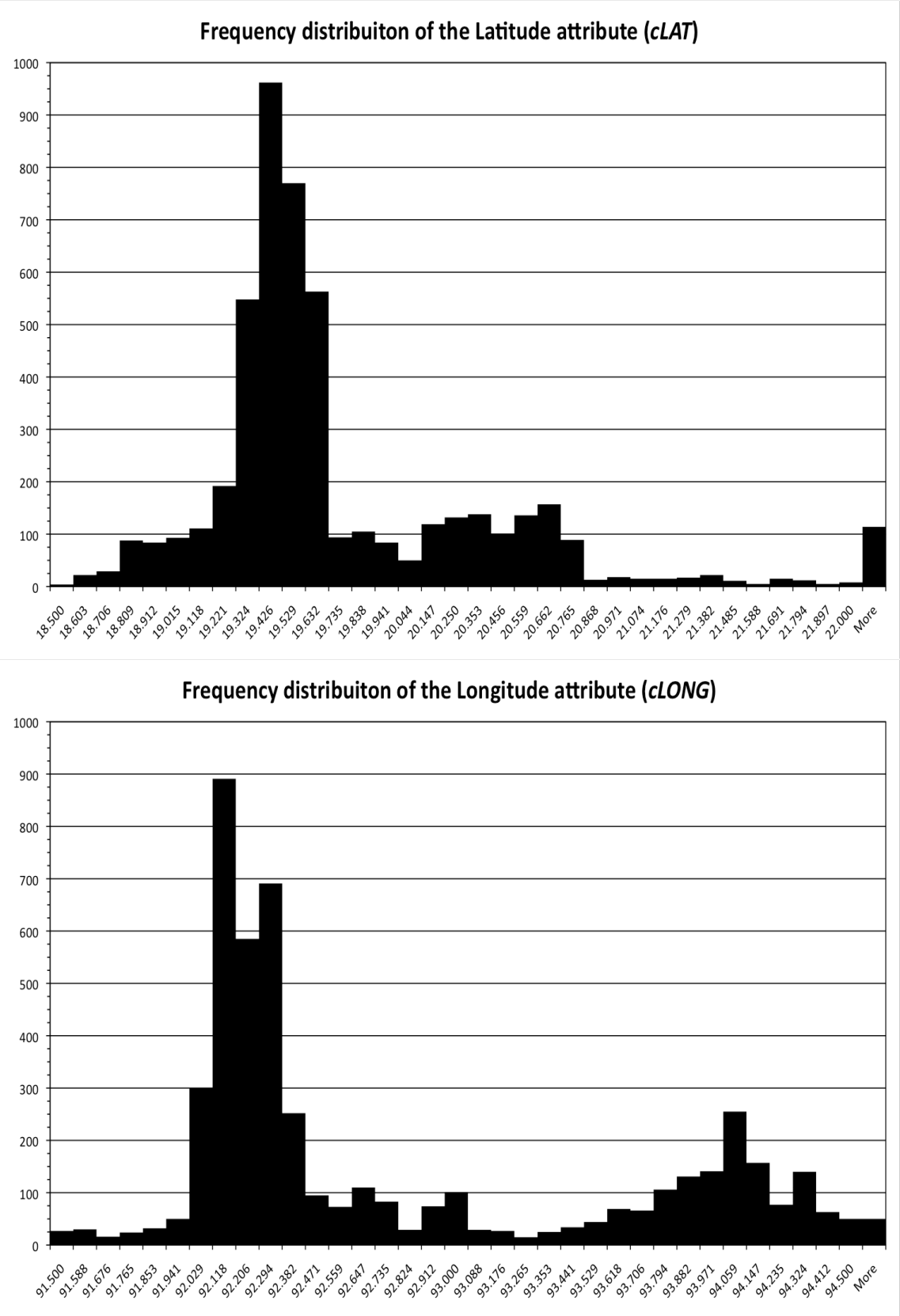

Figure 6-19: Frequency distribution of two contextual attributes that describe the oil slicks within the Campeche Bay Oil Slick Modified Database (CBOS-DScMod): Latitude (*cLAT*) and Longitude (*cLONG*), respectively, top and bottom panels. See also Table 5-4 and Figure 6-24.

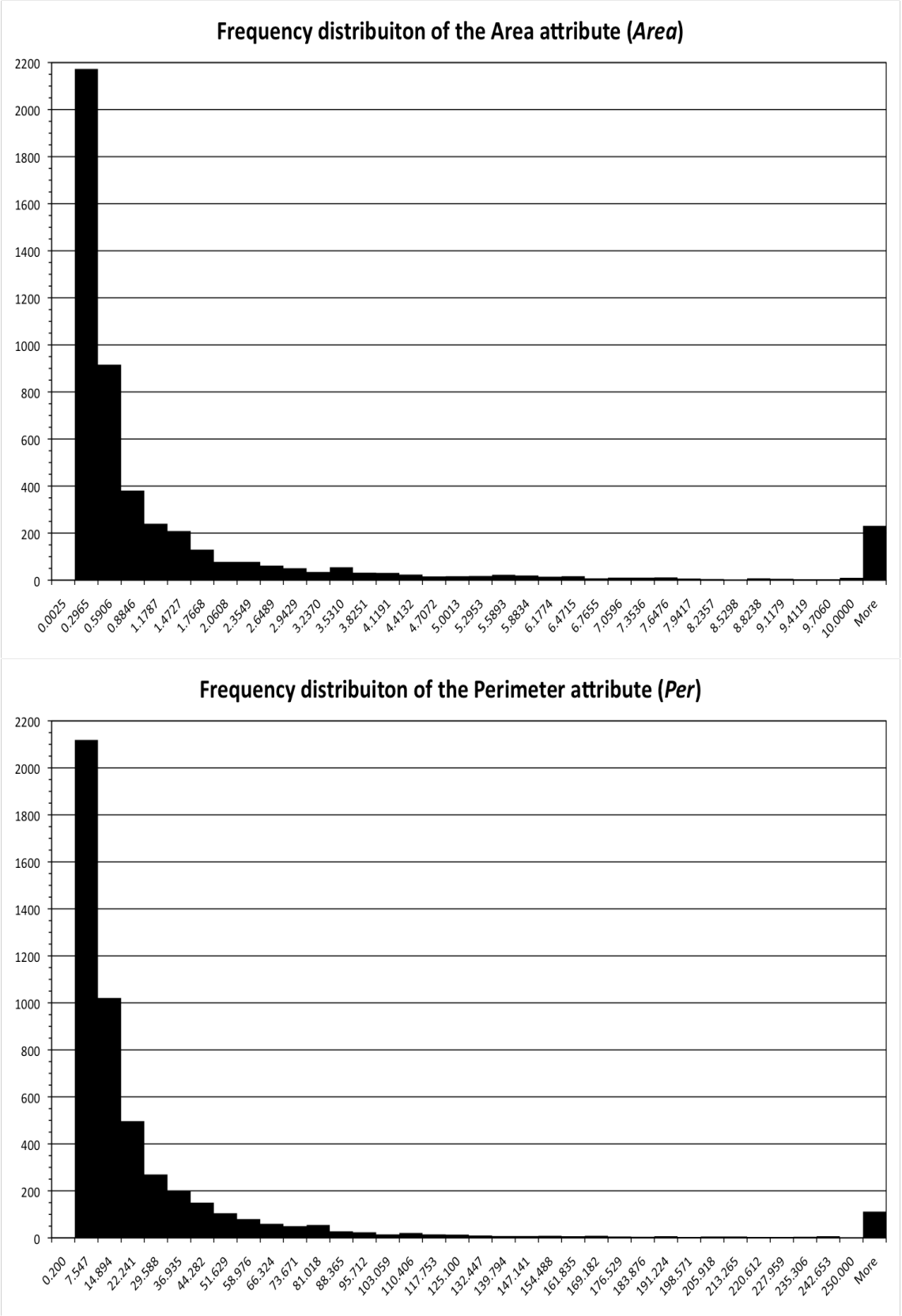

Figure 6-20: Frequency distribution of two contextual attributes that describe the oil slicks within the Campeche Bay Oil Slick Modified Database (CBOS-DScMod): Area (*Area*) and Perimeter (*Per*), respectively, top and bottom panels. See also Table 5-4 and Figure 6-25.

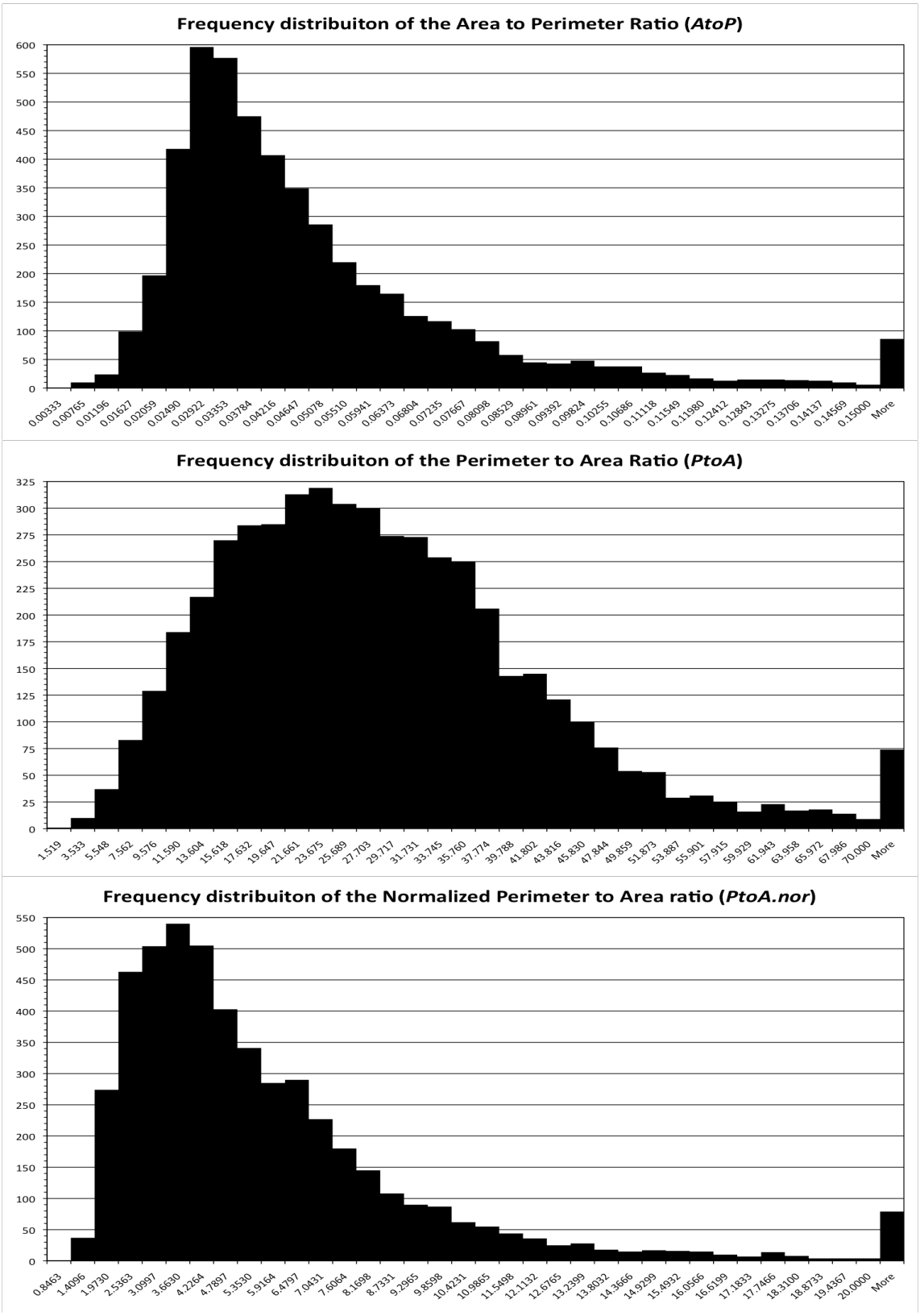

Figure 6-21: Frequency distribution of three attributes of geometry, shape, and dimensions that describe the oil slicks within the Campeche Bay Oil Slick Modified Database (CBOS-DScMod): Area to Perimeter Ratio (*AtoP*), Perimeter to Area Ratio (*PtoA*), and Normalized Perimeter to Area Ratio (*PtoA.nor*), respectively shown on the upper, middle, and lower panels. See also Table 5-4 and Figure 6-26.

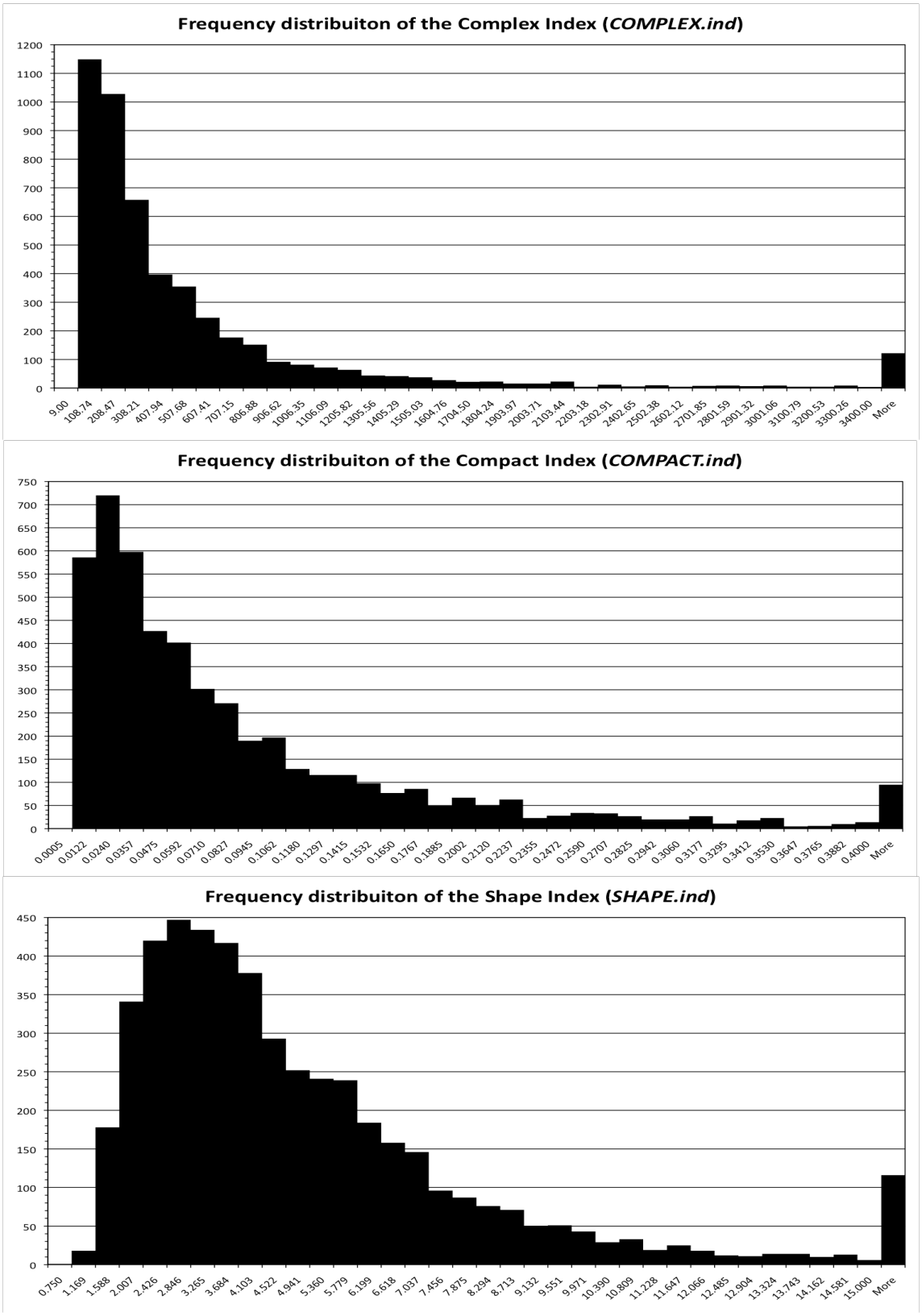

Figure 6-22: Frequency distribution of three attributes of geometry, shape, and dimensions that describe the oil slicks within the Campeche Bay Oil Slick Modified Database (CBOS-DScMod): Complex Index (*COMPLEX.ind*), Compact Index (*COMPACT.ind*), and Shape Index (*SHAPE.ind*), respectively shown on the upper, middle, and lower panels. See also Table 5-4 and Figure 6-27.

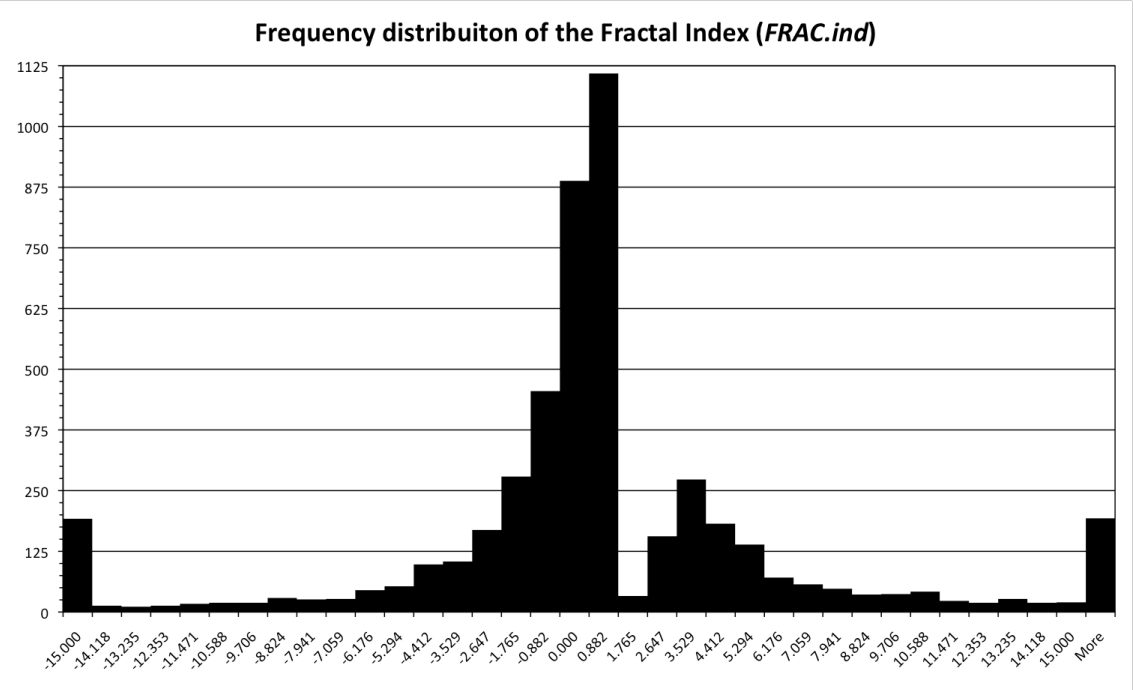

Figure 6-23: Frequency distribution of one attribute of geometry, shape, and dimensions that describes the oil slicks within the Campeche Bay Oil Slick Modified Database (CBOS-DScMod): Fractal Index (*FRAC.ind*). See also Table 5-4 and Figure 6-28.

6.5. PHASE 5: DATA TREATMENT

The information presented on this Section concludes the Workable-Database Preparation (shown as the Green Phases: 1 to 5 on Figure 1-3). Histograms have also been plotted after the application of the Negative Values Scaling and the Log_{10} Transformation. Such histograms illustrate the Log_{10} transformed frequency distributions of some attributes within the CBOS-DScMod: Figure 6-24 (Latitude (*cLAT*) and Longitude (*cLONG*)), Figure 6-25 (Area (*Area*) and Perimeter (*Per*)), Figure 6-26 (Area to Perimeter Ratio (*AtoP*), Perimeter to Area Ratio (*PtoA*), and Normalized Perimeter to Area Ratio (*PtoA.nor*)), and Figure 6-27 (Complex Index (*COMPLEX.ind*), Compact Index (*COMPACT.ind*), and Shape Index (*SHAPE.ind*)).

An exception is the Fractal Index (*FRAC.ind*), shown on Figure 6-28, which has a cubic root transformation applied to it. It is possible to notice that the skewness of most data transformed attributes is smaller in comparison to the frequency distributions shown on Figure 6-19, Figure 6-20, Figure 6-21, Figure 6-22, and Figure 6-23.

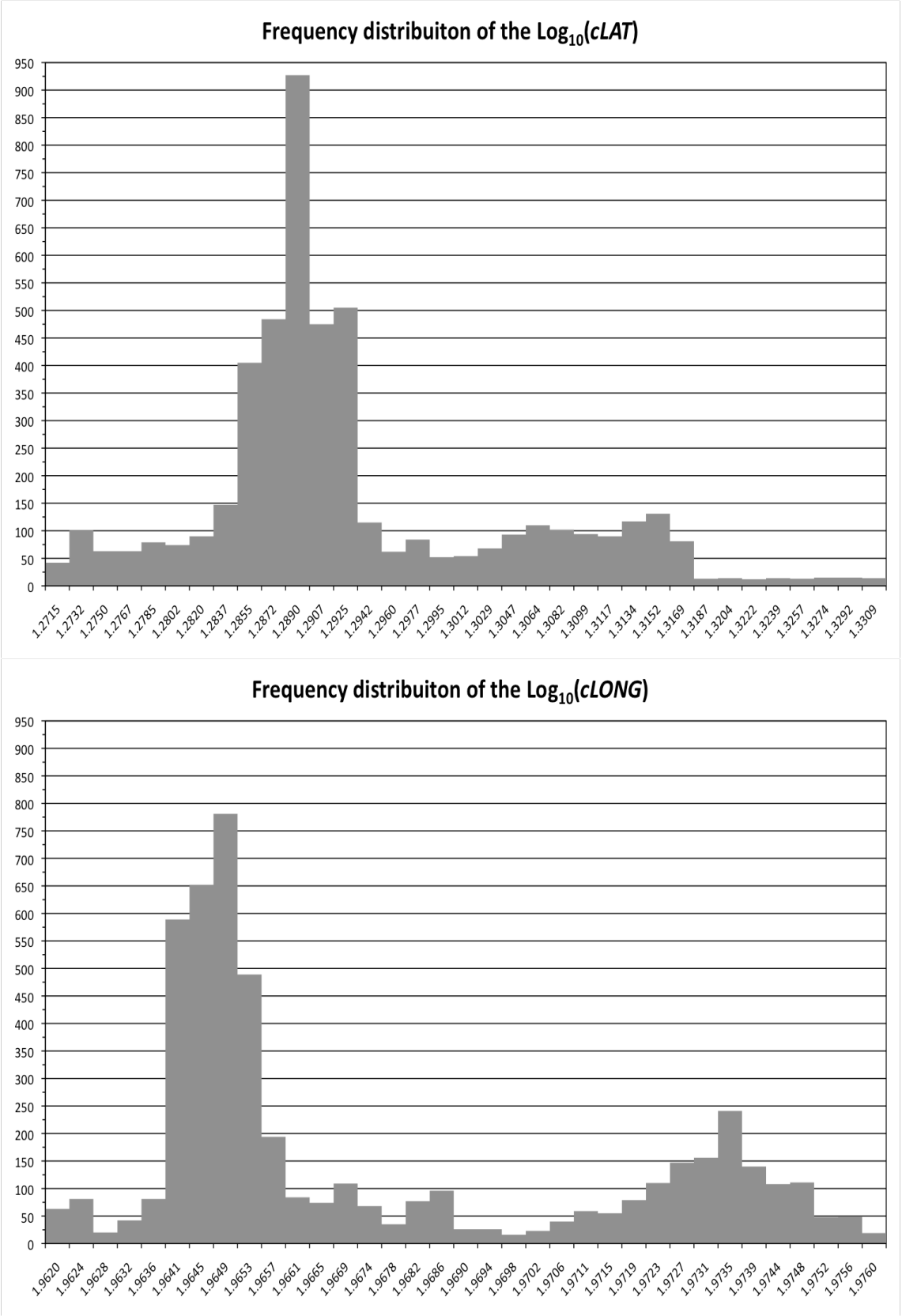

Figure 6-24: Histogram of frequency distribution of two contextual attributes that describe the oil slicks within the Campeche Bay Oil Slick Modified Database (CBOS-DScMod): Latitude (*cLAT*) and Longitude (*cLONG*) with logarithm transformation (Log_{10}), respectively, top and bottom panels. See also Table 5-4 and Figure 6-19.

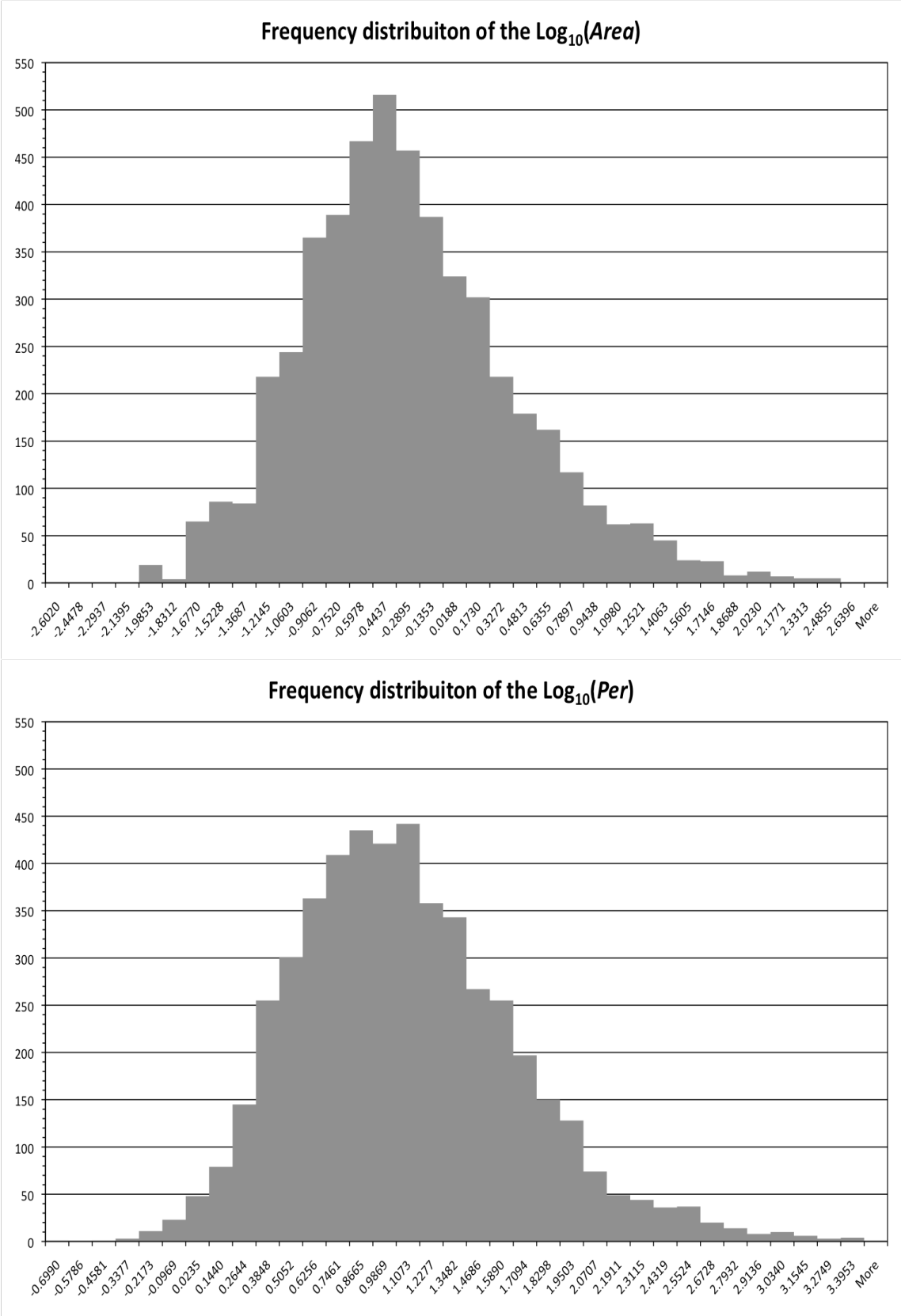

Figure 6-25: Histogram of frequency distribution of two contextual attributes that describe the oil slicks within the Campeche Bay Oil Slick Modified Database (CBOS-DScMod): Area (*Area*) and Perimeter (*Per*) with logarithm transformation (Log_{10}), respectively, top and bottom panels. See also Table 5-4 and Figure 6-20.

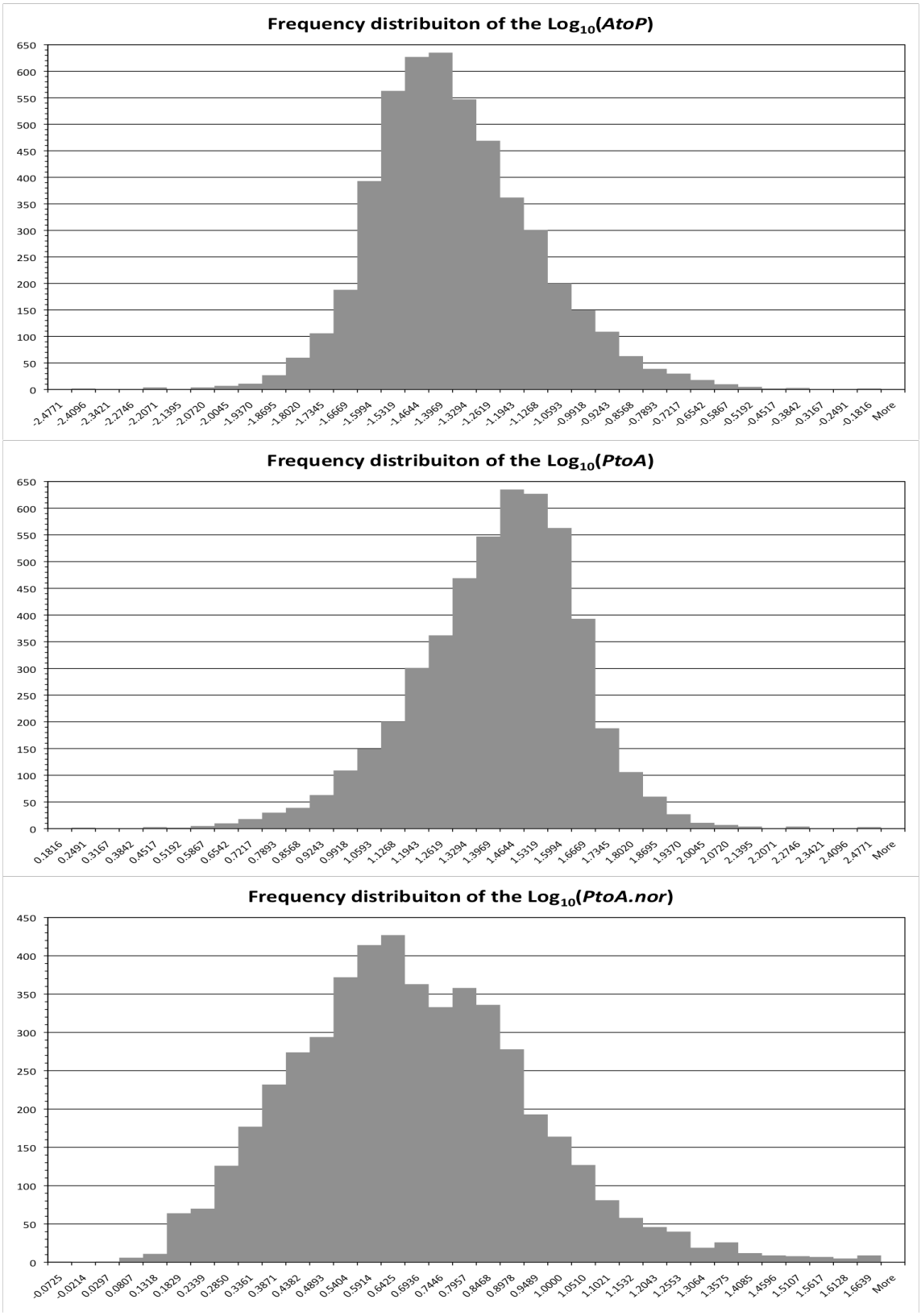

Figure 6-26: Histogram of frequency distribution of three attributes of geometry, shape, and dimensions that describe the oil slicks within the Campeche Bay Oil Slick Modified Database (CBOS-DScMod): Area to Perimeter Ratio (*AtoP*), Perimeter to Area Ratio (*PtoA*), and Normalized Perimeter to Area Ratio (*PtoA.nor*) with logarithm transformation (Log_{10}), respectively shown on the upper, middle, and lower panels. See also Table 5-4 and Figure 6-21.

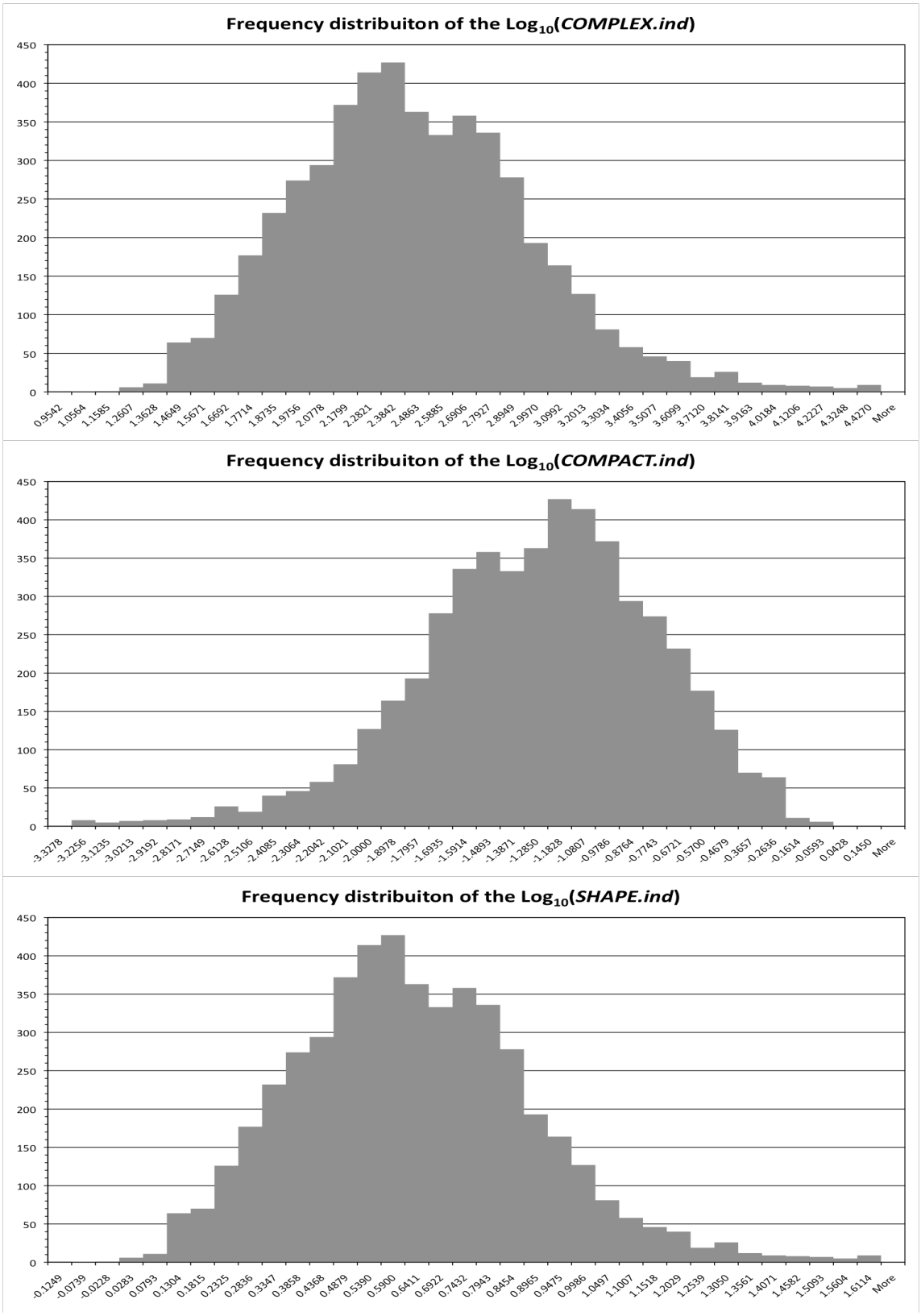

Figure 6-27: Histogram of frequency distribution of three attributes of geometry, shape, and dimensions that describe the oil slicks within the Campeche Bay Oil Slick Modified Database (CBOS-DScMod): Complex Index (*COMPLEX.ind*), Compact Index (*COMPACT.ind*), and Shape Index (*SHAPE.ind*) with logarithm transformation (Log_{10}), respectively shown on the upper, middle, and lower panels. See also Table 5-4 and Figure 6-22.

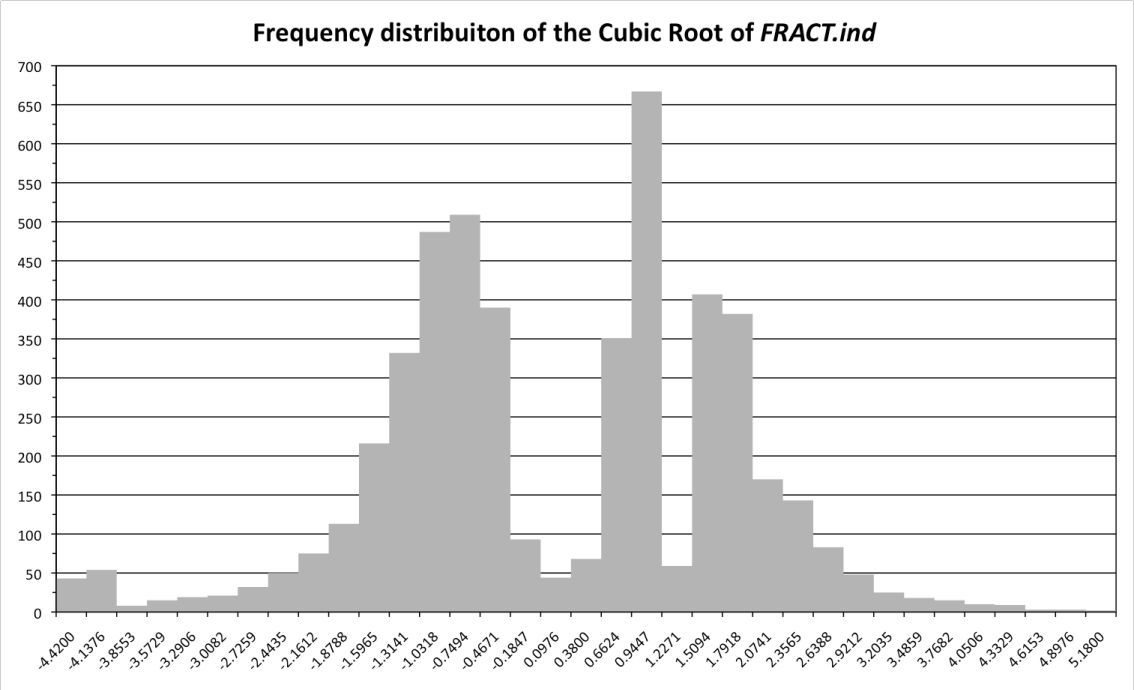

Figure 6-28: Histogram of frequency distribution of one attribute of geometry, shape, and dimensions that describes the oil slicks within the Campeche Bay Oil Slick Modified Database (CBOS-DScMod): Fractal Index (*FRAC.ind*) with a cubic root transformation applied to it. See also Table 5-4 and Figure 6-23.

There are three main consequences of applying the Negative Values Scaling Data Treatment to the pixel values inside individual oil slicks that contained any negative pixel value:

1. All pixels inside such oil slicks have been changed to have a positive value. This means that all attributes are now positive (the only exception is still the *FRAC.ind*), for instance, this includes those measurements given in dB: Table 6-14 (*SIG.dB.AVG*), Table 6-15 (*BET.dB.AVG*), Table 6-16 (*GAM.dB.AVG*), and Table 6-17 (*COV.STD/AVG*);

2. Such liner scaling action alters the values of all other basic statistical characteristics experimentally used herein as new attributes to describe the characteristics of individual oil slicks: central tendency (*AVG*, *MED*, *MOD*, and MDM), dispersion (*STD*, *COD*, *VAR*, *RNG*, *AAD*, and *MAD*), six combined *COV* sets, MIN and MAX (Table 5-5). Now, these measures are all calculated with the "translated" value of the pixels inside the oil slicks. Nevertheless, the pixel relationship within individual oil slicks is unaffected by translation scaling (SNEATH & SOKAL, 1973), and the use of *PIXpos* does not cause any disadvantageous influence to the purposes of this investigation; and

3. The *MIN* attribute of some radiometric-calibrated image products lost its meaning: the *PIXpos* of several oil slicks became 1, as *PIX*=*PIXmin* gives *PIXpos*=1. This happened for 9 products and their *MIN* attribute were removed. Consequently, the CBOS-DScMod is left with 502 variables (instead of 511).

The information (frequency) from the Dummy Variables presented in Table 5-10 to describe the oil slicks is summarized in Table 6-18. This table also presents their respective percentage of occurrence in the CBOS-DScMod.

Table 6-18: Dummy Variables frequency included in the Campeche Bay Oil Slick Modified Database (CBOS-DScMod) to replace the qualitative attributes. These are binary-coded to 1 or 0. See also Table 5-2, Table 5-3, and Table 5-10.

Dummy Variables (Equal to 1)			**n**	**%**
Latitude	Region-1	***RG1.LAT***	3,917	79.7
	Region-2	***RG2.LAT***	999	20.3
Longitude	Region-1	***RG1.LONG***	3,573	72.7
	Region-2	***RG2.LONG***	1,343	27.3
Day (1) or Night (0)		***DoN****	1,448	29.5
Winter	J/F/M	***WNT***	921	18.7
Spring	A/M/J	***SPG***	1,660	33.8
Summer	J/A/S	***SMM***	1,130	23.0
Fall	O/N/D	***FLL***	1,205	24.5
Analyzed Years		***2008***	678	13.8
		2009	755	15.4
		2010	821	16.7
		2011	1,335	27.1
		2012	1,327	27.0
ScanSAR Narrow 1		***SCNA***	2,661	54.1
ScanSAR Narrow 2		***SCNB***	1,899	38.6
Wide 1		***WDE1***	340	7.0
Wide 2		***WDE2***	16	0.3

* Oil slicks image at nighttime correspond to 70.5% (n=3,468): *DoN*=0 (Table 5-6).

6.6. PHASE 6: ATTRIBUTE SELECTION

Two methods were independently investigated to reduce the dimensionality within the attributes domain and to establish hierarchical relationships among the CBOS-DScMod variables within the thirty-three optimal subsets shown on Figure 5-3. The first method to be implemented was the UPGMA (Unweighted Pair Group Method with Arithmetic Mean), in which the attribute selection occurs with the analysis of rooted-tree dendrograms. Figure 6-29 illustrates the use of the two thresholds (i.e. cut-off levels shown as horizontal red lines across the dendrograms) on the complete exploration of the entire dataset (n=502): CCC (in this case: 0.8175) and fixed similarity of 0.5. These two lines are used to define the groups from which the attributes were selected.

When the CCC is utilized, 59 attributes of the CBOS-DScMod are selected to be explored in the subsequent data mining, whereas 46 variables are selected with the fixed similarity cut-off level. Table 6-19 presents the variables selected with both thresholds on the complete exploration.

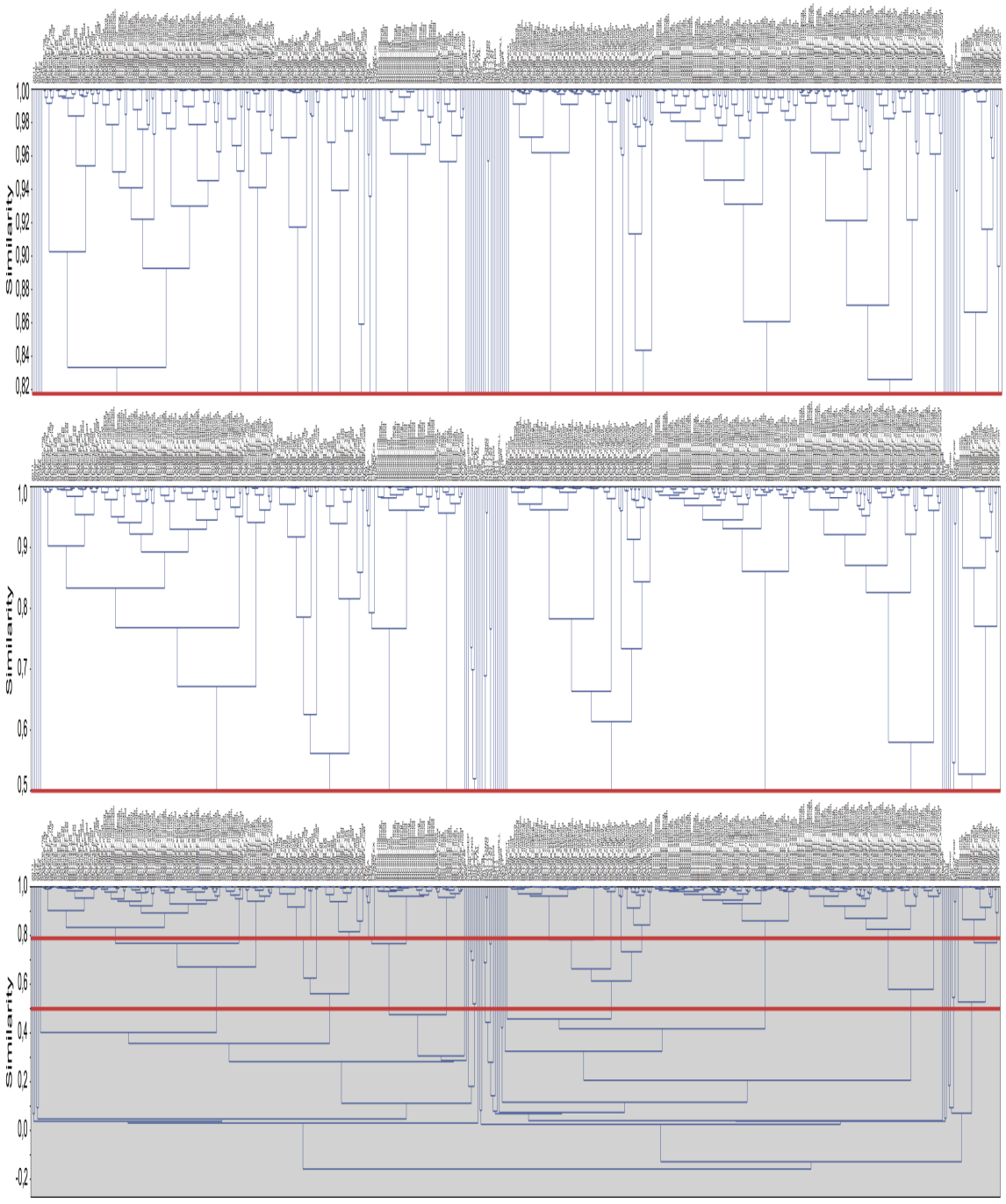

Figure 6-29: Rooted-tree dendrograms for the UPGMA implementation: **complete exploration of the Campeche Bay Oil Slick Modified Database (CBOS-DScMod: n=502)**. In the lower panel, the two horizontal red lines correspond to the Cophenetic Correlation Coefficient (CCC=0.8175) and similarity of 0.5, respectively (top and bottom lines). Same information plotted in the upper and middle panels: respectively for 0.8175 and 0.5.

Table 6-19: Attributes selected (n=59) based on the UPGMA implementation: **complete exploration of the Campeche Bay Oil Slick Modified Database (CBOS-DScMod: n=502)**. These are illustrated in the dendrograms shown on Figure 6-29. While these correspond to the Cophenetic Correlation Coefficient (0.8175), variables in bold (n=46) have been selected using the fixed similarity value of 0.5.

Attributes	n		UPGMA Selected Attributes
Category	**59**	**1**	***oSPILL***
	58	**2**	***oSEEP***
Class	**57**	**1**	***BGT***
	56	**2**	***BGT-1***
	55	**3**	***BGT-2***
	54	**4**	***BGT-3***
	53	**5**	***SHP***
	52	**6**	***orphSP***
	51	**7**	***CANT***
	50	**8**	***CLUS***
	49	**9**	***orphSE***
Latitude and Longitude	**48**	**1**	***RG1.LAT***
	47	**2**	***RG2.LAT***
	46	**3**	***PKD.LAT***
	45	**4**	***RG1.LONG***
	44	**5**	***RG2.LONG***
	43	**6**	***PKD.LONG***
Day or Night	**42**	**1**	***DoN***
Date	**41**	**1**	***DoY***
	40	**2**	***WNT***
	39	**3**	***SPG***
	38	**4**	***SMM***
	37	**5**	***FLL***
	36	**6**	***2008***
	35	**7**	***2009***
	34	**8**	***2011***
	33	**9**	***2010***
	32	**10**	***2012***
Beam Modes	**31**	**1**	***SCNA***
	30	**2**	***SCNB***
	29	**3**	***WDE1***
	28	**4**	***WDE2***
Incidence Angles	**27**	**1**	***INC.ang.AVG***
	26	**2**	***INC.ang.STD***

Continue in the next page.

Table 6-19: Continuation.

Geometry, Shape, and Dimension ¥	**25**	**1**	***LEN***
	24	**2**	***AtoP***
	23	**3**	***PtoA***
	22	**4**	***COMPACT.ind***
	21	5	*COMPLEX.ind*
	20	**6**	***FRAC.ind***
SAR Backscatter Signature ¥¥	**19**	**1**	***SIG.amp.AVG***
	18	**2**	***SIG.amp.STD***
	17	**3**	***SIG.amp.COD***
	16	4	*SIG.amp.FF.AVG*
	15	**5**	***SIG.amp.FF.COD***
	14	6	*SIG.amp.FF.COV.VAR/AVG*
	13	**7**	***SIG.dB.AVG***
	12	8	*SIG.dB.MOD*
	11	9	*SIG.dB.STD*
	10	**10**	***SIG.dB.COD***
	9	11	*SIG.dB.MAD*
	8	12	*SIG.dB.COV.STD/MOD*
	7	13	*SIG.dB.COV.VAR/AVG*
	6	14	*SIG.dB.COV.RNG/AVG*
	5	15	*SIG.dB.COV.RNG/MOD*
	4	**16**	***SIG.dB.FF.AVG***
	3	18	*SIG.dB.FF.MIN*
	2	18	*SIG.dB.FF.MAX*
	1	19	*SIG.dB.FF.COV.RNG/AVG*

¥ Same variables shown on Table 6-20.

¥¥ Same variables shown on Table 6-21.

However, because the complete exploration is performed with the full remote sensing library content of the CBOS-DScMod (n=502), the graphical representation shown on Figure 6-29 is not very instructive. A more intuitive example of the attribute selection using dendrograms is presented on Figure 6-30 (n=151) for the UPGMA implementation that analyzes sigma-naught attributes (σ^o; n=141) together with attributes of geometry, shape, and dimension (n=10). It is possible to observe that the threshold corresponding to the CCC (0.8262) gives 26 groups from which only one variable is selected per group. In the case of using the fixed similarity cut-off (0.5), 12 groups are formed; what leads to the selection of 12 variables.

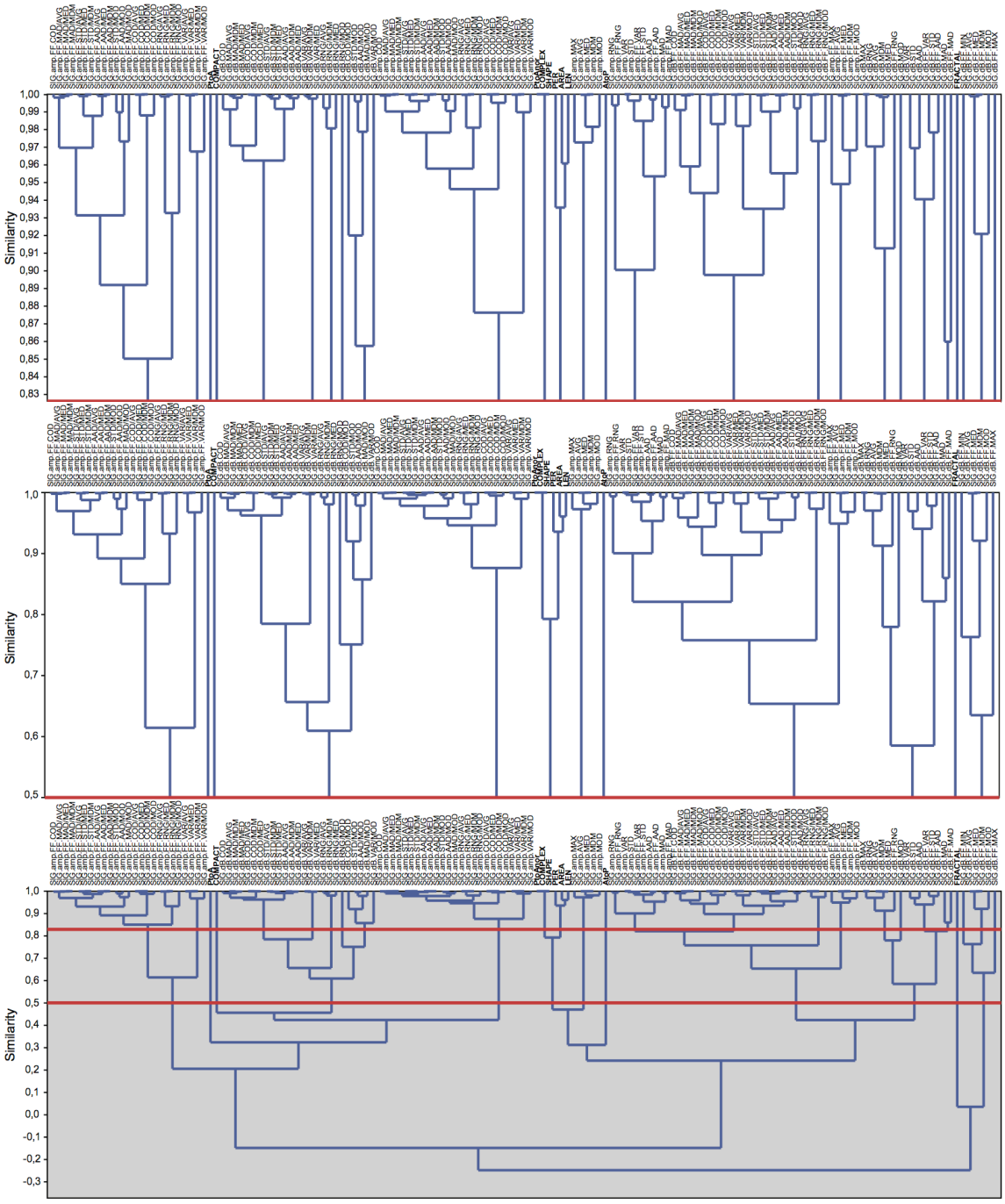

Figure 6-30: Rooted-tree dendrograms for the UPGMA implementation: **sigma-naught (σ^o; n=141) together with the geometry, shape, and dimension attributes (n=10)**. In the lower panel, the two horizontal red lines correspond to the Cophenetic Correlation Coefficient (CCC=0.8262) and similarity of 0.5, respectively (top and bottom lines). Same information plotted in the upper and middle panels: respectively for 0.8262 and 0.5.

Similarly, Figure 6-31 presents the dendrograms assessing the groups formed when exploring only sigma-naught attributes (σ^o; n=141). The variables selected are the same as those from the previous consideration depicted on Figure 6-30, however, not including the ones of geometry, shape, and dimension.

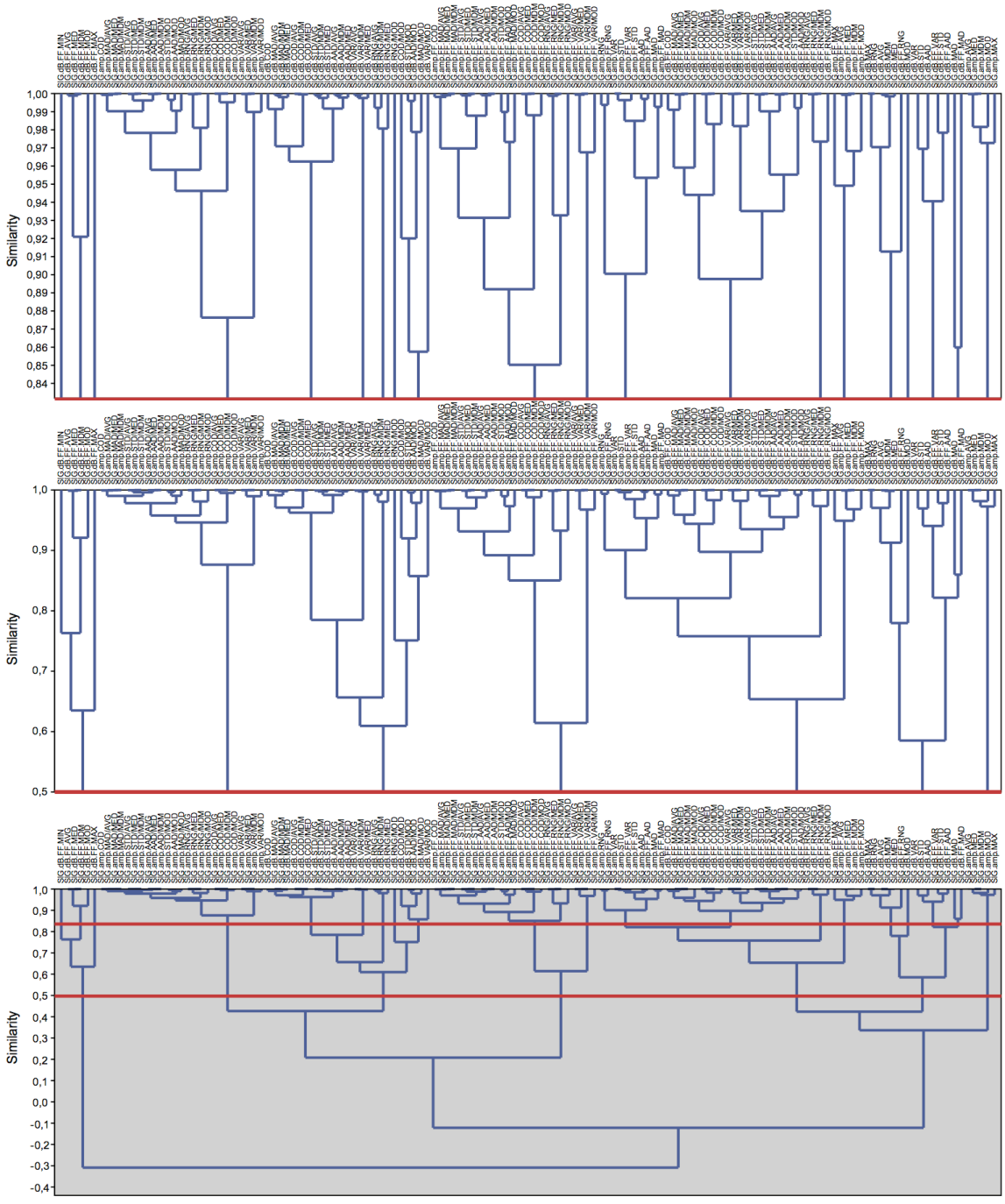

Figure 6-31: Rooted-tree dendrograms for the UPGMA implementation: **sigma-naught (σ^o) variables only (n=141)**. In the lower panel, the two horizontal red lines correspond to the Cophenetic Correlation Coefficient (CCC=0.8319) and similarity of 0.5, respectively (top and bottom lines). Same information plotted in the upper and middle panels: respectively for 0.8319 and 0.5.

Another comprehensible example of the attribute selection process using the UPGMA is depicted on Figure 6-32 exploring only variables of geometry, shape, and dimension (n=10). Of the initial 10 attributes, the CCC threshold (0.9143) forms six groups and the fixed similarity of 0.5 gives five groups: 6 and 5 variables, respectively (Table 6-20).

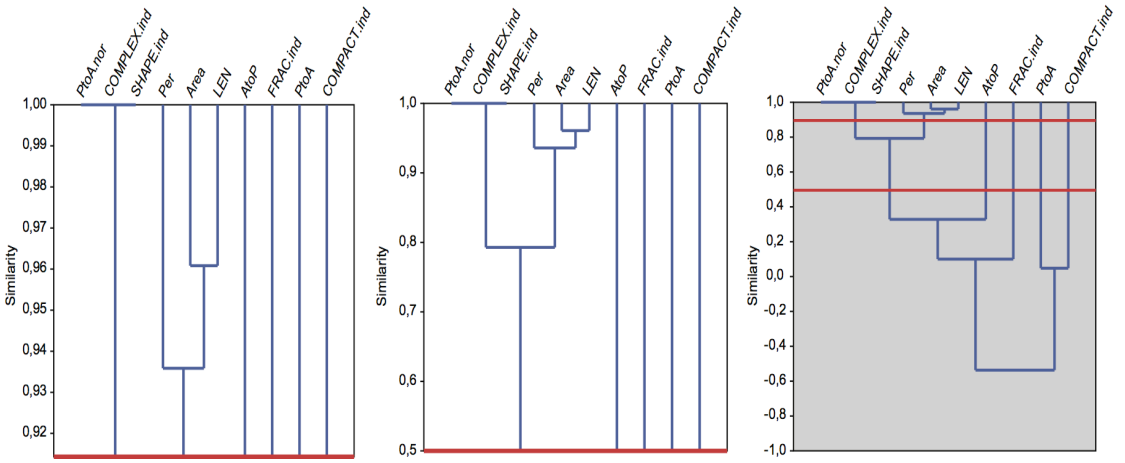

Figure 6-32: Rooted-tree dendrograms for the UPGMA implementation: **only attributes of geometry, shape, and dimension (n=10)**. In the right panel, the two horizontal red lines correspond to the Cophenetic Correlation Coefficient (CCC=0.9143) and similarity of 0.5, respectively (top and bottom lines). Same information plotted in the left and middle panels: respectively for 0.9143 and 0.5.

Table 6-20: Attributes selected (n=6) based on the UPGMA implementation: **only attributes of geometry, shape, and dimension (n=10)**. These are illustrated in the dendrograms shown on Figure 6-30 (CCC=0.8262) and Figure 6-32 (CCC=0.9143). Variables in bold (n=5) were selected using the fixed similarity value of 0.5.

UPGMA	Selected Attributes
1	***LEN***
2	***AtoP***
3	***PtoA***
4	***COMPACT***
5	*COMPLEX*
6	***FRACTAL***

The dendrograms resulting from the separate UPGMA implementation that analyzed the beta-naught (β^o) and gamma-naught (γ^o) variables, with (n=151) and without (n=141) the geometry, shape, and dimension attributes, are presented in Appendix 4. Even though the groups that have been formed are not exactly the same among the different UPGMA implementations, nor are the CCC values (e.g. 0.8175, 0.8262, 0.8319, and 0.9143), the same SAR backscatter signature variables of σ^o, β^o, and γ^o have been selected with or without the geometry, shape, and dimension attributes (Table 6-21). Likewise, the selection of the geometry, shape, and dimension attributes was also the same when these are analyzed together or separately from the SAR backscatter signature variables (Table 6-20).

The same behavior was observed between the complete exploration (n=502) and the two analyses of all SAR backscatter signatures (σ^o, β^o, and γ^o) with (n=433) and without (n=423) the geometry, shape, and dimension attributes (see dendrograms in Appendix 4): the same groups (and variables) were selected as in the separate investigation of the sigma-naught variables: left column of Table 6-21. This is explained because the variable selection strategy defined in Section 5.6 gives preferable representativeness to σ^o variables, and β^o and γ^o variables have been grouped together with the σ^o ones.

Table 6-21: Variables selected based on the UPGMA implementation: **separate analyses of sigma-naught (σ^o), beta-naught (β^o), and gamma-naught (γ^o) with and without the geometry, shape, and dimension attributes**. While these have been selected with the Cophenetic Correlation Coefficient (CCC), variables in bold were selected using the fixed similarity value of 0.5. These are illustrated on the dendrograms shown on Figure 6-30 and Figure 6-31, as well as those in Appendix 4.

UPGMA Selected Attributes		
CCC=0.8262 *	CCC=0.8031 *	CCC=0.8240 *
CCC=0.8319 **	CCC=0.8130 **	CCC=0.8260 **
Sigma-naught (σ^o) (n=20) ¥	Beta-naught (β^o) (n=19)	Gamma-naught (γ^o) (n=20)
SIG.amp.AVG	***BET.amp.AVG***	***GAM.amp.AVG***
SIG.amp.STD	***BET.amp.STD***	***GAM.amp.STD***
SIG.amp.COD	***BET.amp.COD***	***GAM.amp.COD***
SIG.amp.FF.AVG	*BET.amp.FF.AVG*	*GAM.amp.FF.AVG*
SIG.amp.FF.COD	***BET.amp.FF.COD***	***GAM.amp.FF.COD***
SIG.amp.FF.VAR/AVG	*BET.amp.FF.VAR/AVG*	*GAM.amp.FF.VAR/AVG*
	BET.amp.FF.RNG/AVG	
SIG.dB.AVG	***BET.dB.AVG***	***GAM.dB.AVG***
SIG.dB.MOD	*BET.dB.MOD*	*GAM.dB.MOD*
SIG.dB.STD	*BET.dB.STD*	*GAM.dB.STD*
SIG.dB.COD	***BET.dB.COD***	***GAM.dB.COD***
SIG.dB.MAD	*BET.dB.MAD*	*GAM.dB.MAD*
SIG.dB.STD/MOD	*BET.dB.STD/MOD*	*GAM.dB.STD/MOD*
SIG.dB.VAR/AVG	*BET.dB.VAR/AVG*	*GAM.dB.VAR/AVG*
SIG.dB.RNG/AVG	*BET.dB.RNG/AVG*	*GAM.dB.RNG/AVG*
SIG.dB.RNG/MOD	*BET.dB.RNG/MOD*	*GAM.dB.RNG/MOD*
SIG.dB.FF.AVG	***BET.dB.FF.AVG***	***GAM.dB.FF.AVG***
SIG.dB.FF.COD §		*GAM.dB.FF.COD*
SIG.dB.FF.MIN		*GAM.dB.FF.MIN*
SIG.dB.FF.MAX	*BET.dB.FF.MAX*	*GAM.dB.FF.MAX*
	BET.dB.FF.VAR/AVG	
SIG.dB.FF.RNG/AVG		*GAM.dB.FF.RNG/AVG*

* With geometry, shape, and dimension variables.
** Without geometry, shape, and dimension variables.
¥ Also selected in the complete exploration (Table 6-19).
§ Only attribute not selected in the complete exploration (Table 6-19).

Figure 6-33 presents the dendrograms of the assessment investigating DN values (n=35). The CCC (0.8020) and the fixed similarity (0.5) thresholds produced 5 and 3 groups (variables), respectively (Table 6-22).

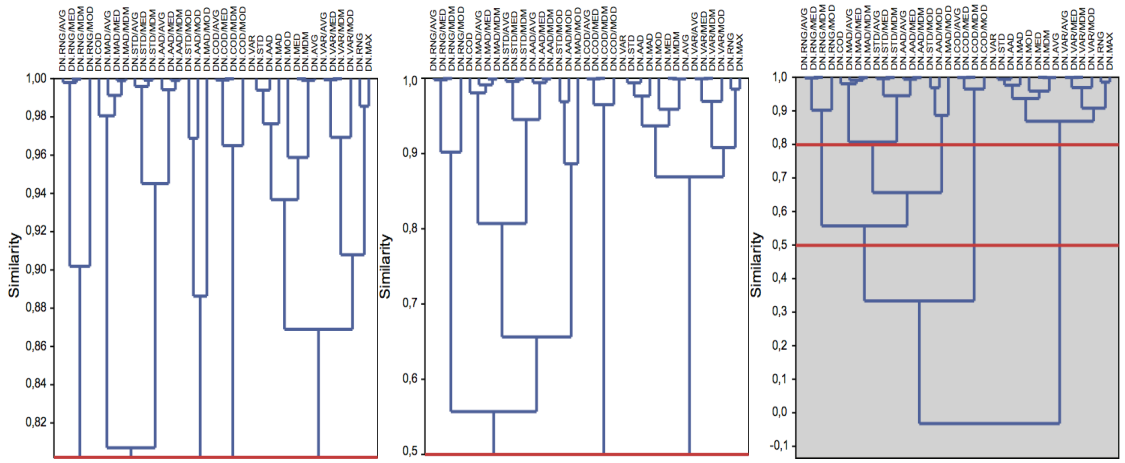

Figure 6-33: Rooted-tree dendrograms based on the UPGMA implementation: **only Digital Number (DN) variables (n=35)**. In the right panel, the two horizontal red lines correspond to the Cophenetic Correlation Coefficient (CCC=0.8020) and similarity of 0.5, respectively (top and bottom lines). Same information plotted in the left and middle panels: respectively for 0.8020 and 0.5.

Table 6-22: Attributes selected (n=5) based on the UPGMA implementation: **only Digital Number (DN) variables (n=35)**. These are illustrated in the dendrograms shown on Figure 6-33 (CCC=0.8020). Variables in bold (n=3) were selected using the fixed similarity value of 0.5.

UPGMA	Selected Attributes
1	***DN.AVG***
2	***DN.COD***
3	*DN.STD/MOD*
4	***DN.COD/AVG***
5	*DN.RNG/AVG*

The CFS (Correlation-Based Feature Selection) was the second method to investigate the dimensionality reduction (attribute-wise) among the thirty-three optimal subsets proposed to analyze the content of the CBOS-DScMod (Figure 5-3). The major difference between the UPGMA and CFS outcomes interpretation is that the CFS does not plots dendrograms. Instead, the CFS attribute selection directly provides a list with the hierarchical relationships among variables. A series of tables are presented below with the results of the several CFS implementations. An interesting aspect depicted on the CFS-tables is that some variables are shown in bold. These correspond to the same ones selected with the UPGMA implementation using the CCC threshold.

The first CFS-table (Table 6-23) presents the results of the complete exploration of all CBOS-DScMod variables (n=502) that selected only 15 attributes, of which almost all (13) are categorical contextual Dummy Variables. However, most of them (e.g. *Category* and *Class* attributes) contain the sought answer of this research embedded on them: information of which oil slick polygon is an oil spill or an oil seep. Even though these variables are not directly used to design the proposed classification algorithm, they are extremely useful to assess the effectiveness of the algorithm.

Table 6-23: Variables selected (n=15) based on the CFS implementation of the **complete exploration of the Campeche Bay Oil Slick Modified Database (CBOS-DScMod: n=502)**. Categorical contextual Dummy Variables are shown in bold (n=13).

Subsets Evaluated: 126,256 Merit: 1.0	
CFS	Selected Attributes
1	***oSPILL***
2	***BGT***
3	***BGT1***
4	***BGT2***
5	***BGT3***
6	***SHP***
7	***orphSP***
8	***oSEEP***
9	***CANT***
10	***orphSE***
11	***RG1.LAT***
12	***RG1.LONG***
13	***Month***
14	*PER*
15	*BET.dB.FF.MIN*

Table 6-24 presents the results (n=3) of CFS implementation that separately analyzed the geometry, shape, and dimension attributes. Table 6-25 and Table 6-26 present, respectively, the attributes selected with the CFS implementation of all SAR backscatter signature (σ^o, β^o, or γ^o) variables analyzed with (n=20) and without (n=36) the attributes of geometry, shape, and dimension. The results of the CFS attribute selection that separately explored each of the three SAR backscatter coefficients with (Table 6-27) and without (Table 6-28) the attributes of geometry, shape, and dimension are also shown below. Table 6-29 presents the DN attributes (n=11) selected with the CFS implementation.

Table 6-24: **Geometry, shape, and dimension variables (n=3)** selected based on the CFS implementation. These also have been selected in the analysis together with the each SAR backscatter coefficients (Table 6-25) and the one in bold was also selected with the UPGMA implementation (Table 6-20).

Subsets Evaluated: 80 Merit: 0.112	
CFS	Selected Attributes
1	***LEN***
2	*PER*
3	*SHAPE*

Table 6-25: Variables selected (n=20) based on the CFS implementation of **all SAR backscatter signature variables (n=423: σ^o, β^o, and γ^o) analyzed together with the attributes of geometry, shape, and dimension (n=10)**. Variables in bold (n=10) are the same as those selected with the UPGMA using the CCC thresholds: Table 6-20 and Table 6-21.

Subsets Evaluated: 93,846 Merit: 0.131	
CFS	Selected Attributes
1	***LEN***
2	*AREA*
3	*PER*
4	***PtoA***
5	***COMPLEX***
6	***COMPACT***
7	*SHAPE*
8	***FRACTAL***
9	***SIG.amp.COD***
10	*SIG.amp.RNG/MDM*
11	***SIG.dB.COD***
12	***SIG.dB.MAD***
13	*SIG.dB.RNG/MED*
14	***SIG.dB.RNG/MOD***
15	*BET.amp.RNG*
16	*BET.amp.MAX*
17	***BET.dB.VAR/AVG***
18	*BET.dB.FF.MAD/AVG*
19	*GAM.dB.FF.RNG*
20	*GAM.dB.FF.MAD*

Table 6-26: Variables selected (n=36) based on the CFS implementation of **all SAR backscatter signature variables only (n=423: σ^o, β^o, and γ^o)**. Variables in bold (n=8) are the same as those selected with the UPGMA using the CCC thresholds for the separate investigation of each SAR backscatter coefficient (Table 6-21).

Subsets Evaluated: 89,185 Merit: 0.103	
CFS	Selected Attributes
1	*SIG.amp.MOD*
2	***SIG.amp.COD***
3	*SIG.amp.MAX*
4	*SIG.amp.RNG/AVG*
5	*SIG.amp.RNG/MDM*
6	*SIG.ampFF.RNG/AVG*
7	*SIG.ampFF.RNG/MOD*
8	***SIG.dB.COD***
9	*SIG.dB.MAD*
10	*SIG.dB.STD/AVG*
11	*SIG.dB.VAR/MOD*
12	*SIG.dB.RNG/MED*
13	***SIG.dB.RNG/MOD***
14	*SIG.dB.FF.RNG*
15	*BET.amp.RNG*
16	*BET.amp.MAX*
17	*BET.amp.FF.RNG*
18	*BET.dB.MED*
19	*BET.dB.STD/AVG*
20	*BET.dB.STD/MED*
21	***BET.dB.VAR/AVG***
22	*BET.dB.VAR/MOD*
23	*BET.dB.FF.MAD*
24	*BET.dB.FF.COD/AVG*
25	*BET.dB.FF.RNG/MOD*
26	*BET.dB.FF.MAD/AVG*
27	*GAM.amp.MOD*
28	*GAM.amp.FF.RNG/AVG*
29	***GAM.dB.STD***
30	***GAM.dB.COD***
31	***GAM.dB.MAD***
32	*GAM.dB.VAR/MED*
33	***GAM.dB.RNG/MOD***
34	*GAM.dB.FF.RNG*
35	*GAM.dB.FF.MAD*
36	*GAM.dB.FF.COD/AVG*

Table 6-27: Attributes selected based on the CFS implementation of the analysis of **each SAR backscatter coefficient (n=141) analyzed together with the attributes of geometry, shape, and dimension (n=10)**. Asterisks (*) indicate variables that have been selected when these subsets were analyzed separately: Table 6-24 and Table 6-28. Variables in bold are the same as those selected with the UPGMA using the CCC thresholds: Table 6-20 and Table 6-21.

CFS Selected Attributes		
Subsets Evaluated: 11,251 Merit: 0.127	Subsets Evaluated: 11,446 Merit: 0.129	Subsets Evaluated: 11,381 Merit: 0.126
Sigma-naught (σ^o) (n=26)	Beta-naught (β^o) (n=15)	Gamma-naught (γ^o) (n=19)
LEN*	***LEN****	***LEN****
AREA	*AREA*	*AREA*
*PER**	*PER**	*PER**
PtoA		***PtoA***
PtoAnor		
COMPACT	***COMPACT***	***COMPACT***
COMPLEX		***COMPLEX***
*SHAPE**	*SHAPE**	*SHAPE**
FRACTAL	***FRACTAL***	***FRACTAL***
*SIG.amp.MOD**		
SIG.amp.COD*	***BET.amp.COD****	***GAM.amp.COD****
*SIG.amp.RNG**	*BET.amp.RNG**	*GAM.amp.RNG**
	*BET.amp.MAX**	
		*GAM.amp.RNG/MED**
*SIG.amp.RNG/MDM**		
*SIG.amp.FF.RNG**		
*SIG.amp.FF.RNG/AVG**		
	*BET.dB.MED**	
SIG.dB.STD*	***BET.dB.STD****	
SIG.dB.COD*		***GAM.dB.COD****
SIG.dB.MAD*		***GAM.dB.MAD****
*SIG.dB.STD/AVG**		
	BET.dB.VAR/AVG*	***GAM.dB.VAR/AVG****
*SIG.dB.VAR/MED**		
*SIG.dB.VAR/MOD**		
*SIG.dB.RNG/MED**		*GAM.dB.RNG/MED**
SIG.dB.RNG/MOD*	***BET.dB.RNG/MOD****	***GAM.dB.RNG/MOD****
*SIG.dB.FF.RNG**		*GAM.dB.FF.RNG**
*SIG.dB.FF.MAD**	*BET.dB.FF.MAD**	*GAM.dB.FF.MAD**
		*GAM.dB.FF.COD/AVG**
SIG.dB.FF.COD/MED		
	*BET.dB.FF.MAD/AVG**	

Table 6-28: Attributes selected based on the CFS implementation of the **separately for each SAR backscatter coefficients (n=141)**. While the asterisks (*) indicate variables that also have been selected when the SAR attributes were analyzed together with the attributes of geometry, shape, and dimension (CFS: Table 6-27), the ones in bold are the same as those selected with the UPGMA using the CCC thresholds: Table 6-21.

CFS Selected Attributes		
Subsets Evaluated: 9,805 Merit: 0.099	Subsets Evaluated: 9,881 Merit: 0.099	Subsets Evaluated: 9,861 Merit: 0.097
Sigma-naught (σ^o) (n=24)	Beta-naught (β^o) (n=21)	Gamma-naught (γ^o) (n=22)
*SIG.amp.MOD **		*GAM.amp.MOD*
SIG.amp.COD *	***BET.amp.COD ****	***GAM.amp.COD ****
*SIG.amp.RNG **	*BET.amp.RNG **	*GAM.amp.RNG **
SIG.amp.MAX	*BET.amp.MAX **	
		GAM.amp.STD/MOD
SIG.amp.STD/MDM		
		*GAM.amp.RNG/MED **
	BET.amp.RNG/MOD	
*SIG.amp.RNG/MDM **		
	BET.amp.MAD/AVG	
*SIG.amp.FF.RNG **	*BET.amp.FF.RNG*	
*SIG.amp.FF.RNG/AVG **	***BET.amp.FF.RNG/AVG***	*GAM.amp.FF.RNG/AVG*
		GAM.amp.FF.RNG/MDM
SIG.amp.FF.RNG/MOD		
SIG.dB.MED	*BET.dB.MED **	*GAM.dB.MED*
SIG.dB.STD *	***BET.dB.STD ****	***GAM.dB.STD***
SIG.dB.COD *	***BET.dB.COD***	***GAM.dB.COD ****
SIG.dB.MAD *	***BET.dB.MAD***	***GAM.dB.MAD ****
*SIG.dB.STD/AVG **	*BET.dB.STD/AVG*	*GAM.dB.STD/AVG*
SIG.dB.STD/MED	*BET.dB.STD/MED*	*GAM.dB.STD/MED*
SIG.dB.VAR/AVG	***BET.dB.VAR/AVG ****	***GAM.dB.VAR/AVG ****
*SIG.dB.VAR/MED **	*BET.dB.VAR/MED*	*GAM.dB.VAR/MED*
*SIG.dB.VAR/MOD **	*BET.dB.VAR/MOD*	*GAM.dB.VAR/MOD*
*SIG.dB.RNG/MED **		*GAM.dB.RNG/MED **
SIG.dB.RNG/MOD *	***BET.dB.RNG/MOD ****	***GAM.dB.RNG/MOD ****
*SIG.dB.FF.RNG **	*BET.dB.FF.RNG*	*GAM.dB.FF.RNG **
*SIG.dB.FF.MAD **	*BET.dB.FF.MAD **	*GAM.dB.FF.MAD **
		*GAM.dB.FF.COD/AVG **
SIG.dB.FF.RNG/MOD	*BET.dB.FF.RNG/MOD*	*GAM.dB.FF.RNG/MOD*
	*BET.dB.FF.MAD/AVG **	
SIG.dB.FF.MAD/MOD		

Table 6-29: Variables selected (n=11) selected based on the CFS implementation of **only Digital Numbers (DN's) variables (n=35)**. Variables in bold are the same as those selected with the UPGMA implementation (Table 6-22).

Subsets Evaluated: 616 Merit: 0.059	
CFS	Selected Attributes
1	***DN.AVG***
2	*DN.MDM*
3	*DN.STD*
4	***DN.COD***
5	*DN.RNG*
6	*DN.COD/MOD*
7	***DN.RNG/AVG***
8	*DN.RNG/MED*
9	*DN.RNG/MOD*
10	*DN.RNG/MDM*
11	*DN.MAD/MED*

Two tables are provided to summarize the Attribute Selection practice introduced on Section 5.8. While Table 6-30 presents the values of CCC (UPGMA) and Merit (CFS), Table 6-31 reviews the number of variables per optimal subsets within the proposed original sets shown on Figure 5-3.

Table 6-30: Summary of the CFS-Merit and of the CCC values resulted from the UPGMA implementation (Figure 5-3).

CCC and CFS-Merit per data sub-divisions	UPGMA (CCC)	CFS (Merit)
Complete Exploration of the CBOS-DScMod	0.8175	1.000
All SAR Backscatter Signature ¥ with Size*	0.8227	0.131
Only all SAR Backscatter Signature ¥	0.8253	0.103
Size* and Sigma-naught (σ^o)	0.8262	0.127
Size* and Beta-naught (β^o)	0.8031	0.129
Size* and Gamma-naught (γ^o)	0.8240	0.126
Only Size*	0.9143	0.112
Only Sigma-naught (σ^o)	0.8319	0.099
Only Beta-naught (β^o)	0.8130	0.099
Only Gamma-naught (γ^o)	0.8260	0.097
Only Digital Numbers (DN's)	0.8020	0.059

* Attributes of geometry, shape, and dimension.

¥ See Table 5-1 and Table 5-5.

Table 6-31: Number of variables per data sub-division, as proposed on Figure 5-3. While the UPGMA uses two user-defined thresholds (CCC and a fixed similarity value), the CFS automatically provides the selected variables. See also Table 6-33 for the number of selected Principal Components (PC's).

Number of variables per data sub-divisions	**Original Sets**	**UPGMA**		**CFS**
		(CCC)	**(0.5)**	
Complete Exploration of the CBOS-DScMod	502	59	46	15 §
All SAR Backscatter Signature ¥ with Size*	433	†	†	20
Only all SAR Backscatter Signature ¥	423	††	††	36
Size* and Sigma-naught (σ^o)	151	26	12	26
Size* and Beta-naught (β^o)	151	25	12	15
Size* and Gamma-naught (γ^o)	151	26	12	19
Only Size*	10	6	5	3
Only Sigma-naught (σ^o)	141	20	7	24
Only Beta-naught (β^o)	141	19	7	21
Only Gamma-naught (γ^o)	141	20	7	22
Only Digital Numbers (DN's)	35	5	3	11

§ Of which 13 are categorical contextual Dummy Variables (Table 6-23).

* Attributes of geometry, shape, and dimension.

¥ See: Table 5-1 and Table 5-5.

σ^o *SIG.amp*, *SIG.amp.FF*, *SIG.dB*, and *SIG.dB.FF*.

β^o *BET.amp*, *BET.amp.FF*, *BET.dB*, and *BET.dB.FF*.

γ^o *GAM.amp*, *GAM.amp.FF*, *GAM.dB*, and *GAM.dB.FF*.

† Same as Size* and Sigma-naught (σ^o).

†† Same as only Sigma-naught (σ^o).

Although the variable selection strategy of the UPGMA-CCC and CFS are very different in essence (Section 5.6), their number of selected variables is not very different (Table 6-31). It is true that the actual selected variables are not exactly the same, but this is not a surprise as the UPGMA-CCC has an arbitrary user-defined variable selection strategy and the CFS is a fully automated process. Variables in bold on Tables 6-23 to 6-29 correspond to the same variables selected by both methods.

From Table 6-30, it is possible to notice the similarity amongst all CCC values. A higher CCC value is observed on the UPGMA implementation that considers only the attributes of geometry, shape, and dimension: 0.9143. The CCC variations on the separate investigations of σ^o, β^o, and γ^o (with and without the geometry, shape, and dimension attributes) is one of the reasons explaining the slight variation in their number of selected variables (Tables 6-21 and 6-31).

The CFS-Merit reveals important information about the predictability of each data sub-division in the process of telling apart spills from seeps (Table 6-30). The CFS implementation using the full remote sensing library of the CBOS-DScMod (i.e. complete exploration: n=502) mostly selected categorical contextual Dummy Variables (Table 6-23) and its merit is the highest as possible: 1.00. The considerable CFS-Merit drop (0.131) when these variables are removed (i.e. all SAR backscatter signature with size variables – Figure 5-3: n=433) depicts the complexity of the problem: the sole use of radiometric and size variables to distinguish spills and seeps is indeed difficult.

Another interesting aspect revealed by the CFS-Merit is observed when the geometry, shape, and dimension variables are involved, as compared to when they are not considered (Table 6-30): all SAR backscatter signature with size (0.131) and without size (0.103). The same pattern is also observed on the separate analysis of each SAR backscatter signature (i.e. σ^o, β^o, or γ^o), e.g. size with σ^o (0.127) versus only σ^o (0.099).

When using only the geometry, shape, and dimension variables, the CFS-Merit (0.112) is higher than when only exploring the SAR backscatter signature (i.e. σ^o, β^o, or γ^o) separately: 0.099, 0.099, and 0.097, respectively (Table 6-30). This is a strong indication that the use of the radiometric variables to differentiate spills from seeps is intricate. It also suggests that the use of the geometry, shape, and dimension attributes has a somewhat better chance in differentiating spills from seeps.

The CFS-Merit resulted from the analysis of DN's showed the worse value: 0.059 (Table 6-30). This agrees with the literature that does not recommend the use of DN values to cross-compare time series of SAR images (FREEMAN, 1992; THOMPSON & MCLEOD, 2004; EL-DARYMLI *et al.*, 2014).

6.7. PHASE 7: PRINCIPAL COMPONENTS ANALYSIS (PCA)

Table 6-32 presents the findings of the thirty-nine (n=39) PCA's completed herein. The variables (Tables 6-19 to 6-29), as well as the number of variables (Table 6-31), used as input on each PCA varied amongst the data sub-divisions proposed on Figure 5-3: original sets and optimal subsets of selected variables (UPGMA-CCC, UPGMA-Fixed, and CFS). The PCA was not applied to some optinal subsets (n=5): the first one was the CFS complete exploration that mostly selected categorical contextual Dummy Variables (Table 6-23), and the other four are the UPGMA implementations considering all SAR backscatter signature variables because it selected the same variables from the UPGMA using only sigma-naught variables.

Table 6-32: Results of the thirty-nine (n=39) Principal Components Analysis (PCA) performed herein. The selected Principal Components (PC's) axes are shown in bold per data sub-division (Figure 5-3). The percentage of variance concentrated on the first two PC's is shown along with the ones from the "Scree Plot" and "Kaiser Criterion" analyses. See also Table 6-31 for the number of variables and Table 6-33 for a summary of selected PC's.

Principal Components (PC's)		**Original Sets**	**UPGMA (CCC)**	**UPGMA (0.5)**	**CFS**
Complete Exploration of the CBOS-DScMod	2 PC's	PC 2: 59.1	PC 2: 28.7	PC 2: 27.4	
	Scree	**PC 10: 92.3**	PC 3: 38.0	PC 3: 35.6	
	Kaiser	PC 29: 97.8	**PC 21: 85.6**	**PC 18: 82.4**	
All SAR Backscatter Signature with the attributes of Geometry, Shape, and Dimension	2 PC's	PC 2: 64.5			PC 2: 56.5
	Scree	**PC 8: 96.8**			PC 2: 56.5
	Kaiser	PC 11: 98.1			**PC 6: 86.8**
Only all SAR Backscatter Signature (see Table 5-1 and Table 5-5)	2 PC's	PC 2: 65.5			PC 2: 58.8
	Scree	**PC 7: 96.9**			**PC 6: 93.1**
	Kaiser	PC 10: 98.5			**PC 6: 93.1**
Attributes of Geometry, Shape, and Dimension and Sigma-naught (σ^o)	2 PC's	PC 2: 63.1	PC 2: 54.0	PC 2: 57.9	PC 2: 54.9
	Scree	**PC 6: 92.1**	PC 2: 54.0	PC 1: 40.3	PC 3: 65.5
	Kaiser	PC 9: 97.4	**PC 7: 88.2**	**PC 3: 70.7**	**PC 7: 88.9**
Attributes of Geometry, Shape, and Dimension and Beta-naught (β^o)	2 PC's	PC 2: 63.9	PC 2: 50.7	PC 2: 57.6	PC 2: 61.0
	Scree	**PC 6: 91.9**	PC 5: 78.0	PC 2: 57.6	PC 2: 61.0
	Kaiser	PC 9: 97.1	**PC 7: 88.4**	**PC 3: 70.6**	**PC 5: 85.5**
Attributes of Geometry, Shape, and Dimension and Gamma-naught (γ^o)	2 PC's	PC 2: 63.0	PC 2: 54.1	PC 2: 57.9	PC 2: 56.5
	Scree	**PC 6: 91.9**	PC 2: 54.1	PC 1: 40.4	PC 2: 56.5
	Kaiser	PC 9: 97.3	**PC 7: 88.2**	**PC 3: 70.7**	**PC 5: 82.0**
Only attributes of Geometry, Shape, and Dimension	2 PC's	**PC 2: 89.6**	**PC 2: 82.9**	**PC 2: 79.7**	**PC 2: 99.4***
	Scree	**PC 2: 89.6**	**PC 2: 82.9**	PC 1: 57.4	No PC
	Kaiser	**PC 2: 89.6**	**PC 2: 82.9**	**PC 2: 79.7**	PC 1: 90.0
Only Sigma-naught (σ^o)	2 PC's	PC 2: 65.4	PC 2: 61.6	**PC 2: 74.8**	PC 2: 60.6
	Scree	**PC 5: 92.9**	PC 3: 73.0	**PC 2: 74.8**	**PC 4: 81.6**
	Kaiser	PC 8: 98.2	**PC 5: 88.5**	**PC 2: 74.8**	PC 6: 93.7
Only Beta-naught (β^o)	2 PC's	PC 2: 66.4	PC 2: 58.2	**PC 2: 74.7**	PC 2: 63.7
	Scree	**PC 5: 92.7**	**PC 4: 81.0**	**PC 2: 74.7**	PC 3: 76.5
	Kaiser	PC 8: 98.0	PC 5: 88.8	**PC 2: 74.7**	**PC 5: 90.5**
Only Gamma-naught (γ^o)	2 PC's	PC 2: 65.3	PC 2: 61.7	**PC 2: 74.8**	PC 2: 60.6
	Scree	**PC 6: 95.2**	PC 3: 73.0	**PC 2: 74.8**	**PC 4: 81.6**
	Kaiser	PC 8: 98.2	**PC 5: 88.5**	**PC 2: 74.8**	PC 6: 93.3
Only Digital Numbers (DN's)	2 PC's	**PC 2: 85.8**	**PC 2: 81.9**	**PC 2: 99.9**	**PC 2: 84.8**
	Scree	**PC 2: 85.8**	**PC 2: 81.9**	**PC 2: 99.9**	**PC 2: 84.8**
	Kaiser	PC 4: 97.7	**PC 2: 81.9**	PC 1: 69.5	PC 3: 97.8

* Because the Discriminant Function (Phase 8) requires at least 2 variables.

Table 6-32 gives a global picture of the percentages of variance concentrated on particular Principal Components (PC's) axes among all data sub-divisions (Figure 5-3). As each PC axis concentrates part of the variance within the dataset, and it is aimed to have more variance on fewer PC's, the variance concentrated on the first two PC's are shown as reference levels (LEGENDRE & LEGENDRE, 2012). The PC's selected using the "Scree Plot" (broken stick and row-wise bootstrapping eigenvalue error bars) are also shown along with PC's selected using the "Kaiser Criterion" (eigenvalue greater than 1). The selection of the PC's to be explored on the subsequent data mining – e.g. Phase 8 (Discriminant Function: Section 5.8) – was based on the overall analysis of all PC's selected with the Scree Plot or Kaiser Criterion (Table 6-32). If the Scree Plot PC concentrated less than 80.0% of the variance, the Kaiser Criterion PC was selected; otherwise, the Scree Plot PC was the chosen one.

The line-wise inspection of Table 6-32 revels that the variance concentration per PC's of the original sets stands out. This is most likely to be caused because of the larger number of input variables (Table 6-31) – see loading plots shown below. The column-wise analysis of Table 6-32 discloses a particularly similar PC-selection within the exploration of SAR backscatter signature (σ^o, β^o, and γ^o separately or together, with and without the geometry, shape, and dimension attributes), for instance, both Scree Plot PC's and Kaiser Criterion PC's, concentrate equivalent variances.

The PCA of the data sub-divisions that considered only only the attributes of geometry, shape, and dimension, and only the DN's, showed the highest variance concentration percentages on the first two PC's: approximately 80.0% or more (Table 6-32). Another aspect about these two data sub-divisions is that the first two PC's have been selected for their original sets and for all optimal subsets (line-wise).

An additional aspect about the information presented on Table 6-32, regards the CFS PC-selection that analyzed only the attributes of geometry, shape, and dimension. Because the Discriminant Function (Phase 8: Sections 5.8 and 6.8) requires at least two variables, the first two PC's were selected even though the Scree Plot did not selected any PC and Kaiser Criterion only selected one PC – see Figure 6-36.

Because Table 6-32 contains a wide-range of information, a summary of selected PC's (shown in bold on Table 6-32) is presented on Table 6-33. The dimensionality reduction promoted by the PCA is evident on a cross-comparison against Table 6-31. These two tables (Tables 6-31 and 6-33) present the number of variables utilized as input on the Discriminant Function (Phase 8: Sections 5.8 and 6.8).

Table 6-33: Summary of selected Principal Components (PC's) per data sub-division (Figure 5-3). See also Table 6-31 for the number of variables and Table 6-32 for the full PCA results.

Number of Principal Components (PC's) per data sub-divisions	**Original Sets**	**UPGMA**		**CFS**
		(CCC)	**(0.5)**	
Complete Exploration of the CBOS-DScMod	10	21	18	§
All SAR Backscatter Signature ¥ with Size*	8	†	†	6
Only all SAR Backscatter Signature ¥	7	††	††	6
Size* and Sigma-naught (σ^o)	6	7	3	7
Size* and Beta-naught (β^o)	6	7	3	5
Size* and Gamma-naught (γ^o)	6	7	3	5
Only Size*	2	2	2	2**
Only Sigma-naught (σ^o)	5	5	2	4
Only Beta-naught (β^o)	5	4	2	5
Only Gamma-naught (γ^o)	6	5	2	4
Only Digital Numbers (DN's)	2	2	2	2

§ PCA not performed: most categorical Dummy Variables (Table 6-23).

* Attributes of geometry, shape, and dimension.

** Because the Discriminant Function (Phase 8) requires at least 2 variables.

¥ See: Table 5-1 and Table 5-5.

σ^o *SIG.amp*, *SIG.amp.FF*, *SIG.dB*, and *SIG.dB.FF*.

β^o *BET.amp*, *BET.amp.FF*, *BET.dB*, and *BET.dB.FF*.

γ^o *GAM.amp*, *GAM.amp.FF*, *GAM.dB*, and *GAM.dB.FF*.

† Same as Size* and Sigma-naught (σ^o).

†† Same as only Sigma-naught (σ^o).

Three Figures are presented below to demonstrate the Principal Components (PC's) selection strategy using the Scree Plot, i.e. broken stick with bootstrapping. Figure 6-34 illustrates the PC-selection for the original set of the complete exploration of the Campeche Bay Oil Slick Modified Database (CBOS-DScMod: n=502). On the top and middle panels it is not really possible to notice where exactly the broken stick curve (dash-dotted read line) crosses the eigenvalue line. But zooming further in (bottom panel) it is clearly observed that the broken stick curve crosses just below the 10th PC. As these 10 PC's concentrate 92.3% of the variance (Table 6-32), 10 PC's were selected (Table 6-33) to be analyzed on the subsequent data mining. Note that the bootstrapping eigenvalue error bars do not touch the broken stick curve.

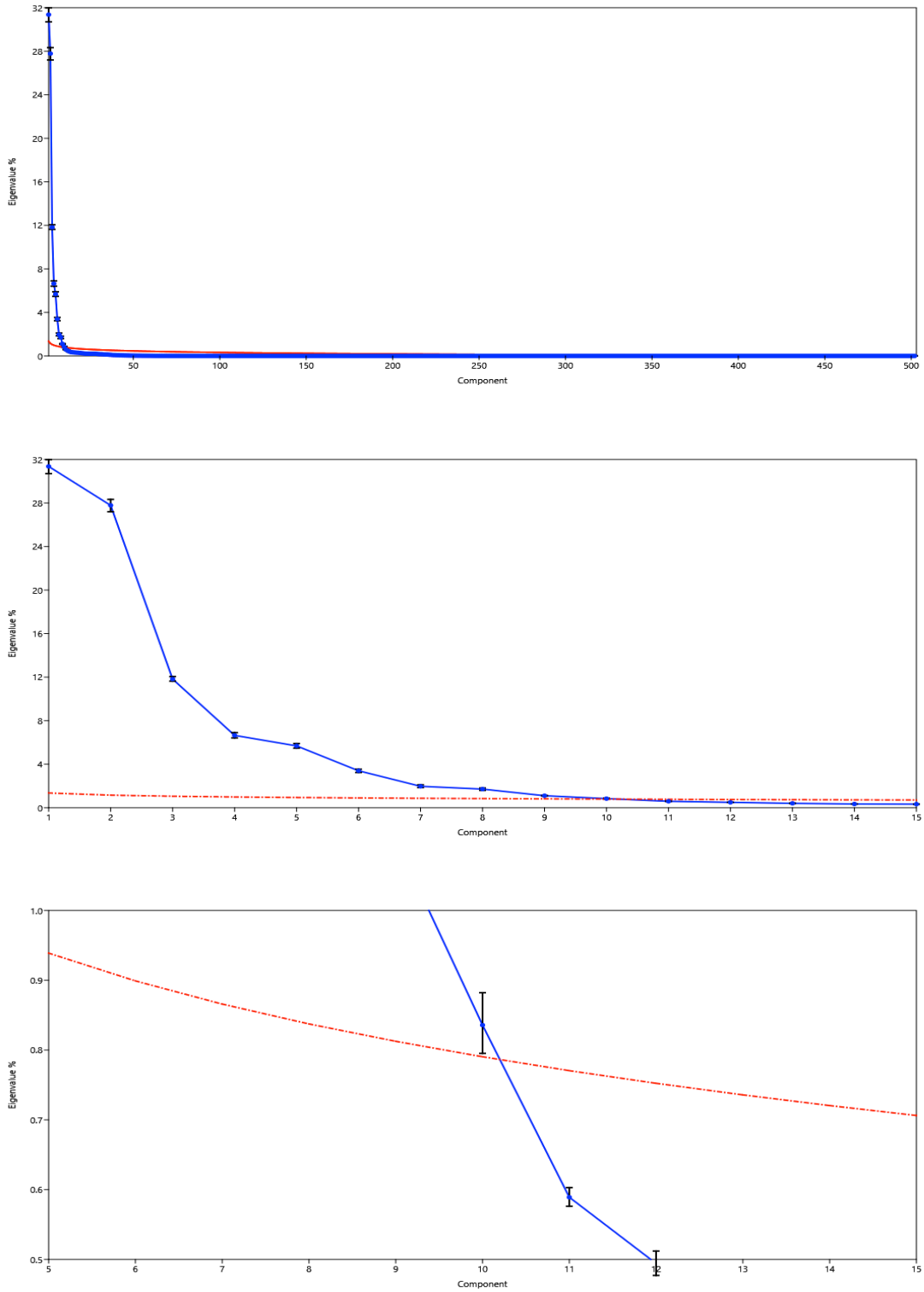

Figure 6-34: Scree Plots from the PCA for the original set of the complete exploration of the Campeche Bay Oil Slick Modified Database (CBOS-DScMod – Figure 5-3: n=502) showing the selected Principal Components (PC's) axes: 10 (Table 6-32 and Table 6-33). A zoom is given from top to bottom panels. The dash-dotted line corresponds to the broken stick curve. Bootstrapping eigenvalue error bars are shown: 2.5% and 97.5%.

Correspondingly, Figure 6-35 depicts the Scree Plots from the different analyses exploring only sigma-naught (σ^o) variables. The top panel shows the PCA of the original set (Table 5-5: n=141) where it is possible to see that the broken stick (dash-dotted red line) crosses the just below the 6th PC. However, the bootstrapping eigenvalue error bars touch the broken stick curve. Therefore, only 5 PC's were selected (Tables 6-32 and 6-33). The 2nd panel from the top shows the UPGMA-CCC (Table 6-21: n=20), where 3 PC's were selected (Table 6-32). However, because these only concentrate 73.0% of the variance, and the 5 PC's selected with the Kaiser Criterion concentrate 88.5%, 5 PC's were selected (Tables 6-32 and 6-33). The last two panels on Figure 6-35 show the PCA for the UPGMA-Fixed (Table 6-21: n=7) and CFS (Table 6-28: n=24): selecting 2 and 4 PC's, respectively.

Similarly, Figure 6-36 illustrates the PCA exploring only attributes of geometry, shape, and dimension. Two PC's were selected with the Scree Plot on the top two panels: original set (Table 5-4: n=10) and UPGMA-CCC (Table 6-20: n=6). Coincidently, these have also been selected with the Kaiser Criterion (Table 6-32). The PCA of the UPGMA-Fixed (Table 6-20: n=5) is shown on the 3rd panel from the top, in which only one PC was selected – concentrating only 57.4% of the variance (Table 6-32). Even though the Kaiser Criterion selected 2 PC's concentrating with less than 80.0% of the variance, these were selected to be analyzed on the subsequent data mining (Table 6-33). The bottom panel shows the PCA of the CFS (Table 6-24: n=3), and because the bootstrapping eigenvalue error bars touch the broken stick curve, no PC has been selected with the Scree Plot. Although the Kaiser Criterion selected one PC concentrating 90.0% of the variance, the Discriminant Function (Phase 8: Sections 5.8 and 6.8) requires at least 2 variables (i.e. in this case, two PC's); therefore, the first two PC's have been selected (Tables 6-32 and 6-33).

As a result, the subsequent data mining analyzing only the attributes of geometry, shape, and dimension are carried with their respective first two PC's (Tables 6-32 and 6-33). The PC's selected for all other data sub-divisions (Figure 5-3) undergone the same PC-selection process illustrated on Figure 6-34, Figure 6-35, and Figure 6-36, and described above: Scree Plot and Kaiser Criterion.

Scatterplots illustrating the relationship between the selected PC's resulted from the PCA have also been investigated. Figure 6-37 and Figure 6-38 show, respectively, the scatterplots of the first two PC's for the PCA exploring only sigma-naught (σ^o) variables and for the PCA exploring only attributes of geometry, shape, and dimension.

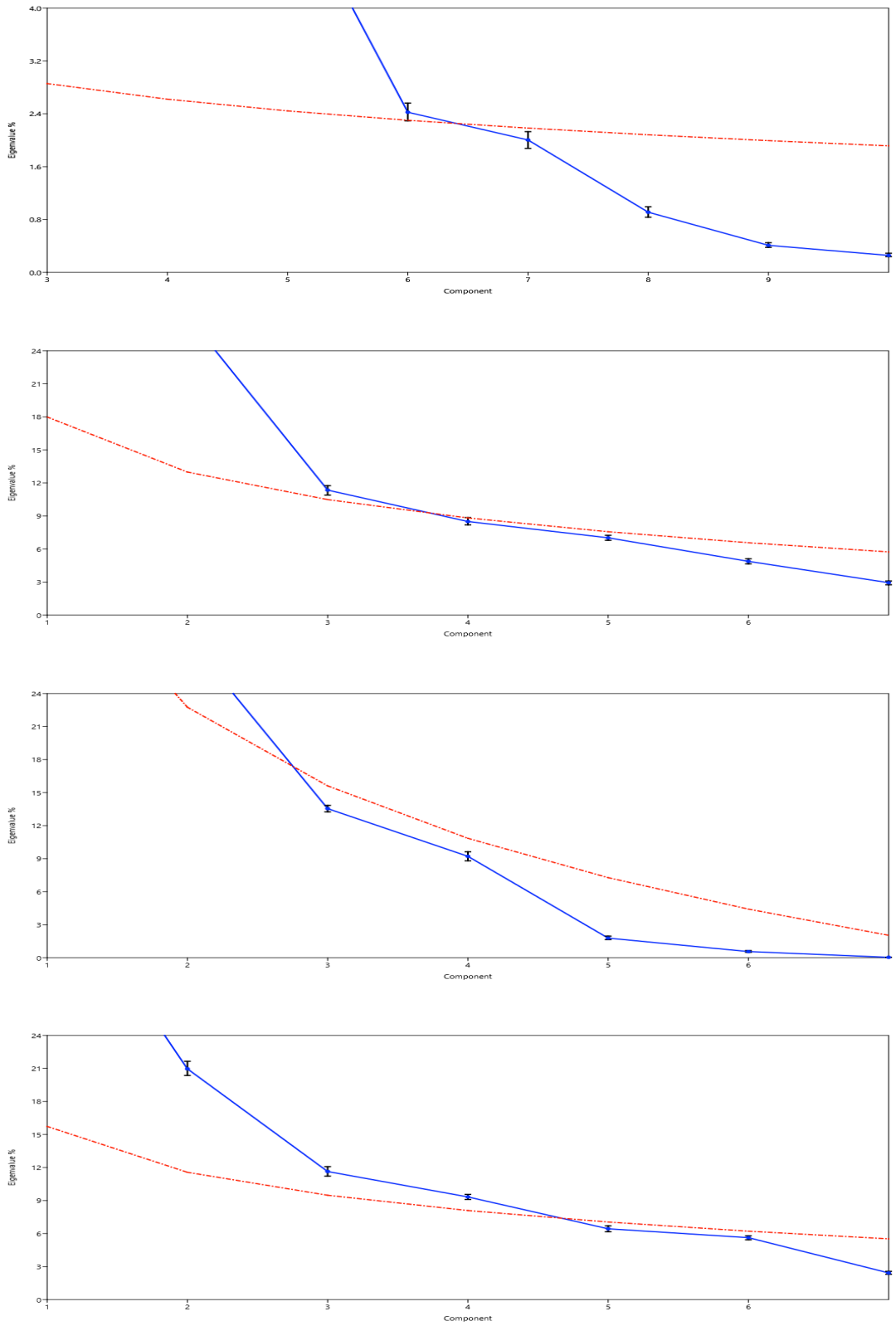

Figure 6-35: Scree Plots from the PCA exploring only sigma-naught (σ^o) variables. From top to bottom: original set (Table 5-5: n=141), UPGMA-CCC (Table 6-21: n=20), UPGMA-Fixed (Table 6-21: n=7), and CFS (Table 6-28: n=24). See also Figure 5-3 for data sub-divisions. The dash-dotted line corresponds to the broken stick curve. Bootstrapping eigenvalue error bars are shown: 2.5% and 97.5%.

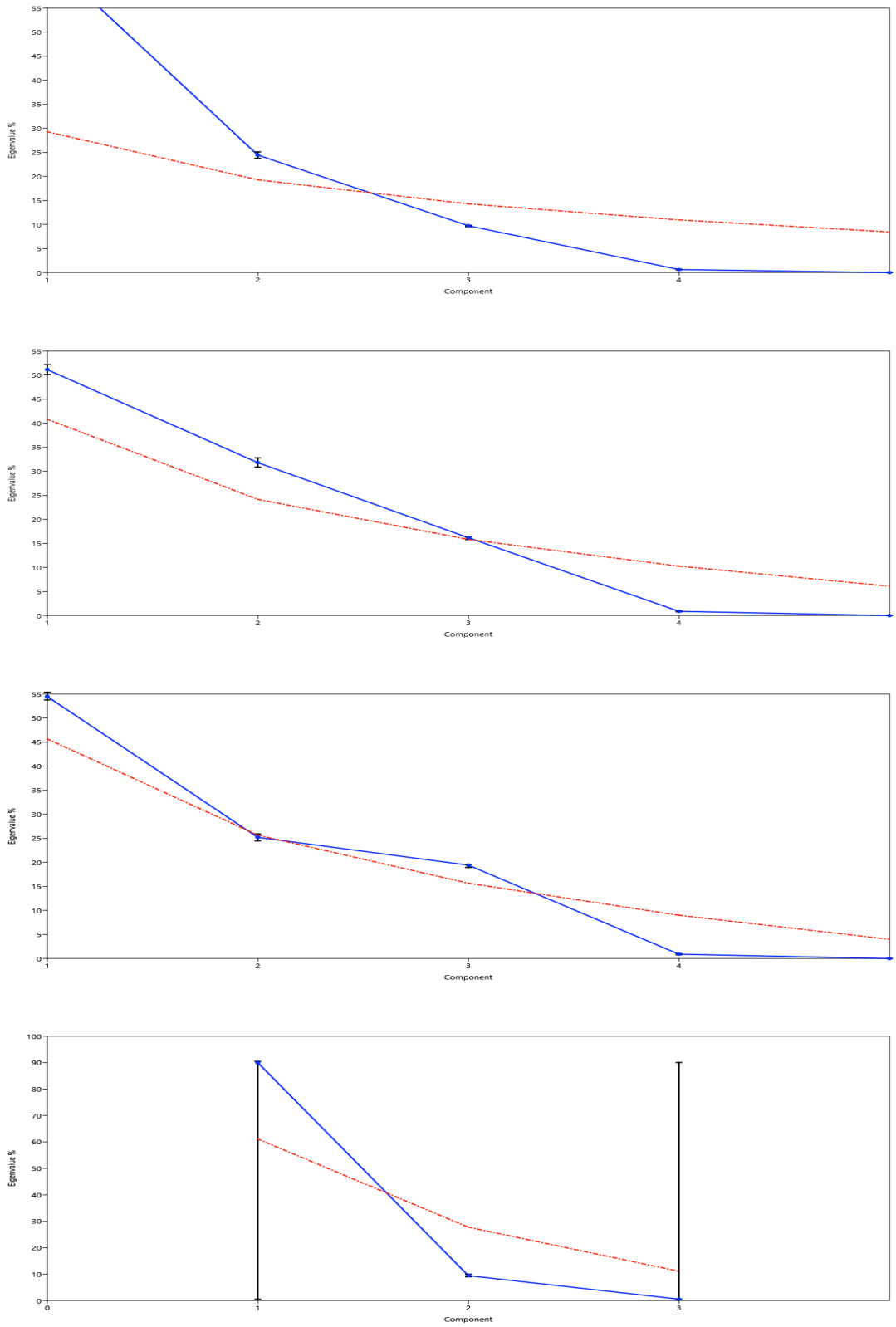

Figure 6-36: Scree Plots from the PCA exploring only attributes of geometry, shape, and dimension. From top to bottom: original set (Table 5-4: n=10), UPGMA-CCC (Table 6-20: n=6), UPGMA-Fixed (Table 6-20: n=5), and CFS (Table 6-24: n=3). See also Figure 5-3 for data sub-divisions. The dash-dotted line corresponds to the broken stick curve. Bootstrapping eigenvalue error bars are shown: 2.5% and 97.5%.

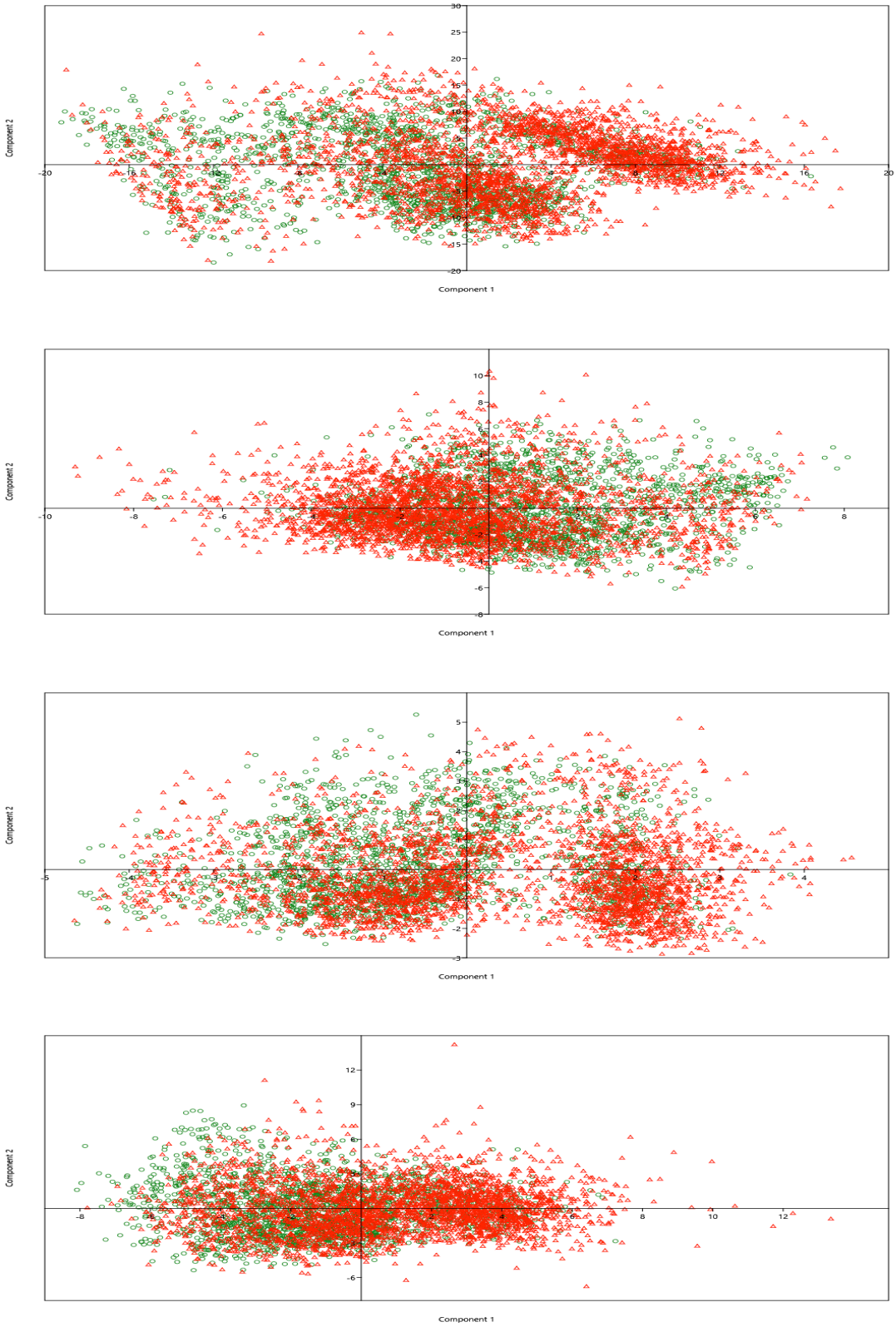

Figure 6-37: Scatterplots of the first two Principal Components resulted from the PCA exploring only sigma-naught (σ^o) variables. From top to bottom: original set (Table 5-5: n=141), UPGMA-CCC (Table 6-21: n=20), UPGMA-Fixed (Table 6-21: n=7), and CFS (Table 6-28: n=24). See also Figure 5-3 for data sub-divisions. Open red triangles: oil spills. Open green circles: oil seeps.

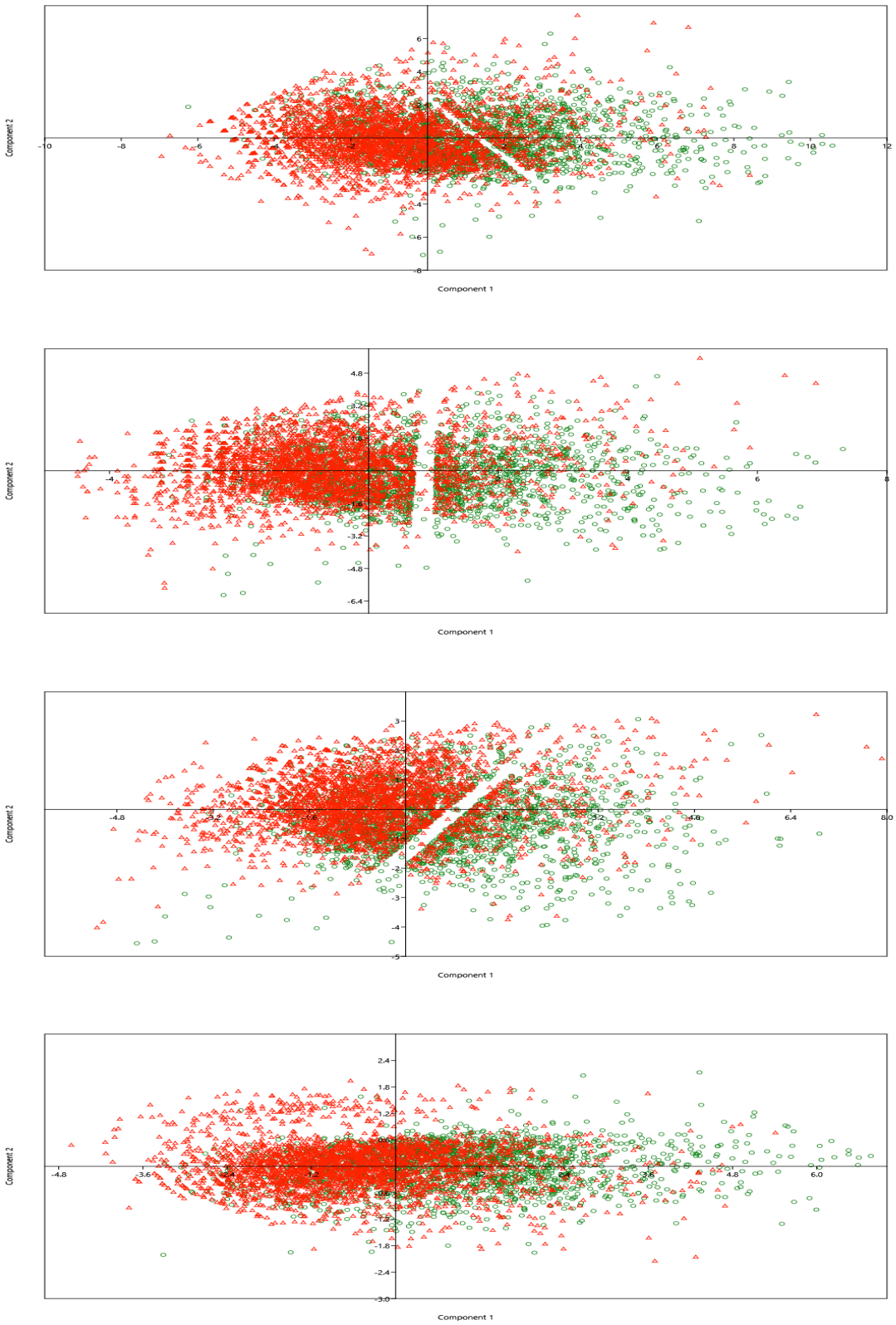

Figure 6-38: Scatterplots of the first two Principal Components resulted from the PCA exploring only attributes of geometry, shape, and dimension. From top to bottom: original set (Table 5-4: n=10), UPGMA-CCC (Table 6-20: n=6), UPGMA-Fixed (Table 6-20: n=5), and CFS (Table 6-24: n=3). See also Figure 5-3 for data sub-divisions. Open red triangles: oil spills. Open green circles: oil seeps.

From Figure 6-37 and Figure 6-38, it is possible to notice the considerable overlap between the scores of the two populations: oil spills (red triangles) and oil seeps (green circles). The same pattern is observed on all other scatterplots independent of optimal subsets within the proposed original sets of the CBOS-DScMod shown on Figure 5-3. This holds true not only for the relationship between the first two PC's, but also for all other combinations of PC's, for instance, PC1xPC3, PC1xPC4, PC3xPC4, PC5xPC6, PC7xPC8, amongt others.

A remarkable feature to note on the top three panels of Figure 6-38 (n=10, 6, and 5 variables) is a peculiar gap in data cloud of data points that affects both populations, i.e. oil spills (red triangles) oil seeps (green circles). This is most likely to be due to the presence of the Fractal Index (*FRAC.ind*) attributs – is bi-modal (multi-modal) frequency distribution is evidently disclosed on the histograms shown on Figure 6-23 and Figure 6-28. The bottom panel of Figure 6-38, resulted from the CFS (Table 6-24: n=3) analysis, does not show such gap, as it did not account for the *FRAC.ind* attribute.

However, this gap is not as prominent on the PCA scatterplots when the geometry, shape, and dimension attributes (that account for the *FRAC.ind* attribute) are analyzed together with the original set of the SAR backscatter signature (i.e. σ^o, β^o, or γ^o) variables, e.g. Figure 6-39. This is probably because each PC is influenced by a large number of variables: n=433 or n=151 (Tables 5-4 and 5-5). Interesting to note, is that a somewhat similar gap-like pattern is oberved on the top 3 panels of Figure 6-37 that do not consider size variables.

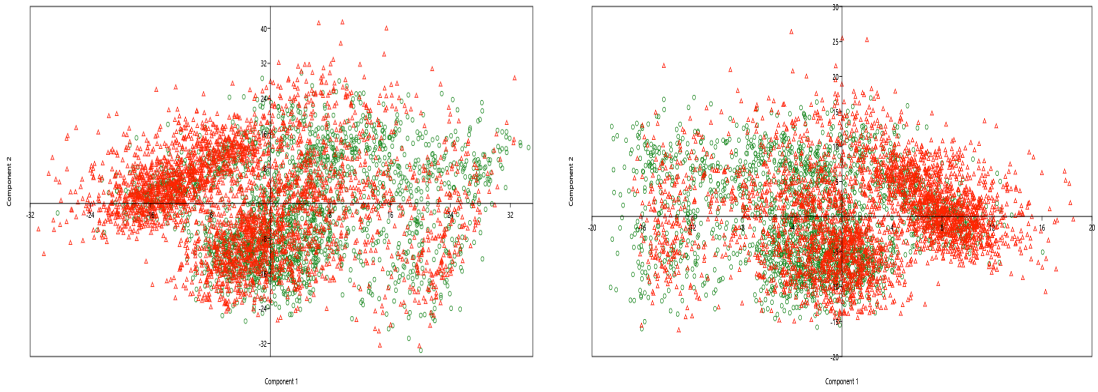

Figure 6-39: Scatterplots of the first two Principal Components resulted from the PCA exploring the geometry, shape, and dimension attributes (Table 5-4: n=10) together with all SAR backscatter signature (i.e. σ^o, β^o, and γ^o; Table 5-5: n=423 – left panel) and together with sigma-naught (σ^o) variables only (Table 5-5: n=141 – right panel). Open red triangles: oil spills. Open green circles: oil seeps.

The influence (i.e. meaning) of each original variable to each PC has been quantified by the inspection of Loadings plots. Figure 6-40 illustrates the first PC for the original sets (n=141) of sigma-naught (σ^o), beta-naught (β^o), and gamma-naught (γ^o). Likewise, Figure 6-41 depicts the first PC of the separate UPGMA-CCC implementation of the three SAR backscatter signature (σ^o, β^o, and γ^o) with the attributes of geometry, shape, and dimension. It is possible to observe that almost all variables are largely influencing the respective PC.

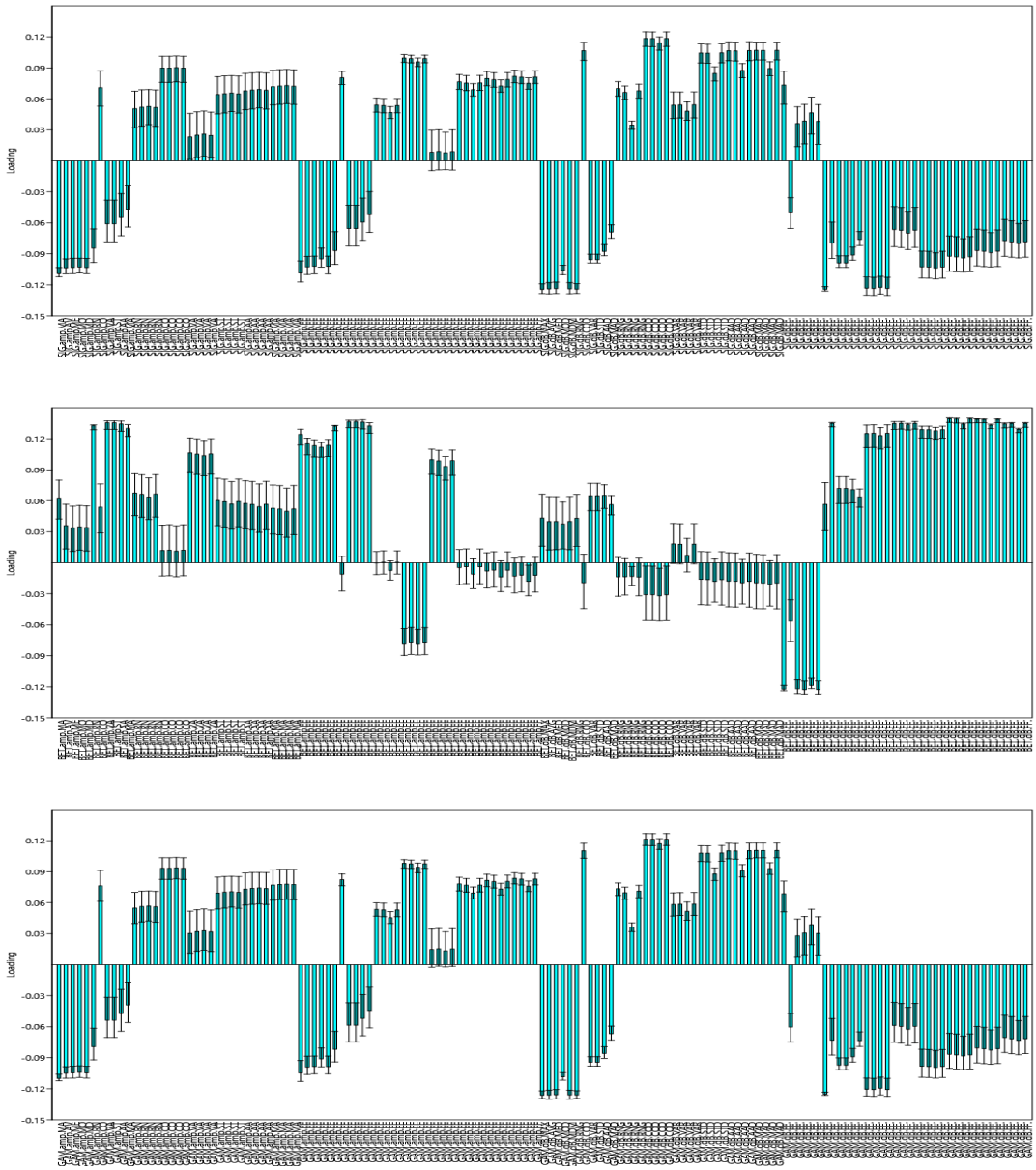

Figure 6-40: Loadings expressing the relationship between the original variables (n=141) and the first Principal Component of sigma-naught (σ^o), beta-naught (β^o), and gamma-naught (γ^o), respectively, top, middle, and bottom panels. See also Table 5-5 for the original attributes.

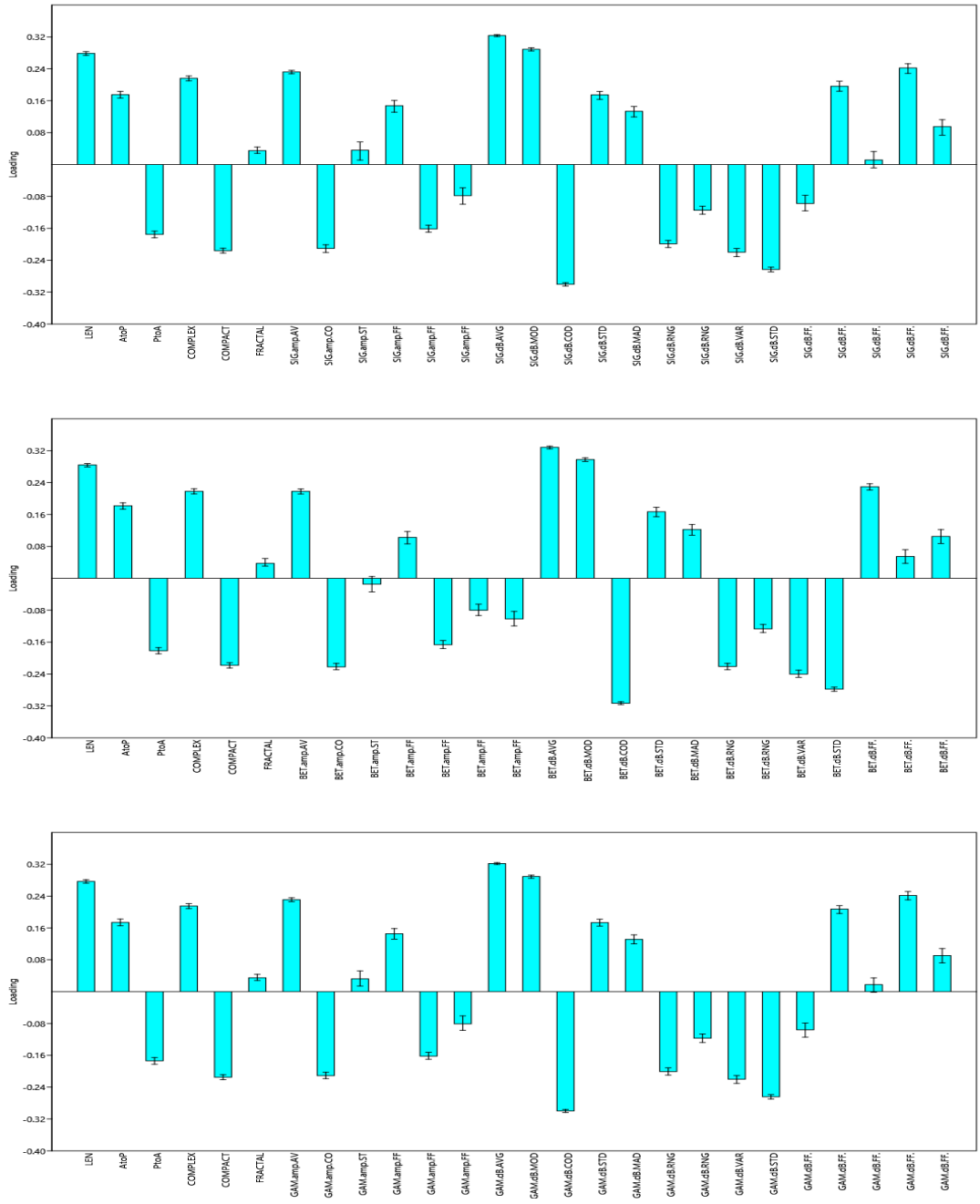

Figure 6-41: Loadings expressing the relationship between the optimal subset variables and the first Principal Component of sigma-naught (σ^o), beta-naught (β^o), and gamma-naught (γ^o), respectively, top (n=26), middle (n=25), and bottom (n=26) panels. See also Tables 6-20 and 6-21 for the original attributes.

The loadings plot for the analyses of the attributes of geometry, shape, and dimension and the first Principal Component show the same pattern of a fairly even influence of all 10 original variables on the first PC (Figure 6-42). The exception is on the CFS that has the perimeter (*Per*) being the sole one to account for the variance on the first PC – the second PC of this CFS PCA has the opposite occuring.

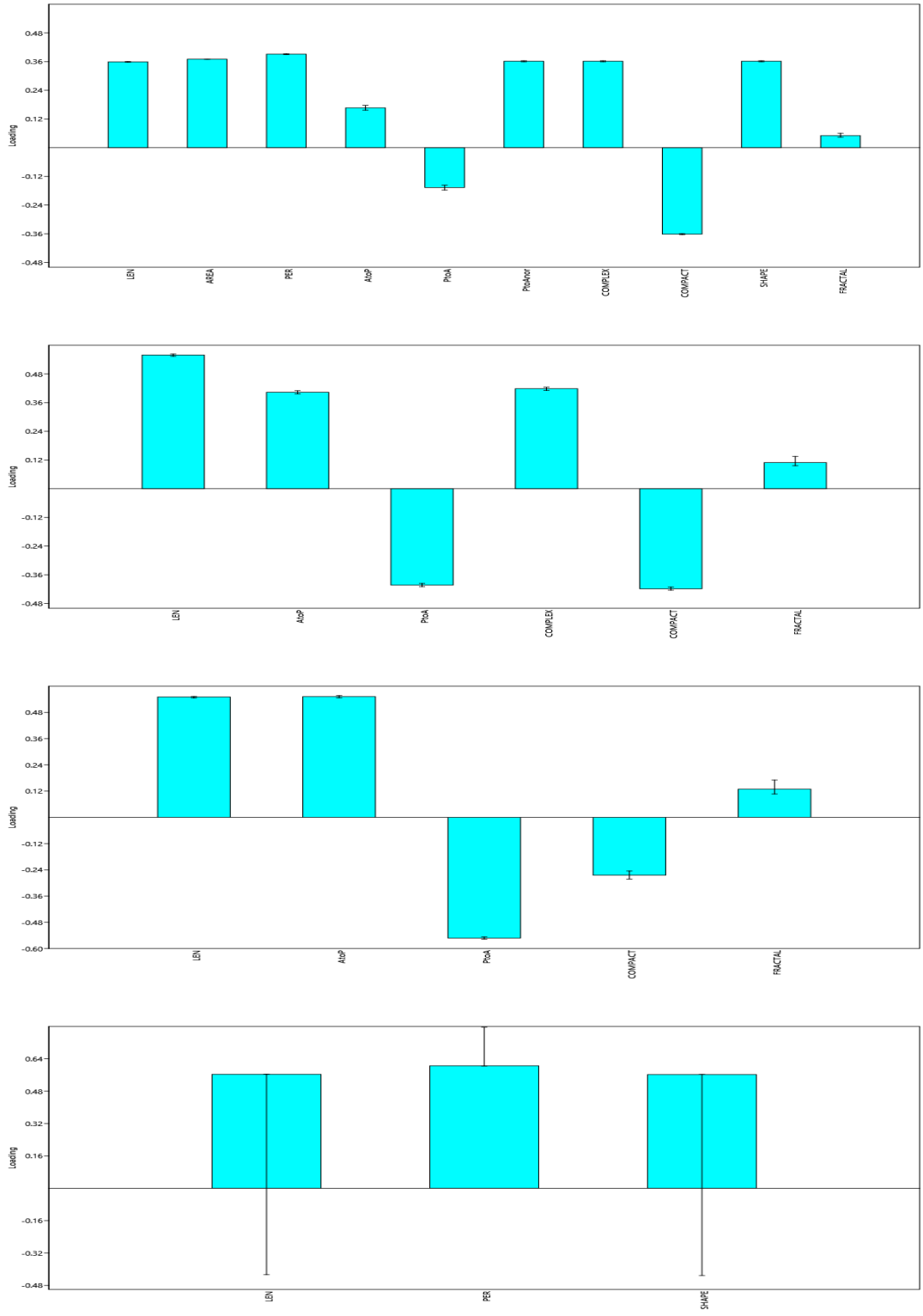

Figure 6-42: Loadings expressing the relationship between the attributes of geometry, shape, and dimension and the first Principal Component. From top to bottom: original set (Table 5-4: n=10), UPGMA-CCC (Table 6-20: n=6), UPGMA-Fixed (Table 6-20: n=5), and CFS (Table 6-24: n=3).

The only PC of all PCA performed herein that had a preferable influence was indeed the case shown on the bottom panel of Figure 6-42. Roughly speaking, the loadings expressions of all PC of all data sub-divisions (i.e. original sets and optimal subsets of selected variables, as proposed on Figure 5-3) have shown that each PC receives the influence of every variable.

6.8. PHASE 8: DISCRIMINANT FUNCTION

This Section summarizes the results of seventy-eight (n=78) Discriminant Functions. This effort, which is twice of the one put on the PCA's (Table 6-32: n=39), is explained based on the Discriminant Analyses that have been completed with the original values of the CBOS-DScMod variables (no PCA applied: Table 6-31) and with the scores of the selected PC's (with PCA applied: Table 6-33).

The main findings of the Discriminant Analyses are condensed on two tables: Table 6-34 that presents the Hotelling's t^2 and Table 6-35 that provides the percent of correct identification (Overall Accuracy). Another table including the constant offsets (C_{off}) is found in Appendix 5. This information is shown for all data sub-division (i.e. original sets, as well as for each optimal subset of selected variables – UPGMA-CCC, UPGMA-Fixed, and CFS), as shown on Figure 5-3. Initially, only the Overall Accuracy is explored, as the Discriminant Function results are subject to a further processing stage performed on the next Phase (Correlation Matrixes: Sections 5.9 and 6.9). This aims to measure eventual residual inter-variable correlation left from the previsous two Secions: Attribute Selection and PCA. The full assessment of other metrics (Table 5-11) is presented on the Algorithm Section (Phase 10: Sections 5.10 and 6.10).

Indeed, the reader should pay special attention to the corresponding information between Tables 6-34 and 6-35. Hotelling's t^2 represents a measure of equality of the means of the groups been discriminated (i.e. spills and seeps) in which larger values correspond to better discrimination of the *a priori* informed groups. Likewise, the Overall Accuracy is the total classification efficiency that reports the success rate in correctly telling apart the *a priori* known spills from seeps samples (Table 5-11).

The content of the Tables 6-34 and 6-35 is organized following Table 6-31 (number of variables) and Table 6-33 (summary of selected PC's). Therefore, these tables are provided with two "floors": the information from the original variables values (no PCA applied) is shown on the top and the information from selected PC's scores (with PCA applied) on the bottom. The major size difference (data reduction) should be highlighted.

Table 6-34: **Hotelling's t^2 values** per data sub-divisions (Figure 5-3).

No PCA: See Table 6-31 for the number of variables.	**Original Sets**	**UPGMA (CCC)**	**UPGMA (0.5)**	**CFS**
Complete Exploration of the CBOS-DScMod	11,509.0	10,598.0	10,529.0	§
All SAR Backscatter Signature ¥ with Size*	1,919.7	†	†	1,485.3
Only all SAR Backscatter Signature ¥	1,558.3	††	††	1,115.8
Size* and Sigma-naught (σ^o)	1,583.5	1,508.3	1,383.0	1,462.4
Size* and Beta-naught (β^o)	1,577.5	1,510.1	1,401.8	1,299.3
Size* and Gamma-naught (γ^o)	1,563.4	1,490.0	1,366.4	1,436.2
Only Size*	1,141.3	1,141.3	1,141.3	1,138.3
Only Sigma-naught (σ^o)	1,236.5	985.4	647.6	974.8
Only Beta-naught (β^o)	1,231.4	1,019.8	632.8	919.1
Only Gamma-naught (γ^o)	1,213.4	968.68	635.7	950.7
Only Digital Numbers (DN's)	663.7	218.8	138.4	550.35
With PCA: See Table 6-33 for the selected PC's.	**Original Sets**	**UPGMA (CCC)**	**UPGMA (0.5)**	**CFS**
Complete Exploration of the CBOS-DScMod	17,056.0	89,403.0	94,086.0	§
All SAR Backscatter Signature ¥ with Size*	1,065.5	†	†	1,044.5
Only all SAR Backscatter Signature ¥	598.9	††	††	632.4
Size* and Sigma-naught (σ^o)	891.0	1,123.5	769.8	1,065.8
Size* and Beta-naught (β^o)	908.7	1,099.5	722.3	1,106.2
Size* and Gamma-naught (γ^o)	863.1	1,115.4	753.4	1,028.4
Only Size*	1,034.2	1,064.7	1,086.4	1,085.9
Only Sigma-naught (σ^o)	594.1	589.5	447.7	640.9
Only Beta-naught (β^o)	584.1	464.5	435.7	612.6
Only Gamma-naught (γ^o)	579.2	574.7	432.2	606.7
Only Digital Numbers (DN's)	138.0	163.0	138.4	210.5

§ Discriminant Function not performed (see Table 6-23).

* Attributes of geometry, shape, and dimension.

¥ See: Table 5-1 and Table 5-5.

σ^o *SIG.amp*, *SIG.amp.FF*, *SIG.dB*, and *SIG.dB.FF*.

β^o *BET.amp*, *BET.amp.FF*, *BET.dB*, and *BET.dB.FF*.

γ^o *GAM.amp*, *GAM.amp.FF*, *GAM.dB*, and *GAM.dB.FF*.

† Same as Size* and Sigma-naught (σ^o).

†† Same as only Sigma-naught (σ^o).

The first aspect to notice while considering the Hotteling's t^2 (Table 6-34) is that these values are larger on the top floor (original values of variables prior to the PCA) than on the bottom floor (scores of the PC's selected on the PCA's).

The second aspect is that the complete exploration of the CBOS-DScMod that undergone a major data reduction (Table 6-31: 502, 59, and 46 variables, and Table 6-33: 10, 21, and 18 PC's), presents the higher Hotelling's t^2 values. This is anticipated as many categorical contextual Dummy Variables (Table 5-10) are accounted for. An enormous increase is evident on the PCA floor, from this original set to the two UPGMA optimal subsets.

One can clearly see that the Hotelling's t^2 values for the analysis considering only DN's (e.g. UPGMA-CCC: 163.0) has the lower value by far. As with the CFS-Merit (Table 6-30: DN=0.059), this agrees with literature that do not recommend DN values to cross-compare time series of SAR images (FREEMAN, 1992; THOMPSON & MCLEOD, 2004; EL-DARYMLI *et al.*, 2014). Important to highlight that the magnitude of the Hotelling's t^2 values is not comparable to the one from the CFS-Merit; therefore, such assessment should not be exercised.

Column-wise, the Hotelling's t^2 behavior is fairly similar to the one from the CFS-Merit presented on the very end of Phase 6 (Attribute Selection: Section 5.6) – Table 6-30. The pattern shown by the sole analyses of the attributes of geometry, shape, and dimension present a higher Hotelling's t^2 values as compared to when these attributes are not included.

Line-wise, the higher Hotelling's t^2 values are usually observed for the UPGMA-CCC optimal subset. Again, the sole use of the attributes of geometry, shape, and dimension has about the same effectiveness to discriminate spills from seeps, as when these attributes are combined with the SAR backscatter signature: σ^o, β^o, and γ^o. Thus showing that the SAR backscatter signature is not adding much to the whole differentiation process.

Continuing on the line-wise observation of Table 6-34, the UPGMA-Fixed optimal subsets tend to present almost always the lower Hotelling's t^2 values. With the above noticed about the UPGMA-CCC optimal subset, it is possible to confirm that the number of variables has some influence on the discrimination process. This might be related not only to the amount of variables, but also to their quality (i.e. redundant correlated information or not).

Table 6-35: **Overall Accuracy** per data sub-divisions (Figure 5-3).

No PCA: See Table 6-31 for the number of variables.	**Original Sets**	**UPGMA (CCC)**	**UPGMA (0.5)**	**CFS**
Complete Exploration of the CBOS-DScMod	90.70%	90.56%	90.40%	§
All SAR Backscatter Signature ¥ with Size*	73.33%	†	†	72.36%
Only all SAR Backscatter Signature ¥	70.87%	††	††	68.53%
Size* and Sigma-naught (σ^o)	72.88%	72.90%	71.95%	72.17%
Size* and Beta-naught (β^o)	72.44%	72.62%	71.87%	70.50%
Size* and Gamma-naught (γ^o)	72.90%	72.64%	71.77%	71.89%
Only Size*	70.40%	70.40%	70.40%	70.28%
Only Sigma-naught (σ^o)	69.89%	67.51%	64.06%	67.41%
Only Beta-naught (β^o)	70.00%	68.31%	64.16%	67.49%
Only Gamma-naught (γ^o)	69.87%	67.21%	63.63%	67.41%
Only Digital Numbers (DN's)	66.68%	58.67%	56.75%	64.99%
With PCA: See Table 6-33 for the selected PC's.	**Original Sets**	**UPGMA (CCC)**	**UPGMA (0.5)**	**CFS**
Complete Exploration of the CBOS-DScMod	90.04%	99.98%	99.96%	§
All SAR Backscatter Signature ¥ with Size*	68.61%	†	†	68.71%
Only all SAR Backscatter Signature ¥	63.63%	††	††	63.93%
Size* and Sigma-naught (σ^o)	67.64%	69.51%	65.46%	69.18%
Size* and Beta-naught (β^o)	68.02%	69.57%	65.58%	69.55%
Size* and Gamma-naught (γ^o)	67.47%	69.32%	65.79%	68.59%
Only Size*	69.59%	70.00%	70.02%	70.22%
Only Sigma-naught (σ^o)	63.28%	63.16%	63.26%	64.12%
Only Beta-naught (β^o)	63.53%	63.20%	63.02%	64.46%
Only Gamma-naught (γ^o)	63.16%	63.02%	63.24%	64.18%
Only Digital Numbers (DN's)	57.65%	57.89%	56.75%	59.48%

§ Discriminant Function not performed (see Table 6-23).

* Attributes of geometry, shape, and dimension.

¥ See: Table 5-1 and Table 5-5.

σ^o *SIG.amp*, *SIG.amp.FF*, *SIG.dB*, and *SIG.dB.FF*.

β^o *BET.amp*, *BET.amp.FF*, *BET.dB*, and *BET.dB.FF*.

γ^o *GAM.amp*, *GAM.amp.FF*, *GAM.dB*, and *GAM.dB.FF*.

† Same as Size* and Sigma-naught (σ^o).

†† Same as only Sigma-naught (σ^o).

The UPGMA-CCC Hotelling's t^2 values are somewhat equivalent to those of the CFS. Even though their variables are similar, they are not the same (Tables 6-19 to 6-29). This also corroborates the importance of reducing the dimensionality on the attribute-domain, for instance, Attribute Selection (Phase 6: Section 5.6) and PCA practices (Phase 7: Section 5.7). These two processes should be applied with caution not to lose information (i.e. underestimation) or to include noise (i.e. overestimation) (PERES-NETO *et al.*, 2003; 2005; HAIR *et al*., 2005).

Table 6-35 reports a summary of the Overall Accuracy distribution. The percentages from the complete exploration stand out (>90.0%). To some extent, improved accuracies are observed on the top floor that considers the original variables. Digital Numbers (DN's) are again the worse ones. There is a slight better discrimination while using only the attributes of geometry, shape, and dimension. In general, the Overall Accuracy somewhat matches the observations from Hotelling's t^2 values (Table 6-34).

6.9. PHASE 9: CORRELATION MATRIX

Once the Discriminant Functions were explored, Correlation Matrixes were computed to verify the linear correlation among the variables and PC's. PAST (version 2.17c) was used for this task and it provides matrixes of linear correlation of Pearson's r correlation coefficient and p(uncorrelated).

Roughly all information from the original values of the CBOS-DScMod variables (no PCA applied: Table 6-31) showed residual inter-variable correlation. This included all data sub-division, i.e. original sets, as well as the optimal subsets of selected variables (UPGMA-CCC, UPGMA-Fixed, and CFS) – Figure 5-3. On the other hand, as expected, all information from the scores of the selected PC's (with PCA applied – Table 6-33) presented no inter-variable correlation. These, respectively, correspond to the two "floors" explored on the Discriminant Function Tables 6-34 and 6-35.

While Table 6-36 (UPGMA-CCC: n=26) provides a clear example of the inter-variable correlation, Table 6-37 (UPGMA-CCC: 7 PC's) shows the anticipated lack of inter-PC correlation. The linear correlation of Pearson r and p(uncorrelated) are shown on the bottom and top of the table, respectively. Shown on grey are the uncorrelated relations. This pattern was roughly the same for all other data sub-divisions (Figure 5-3). Most original values of the CBOS-DScMod variables prior to the PCA are correlated, whereas the scores of the selected PC's are not. This brings to a close that only the information of the Discriminant Function "floor" with the PCA is carried to design the classification algorithm (Tables 6-34 and 6-35).

Table 6-36: Correlation Matrix of the optimal subset derived from the UPGMA-CCC Sigma-naught with the attributes of geometry, shape, and dimensions (n=26). The linear Pearson's r correlation coefficient and p(uncorrelated) are shown on the bottom (lower triangle of the matrix) and top (upper triangle of the matrix), respectively. Uncorrelated relations are shown on grey, i.e. above 0.05. See also the dendrogram (Figure 6-30), variables (Tables 6-20 and 6-21), and number of variables (Table 6-31).

upgmaCCC 26	LEN	AtoP	PtoA	COMPLEX	COMPACT	FRACTAL	SIG.amp.AVG	SIG.amp.COD	SIG.amp.STD	SIG.amp.FF.AVG
LEN		0	0	0	0	4.37E-14	0	0	0.45532	5.59E-35
AtoP	0.67394		0	0.00075	0.00076	1.14E-14	9.95E-95	2.32E-140	2.59E-12	0.00228
PtoA	-0.67394	-1		0.00075	0.00075	1.14E-14	9.94E-95	2.33E-140	2.60E-12	0.00228
COMPLEX	0.71644	0.04803	-0.04803		0	1.08E-02	3.69E-213	1.53E-177	0.01199	7.17E-53
COMPACT	-0.71644	-0.04803	0.04803	-1		1.09E-02	3.73E-213	1.55E-176	0.01199	7.20E-57
FRACTAL	0.11944	0.12534	-0.12534	0.06947	-0.06947		0.00723	0.00025	0.03557	0.5545
SIG.amp.AVG	0.53170	0.29418	-0.29418	0.42706	-0.42705	0.03830		0	1.00E-39	1.19E-98
SIG.amp.COD	-0.54830	-0.35315	0.35315	-0.39225	0.39225	-0.05215	-0.85498		4.17E-113	0.05833
SIG.amp.STD	-0.05812	-0.11646	0.11645	0.03583	-0.03583	-0.02998	0.19591	0.31823		0
SIG.amp.FF.AVG	0.18225	0.04351	-0.04351	0.22384	-0.22383	0.00843	0.29981	0.02700	0.66718	
SIG.amp.FF.COD	-0.28681	-0.15494	0.15495	-0.25619	0.25619	-0.02977	-0.22328	0.27376	-0.00869	-0.72790
SIG.amp.FF.VAR/AVG	-0.23063	-0.18113	0.18113	-0.14715	0.14714	-0.04415	0.00341	0.38056	0.73026	-0.01508
SIG.dB.AVG	0.68231	0.42652	-0.42653	0.49574	-0.49573	0.07307	0.57360	-0.52850	0.08824	0.37128
SIG.dB.MOD	0.51866	0.33230	-0.33230	0.38740	-0.38739	0.04800	0.45457	-0.40544	0.09512	0.29866
SIG.dB.COD	-0.64683	-0.36178	0.36179	-0.50886	0.50886	-0.05945	-0.52802	0.53629	0.00656	-0.27855
SIG.dB.STD	0.17235	0.15002	-0.15002	0.07186	-0.07186	0.03235	0.32688	-0.21460	0.28083	0.43971
SIG.dB.MAD	0.23964	0.23553	-0.23553	0.09588	-0.09587	0.04867	0.23971	-0.11604	0.22363	0.29226
SIG.dB.RNG/AVG	-0.28801	-0.12981	0.12981	-0.24305	0.24305	-0.04523	-0.31822	0.28593	0.07171	-0.08566
SIG.dB.RNG/MOD	-0.05635	-0.03159	0.03159	-0.06851	0.06851	0.00114	-0.10124	0.06988	-0.01593	-0.03337
SIG.dB.VAR/AVG	-0.67213	-0.37532	0.37532	-0.54492	0.54492	-0.05725	-0.37205	0.43460	0.18724	0.00108
SIG.dB.STD/MOD	-0.52682	-0.32230	0.32230	-0.41537	0.41536	-0.04245	-0.39409	0.38109	-0.00075	-0.17239
SIG.dB.FF.MIN	-0.18123	-0.05045	0.05046	-0.19853	0.19853	0.00619	-0.26311	-0.15360	-0.85360	-0.64757
SIG.dB.FF.MAX	0.45170	0.34658	-0.34658	0.27901	-0.27900	0.07549	0.20040	-0.52950	-0.56379	-0.10391
SIG.dB.FF.AVG	0.12181	0.18073	-0.18072	-0.00700	0.00700	0.03938	-0.11708	-0.39422	-0.91138	-0.52493
SIG.dB.FF.RNG/AVG	0.47449	0.25058	-0.25059	0.40925	-0.40925	0.03508	0.50428	-0.13755	0.70522	0.70006
SIG.dB.FF.COD	0.10454	0.08301	-0.08301	0.08038	-0.08037	0.02293	0.26350	0.18906	0.81657	0.59398

upgmaCCC 26	SIG.amp.FF.COD	SIG.amp.FF.VAR/AVG	SIG.dB.AVG	SIG.dB.MOD	SIG.dB.COD	SIG.dB.STD	SIG.dB.MAD	SIG.dB.RNG/AVG
LEN	9.94E-90	2.33E-56	0	0	0	4.37E-30	3.69E-61	1.58E-90
AtoP	8.56E-24	1.58E-33	1.46E-212	4.76E-123	6.40E-148	3.86E-22	6.07E-59	6.35E-16
PtoA	8.54E-24	1.58E-33	1.45E-212	4.75E-124	6.36E-148	3.85E-26	6.07E-59	6.36E-16
COMPLEX	1.61E-70	3.36E-21	2.53E-299	8.95E-173	3.7549E-322	4.56E-03	1.63E-07	4.95E-63
COMPACT	1.61E-70	3.37E-21	2.59E-299	9.12E-172	3.8537E-322	4.57E-03	1.63E-07	4.99E-63
FRACTAL	0.03685	0.00196	2.91E-03	0.000760	0.30356	0.023327	0.00064	0.00151
SIG.amp.AVG	1.38E-52	0.81119	0	2.51E-245	0	9.13E-120	3.39E-61	4.26E-112
SIG.amp.COD	3.09E-81	3.39E-165	0	6.70E-190	0	2.58E-48	3.31E-12	3.84E-89
SIG.amp.STD	0.54248	0	5.75E-06	2.35E-07	0.64546	8.91E-86	9.11E-53	4.82E-03
SIG.amp.FF.AVG	0	0.29036	1.63E-157	7.73E-98	2.66E-84	1.39E-227	2.07E-94	1.79E-05
SIG.amp.FF.COD		0	1.83E-200	4.35E-107	2.29E-184	2.13E-136	4.46E-19	3.09E-05
SIG.amp.FF.VAR/AVG	0.64122		7.22E-38	3.55E-13	5.38E-65	0.16053	3.14E-02	2.66E-35
SIG.dB.AVG	-0.41545	-0.19161		0	0	0	1.32E-251	0
SIG.dB.MOD	-0.31151	-0.11979	0.80148		0	0	1.04E-155	0
SIG.dB.COD	0.40005	0.24657	-0.90712	-0.72719		3.87E-135	0.23949	0
SIG.dB.STD	-0.34852	0.02002	0.63761	0.51797	-0.34584		0	2.60E-61
SIG.dB.MAD	-0.14044	0.06642	0.45966	0.37040	-0.06021	0.78254		2.69E-17
SIG.dB.RNG/AVG	0.08440	0.18549	-0.66146	-0.53750	0.68710	-0.23992	-0.13454	
SIG.dB.RNG/MOD	-0.00199	0.00919	-0.22529	-0.74469	0.23290	-0.09546	-0.05160	0.34334
SIG.dB.VAR/AVG	0.15096	0.26130	-0.57680	-0.45493	0.76982	0.26152	0.25388	0.57435
SIG.dB.STD/MOD	0.22217	0.14468	-0.67127	-0.94431	0.69856	-0.20766	-0.12256	0.52237
SIG.dB.FF.MIN	0.14550	-0.56363	-0.23425	-0.19604	0.16613	-0.27469	-0.20081	-0.08637
SIG.dB.FF.MAX	-0.39733	-0.62399	0.63984	0.49281	-0.57988	0.44111	0.29129	-0.36576
SIG.dB.FF.AVG	-0.15505	-0.72110	0.08120	0.04373	-0.08808	0.01752	0.00508	-0.01386
SIG.dB.FF.RNG/AVG	-0.29889	0.33113	0.69337	0.56974	-0.57012	0.57977	0.43876	-0.30369
SIG.dB.FF.COD	0.01087	0.56723	0.28181	0.24787	-0.03340	0.53834	0.59477	-0.10406

upgmaCCC 26	SIG.dB.RNG/MOD	SIG.dB.VAR/AVG	SIG.dB.STD/MOD	SIG.dB.FF.MIN	SIG.dB.FF.MAX	SIG.dB.FF.AVG	SIG.dB.FF.RNG/AVG	SIG.dB.FF.COD
LEN	0.77196	0	0	1.45E-33	7.90E-242	1.03E-13	1.60E-270	2.01E-09
AtoP	0.02675	2.97E-160	3.28E-115	0.00040	9.22E-136	2.31E-33	2.87E-67	5.59E-09
PtoA	0.02677	2.97E-160	3.28E-115	0.00040	9.20E-135	2.31E-33	2.85E-67	5.58E-05
COMPLEX	1.52E-02	0	2.24E-200	7.05E-41	1.36E-84	0.62373	6.98E-194	1.67E-04
COMPACT	1.53E-02	0	2.28E-200	7.06E-41	1.36E-84	0.62371	6.99E-194	1.67E-04
FRACTAL	0.93645	0.59058	0.00291	0.66416	1.17E-03	0.00576	0.01391	0.10792
SIG.amp.AVG	1.12E-08	3.19E-157	2.27E-179	1.22E-74	1.03E-41	1.79E-12	1.7544E-315	7.06E-76
SIG.amp.COD	9.39E-04	1.10E-221	1.07E-169	2.46E-23	0	1.71E-178	3.39E-19	8.63E-37
SIG.amp.STD	0.26417	5.03E-36	0.95828	0	0	0	0	0
SIG.amp.FF.AVG	0.01930	0.93944	4.23E-30	0	2.80E-09	0	0	0
SIG.amp.FF.COD	0.88888	1.88E-22	4.94E-52	1.14E-20	1.30E-181	7.85E-24	5.30E-98	0.44599
SIG.amp.FF.VAR/AVG	0.51940	1.50E-73	2.08E-20	0	0	0	4.05E-122	0
SIG.dB.AVG	1.32E-53	0	0	2.91E-58	0	1.19E-04	0	2.02E-86
SIG.dB.MOD	0	9.17E-247	0	8.79E-40	3.15E-296	0.00216	0	9.97E-66
SIG.dB.COD	1.50E-57	0	0	9.30E-28	0	6.17E-06	0	0.019186
SIG.dB.STD	2.00E-07	1.10E-73	4.99E-45	7.95E-82	3.29E-229	0.21950	0	0
SIG.dB.MAD	0.00030	3.58E-69	6.49E-14	6.75E-42	9.53E-93	0.72188	1.77E-226	0
SIG.dB.RNG/AVG	4.75E-132	0	0	1.31E-05	1.76E-151	0.33135	2.11E-101	2.60E-10
SIG.dB.RNG/MOD		1.72E-33	0	0.37613	3.93E-07	0.04810	2.26E-15	5.63E-03
SIG.dB.VAR/AVG	0.18105		0	0.87663	2.42E-124	5.23E-05	3.29E-69	7.50E-50
SIG.dB.STD/MOD	0.81488	0.62084		7.62E-13	3.73E-178	0.00241	8.73E-215	8.26E-04
SIG.dB.FF.MIN	-0.01263	0.00221	0.11852		4.58E-136	0	0	0
SIG.dB.FF.MAX	-0.09404	-0.33392	-0.39388	0.34813		0	2.34E-06	5.72E-110
SIG.dB.FF.AVG	0.02819	-0.08316	-0.04327	0.76767	0.73936		0	0
SIG.dB.FF.RNG/AVG	-0.12787	-0.25395	-0.42851	-0.75972	0.08505	-0.56604		0
SIG.dB.FF.COD	-0.07129	0.21777	-0.07637	-0.70639	-0.31539	-0.72254	0.74462	

Table 6-37: Correlation Matrix of the optimal subset: UPGMA-CCC Sigma-naught with the attributes of geometry, shape, and dimensions (n=26): Principal Component (PC's) selected on the PCA: 7 PC's. The linear Pearson's r correlation coefficient and p(uncorrelated) are shown on the bottom (lower triangle of the matrix) and top (upper triangle of the matrix), respectively. Uncorrelated relations are shown on grey. See also the dendrogram (Figure 6-30), variables (Tables 6-20 and 6-21), and number of PC's (Tables 6-32 and 6-33).

upgmaCCC 26 PC7	PC1	PC2	PC3	PC4	PC5	PC6	PC7
PC1		0.99999	0.99999	0.99998	1	0.99998	1
PC2	2.38E-03		0.99997	0.99999	0.99998	0.99999	0.99999
PC3	1.80E-03	-5.87E-03		0.99996	0.99999	0.99999	1
PC4	-2.84E-03	-2.49E-03	6.35E-03		0.99994	0.99992	0.99999
PC5	-1.36E-04	-2.79E-03	2.36E-03	1.10E-02		0.99998	0.99994
PC6	3.29E-04	9.64E-04	1.46E-04	1.51E-02	-3.94E-03		0.99999
PC7	2.03E-04	9.78E-05	8.31E-04	1.98E-03	-1.12E-02	-2.31E-03	

6.10. PHASE 10: OIL SLICK CLASSIFICATION ALGORITHM

Once the inter-variable correlation has been established giving a picture of the remaining relationship among the original values of the CBOS-DScMod variables prior to the application of the PCA, the additional devided goal of this D.Sc. research can be addressed: design a qualitative-quantitative classification algorithm to distinguish natural from man-made oil slicks using RADARSAT-derived measurements. This is accomplished solely with the use of the scores of the selected PC's (Tables 6-32 and 6-33) that have been explored with Discriminant Functions (Tables 6-34 and 6-35).

Two lines of attack are approached in this Section. The first explores the individual information provided on Figure 5-3: forty-four data sub-division (i.e. eleven original sets and thirty-three optimal subsets of selected variables: UPGMA-CCC, UPGMA-Fixed, and CFS). The second explores a synergistic combination of variables.

The full set of metrics proposed in Table 5-11 is assessed on a series of Confusion Matrixes that follows below: Tables 6-38 to 6-44. The same color-code previously introduced (Section 6.1) is followed to identify spills and seeps. The most important metrics taken into account are shown in yellow font: Specificity, Sensitivity, Positive and Negative Predictive Values.

The results of the complete exploration of the of the full remote sensing library content of the CBOS-DScMod (Figure 5-3: n=502) are not shown, but, because it accounted for categorical contextual Dummy Variables (Table 5-10) its discrimination power was above 90%, topping almost 100% of accuracy. This corroborates the quality of the explored dataset, i.e. CBOS-Data and CBOS-DScMod.

The finding from the use of the PC's from the UPGMA-Fixed are also not presented because the initial analysis of the Overall Accuracy (Table 6-35) showed a lower discriminating power that of the UPGMA-CCC and CFS, which indeed is reflected on the other methics. Consequently, the results shown on this Section focuses on PC's selected with the variables from the UPGMA-CCC and CFS: respectively, left and right tables of Tables 6-38 to 6-43.

Table 6-38 presents the findings from the analysis that investigates all SAR backscatter signature variables together (Table 5-5: n=423: σ^o, β^o, and γ^o), with and without the attributes of geometry, shape, and dimension (Table 5-4: n=10). The influence of the size variables is clearly observed, as all metrics evaluated show an improvement when size information is accounted for (from bottom to top tables).

With the initial analysis of Table 6-38, the reader should get acquainted to better obtain useful information of the capabilities shown herein to differentiate spills from seeps. It is crucial for the full comprehension of the proposed algorithms that the metrics introduce on Table 5-11, and largely explored on this Section, are understood.

Using the upper left tables on Table 6-38, one should be able to answer the first set of four questions focusing on the lines of the table:

Q1-PA-CE: How many known oil seep samples are correctly identified? As there are 2,021 oil seeps on the CBOS-DScMod, and 1,395 have been identified by this Discriminant Function as being oil seeps, the answer is 69.03%. This is the Sensitivity of this Function.

Q2-PA-CE: How many known oil spill samples are correctly identified? As there are 2,895 oil spills on the CBOS-DScMod, and 1,978 have been identified by this Discriminant Function as being oil spills, the answer is 68.32%. This is the Specificity of this Function.

Q3-PA-CE: How many known oil seep samples are misidentified? These are the False Negative cases (n=626) that are coupled with Sensitivity. Therefore, the answer is 30.97% oil seeps have been misidentified as being oil spills.

Q4-PA-CE: How many known oil spill samples are misidentified? These are the cases of False Positive (n=917) that are linked to Specificity. So, 31.68% of the oil spills have been misidentified as being oil seeps.

Table 6-38: Confusion Matrixes of the Discriminant Functions using the Principal Components (PC's). Top tables: all SAR backscatter signature variables (Table 5-5: σ^o, β^o, and γ^o – n=423) analyzed together with the attributes of geometry, shape, and dimension (Table 5-4: n=10 – Size Information). Bottom tables: only all SAR backscatter signature variables (Table 5-5: σ^o, β^o, and γ^o – n=423). Left side tables: CCC (Cophenetic Correlation Coefficient). Right side tables: CFS (Correlation-Based Feature Selection). Refer to Figure 5-3 for further information on data sub-divisions. See also Tables 6-32 and 6-33 for the number of PC's selected per subset, and Tables 6-34 and 6-35 for more details about the Discriminant Functions.

PC7	Size with SAR	
CCC	Seep	Spill
Seep	60.34%	24.04%
Spill	39.66%	75.96%
	100.00%	100.00%

CCC	Seep	Spill	
Seep	69.03%	30.97%	100.0%
Spill	31.68%	68.32%	100.0%

CCC	Seep	Spill		
Seep	1,395	626	2,021	
Spill	917	1,978	2,895	
	2,312	2,604	4,916	Overall A.
				68.61%

PC6	Size with SAR	
CFS	Seep	Spill
Seep	61.15%	25.34%
Spill	38.85%	74.66%
	100.00%	100.00%

CFS	Seep	Spill	
Seep	65.51%	34.49%	100.0%
Spill	29.05%	70.95%	100.0%

CFS	Seep	Spill		
Seep	1,324	697	2,021	
Spill	841	2,054	2,895	
	2,165	2,751	4,916	Overall A.
				68.71%

PC5	Only SAR	
CCC	Seep	Spill
Seep	54.43%	25.82%
Spill	45.57%	74.18%
	100.00%	100.00%

CCC	Seep	Spill	
Seep	70.76%	29.24%	100.0%
Spill	41.35%	58.65%	100.0%

CCC	Seep	Spill		
Seep	1,430	591	2,021	
Spill	1,197	1,698	2,895	
	2,627	2,289	4,916	Overall A.
				63.63%

PC6	Only SAR	
CFS	Seep	Spill
Seep	54.96%	26.76%
Spill	45.04%	73.24%
	100.00%	100.00%

CFS	Seep	Spill	
Seep	68.04%	31.96%	100.0%
Spill	38.93%	61.07%	100.0%

CFS	Seep	Spill		
Seep	1,375	646	2,021	
Spill	1,127	1,768	2,895	
	2,502	2,414	4,916	Overall A.
				63.93%

The upper left tables on Table 6-38 provide the answers of the second set of four questions focusing on the columns of the table:

Q1-UA-OE: How many oil seeps identified by the Function are indeed known oil seeps? As there are 2,312 samples that have been identified oil seeps, and 1,395 have been correctly identified as being oil seeps, the answer is: 60.34%. This is the Positive Predictive Value of this Function.

Q2-UA-OE: How many oil spills identified by the Function are indeed known oil spills? As 2,604 samples were identified as oil spills, and 1,978 have been identified by this Discriminant Function as being oil spills, the answer is: 75.96%. This is the Negative Predictive Value of this Function.

Q3-UA-OE: Of samples identified by the Function as oil seeps, how many are oil spills? This is the Inverse of the Positive Predictive Value (n=917). This is the amount of samples that the Function misidentified when it classified the oil seeps: 39.66%.

Q4-UA-OE: Of samples identified by the Function as oil spills, how many are oil seeps? This is the Inverse of the Negative Predictive Value (n=626). This informs how many samples that the Function misidentified when it classified the oil spills: 24.04%.

This is a fairly balanced result when it is compared to the Overall Accuracy: 68.61%. However, if looking into the lower left tables on Table 6-38, it is possible to notice that the Overall Average (63.63%) informs an averaged effectiveness of the Function. Yet, this information mislead the used about the real performance of the Function, as, for instance, the Specificity (58.65%) and Positive Predictive Value (54.43%) present low values. The take home message of the analyses of these metrics is that the user needs to be aware of the real accuracy of the predictor (CARVALHO *et al.*, 2010; 2011).

In fact, a comparison between the top left and the lower left tables on Table 6-38, illustrates the influence of the attributes of geometry, shape, and dimension (Table 5-4: n=10) on the discrimination of spills and seeps. A better result is observed on the top left than compared to the lower left, respectively, when the size information is accounted for than when it is not.

Two series of Confusion Matrixes follow below showing the results of the separate anlayses of sigma-naught (σ^o), beta-naught (β^o), and gamma-naught (γ^o) variables with (Table 6-39) and without (Table 6-40) the attributes of geometry, shape, and dimension. Again it is possible to observe the improvement when the size information is considered, as well as of the use of the Overall Accuracy versus the other metrics. The UPGMA-CCC utilizes the PC's found from variables presented on Tables 6-20 and 6-21. The CFS variables that were used to find the PC's are shown on Table 6-27.

Table 6-39: Confusion Matrixes of the Discriminant Functions (PC's) of sigma (top), beta (middle), and gamma (bottom) analyzed together with geometry, shape, and dimension variables – Size Information. Left tables: UPGMA-CCC. Right tables: CFS.

PC7	Size with Sigma	
CCC	Seep	Spill
Seep	61.98%	24.51%
Spill	38.02%	75.49%
	100.00%	100.00%

CCC	Seep	Spill	
Seep	66.80%	33.20%	100.0%
Spill	28.60%	71.40%	100.0%

CCC	Seep	Spill		
Seep	1,350	671	2,021	
Spill	828	2,067	2,895	
	2,178	2,738	4,916	Overall A.
				69.51%

PC7	Size with Sigma	
CFS	Seep	Spill
Seep	61.53%	24.65%
Spill	38.47%	75.35%
	100.00%	100.00%

CFS	Seep	Spill	
Seep	66.80%	33.20%	100.0%
Spill	29.15%	70.85%	100.0%

CFS	Seep	Spill		
Seep	1,350	671	2,021	
Spill	844	2,051	2,895	
	2,194	2,722	4,916	Overall A.
				69.18%

PC7	Size with Beta	
CCC	Seep	Spill
Seep	62.15%	24.61%
Spill	37.85%	75.39%
	100.00%	100.00%

CCC	Seep	Spill	
Seep	66.45%	33.55%	100.0%
Spill	28.26%	71.74%	100.0%

CCC	Seep	Spill		
Seep	1,343	678	2,021	
Spill	818	2,077	2,895	
	2,161	2,755	4,916	Overall A.
				69.57%

PC5	Size with Beta	
CFS	Seep	Spill
Seep	62.23%	24.80%
Spill	37.77%	75.20%
	100.00%	100.00%

CFS	Seep	Spill	
Seep	65.96%	34.04%	100.0%
Spill	27.94%	72.06%	100.0%

CFS	Seep	Spill		
Seep	1,333	688	2,021	
Spill	809	2,086	2,895	
	2,142	2,774	4,916	Overall A.
				69.55%

PC7	Size with Gamma	
CCC	Seep	Spill
Seep	61.79%	24.70%
Spill	38.21%	75.30%
	100.00%	100.00%

CCC	Seep	Spill	
Seep	66.50%	33.50%	100.0%
Spill	28.70%	71.30%	100.0%

CCC	Seep	Spill		
Seep	1,344	677	2,021	
Spill	831	2,064	2,895	
	2,175	2,741	4,916	Overall A.
				69.32%

PC5	Size with Gamma	
CFS	Seep	Spill
Seep	61.03%	25.46%
Spill	38.97%	74.54%
	100.00%	100.00%

CFS	Seep	Spill	
Seep	65.31%	34.69%	100.0%
Spill	29.12%	70.88%	100.0%

CFS	Seep	Spill		
Seep	1,320	701	2,021	
Spill	843	2,052	2,895	
	2,163	2,753	4,916	Overall A.
				68.59%

Table 6-40: Confusion Matrixes of the Discriminant Functions (PC's) of only sigma-naught (σ^o; top tables), beta-naught (β^o; middle tables), and gamma-naught (γ^o; bottom tables) analyzed separately. Left tables: UPGMA-CCC. Right tables: CFS.

PC5	Only Sigma	
CCC	Seep	Spill
Seep	54.00%	26.31%
Spill	46.00%	73.69%
	100.00%	100.00%

CCC	Seep	Spill	
Seep	70.21%	29.79%	100.0%
Spill	41.76%	58.24%	100.0%

CCC	Seep	Spill		
Seep	1,419	602	2,021	
Spill	1,209	1,686	2,895	
	2,628	2,288	4,916	Overall A.
				63.16%

PC4	Only Sigma	
CFS	Seep	Spill
Seep	55.07%	26.23%
Spill	44.93%	73.77%
	100.00%	100.00%

CFS	Seep	Spill	
Seep	69.12%	30.88%	100.0%
Spill	39.38%	60.62%	100.0%

CFS	Seep	Spill		
Seep	1,397	624	2,021	
Spill	1,140	1,755	2,895	
	2,537	2,379	4,916	Overall A.
				64.12%

PC4	Only Beta	
CCC	Seep	Spill
Seep	54.44%	28.52%
Spill	45.56%	71.48%
	100.00%	100.00%

CCC	Seep	Spill	
Seep	64.32%	35.68%	100.0%
Spill	37.58%	62.42%	100.0%

CCC	Seep	Spill		
Seep	1,300	721	2,021	
Spill	1,088	1,807	2,895	
	2,388	2,528	4,916	Overall A.
				63.20%

PC5	Only Beta	
CFS	Seep	Spill
Seep	55.62%	26.85%
Spill	44.38%	73.15%
	100.00%	100.00%

CFS	Seep	Spill	
Seep	67.05%	32.95%	100.0%
Spill	37.34%	62.66%	100.0%

CFS	Seep	Spill		
v	1,355	666	2,021	
spill	1,081	1,814	2,895	
	2,436	2,480	4,916	Overall A.
				64.46%

PC5	Only Gamma	
CCC	Seep	Spill
Seep	53.83%	26.27%
Spill	46.17%	73.73%
	100.00%	100.00%

CCC	Seep	Spill	
Seep	70.51%	29.49%	100.0%
Spill	42.21%	57.79%	100.0%

CCC	Seep	Spill		
Seep	1,425	596	2,021	
Spill	1,222	1,673	2,895	
	2,647	2,269	4,916	Overall A.
				63.02%

PC4	Only Gamma	
CFS	Seep	Spill
Seep	55.33%	27.10%
Spill	44.67%	72.90%
	100.00%	100.00%

CFS	Seep	Spill	
Seep	66.80%	33.20%	100.0%
Spill	37.65%	62.35%	100.0%

CFS	Seep	Spill		
Seep	1,350	671	2,021	
Spill	1,090	1,805	2,895	
	2,440	2,476	4,916	Overall A.
				64.18%

Table 6-41 presents the results of two Discriminant Functions: for the attributes of geometry, shape, and dimension (Table 5-4: n=10) and for the Digital Numbers (DN's) variables. While the Discriminant Function considering the size information presents the best of all results, the one using only DN's present the worse results. These are extremely positive outcomes, both, showing the relevancy of the size information on distinguishing natural from man-made oil slicks on the sea surface of the Campeche Bay region and the corroboration with the literature that DN images are not meant to be used to compare time-series of SAR imagery.

Table 6-41: Confusion Matrixes of the Discriminant Functions using the PC's: Top tables: attributes of geometry, shape, and dimension (Size Information). Bottom tables: only Digital Numbers (DN's). Left side: CCC (Cophenetic Correlation Coefficient). Right side: CFS (Correlation-Based Feature Selection). Refer to Figure 5-3 for information on data sub-divisions. See also Tables 6-32 and 6-33 for the number of PC's selected per subset, Tables 6-34 and 6-35 for more details about the Discriminant Functions, and Table 6-20 (UPGMA-CCC) and Table 6-24 (CFS) for the original variables.

PC2	Only Size	
CCC	Seep	Spill
Seep	63.11%	24.95%
Spill	36.89%	75.05%
	100.00%	100.00%

CCC	Seep	Spill	
Seep	65.02%	34.98%	100.0%
Spill	26.53%	73.47%	100.0%

CCC	Seep	Spill		
Seep	1,314	707	2,021	
Spill	768	2,127	2,895	
	2,082	2,834	4,916	Overall A.
				70.00%

PC2	Only Size	
CFS	Seep	Spill
Seep	63.16%	24.44%
Spill	36.84%	75.56%
	100.00%	100.00%

CFS	Seep	Spill	
Seep	66.16%	33.84%	100.0%
Spill	26.94%	73.06%	100.0%

CFS	Seep	Spill		
Seep	1,337	684	2,021	
Spill	780	2,115	2,895	
	2,117	2,799	4,916	Overall A.
				70.22%

PC2	Only DN's	
CCC	Seep	Spill
Seep	48.88%	34.83%
Spill	51.12%	65.17%
	100.00%	100.00%

CCC	Seep	Spill	
Seep	53.14%	46.86%	100.0%
Spill	38.79%	61.21%	100.0%

CCC	Seep	Spill		
Seep	1,074	947	2,021	
Spill	1,123	1,772	2,895	
	2,197	2,719	4,916	Overall A.
				57.89%

PC2	Only DN's	
CFS	Seep	Spill
Seep	50.68%	33.87%
Spill	49.32%	66.13%
	100.00%	100.00%

CFS	Seep	Spill	
Seep	53.09%	46.91%	100.0%
Spill	36.06%	63.94%	100.0%

CFS	Seep	Spill		
Seep	1,073	948	2,021	
Spill	1,044	1,851	2,895	
	2,117	2,799	4,916	Overall A.
				59.48%

As depicted so far, especially on Table 6-41, the differentiation of spills and seeps has shown to be feasible. Consequently, after analyzing the outcomes of all Discriminant Functions, two simple algorithms are proposed combining the synergy of the SAR backscatter signatures with the size information. These aim to enhance the discrimination capacity based on the combination of the previous Discriminant Functions.

- **Classification Algorithm:** First Design

The first classification algorithm focuses on using the information on Table 6-39: separate anlayses of sigma-naught (σ^o), beta-naught (β^o), and gamma-naught (γ^o) variables with the attributes of geometry, shape, and dimension. This idea of this algorithm is to give equal weights to the discrimination of each of the three sets of variables: sigma with size, beta with size, and gamma with size.

The configuration of this first algorithm is illustrated on Appendix 6 and its Discriminant Functions results on Table 6-42. This algorithm considers three or two of them independent of which one is identifying it correctly. This works the same when unknown samples come into play: if there are at last two identical classifications, the sample is flagged as such.

Table 6-42: Confusion Matrixes of the Discriminant Functions using the Principal Components (PC's) showing the results of the first proposed algorithm. The configuration of this algorithm is presented on Appendix 6. Left tables: UPGMA-CCC. Right tables: CFS. See text for further details.

1st Algorithm

CCC	Seep	Spill
Seep	61.87%	24.54%
Spill	38.13%	75.46%
	100.00%	100.00%

CCC	Seep	Spill	
Seep	66.80%	33.20%	100.0%
Spill	28.74%	71.26%	100.0%

CCC	Seep	Spill		
Seep	1,350	671	2,021	
Spill	832	2,063	2,895	
	2,182	2,734	4,916	Overall A.
				69.43%

1st Algorithm

CFS	Seep	Spill
Seep	61.83%	24.93%
Spill	38.17%	75.07%
	100.00%	100.00%

CFS	Seep	Spill	
Seep	65.96%	34.04%	100.0%
Spill	28.43%	71.57%	100.0%

CFS	Seep	Spill		
Seep	1,333	688	2,021	
Spill	823	2,072	2,895	
	2,156	2,760	4,916	Overall A.
				69.26%

- **Classification Algorithm:** Second Design

The second classification algorithm uses the information on Table 6-40 (i.e. separate anlayses of sigma-naught (σ^o), beta-naught (β^o), and gamma-naught (γ^o)) and on the top tables of Table 6-41 (i.e. attributes of geometry, shape, and dimension only). Appendix 6 presents the conceptual classification design, whereas Table 6-43 presents the accuracy assessment.

With a similar idea than on the first one, however, the second algorithm has four independent options of classification: size, sigma, beta, and gamma. When there is an even result for the same sample (i.e. two seep classifications and two spill classifications), the user can decide what to do. For instance, a decision can be taken to classify it as a seep if it is on a region where seeps usually occur (1st Mode) or he can consider this sample as a spill (3rd Mode) based on site location or any other decision making process.

But on the 2nd Mode, the user can leave it as an unknown oil slick, following the nomenclature utilized during the present D.Sc. research, Orphan, but on this case, an Orphan Slick. The middle tables on Table 6-43 do not consider these unknown samples as the total number of oil slicks is less than the number of oil slicks within the CBOS-DScMod: 4,916. On both cases (UPGMA-CCC and CFS), about 5.5% of the oil slicks would fall into the Orphan Slick case: n=266 and n=201, respectively. This is about one sixth to one tenth of the Orphan cases present on the CBOS-Data that were analyzed during the Data Familiarization (Phase 1: Section 6.1), as show on Figure 6-7: Orphan Spills (n=1,851; 13.0%) and Orphan Seeps (n=1,592; 11.2%).

- **The Sole Use of Two Attributes:** Area and Perimeter

Because it has been shown throughout the encompassed Multivariate Data Analysis Practice (Yellow Phases: 6 to 10, as portrayed on Figure 1-3) that the attributes of geometry, shape, and dimension (i.e. size information – 3rd Attribute Type: Table 5-4) have stood out in distinguishing natural from man-made oil slicks on the sea surface of Campeche Bay, these attributes are further explored. This means that the two basic attributes of geometry, shape, and dimensions present in the CBOS-Data content (Table 2-2) are explored in more details: area (*Area*) and perimeter (*Per*). The same Data Treatment (Phase 5: Sections 5.5 and 6.5) have been applied preceding the PCA. Two PC's have been selected. The accuracy accessment is shown on Table 6-44.

Table 6-43: Confusion Matrixes (PC's) showing the second proposed algorithm that separately explores sigma, beta, gamma, and size attributes. Left tables: UPGMA-CCC. Right tables: CFS. See text for further details.

1st Mode

CCC	Seep	Spill
Seep	52.33%	28.55%
Spill	47.67%	71.45%
	100.00%	100.00%

CCC	Seep	Spill	
Seep	67.24%	32.76%	100.0%
Spill	42.76%	57.24%	100.0%

CCC	Seep	Spill		
Seep	1,359	662	2,021	
Spill	1,238	1,657	2,895	
	2,597	2,319	4,916	Overall A.
				61.35%

1st Mode

CFS	Seep	Spill
Seep	53.89%	28.11%
Spill	46.11%	71.89%
	100.00%	100.00%

CFS	Seep	Spill	
Seep	66.11%	33.89%	100.0%
Spill	39.48%	60.52%	100.0%

CFS	Seep	Spill		
Seep	1,336	685	2,021	
Spill	1,143	1,752	2,895	
	2,479	2,437	4,916	Overall A.
				62.82%

2nd Mode

CCC	Seep	Spill
Seep	56.16%	25.70%
Spill	43.84%	74.30%
	100.00%	100.00%

CCC	Seep	Spill	
Seep	70.34%	29.66%	100.0%
Spill	39.04%	60.96%	100.0%

CCC	Seep	Spill		
Seep	1,359	573	1,932	
Spill	1,061	1,657	2,718	
	2,420	2,230	4,650	Overall A.
				64.86%

2nd Mode

CFS	Seep	Spill
Seep	57.03%	26.68%
Spill	42.97%	73.32%
	100.00%	100.00%

CFS	Seep	Spill	
Seep	69.27%	30.73%	100.0%
Spill	38.19%	61.81%	100.0%

CFS	Seep	Spill		
Seep	1,359	603	1,962	
Spill	1,024	1,657	2,681	
	2,383	2,260	4,643	Overall A.
				64.96%

3rd Mode

CCC	Seep	Spill
Seep	57.71%	23.81%
Spill	42.29%	76.19%
	100.00%	100.00%

CCC	Seep	Spill	
Seep	71.65%	28.35%	100.0%
Spill	36.65%	63.35%	100.0%

CCC	Seep	Spill		
Seep	1,448	573	2,021	
Spill	1,061	1,834	2,895	
	2,509	2,407	4,916	Overall A.
				66.76%

3rd Mode

CFS	Seep	Spill
Seep	58.07%	24.37%
Spill	41.93%	75.63%
	100.00%	100.00%

CFS	Seep	Spill	
Seep	70.16%	29.84%	100.0%
Spill	35.37%	64.63%	100.0%

CFS	Seep	Spill		
Seep	1,418	603	2,021	
Spill	1,024	1,871	2,895	
	2,442	2,474	4,916	Overall A.
				66.90%

Table 6-44: Confusion Matrixes of the Discriminant Functions using the Principal Components (PC's) exploring only the two basic attributes of geometry, shape, and dimension (Table 2-2): area (*Area*) and perimeter (*Per*).

PC2	Area & Perimeter	
	Seep	Spill
Seep	62.33%	25.18%
Spill	37.67%	74.82%
	100.00%	100.00%

	Seep	Spill	
Seep	65.02%	34.98%	100.0%
Spill	27.43%	72.57%	100.0%

	Seep	Spill		
Seep	1,314	707	2,021	
Spill	794	2,102	2,895	
	2,108	2,808	4,916	OVERALL
				69.47%

Interesting to note is that the results presented on Table 6-44 are not that different from those shown on the top tables of Table 6-41 that accounts for the PC's of different combination of variables: UPGMA-CCC (Table 6-20) and CFS (Table 6-24). The findings expressed on Table 6-44 demostrate that the sole use of area and perimeter of the oil slicks is also capable of distinguishing the oil slick type to a useful accuracy.

- **Publication:** Scientific Journal Submission

The bulk of the data mining results achieved during this D.Sc. dissertation, i.e. Workable-Database Preparation (Phases: 3 to 5) and Multivariate Data Analysis Practice (Phases: 6 to 10), have been submitted to the Remote Sensing of Environment (RSE) journal – see Appendix 1: CARVALHO *et al.* (2015c). This paper summarizes most of the outcomes of the second proposed specific goal of the present D.Sc. research: the use of RADARSAT measurements to evaluate the capacity of distinguishing the oil slick type by means of multivariate data analysis techniques.

CHAPTER 7

DISCUSSION

- **Phase 1:** Data Familiarization

The first pre-processing data verification Phase (Section 5.1 and Section 6.1) organized and analyzed the entire content of the Campeche Bay Oil Slick Satellite Database (CBOS-Data). This dataset has been produced during the Campeche Bay Oil Slick Satellite Project (CBOS-SatPro) that lasted for approximately 13 years (2000-2012) with a regular SAR image acquisition of about one RADARSAT scene per week (Table 6-3: n=766). Undeniably, the familiarization with this dataset provided means to reveal a substantial amount of information related to the spatio-temporal distribution and occurrence of 14,210 oil slicks, as reported in CARVALHO *et al.* (2015a) and CARVALHO *et al.* (2015b) – see Appendix 1.

The slightly uneven distribution pattern of oil slicks per category (Figure 6-1: n=14,210) is inverted when considering the area covered by all oil slicks (Figure 6-2: 46,693 km^2). Even though oil spills occur a little more frequently (n=8,008; 56.3%) than oil seeps (n=6,202; 43.7%), the oil spills' area coverage (15,246 km^2; 32.6%) is about half of the oil seeps (31,447 km^2; 67.4%). However, when looking into the overall class distribution, it is possible to notice that this strong pattern inversion occurs because of the relative small frequency of the Cantarell Oil Seep (Figure 6-7: n=653; 4.6%) that contrasts to its massive area coverage (Figure 6-8: 19,743 km^2; 42.3%).

An exercise of removing the Cantarell Oil Seep influence is illustrated on Figure 7-1. The total surface area coverage of oil spills (15,246 km^2; 56.6%) becomes larger than of the oil seeps without Cantarell (11,704 km^2; 43.4%), revealing that the frequency and the area covered by oil spills are larger if compared to all other oil seeps. Indeed, the Cantarell Oil Seep signature has been present in most RADARSAT scenes analyzed during the CBOS-SatPro: 85%. This exercise corroborates previous findings about its massive HC contribution in this region as the most prominent in area coverage, dimension, flow magnitude, and persistence (e.g. MENDOZA *et al.*, 2004a).

An analysis presented by QUINTERO-MARMOL *et al.* (2003) uses data from the first few years of CBOS-SatPro (2000-2002) to give a picture of Cantarell Oil Seep activity. Out of the analyzed 83 SAR scenes, its signature was observed in 66 images: 79.5%. The area covered by its seeped oil ranged from 0.04 to 207.4 km^2, having an average

of 32 km^2. Even though these authors used a small sample ([(83/766)*100]=11%) of the RADARSAT scenes explored herein, their findings match the values observed on the present D.Sc. research, for instance, 85% ([(653/766)*100]) for the Cantarell Oil Seep observation rate (Table 6-3) and 30.2 km^2 for its surface area coverage (Table 6-8), respectively.

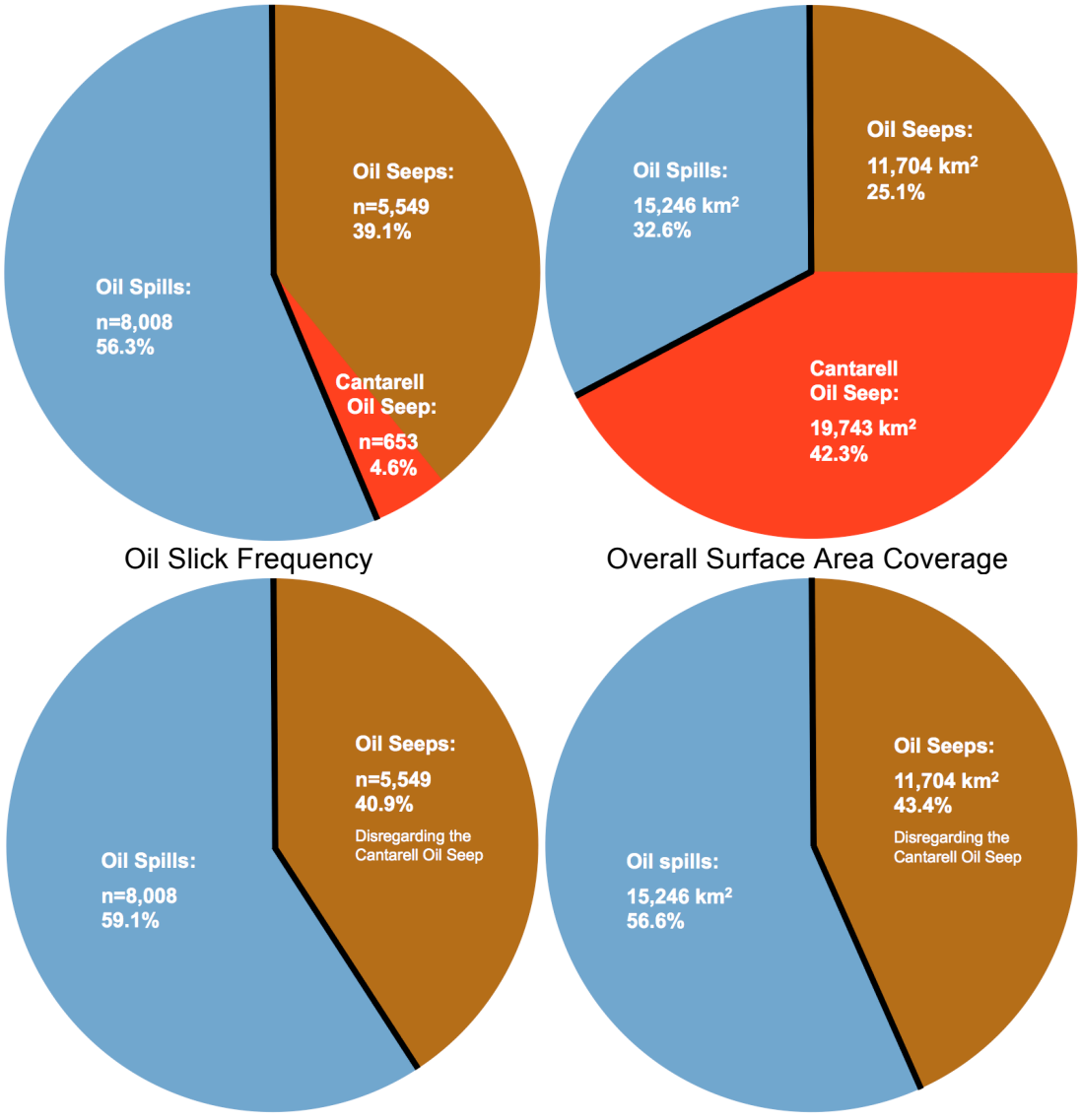

Figure 7-1: Exercise of removing the influence (or occurrence) of the Cantarell Oil Seep from the Campeche Bay Oil Slick Satellite Database (CBOS-Data), thus revealing its massive contribution achieved with its small frequency of occurrence. This also shows that the frequency and the area coverage by oil spills are larger if compared to all other oil seeps. Left panels: oil slick frequency. Right panels: total surface area coverage. Upper and lower panels show results respectively, with (shown in red) and without the Cantarell Oil Seep.

The information depicted on Figure 6-5 and Figure 6-6 contains a few worthy of note observations:

1. The 88 identified Clusters (n=3,957; 63.8% of oil seeps) have larger representativeness frequency than Orphan Seeps (n=1,592; 25.7%), as well as they occupy a larger surface area: 8,947 km^2 (28.4%) versus 2,757 km^2 (8.8%). This is consistent with the hypothesis that seeped oil moves vertically through the water column in most of the Campeche Bay region – see Section 2.3.4 for Cluster definition and Section 3.2 for information about natural hydrocarbon seepages at sea;

2. The 10 Brightspots ≥ 100 different oil spill observations correspond to more than half (i.e. n=4,342; 54.2%) of the oil spill entries, but its superficial area coverage (5,424 km^2; 35.6%) is quite similar to the one of the 61 Brightspots with ≤ 99 different oil spill observations (5,690 km^2; 37.3%) that have a much smaller frequency (n=1,263; 15.8%). This reveals that despite the larger frequency, such oil spills from those 10 Brightspots are of a much smaller size; and

3. The number of identified sources within the observed oil spills (i.e. Brightspots and Ship Spills: n=6,157; 76.9%) is much larger than the number of Orphan Spills (n=1,851; 23.1%). This revels the high rate of correct identification of the CBOS-SatPro, and demonstrates the success of the Pemex Validation (CBOS-SatPro Part 6: Section 2.3.6) that corroborates the operator interpretations.

Regarding the Brightspot class information, the 10 Brightspots that have been registered having ≥ 100 different oil spill observations, which are color-coded in light blue (Figure 6-3: n=4,342), correspond to more than half of the observed oil spills (Figure 6-5: 54.2%) and to about one third of the oil slicks entries of the CBOS-Data (Figure 6-7: 30.5%). Nevertheless, its surface area coverage contributions (Figure 6-6: total coverage 35.6% and Figure 6-8: overall coverage 11.6%) is about the same as of the other 61 Brightspots that have ≤ 99 different oil spill observations (Figure 6-6: total coverage 37.3% and Figure 6-8: overall coverage 12.2%), even though these have 3.5 times less oil spills (Figure 6-5: n=1,263).

From the size distribution shown on Table 6-8, oil spills from the 10 Brightspots have a much smaller average size (i.e. 1.3 km^2 against 4.5 km^2); however, the larger average size of the 61 Brightspots is taking into account a major oil spill event occurred in November 2007 in one of its Brightspots – this has been imaged at least 8 times as shown on Table 6-8 with one asterisk.

An exercise can be executed by taking the oil spills from this atypical event (that sum 3,006.4 km^2 – Table 6-8) out of the size distribution calculation. In doing so, the average size of the oil slicks from the 61 Brightspots with ≤ 99 different oil spill observations drastically lowers to from 4.5 to 2.2 km^2 (Table 6-8). A slight drop is also observed on the average sizes of all oil spills (from 1.9 to 1.5 km^2) and all oil slicks (from 3.3 to 3.0 km^2). Hence, this exercise demonstrates that a single major oil spillage can largely influence not only the environment, but also the oil slicks' statistics information of any dataset.

Another disclosure about the size distribution of the oil slicks (Table 6-5) is that most of them (n=9,398; 66.1%) have "small" surface area coverage (i.e. < 1 km^2). This pattern is more preeminent among oil spills (Table 6-6: n=6,196; 77.4%) than oil seeps (Table 6-7: n=3,202; 51.7%), independent of the RADARSAT satellite. Oil slicks with "large" surface area coverage (i.e. ≥ 10 km^2) correspond to a minor part of the observations (Table 6-5: n=734; 5.2%).

An additional aspect to highlight considering the size distribution is that the average oil slick size is 3.3 km^2 (Table 6-8). Also, oil seeps (5.1 km^2) tend to be larger on average than the oil spills (1.9 km^2). However, this averaging calculation takes into account the Cantarell Oil Seep influence, and its removal drops the oil slicks' size to 3.0 km^2 and the oil seeps's size to 2.1 km^2.

A worth of notice comparison can be made between the Campeche Bay oil spills within the CBOS-Data and the oil spills analyzed by BENTZ (2006) off the SE of Brazil (Campos Basin). BENTZ analysis is based on 402 RADARSAT-1 images acquired from July 2001 to June 2003 and the average size of the 358 oil spills (~6.5 km^2) is more about three times larger than the average size of the oil spills observed in Campeche Bay during the CBOS-SatPro.

The water column depth (i.e. *Wdepth* attribute) in the location where the oil slicks have been observed on the sea surface revealed an interesting aspect about the oil slicks' occurrence. For instance, on Figure 6-16, oil spills (96%) usually tend to occur in water depths shallower than 100 m (corresponding to the location of the Campeche Bay OGEPI activity), whereas oil seeps (63%) commonly occur in waters deeper than 1000 m (related to the offshore salt tectonic province). The average water depths are: 484 m (oil slicks), 73 m (oil spills), and 1,296 m (oil seeps) – Table 6-10.

- **Phase 2:** Quality Control (QC)

Despite this major data reduction that eliminated a fairly amount of information from the CBOS-Data, i.e. from 14,210 oil slicks to 4,916 oil slicks (35%), the outcomes of the QC-standards guaranteed that its handful basic attributes met certain requirements to enable high-quality data to be used in the workable database preparation. This surely supports the conciseness of the Campeche Bay Oil Slick Modified Database (CBOS-DScMod) information to reach the goals of the present D.Sc. research.

The 277 RADARSAT-2 images (Table 6-11: 16-bit, VV-polarized) corresponds to approximately 36% of 766 scenes utilized during the CBOS-SatPro (Table 6-3). Likewise, the other reduction, i.e. on the oil slick of frequency (n=4,916), leaves to be explored herein, only about 35% of the initial 14,210 oil slicks (Figure 6-1). Conversely, if a comparison is made only regarding the RADARSAT-2 imagery (Figure 6-10), this cut is less prominent, as 97% (n=277) out of the 284 scenes (Table 6-3) and 87% (n=4,916) out of the 5,314 oil slicks are kept in the analysis.

As anticipated, this data reduction pattern also occurs on the frequency of oil slicks per category. The QC-Standards reduce oil seeps to 2,021 (33% of 6,202) and oil spills to 2,895 (36% of 8,008) – see Figure 6-1. Considering only RADARSAT-2 imagery: 95% (n=2,021) out of the 2,136 oil seeps and 91% (n=2,895) out of the 3,178 oil spills are kept in the analysis – see Figure 6-11.

- **Phase 3:** RADARSAT Image Re-Processing

The re-processing of the RADARSAT-2 images has been accomplished following the processing procedures executed during the CBOS-SatPro (Figure 2-2). However, three steps were not performed herein: APC, image contrast enhancement, and radiometric re-scalling. In addition, the DN values were converted to radiometric-calibrated image products (Table 5-1: σ^o, β^o, and γ^o).

These procedures assured the successful investigation of the three types of SAR backscatter coefficients to distinguish oil spills from oil seeps. With these image-processing procedures, the use of RADARSAT-2 measurements to design the classification has been demostrated.

- **Phase 4:** New Slick-Feature Attributes

Even though the CBOS-DScMod (2008-2012: Section 5.4) represents a spatio-temporal sample of the CBOS-Data (2000-2012: Section 2.3), it surely serves as a benchmark describing the oil slicks' observed in the Campeche Bay region. A collection of slick-feature attributes used to describe the oil slicks observed in Campeche Bay are represented by contextual information (Table 5-2: n=6), satellite scene descriptors (Table 5-3: n=37), geometry, shape, and dimension attributes (Table 5-4: n=10 –, size information), and SAR backscatter signature (Table 5-5: n=432). These account for 485 different descriptors that are further expanded once undergoing the Data Treatments (Phase 5). Indeed, the reference levels shown on Section 6.4 (and in Appendices 2 and 3) conclusively characterize the analyzed radiometric-calibrated image products (Table 5-1: σ^o, β^o, and γ^o) and their typical values (i.e. a set of basic qualitative-quantitative statistics: minimum, maximum, average, and standard deviation).

- **Phase 5:** Data Treatment

The amount of work put into the Data Treatment has shown to be successful on the course of this D.Sc. research. It guaranteed quality of the statistical data comparison of attributes with different units and those with qualitative values. The 485 different attributes used to describe the CBOS-DScMod's oil slicks have undergone four Data Treatments, thus accounting for 511 variables (485-7+33): Negative Values Scaling (altering the values of all pixels inside the oil slicks to positive values), Log_{10} Transformation (bringing the frequency of distribution of all variables to, or at least close to, a Gaussian distribution), Ranging Standardization (coding all qualitative variables to have values between 0 and 1), and Dummy Variables. The latter is responsible for the replacement of 7 qualitative attributes (e.g. Category, Class, Bmode, etc.) with 33 new Dummy Variables (binary-coded to 1 or 0) – Table 5-10.

The two contextual *cLAT* and *cLONG* attributes have been replaced by six new variables: three for the latitude domain (*RG1.LAT*, *RG2.LAT*, and *PKD.LAT*) and three analogous ones for the longitude domain (*RG1.LONG*, *RG2.LONG*, and *PKD.LONG*). The former two are Dummy Variables and the latter is an unusual data treated makeover. These variables reveal the existence of two populations that are domain-specific and directly coupled with the two regions: *POP1.LAT* and *POP2.LAT*, and *POP1.LONG* and *POP2.LONG* – such acronyms have not been further used on this research.

- **Phase 6:** Attribute Selection

The two attribute selection methods, i.e. UPGMA (Unweighted Pair Group Method with Arithmetic Mean) and CFS (Correlation-Based Feature Selection), have proposed thirty-three optimal subsets of attributes to reduce the dimensionality of the eleven original sets of data within the CBOS-DScMod (Figure 5-3). These optimal subsets were explored in the Multivariate Data Analysis Practices shown as the Yellow Phases (6 to 10) on Figure 1-3. As anticipated, the removal of variables with similar characteristics yields good results in designing the proposed classification algorithm. As expected, the optimal variable subsets (attribute-wise) helped to verify eventual associated uncertainties in the process of distinguishing the oil slick type (HALL, 1999).

- **Phase 7:** Principal Components Analysis (PCA)

The application of the PCA's has added value to the data reduction proposed by the Attribute Selection (Phase 6). There was not a rigorous unchanging cut-off to select the Principal Components (PC's), instead, the new set of variables (i.e. PC's) were selected using a compound strategy based on the analysis of the Scree Plot (i.e. broken stick with bootstrapping) and the Kaiser-Guttman criterion (i.e. eigenvalue greater than 1). This seems a reasonable practice that followed strict guiding principles from the literature to make sure a handful of meaningful PC's were selected. In fact, the the Discriminant Analysis (Phase 8) explored the score values of the selected PC's.

- **Phase 8:** Discriminant Function

The several Discriminant Functions (n=78) are, in essence, one of the cores outcomes of the present D.Sc. research. Various metrics have been used to assess the accuracy of the Discriminant Analyses completed: Overall accuracy, Sensitivity, Specificity, False Negative and Positives, Positive and Negative Predictive Values and their Inverse. These help to decide the cost of misdiscrimination.

- **Phase 9:** Correlation Matrix

Even after a thorough data reduction (Attribute Selection: Phase 6), there optimal subsets were still presenting inter-variable correlation. However, the use of meaningful PC's strictly selected made possible the use of half of the Discriminant Functions, i.e. those exploring the PC's, to accomplish the distinguishment of the oil slick type.

- **Phase 10:** Oil Slick Classification Algorithm

The assessment of the accuracy of the Discriminant Function exploring the PC's has demonstrated that the differentiation between oil spills and oil seeps is indeed not an easy task to be achieved. This might explain why this subject is not that much discussed on the published peer reviewed literature, or even on grey literature. However, the way the present D.Sc. research has been guided towards the extensive use of Data Treatments and multivariate data analysis techniques has shown that it is possible to distinguish natural from man-made oil slicks using RADARSAT measurements.

CHAPTER 8

CONCLUSIONS

As peer-reviewed and grey literature are somewhat short about the topic of differentiating oil seeps from oil spills, the investigation carried out during the present D.Sc. research has largely contributed to the scientific remote sensing research community, as well as to the oil and gas exploration and production industry (OGEPI). The field of environment monitoring also has gained knowledge with the fruitful outcomes shown herein. The main objective of performing an exploratory data analysis (EDA) to distinguish natural from man-made oil slicks observed on the sea surface of Campeche Bay using RADARSAT measurements has been successfully accomplished achieving up to 70% of Overall Accuracy on the distinguishment between natural and man-made oil slicks on the sea surface observed on the Campeche Bay region (Gulf of Mexico). This has been completed using classical multivariate data analysis of satellite-derived measurements of the Canadian RADARSAT satellite.

The first proposed specific goal has also been accomplished with high-quality outcomes. The spatio-temporal distribution of the oil slicks present on Campeche Bay Oil Slick Satellite Database (CBOS-Data) has been thoroughly investigated. These oil slicks were observed during the Campeche Bay Oil Slick Satellite Project (CBOS-SatPro). The scientific investigation exploring this dataset has disclosed interesting aspects about the occurrence of oil slicks observed on the sea surface. This is not only relevant to a specific region, i.e. Campeche Bay, as the findings presented herein can serve as a reference for comparison with other regions where oil slicks are observed on the surface of the ocean. An entirely dedicated Section promoted an enormous amount of information about oil slicks distribution. A complete extended abstract and a scientific publication have come out of the Data Familiarization practice: CARVALHO *et al*. (2015a; 2015b). The description of the spatio-temporal distribution of 14,210 oil slicks using RADARSAT-derived measurements has also proven the capabilities of this remote sensing tool to perform long-term operational environmental monitoring.

Even though the present D.Sc. research is not the first study to analyze the information produced during the Campeche Bay Oil Slick Satellite Project (CBOS-SatPro) – e.g. BEISL *et al.*, 2004; MENDOZA *et al.*, 2004a; PEDROSO *et al.*, 2007 – it is the first one to investigate all oil slicks within the Campeche Bay Oil Slick Satellite Database (CBOS-Data: n=14,210). Another distinguishing aspects of the present investigation

are the strategy of inspecting a considerable fraction of this dataset – i.e. Campeche Bay Oil Slick Modified Database (CBOS-DScMod: n=4,916) – with a comprehensive data filtering, an expansive data customization, and a multivariate data analysis approach. An additional original aspect about the present D.Sc. research is indeed the exploration of the different subset divisions (attribute-wise: Figure 5-3).

The core of the large historical archive of oil slick sites in the Campeche Bay region, i.e. Campeche Bay Oil Slick Satellite Database (CBOS-Data), is threefold: date/time of the SAR overpasses, the location of the oil slicks, and their vectorized shape polygon (*.shp* file). Indeed, the foremost outcome of the Campeche Bay Oil Slick Satellite Project (CBOS-SatPro) is the validated categorization and classification of the observed oil slick. While the former corresponds to oil spills and oil seeps, the latter classifies the member of these two categories into classes: OGEPI facility or ship information help to indicate whether the oil slick is a Brightspot or Ship Spill, and their absence usually indicates an oil seep Cluster, e.g. Cantarell Oil Seep (Figure 1-1 and Figure 2-1). Exceptions are Orphan Seeps and Orphan Spills.

Even though the CBOS-SatPro is mostly focused on finding oil slicks directly related to Pemex's sphere of influence, two aspects confirm that the content of the CBOS-Data is capable of depicting the seasonality of the oil slick occurrence in Campeche Bay. The first one is the regional context of the explored RADARSAT image frames that covers a considerable area surrounding the Cantarell Oil Field. The second one is the documented timescale of more than a decade of Pemex's monitoring program, acquiring enough data (i.e. 766 SAR images that imaged 14,210 oil slicks) to picture, understand, and provide useful information about the dynamics of oil slicks observed in the Campeche Bay region.

The use of an assorted pool of classical multivariate data analysis techniques have been effectively applied to analyze the remote sensing library content of the Campeche Bay Oil Slick Modified Database (CBOS-DScMod). It is true that the existence of the CBOS-Data served as a justification for this research, but the Data Treatment and the data mining practice surely assured the accomplishment of the main objective of this D.Sc. research, i.e. distinguishing seeps from spills (CARVALHO *et al*., 2015c).

The three scientific questions are also answered based on the solid research findings presented on this D.Sc. manuscript:

- Does seeped oil floating on the ocean surface have SAR backscatter signature distinctive enough to distinguish it from anthropogenically-spilled oil?

Yes, oil seeps and oil spills can be differentiated, to some extent (63-68% of Overall Accuracy), by looking into only the SAR backscatter signature, i.e. sigma-naught (σ^o), beta-naught (β^o), and gamma-naught (γ^o), as retrieved by satellite remote sensing.

- Can the geometry, shape, and dimensions of oil slicks, as determined by digital image classification of satellite imagery, be used to distinguish seeps from spills?

Yes, oil seeps and oil spills can be differentiated to a better accuracy (~70% of Overall Accuracy) by looking into size information (i.e. attributes of geometry, shape, and dimension: e.g. area and perimeter) as determined by digital image classification.

- Which combination of characteristics leads to the generation of a system capable of distinguishing between seeped and spilled oil?

The exploratory data analysis performed during the present D.Sc. research have shown that different combinations of variables are able to promoted similar differentiation between oil seeps and oil spills. The combination leading to the most effective classification of the oil slick type uses several attributes of geometry, shape, and dimensions – more specifically, area and perimeter of the oil slicks. On the other way, the attributes with the worse capabilities are those expressed in Digital Numbers (DN's).

Different qualitative-quantitative classification algorithms have been proposed, all simple-to-use. There is no complicatedness at all on their formulation or design. These ranged from very simple ones based on the sole use of SAR backscatter signature or size information, to orher also uncomplicated and simple algorithms combining the synergy of different variables.

The algorithms herein investigated encourage a novel way to link geochemistry and remote sensing research, thus suggesting that geophysical differences between seeped and spilled oil can indeed be used to distinguish the oil slick type by means of satellite measurements. In fact, the outcomes of the present D.Sc. research are indications that the differentiation between oil seeps and oil spills should be deeper investigated with convention approaches commonly used to identify dark spots in SAR imagery, e.g. Artificial Neural Networks (ANN) (e.g. GARCIA-PINEDA *et al.*, 2008; 2009; 2010). In the same direction, ways to differentiate oil slick type could indeed investigate polarimetric SAR measurements (e.g. VELOTTO *et al.*, 2010; 2011).

The successful findings of the present D.Sc. research open a new way, i.e. by means of classical multivariate data analysis techniques, to investigate the differentiation of the various targets observed in SAR imagery, e.g. oil slicks from look-alike features. Conclusively, as the most effective differentiation achieved herein has been accomplished using the oil slick size information, this is a significant result for the scientific community. In fact, if the techniques applied herein are capable of distinguishing oil from oil, what can they achieve if applied with the purpose of discriminating oil from, for instance, a harmful algal bloom or even a low wind zone signature on SAR imagery?

CHAPTER 9

RECOMMENDATIONS FOR FUTURE WORK

- **Phase 1:** Data Familiarization

Despite the careful labor-intensive data inspection performed to organize and become familiarized with the CBOS-Data information (Phase 1: Sections 5.1 and 6.1), some discrepant entries have not been corrected or removed during this initial pre-processing data verification. For instance, the polygon representing the largest Cantarell Oil Seep record (Area: 1,789.0 km^2) has a very small measurement of its border (Perimeter: 18.3 km) – incompatible to its size (Figure 6-15). Although this has been observed in December of 1999 with RADARSAT-1 and does not bring to much concern to the designed oil slick classification algorithm, the spatio-temporal distribution is indeed influenced by particular inaccuracies of this nature. In addition, this calls the attention to the fact that any other inconsistency may have passed through the analysis performed during Phase 1: Data Familiarization. Perhaps, an assessment based on the actual values of each slick-feature attribute (Table 2-2) could avoid the insertion of any inconsistent data entries of this nature and reduce the propagation of eventual errors in the processing chain – i.e. an evaluation of the original CBOS-Data could be carried out with more stringent criteria than those performed herein.

The water column depth attribute (*Wdepth*) disclosures valuable information about the spatial distribution of the oil slicks observed in the Campeche Bay region (Figure 6-16) However, such information was not logged for oil slicks within the CBOS-Data (Table 6-10: n=5,669; 40%). As this is a relevant contextual aspect to be considered, a finer picture of local bathymetry can be obtained to the position of the oil slick centroid from public domain dataset of the Earth TOPOgraphy database at one-minute grid resolution (ETOPO1, 2013).

- **Phase 2:** Quality Control (QC)

An investigation could be performed with less stringent QC-Standards, and, for instance, ana anslysis could explore the entired content of the CBOS-Data that includes measurements from the two RADARSAT satellites – both 16-bit and 8-bit, as well as VV and HH polarized images. Such assessment could reveal differences, or not, based on the sensors' characteristics to distinguish the oil slick type.

Data separation in various regions and seasons of the year radically reduces the number of valid samples to work with (CARVALHO *et al.*, 2010d; 2011). Undeniably, this justifies the use of the whole content of the CBOS-DScMod to start the analysis performed herein. The exercise of analyzing a specific spatio-temporal distribution of oil slicks separated by region and/or by season or by years (e.g. CARVALHO, 2008), could be a singularity of a further investigation aiming to distinguish the oil slick type.

- **Phase 3:** RADARSAT Image Re-Processing

Because the present D.Sc. research only investigated the various forms of radiometric-calibrated image products together (i.e. *SIG.amp*, *SIG.amp.FF*, *SIG.dB*, *SIG.dB.FF*, *BET.amp*, *BET.amp.FF*, *BET.dB*, *BET.dB.FF*, *GAM.amp*, *GAM.amp.FF*, *GAM.dB*, and *GAM.dB.FF* – C_1 and C_2 – 12x2=24), a study could be designed that the different SAR backscatter signature could be explored in separate. This could disclose which of them brings the best distinguishment capabilities.

- **Phase 4:** New Slick-Feature Attributes

As the investigation carried out herein only explored information from the inside of polygons delimiting the oil slicks, the information from the area surrounding oil seeps and oil spills (i.e. background oil-free surface – damping ratio) could come into play (HOLT, 2004). BENTZ (2006) suggests using a buffer zone of 20 km from the border of the oil slick; however, this practice does not guarantee that the selected surrounding region does not have any oil influence.

The SAR backscatter signature can give a picture of the local area contrast (TOPOUZELIS *et al.*, 2007). FISCELLA *et al.* (2010) suggest the use of an intensity ratio (ITR) to relate the averaged properties inside of the oil slicks with the ones of the water outside the oil slicks. However, this has only been evaluated in the differentiation between oil slicks and look-alike features: high contrast (i.e. large ITR) are related to oil, whereas low contrast (i.e. small ITR) are due to look-alike features (SENGUPTA & SAHA, 2008). Another ratio from FISCELLA *et al.* (2010) is the intensity standard deviation ratio (ITRstd), which is the ITR divided by the standard deviation inside and outside of the oil slick.

Fractal geometry can be used to characterize the roughness and self-similarity of different features on satellite imagery (SARKAR & CHAUDHURI, 1994). The concept of fractal dimension can be used to measure, analyze, and classify shapes and textures. Several authors have proposed different approaches to estimate fractal dimension of features in satellite images (e.g. GADE & REDONDO, 1999; MARGHANY *et al.*, 2009).

The fractal dimension of the oil slicks' polygons could be calculated with the box-counting method (KLINKENBERG, 1994) or with the dynamic fractal approach (BEVILACQUA *et al.,* 2008).

A noteworthy assessment of the oil volume of the Cantarell Oil Seep has been performed by QUINTERO-MARMOL *et al.* (2003). Using SAR measurements from 2000-2002 these authors obtain the typical color of the Cantarell Oil Seep oil, which varies from Silvery to Rainbow. An equivalent oil volume equivalency input per square kilometer is achieved based on a color-to-density scale (BONN, 2009). They used the minimum and maximum area and estimated a median volume contribution of 3.24 tons per day, giving 1,182 tons per year. In the same way, using the Oil Appearance Code presented on the Bonn Agreement Aerial Operations Handbook (BONN, 2009), volume estimations of each polygon could be accounted for the minimum and maximum typical volume of the oil slicks observed in the Campeche Bay region.

The number of individual non-contiguous oil slick's parts forming the polygons (*NUMparts*) could also be explored (BENTZ, 2006). BENTZ (2006) also suggests other contextual entries such as centroid distance from its point source (*Dsource*) that can be a oil rig complex or an oil seep Cluster, and centroid distance from shoreline (*Dshore*).

- **Phase 5:** Data Treatment

Other approaches could be applied during the Data Treatment practice, for instance, cubic root instead of Log_{10} Transformation, and z-score instead of Ranging Standardization.

- **Phase 6:** Attribute Selection

Instead of forming groups using the two the threshold (i.e. cut-off level – UPGMA-CCC and UPGMA-Fixed) in the implementation of the UPGMA (Unweighted Pair Group Method with Arithmetic Mean), a visual analysis of the dendograms could be instituted to choose the groups of variables. However, this would introduce a somewhat subjectivity that could invalidate replicability, as of the individual interpretations. The use of other methods is also recommended (e.g. Ward's).

- **Phase 7:** Principal Components Analysis (PCA)

Different "stopping rule" methods, other then the Jolliffe Cut, Knee Test, Scree Plot, or Kaiser Criterion, could be used in the process of selecting meaningful Principal Components (PC's) (PERES-NETO *et al.*, 2003; 2005; LEDESMA & VALERO-MORA, 2007).

- **Phase 8:** Discriminant Function

Herein, only the first exploratory part of the Discriminant Analysis has been accomplished to discriminate (i.e. discriminate) “old” objects (HAIR *et al.*, 2005). Perhaps, the second part of the Discriminant Analysis that classify “new” objects could be exercised with samples from a separate dataset, or by dividing the CBOS-DScMod into small portions to perform such classification.

- **Phase 9:** Correlation Matrix

This seems a required stage in the use of Discriminant Functions, thus guaranteeing that no inter-variable correlation is present.

- **Phase 10:** Oil Slick Classification Algorithm

Among the many studies found in the published scientific literature, there is a gap regarding the use of several satellites for detecting and monitoring oil slicks (BREKKE & SOLBERG, 2005a; 2005b). the use of data mining techniques to find useful Association Rules and to build classification algorithms is not the subject of many oil slick detection analyses (QUISPE, 2003; DA SILVA, 2008). This could be used to distinguish the oil slick type. In addition to that, such activity would also be explored by using commonly approaches used to identify dark spots in SAR imagery, e.g. Artificial Neural Networks (ANN) (e.g. GARCIA-PINEDA *et al.*, 2008; 2009; 2010). Last but not least, the multivariate data analysis approach explored herein could be used to diferentiate oil slicks from look-alike features.

- **Further Research:** Clustering Analysis

Clustering Analyses (e.g. K-means) could reveal natual groupings among the oils slicks observed in the Campeche Bay region, thus supporting the differentiation of the oil slick type.

REFERENCES

ABDI, H., WILLIAMS, L. J., 2010, “Principal component analysis, Overview”, *WIREs Computational Statistics*, v. 2, pp. 433-459, doi: 10.1002/wics.101. Available online: < https://www.utdallas.edu/~herve/abdi-awPCA2010.pdf >. Accessed on: 15 November 2015.

ABRAMS, M. A., 1996, "Distinction of surface hydrocarbon seepage in near-surface marine sediments". In: Schumacher, S., ABRAS, M. A. (eds), *Hydrocarbon migration and its near-surface expression*, AAPG Memoir 66, Tulsa, Oklahoma, American Association of Petroleum Geologists, pp. 1-14.

ADAMO, M., DE CAROLIS, G., DE PASQUALE, V., PASQUARIELLO, G., 2006, "Oil spill surveillance and tracking with combined use of SAR and MODIS imagery: a case study". In: *Proceedings of the International Geoscience and Remote Sensing Symposium (IGARSS '06), IEEE,* pp. 1327-1330, Denver, Colorado, 31July-4 August.

ADAMO, M., DE CAROLIS, G., DE PASQUALE, V., PASQUARIELLO, G., 2005, "Combined use of SAR and Modis imagery to detect marine oil spills". In: *Proceedings of the Symposium in Remote Sensing: SAR Image Analysis, Modeling, and Techniques VII, SPIE*, v. 5980, 12p., Bruges, doi: 10.1117/12.627505.

ADAMO, M., DE CAROLIS, G., DE PASQUALE, V., PASQUARIELLO, G., 2007, "Exploring sunglint signatures from MERIS and MODIS imagery in combination to SAR data to detect oil slicks". In: *Proceedings of the Envisat Symposium, ESA,* 6p., Montreux, Switzerland, 23-27 April.

AHA, D. W., BANKERT, R. L., 1994, "Feature selection for case-based classification of cloud types: An empirical comparison", *Case-Based Reasoning: Papers from the 1994 Workshop (Technical Report WS-94-01)*, *Advancement of Artificial Intelligence (AAAI),* p.106-112, Menlo Park, CA. Available online: < https://www.aaai.org/Papers/Workshops/1994/WS-94-01/WS94-01-019.pdf >. Accessed on: 14 November 2015.

AIRBUS (Defense & Space), 2014a, *Radiometric Calibration of TerraSAR-X Data: Beta Naught and Sigma Naught Coefficient Calculation*. In: Technical Report TSXX-ITD-TN-0049, May, 15p. Available online: < http://www2.geo-airbusds.com/files/pmedia/public/r465_9_tsx-x-itd-tn-0049-radiometric_calculations_i3.00.pdf >. Accessed on: 14 November 2015.

AIRBUS (Defense & Space), 2014b, *TerraSAR-X Value Added Product Specification*. In: Technical Report TSXX-ITD-SPE-0009, Issue/Revision: 1/3, 17 of June, 26p. Available online: < http://www2.geo-airbusds.com/files/pmedia/public/r20200_9_tsx-x-itd-spe-0009_va_product_spec_i1.3ext.pdf >. Accessed on: 14 November 2015.

ALBERG, A. J., PARK, JI W., HAGER, B. W., BROCK, M. V., DIENER-WEST, M., 2004, "The use of 'Overall Accuracy' to evaluate the validity of screening or diagnostic tests", *Journal of General Internal Medicine*, v. 19, n. 5, part 1, pp. 460-465, doi: 10.1111/j.1525-1497.2004.30091.x. Available online: < http://www.ncbi.nlm.nih.gov/pmc/articles/PMC1492250/pdf/jgi_30091.pdf pdf >. Accessed on: 18 November 2015.

ALBUQUERQUE, R. C. L., 2004, *Aplicação do sensoriamento remoto e do sistema de informações geográficas na detecção de manchas de óleo na região do Pólo de Exploração de Guamaré, R.N.* M.Sc. Thesis, Universidade Federal do Rio Grande Do Norte (UFRN), Natal, Brazil, 74p., in Portuguese. Available online: < http://repositorio.ufrn.br:8080/jspui/handle/123456789/18786 >. Accessed on: 14 November 2015.

ALEXANDER, I. ,2008, "Evaluating design options against requirements: How far can statistics help?". In: *Proceedings of the 16th International Requirements Engineering Conference, RE 2008*, *IEEE*, pp. 259-264, Barcelona, Catalunya, Spain, 8-12 September, doi: 10.1109/RE.2008.14. Available online: < http://www.scenarioplus.org.uk/papers/statistics.pdf >. Accessed on: 15 November 2015.

ALI, Z., BARNARD, I., FOX, P., DUGGAN, P., GRAY, R., ALLAN, P., BRAND, A., STE-MARI, R., 2004a, "Description of RADARSAT-2 synthetic aperture radar design", *Canadian Journal of Remote Sensing*, v. 30, n. 3, pp. 336-344, doi: 10.5589/m03-078.

ALI, Z., KROUPNIK, G., MATHARU, G., GRAHAM, J., BARNARD, I., FOX, P., RAIMONDO, G., 2004b, "RADARSAT-2 space segment design and its enhanced capabilities with respect to RADARSAT-1", *Canadian Journal of Remote Sensing*, v. 30, n. 3, pp. 235-245, doi: 10.5589/m03-077.

ALMEIDA-FILHO, R., MIRANDA, F. P., LORENZZETTI, J, A., PEDROSO, E. C., BEISL, C. H., LANDAU, L., BAPTISTA, M. C., CAMARGO, E. G., 2005, "RADARSAT-1 images in support of petroleum exploration: the offshore Amazon River mouth example", *Canadian Journal of Remote Sensing*, v. 31, n. 4, pp. 289-303, doi: 10.5589/m05-013.

ALPERS, W., 2002, "Remote sensing of oil spills". In: *Proceedings of the Symposium of Maritime Disaster Management*, pp. 57-68, Dhahran, Saudi Arabia, 19-23 January.

ALPERS, W., ESPEDAL, H. A., 2004, "Oils and surfactants". In: Jackson, C. R., Apel, J. R. (eds), *Synthetic Aperture Radar Marine User's Manual,* NOAA/NESDIS, Office of Research and Applications, Chapter 11, pp. 263-275. Washington, DC, USA. Available online: < http://www.sarusersmanual.com >. Accessed on: 14 November 2015.

ALPERS, W., HUHNERFUSS, H., 1989, "The damping of ocean waves by surface films: A new look at an old problem", *Journal of Geophysical Research: Oceans*, v. 94, n. C5, pp. 6251-6265, doi: 10.1029/JC094iC05p06251.

ALZAGA-RUIZ, H., LOPEZ, M., ROURE, F., SÉRANNE., M., 2009, "Interactions between the Laramide Foreland and the passive margin of the Gulf of Mexico: Tectonics and sedimentation in the Golden Lane area, Veracruz State, Mexico, *Marine and Petroleum Geology*, v. 26, pp. 951-973, doi: 10.1016/j.marpetgeo.2008.03.009.

ANDERSON L. O., LATORRE, M. L., SHIMABUKURO, Y. E., ARAI., E., CARVALHO JÚNIOR, O., A., 2003, *Sensor MODIS: Uma abordagem geral.* In: INPE-10131-RPQ/752, INPE, São José dos Campos, 58p.

ANDERSON, S., RAUDSEPP, U., UIBOUPIN, R., 2010a, "Oil Spill statistics from SAR images in the North Eastern Baltic Sea ship route in 2007–2009". In: *Proceedings of the International Geoscience and Remote Sensing Symposium (IGARSS '10), IEEE,* pp. 1883-1886, Honolulu, Hawaii, 25-30 July, doi: 10.1109/IGARSS.2010.5653222.

ANDERSON, S., UIBOUPIN, R., VERJOVKINA, S., RAUDSEPP, U., 2010b, "SAR imagery and Seatrack Web as decision making tools for illegal oil spill combating – a case study". In: *Proceedings of the IEEE/OES US/EU Baltic International Symposium (BALTIC),* 5p., Riga, Latvia, 25-27 August.

ANDRADE, M., SZLAFSZTEIN, C., 2012, "Remote Sensing and Environmental Sensitivity for Oil Spill in the Amazon, Brazil". In: Escalante-Ramirez, B. (ed), *Remote Sensing - Applications*, Chapter 13, 528p., ISBN: 978-953-51-0651-7, doi: 10.5772/48001. Available online: < http://cdn.intechopen.com/pdfs-wm/37541.pdf >. Accessed on: 14 November 2015.

ANGIULI, E., DEL FRATE, F., SALVATORI, L., 2006, "Neural networks for oil spill detection using ERS and ENVISAT imagery". In: *Proceedings of the SEASAR '06 Workshop, ESA-ESRIN (ESA SP-613)*, 6p., Frascati, Italy, 23-26 January.

ASANUMA, I., MUNEYAMA, K., SASAKI, Y., IISAKA, J., YASUDA, Y., EMORI, Y., 1986, "Satellite thermal observation of oil slicks on the Persian Gulf", *Remote Sensing of Environment*, v. 19, n. 2, pp. 171-186.

ASF (Alaska Satellite Facility), 2015, *MapReady User Manual Remote Sensing Tool Kit*, Engineering Group, 120p. Available online: < https://media.asf.alaska.edu/uploads/pdf/mapready_manual_3.1.22.pdf >. Accessed on: 14 November 2015.

BAILEY, S. W., WERDELL, P. J., 2006, "A multi-sensor approach for the on-orbit validation of ocean color satellite data products", *Remote Sensing of Environment*, v. 102, pp. 12-23. Available online: < http://oceancolor.gsfc.nasa.gov/staff/jeremy/bailey_and_werdell_2006_rse.pdf >. Accessed on: 14 November 2015.

BANNERMAN, K., RODRÍGUEZ, M. H., MIRANDA, F. P., PEDROSO, C. E., CÁCERES; R. G., CASTILLO, O. L., 2009, "Operational applications of RADARSAT-2 for the environmental monitoring of oil slicks in the southern Gulf of Mexico". In: *Proceedings of the International Geoscience and Remote Sensing Symposium (IGARSS '09), IEEE,* v. 3, pp. iii-381-iii-383, Cape Town, South Africa, 12-17 July, doi: 10.1109/IGARSS.2009.5417782.

BATISTA NETO, J. A., WALLNER-KERSANACH, M., PATCHINEELAM, S. M., 2008, *Poluição Marinha*, Editora Interciência, 440p., ISBN: 978-85-7193-206-7.

BEISL, C. H., MIRANDA, F. P., SILVA JR., C. L., 2001, "Combined use of RADARSAT-1 and AVHRR data for the identification of mesoscale oceanic features in the Campos Basin, Brazil". In: *Proceedings of the X Brazilian Remote Sensing Symposium (SBSR), INPE,* 8p., Foz do Iguaçu, Brazil, 21-26 April. Available online: < http://www.dsr.inpe.br/sbsr2001/oral/076.pdf >. Accessed on: 14 November 2015.

BEISL, C. H., PEDROSO, E. C., SOLER, L. S., EVSUKOFF, A. G., MIRANDA, F. P., MENDOZA, A., VERA, A., MACEDO, J. M., 2004, "Use of genetic algorithm to identify the source point of seepage slick clusters interpreted from RADARSAT-1 images in the Gulf of Mexico". In: *Proceedings of the International Geoscience and Remote Sensing Symposium (IGARSS '04), IEEE,* pp. 4139-4142, Anchorage, Alaska, 20-24 September.

BENTZ, C. M., 2006, *Reconhecimento Automático de Eventos Ambientais Costeiros e Oceânicos em Imagens de Radares Orbitais*. D.Sc. Dissertation, Universidade Federal do Rio de Janeiro, COPPE, 115p. Available online: < http://www.coc.ufrj.br/index.php/teses-de-doutorado/150-2006/1048-cristina-maria-bentz >. Accessed on: 14 November 2015.

BENTZ, C. M., LORENZZETTI, J. A., KAMPEL, M., 2004, "Multi-sensor synergetic analysis of mesoscale oceanic features: Campos Basin, south-eastern Brazil", *International Journal of Remote Sensing*, v. 25, n. 21, pp. 4835-4841.

BENTZ, C. M., LORENZZETTI, J. A., KAMPEL, M., POLITANO, A. T., GENOVEZ, P., LUCCA, E. V. D., 2007a, "Contribuição de dados ASTER, CBERS, R99/SIPAM e OrbiSAR-1 para o monitoramento oceânico – Resultados do projeto FITOSAT". In: *Proceedings of the XIII Brazilian Remote Sensing Symposium (SBSR), INPE,* pp. 3755-3762, Florianópolis, Brasil, 21-26 April. Available online: < http://marte.sid.inpe.br/col/dpi.inpe.br/sbsr@80/2006/11.14.19.25.29/doc/3755-3762.pdf >. Accessed on: 14 November 2015.

BENTZ, C. M., LORENZZETTI, J., KAMPEL, M., MORAIS, M. C., BARROS, J. O., HARGREAVES, F. M., 2003, "Multi-sensor synergetic analysis of mesoscale oceanic features in a SAR image: Campos Basin, southeastern Brazil". In: *Proceedings of the XI Brazilian Remote Sensing Symposium (SBSR), INPE*, pp. 1493-1500, Belo Horizonte, Brasil, in Portuguese. Available online: < http://marte.sid.inpe.br/col/ltid.inpe.br/sbsr/2002/11.17.19.30/doc/13_328.pdf >. Accessed on: 14 November 2015.

BENTZ, C. M., MIRANDA, F. P., 2001a, "Application of remote sensing data for oil spill monitoring in the Guanabara Bay, Rio de Janeiro, Brazil". In: *Proceedings of the X Brazilian Remote Sensing Symposium (SBSR), INPE,* pp. 747-752, Foz do Iguaçu, Brasil, 21-26 April. Available online: < http://marte.sid.inpe.br/col/dpi.inpe.br/lise/2001/09.19.12.02/doc/0747.752.262.pdf >. Accessed on: 14 November 2015.

BENTZ, C. M., MIRANDA, F. P., 2001b, "Application of remote sensing data for oil spill monitoring in the Guanabara Bay, Rio de Janeiro, Brazil". In: *Proceedings of the International Geoscience and Remote Sensing Symposium (IGARSS '01), IEEE*, pp. 333-335, Sydney, Austrália, 9-13 July.

BENTZ, C. M., POLITANO, A. T., EBECKEN, N. F. F., 2007b, "Automatic recognition of coastal and oceanic environmental events with orbital radars". In: *Proceedings of the International Geoscience and Remote Sensing Symposium (IGARSS '07), IEEE,* pp. 914-916, Barcelona, Spain, 23-28 July.

BENTZ, C. M., POLITANO, A. T., EBECKEN, N. F. F., 2012, "Classification of oil spills and meteo oceanographic events detected in SAR images". In: *Proceedings of the 4th GEOBIA,* pp. 618-621, Rio de Janeiro, 7-9 May.

BENTZ, C. M., POLITANO, A. T., GENOVEZ, P., 2005, "Monitoramento ambiental de áreas costeiras e oceânicas com múltiplos sensores orbitais", *Revista Brasileira de Cartografia*, v. 57, n. 1, pp. 43-47, ISSN 1808-0936.

BENTZ, C. M., POLITANO, A. T., GENOVEZ, P., LORENZZETTI, J. A., KAMPEL, M., 2007c, "The contribution of ASTER, CBERS, R99/SIPAM e OrbiSAR-1 data to improve the oceanic monitoring". In: *Proceedings of the International Geoscience and Remote Sensing Symposium (IGARSS '07), IEEE*, pp. 994-996, Barcelona, Spain, 23-28 July, doi: 10.1109/IGARSS.2007.4422967.

BERN, T.-I., WAHL, T., ANDERSSEN, T., OLSEN, R., 1993, "Oil Spill Detection Using Satellite Based SAR: Experience from a Field Experiment", *Photogrammetric Engineering & Remote Sensing*, v. 59, n. 3, pp. 423-428.

BEVILACQUA, L., BARROS, M., M., GALEÃO, A. C. R. N., 2008, "Geometry, dynamics and fractals", *Journal of the Brazilian Society of Mechanical Sciences and Engineering*, v. 30, n. 1, doi: 10.1590/S1678-58782008000100003. Available online: < http://www.scielo.br/pdf/jbsmse/v30n1/a03v30n1.pdf >. Accessed on: 14 November 2015.

BIRK, R., CAMUS, W., VALENTI, E., MCCANDLES, W. J., 1995, "Synthetic aperture radar imaging systems", *IEEE Aerospace and Electronic Systems Magazine*, v. 10, n. 11, p. 15-23, doi: p10.1109/62.473408.

BOESCH, D. F., RABALAIS, N. N., 1987, *Long-term Effects of Offshore Oil and Gas Development*, New York, Elsevier Applied Science, 695 p.

BONN (Bonn Agreement Aerial Operations Handbook), 2009, Part 3: Guidelines for Oil Pollution Detection, Investigation and Post Flight Analysis/Evaluation for Volume Estimation. Available online: < http://www.bonnagreement.org/site/assets/files/1081/ba-aoh_revision_2_april_2012-1.pdf >. Accessed on: 14 November 2015.

BOUCKAERT, R. R., FRANK, E., HALL, M., KIRKBY, R., REUTEMANN, P., SEEWALD, A., SCUSE, D., 2008, *WEKA Manual for Version 3-6-0*, Hamilton, New Zealand, The University of Waikato, 212p. Available online: < http://citeseerx.ist.psu.edu/viewdoc/download?doi=10.1.1.153.9743&rep=rep1&type=pdf >. Accessed on: 14 November 2015.

BOYD, J. N., KUCKLICK, J. H., SCHOLZ, D. K., WALKER, A. H., POND, R. G., BOSTROM, A., 2001, *Effects of oil and chemically dispersed oil in the environment, Health and Environmental Sciences Department*, Cape Charles, Virginia, Scientific Environmental Associates Inc., 50p.

BREAKER, L. C., KRASNOPOLSKY, V. M., MATURI, E. M., 2000, GOES-8 Imagery as a new source of data to conduct ocean feature tracking", *Remote Sensing of Environment*, v. 73, pp. 198-206.

BREKKE, C., 2007, *Automatic screening of Synthetic Aperture Radar imagery for detection of oil pollution in the marine environment*. Ph.D. Dissertation, Universitetet i Oslo (UIO), 189p.

BREKKE, C., SOLBERG, A. H. S., 2005a, "Feature extraction for oil spill detection based on SAR images, *Lecture Notes in Computer Science (LNCS 3540), SCIA*, Springer-Verlag Berlin Heidelberg, p. 75-84. Available online: < http://dx.doi.org/10.1007/b137285 >. Accessed on: 14 November 2015.

BREKKE, C., SOLBERG, A. H. S., 2005b, "Review: Oil spill detection by satellite remote sensing", *Remote Sensing of Environment*, v. 95, n. 1, pp. 1-13, doi: 10.1016/j.rse.2004.11.015.

BROOKS, J., 1990, "Classic petroleum provinces", *Geological Society, London, Special Publications,* v. 50, pp. 1-8, doi: 10.1144/GSL.SP.1990.050.01.01.

BROWN, C. E., FINGAS, M., 2001, "New space-borne sensors for oil spill response". In: *Proceedings of the International Oil Spill Conference, American Petroleum Institute,* pp. 911-916, Washington, DC.

BROWN, J., COLLING, A., PARK, D., PHILLIPS, J., ROTHERY, D., WRIGHT, J., 1997, *Waves, tides and shallow-water processes*, The Open University Course Team, UK, 5th edition (3rd reprint), Butterworth-Heinemann (BH), 187p., ISBN: 0-7506-2827-8.

BULGARELLI B., DJAVIDNIA, S., 2012, "On MODIS retrieval of oil spill spectral properties in the marine environment", *IEEE Geoscience and Remote Sensing Letters*, v. 9, n. 3, pp. 398-402, doi: 10.1109/LGRS.2011.2169647.

BUONO, A., PAES, R. L., NUNZIATA, F., MIGLIACCIO, M., 2015, "Synthetic Aperture Radar for oil spill monitoring: a brief review". In: *Proceedings of the XVII Brazilian Remote Sensing Symposium (SBSR), INPE*, pp. 2806-2813, João Pessoa-PB, Brasil, 25-29 April. Available online: < http://www.dsr.inpe.br/sbsr2015/files/p0556.pdf >. Accessed on: 14 November 2014.

BYFIELD, V., 1998, *Optical remote sensing of oil in the marine environment: An investigation into the optical properties of surface and dispersed oil and the means by which oil pollution may be detected using airborne optical instruments at Visible and Near-Infrared wavelengths*. Ph.D. Dissertation, University of Southampton, 286p.

CALABRESI, G., DEL FRATE, F., LICHTENEGGER, I., PETROCCHI, A., TRIVERO, P., 1999, "Neural networks for the oil spill detection using ERS–SAR data". In: *Proceedings of the International Geoscience and Remote Sensing Symposium*

(IGARSS '99), IEEE, pp. 215-217, Hamburgo, Germany, 28 Jun-02 Jul, v. 1, doi: 10.1109/IGARSS.1999.773451.

CAMPOS, E. J. D., GONÇALVES, J. E., IKEDA, Y., 1995, "Water mass characteristics and geostrophic circulation in the south Brazil Bight: summer of 91", *Journal of Geophysical Research*, v. 100, n. C9, pp. 18573-18550.

CANNIZZARO, J. P., CARDER, K. L., CHEN, F. R., HEIL, C. A., VARGO, G. A., 2008, "A novel technique for detection of the toxic dinoflagellate *Karenia brevis* in the Gulf of Mexico from remotely sensed ocean color data", *Continental Shelf Research*, v. 28, n. 1, pp. 137-158, doi: 10.1016/j.csr.2004.04.007.

CARDER, K. L., CHEN, F. R., LEE, Z. P., HAWES, S. K., KAMYKOWSKI, D., 1999, "Semi-analytic Moderate-Resolution Imaging Spectrometer algorithms for chlorophyll a and absorption with bio-optical domains based on nitrate-depletion temperatures", *Journal of Geophysical Research*, v. 104, n. 3, pp. 5403-5421.

CARMALT, S. W., ST. JOHN, B., 1986, "Giant oil and gas fields". In: Halbouty, M. T. (ed), Future petroleum provinces of the world, American Association of Petroleum Geologists Memoir 40, pp. 11-53.

CARVALHO, G. A., 2002, *Wind influence on the Sea Surface Temperature of the Cabo Frio Upwelling (23ºS/42ºW - RJ/Brazil) during 2001, through the analysis of satellite measurements (Seawinds-QuikScat/AVHRR-NOAA),* B.Sc. Undergraduate Thesis, UERJ, Rio de Janeiro, Brazil, 210p, in Portuguese.

CARVALHO, G. A., 2008, *The use of satellite-based ocean color measurements for detecting the Florida Red Tide (Karenia brevis).* M.Sc. Thesis, University of Miami (UM/RSMAS/MPO), Florida, USA, 156p. Available online: < http://scholarlyrepository.miami.edu/oa_theses/116/ >. Accessed on: 14 November 2015.

CARVALHO, G. A., CABRAL, A. P., FERNANDEZ, M. A. S., 2002, "A preliminary study about the wind influence on the superficial oceanic circulation of Cabo Frio adjacent region (23ºS - 42ºW), through the analysis of orbital data (AVHRR/QUIKSCAT)". In: *Proceedings of the III Oceanic Detection Seminary Using Space Sources*, IEAPM, Arraial do Cabo, RJ, Brazil, in Portuguese.

CARVALHO, G. A., CABRAL, A. P., FERNANDEZ, M. A. S., 2003a, "Correlation between average wind field and upwelling intensity index on Cabo Frio region (23ºS - 42ºW), through the analysis of orbital data (AVHRR/QUIKSCAT)". In: *Proceedings of the XI Brazilian Remote Sensing Symposium (SBSR),* INPE, pp. 1509-1514, Belo Horizonte, Brazil, in Portuguese. Available online: < http://marte.dpi.inpe.br:80/col/ltid.inpe.br/sbsr/2002/11.18.01.27/doc/13_366.pdf >. Accessed on: 14 November 2015.

CARVALHO, G. A., CABRAL, A. P., FERNANDEZ, M. A. S., 2003b, "The evaluation of Cabo Frio (23ºS - 42ºW) upwelling intensity through the analysis of orbital data (SST/Wind)". In: *Proceedings of the X Latin-American Ocean Science Meeting (COLACMAR),* San Jose, Costa Rica.

CARVALHO, G. A., LANDAU, L., MIRANDA, F. P., MINNET, P., MOREIRA, F., BEISL, C., 2015a, "The use of RADARSAT-derived information to investigate oil slick occurrence in Campeche Bay, Gulf of Mexico". In: *Proceedings of the XVII Brazilian Remote Sensing Symposium (SBSR), INPE,* pp. 1184-1191, João Pessoa-PB, Brasil, 25-29 April. Available online: < http://www.dsr.inpe.br/sbsr2015/files/p0217.pdf >. Accessed on: 14 November 2015.

CARVALHO, G. A., MINNETT, P. J., BARINGER, W., BANZON, V. F., 2007, "Detection of Florida “red tides” from SeaWiFS and MODIS imagery". In: *Proceedings of the XIII Brazilian Remote Sensing Symposium (SBSR), INPE*, pp. 4581-4588, Florianópolis, Brasil, 21-26 April. Available online: < http://marte.dpi.inpe.br/col/dpi.inpe.br/sbsr%4080/2006/11.07.00.35/doc/4581-4588.pdf >. Accessed on: 14 November 2015.

CARVALHO, G. A., MINNETT, P. J., BARINGER, W., BANZON, V. F., 2008, "Spatial and temporal variability of three distinct satellite ocean color algorithms to identify harmful algal blooms off the west Florida coast". In: *Proceedings of the AGU Ocean Sciences Meeting*, Orlando, Florida, USA, 2-7 March, 1p.

CARVALHO, G. A., MINNETT, P. J., BARINGER, W., BANZON, V. F., 2010a, "Annual (2002-2006) accuracy assessment of a new multi-algorithm method for detecting harmful algal blooms of *Karenia brevis* along the central west Florida shelf during the boreal Summer-Fall". In: *Proceedings of the AGU Ocean Sciences Meeting*, Portland, Oregon, USA, 22-26 February.

CARVALHO, G. A., MINNETT, P. J., FLEMING, L. E., BANZON, V. F., BARINGER, W., FRAMINAN, M., HEIL, C.A., 2010b, "Validation of three different algorithms specifically designed for detecting the Florida Red Tide (*Karenia brevis*) using ocean color satellite measurements (MODIS)". In: *Proceedings of the AGU Meeting of the Americas*, Foz do Iguaçu, Paraná, Brazil.

CARVALHO, G. A., MINNETT, P. J., FLEMING, L. E., BANZON, V. F., BARINGER, W., FRAMINAN, M., HEIL, C.A., 2010c, "Long-term (2002-2006) accuracy assessment of a new multi-algorithm method for detecting harmful algal blooms of *Karenia brevis* along the central west Florida shelf". In: *Proceedings of the Oceans from Space*, Venice, Italy.

CARVALHO, G. A., MINNETT, P. J., FLEMING, L. E., BANZON, V. F., BARINGER, W., 2010d, "Satellite remote sensing of harmful algal blooms: A new multi-algorithm method for detecting the Florida Red Tide (*Karenia brevis*)", *Harmful Algae*, v. 9, n. 5, pp. 440-448, doi: 10.1016/j.hal.2010.02.002. Available online: < http://www.ncbi.nlm.nih.gov/pubmed/21037979 >. Accessed on: 25 December 2015.

CARVALHO, G. A., MINNETT, P. J., FLEMING, L. E., BANZON, V. F., BARINGER, W., HEIL C. A., 2011, "Long-term evaluation of three satellite ocean color algorithms for identifying harmful algal blooms (*Karenia brevis*) along the west coast of Florida: A matchup assessment", *Remote Sensing of Environment*, v. 115, pp. 1-18, doi: 10.1016/j.rse.2010.07.007. Available online: < http://www.ncbi.nlm.nih.gov/pubmed/22180667 >. Accessed on: 25 December 2015.

CARVALHO, G. A., MINNETT, P. J., MIRANDA, F. P., LANDAU, L., MOREIRA, F., 2015b (Submitted), "The use of a RADARSAT-derived long-term dataset to investigate the sea surface expressions of naturally-occurring oil seeps and human-related oil spills in Campeche Bay, Gulf of Mexico", *Canadian Journal of Remote Sensing (Special Issue: Long-Term Satellite Data and Applications)*. Available online: < goo.gl/DlfL94 >. Accessed on: 5 January 2016.

CARVALHO, G. A., MINNETT, P. J., MIRANDA, F. P., LANDAU, L., PAES, E. T., 2015c (Submitted), "The use of Synthetic Aperture Radar (SAR) measurements to distinguish naturally-occurring oil seeps from human-related oil spills on the sea surface of Campeche Bay (Gulf of Mexico) using multivariate data analysis techniques, *Remote Sensing of Environment*. Available online: < goo.gl/DlfL94 >. Accessed on: 5 January 2016.

CASCIELLO, D., LACAVA, T., PERGOLA, N., TRAMUTOLI, V., 2011, "Robust satellite techniques for oil spill detection and monitoring using AVHRR thermal infrared bands", *International Journal of Remote Sensing*, v. 32, n. 14, pp. 4107-4129, doi: 10.1080/01431161.2010.484820.

CATTELL, R. B., 1966, “The Scree Test for the number of factors”, *Multivariate Behavioral Research*, v. 1, n. 2, pp. 245-276, doi: 10.1207/s15327906mbr0102_10.

CH (Campeche Hoy), 2014, *Rudesindo Cantarell de la gloria a la ignominia*. Available online: < http://www.campechehoy.mx/notas/index.php?ID=182736 >. Accessed on: 15 November 2015.

CHAN, Y. K., KOO, V. C., 2008, "An introduction to synthetic aperture radar (SAR)", *Progress In Electromagnetics Research B*, v. 2, pp. 27-60. Available online: < http://www.jpier.org/PIERB/pierb02/03.07110101.pdf >. Accessed on: 14 November 2015.

CHEN, S., HU, C., 2014, "In search of oil seeps in the Cariaco basin using MODIS and MERIS medium-resolution data", *Remote Sensing Letters*, v. 5, n. 5, pp. 442-450, doi: 10.1080/2150704X.2014.917218.

CHRISTIANSEN, M. B., KOCH, W., HORSTMANN, J., HASAGER, C. B., NIELSEN, M., 2006, "Wind resource assessment from C-band SAR", *Remote Sensing of Environment*, v. 105, pp. 68-81.

CLARK, C. D., 1993, "Satellite remote sensing for marine pollution investigations, Review Article", *Marine Pollution Bulletin*, v. 26, n. 7, pp. 357-368.

CLARK, P. E., RILEE, M., 2010, *Remote sensing tools for exploration observing and interpreting the electromagnetic spectrum*, Berlin, Springer, 346p., ISBN: 978-1-4419-6829-6.

CLARKE, R. H., CLEVERLY, R. W., 1991, "Petroleum seepage and post-accumulation migration". In: England, W. A., Fleet, A. J. (eds), *Petroleum Migration Geological Society, Special Publication*, n. 59, pp. 265-271.

CLARO, M. S., 2007, *Extração do campo de vento na Bacia de Campos, RJ, a partir de imagens ENVISAT/ASAR*. M.Sc. Thesis, INPE, São José dos Campos, Brazil, INPE-15218-TDI/1312, 112p. Available online: < http://mtc-m17.sid.inpe.br/col/sid.inpe.br/mtc-m17@80/2007/12.07.12.17/doc/publicacao.pdf >. Accessed on: 14 November 2015.

COCOCCIONI, M., CORUCCI, L., LAZZERINI, B., 2009, “Issues and preliminary results in oil spill detection using optical remotely sensed images”, In: *Proceedings of* the Oceans '05, IEEE, 4p.

CROUT, R. L., 2011, "Measurements in support of the Deepwater Horizon (MC-252) oil spill response". In: *Proceedings of the SPIE 8030, Ocean Sensing and Monitoring III,* 80300J; doi: 10.1117/12.888006.

CRSS (Canadian Remote Sensing Society), 1993, "RADARSAT Special Issue", *Canadian Journal of Remote Sensing*, v. 19, n. 4, ISSN 0703-8992. Available online: < http://www.tandfonline.com/toc/ujrs20/19/4#.Vd_FvOlPL60 >. Accessed on: 14 November 2015.

CRSS (Canadian Remote Sensing Society), 2004, "Special issue: RADARSAT-2*", Canadian Journal of Remote Sensing*, v. 30, n. 3, ISSN 0703-8992. Available

online: < http://www.tandfonline.com/toc/ujrs20/30/3#.Vd_GsOlPL60 >. Accessed on: 14 November 2015.

CSBPD (County of Santa Barbara Planning and Development), 2015. Available online < http://www.sbcountyplanning.org/energy/information.asp >. Accessed on: 14 November 2015.

DA SILVA, A. F. T., 2008, *Identification of interesting association rules in a database about oil seeps in the Gulf of Mexico*. M.Sc. Thesis, LABSAR, PEC, COPPE, UFRJ, Rio de Janeiro, 91p., in Portuguese. Available online: < http://wwwp.coc.ufrj.br/teses/mestrado/Novas_2008/resumos/SILVA_AFT_08_RA_M.pdf >. Accessed on: 14 November 2015.

DASSENAKIS, M., PARASKEVOPOULOU, V., CARTALIS, C., ADAKTILOU, N., KATSIABANI, K., 2012, "Remote sensing in coastal water monitoring: Applications in the eastern Mediterranean Sea (IUPAC Technical Report)", *Pure Applied Chemistry*, v. 84, n. 2, pp. 335-375, doi: 10.1351/PAC-REP-11-01-11.

DAVIS, P. H., SPIES, R. B.,1980, "Infaunal benthos of a natural petroleum seep: Study of community structure", *Marine Biology*, n. 59, pp. 31-41.

DE LEEUW, J., 2011, “History of nonlinear principal component analysis”, In: *Proceedings of* the *International Conference on Correspondence Analysis and Related Methods, CARME*, Rennes, France, 8-11 February, 29p. Available online: < http://gifi.stat.ucla.edu/janspubs/2014/chapters/deleeuw_C_14.pdf >. Accessed on: 18 November 2015.

DE LEEUW, J., 2013, *History of Nonlinear Principal Component Analysis*, Department of Statistics, UCLA, 14p. Available online: < http://escholarship.org/uc/item/1vp9f9kz >. Accessed on: 18 November 2015.

DEL FRATE, F., GIACOMINI, A., LATINI, D., SOLIMINI, D., EMERY, W. J., 2011, "The Gulf of Mexico oil rig accident: analysis by different SAR satellite images". In: *Proceedings of the SAR for Maritime Applications: SAR Image Analysis, Modeling, and Techniques XI, SPIE*, v. 8179, 81790F1-7, 26 October, doi: 10.1117/12.898599.

DEL FRATE, F., PETROCCHI, A., LICHTENEGGER, J., CALABRESI, G., 2000, "Neural networks for oil spill detection using ERS-SAR data", *IEEE Transactions on Geoscience and Remote Sensing*, v. 38, n. 5, pp. 2282-2287, doi: 10.1109/36.868885.

DENMAN, K. L., ABBOTT, M. R., 1994, "Timescales of pattern evolution from cross-spectrum analysis of Advanced Very High Resolution Radiometer and Coastal Zone Color Scanner imagery", *Journal of Geophysical Research*, v. 99, pp. 7433-7442.

DICKEY, T. D., 1991, "The emergence of concurrent high-resolution physical and biooptical measurements in the upper ocean and their applications", *Reviews of Geophysics*, v. 29, n. 3, pp. 383-413, doi: 10.1029/91RG00578.

DIETRICH, G., KALLE, K., KRAUSS, W., SIEDLER, G., 1980, *General Oceanography, An introduction*, Wiley-Interscience Publication, 2nd Edition, 626p.

DIETRICH, J. C., TRAHAN, C. J., HOWARD, M. T., FLEMING, J. G., WEAVER, R. J., TANAKA, S., YU, L., LUETTICH JR., R. A., DAWSON, C. N., WELLS, G., WESTERINK, J. J., LU, A., VEGA, K., KUBACH, A., DRESBACK, K. M., KOLAR, R. L., KAISER, C., TWILLEY, R. R., 2012, "Surface trajectories of oil transport along the northern coastline of the Gulf of Mexico", *Continental Shelf Research*, v. 41, n. 1, pp. 17-47, doi: 10.1016/j.csr.2012.03.015.

DIGIACOMO, P. M., HOLT, B., 2001, "Satellite observations of small coastal ocean eddies in the Southern California Bight", *Journal of Geophysical Research*, v. 106, n. C10, pp. 22521-22543.

DIGIACOMO, P. M., WASHBURN, L., HOLT, B., JONES, B. H., 2004, "Coastal pollution hazards in southern California observed by SAR imagery: stormwater plumes, wastewater plumes, and natural hydrocarbon", *Marine Pollution Bulletin*, v. 49, pp. 1013-1024. doi: 10.1016/j.marpolbul.2004.07.016.

DPI (Divisão de Processamento de Imagens), 2015, *Manuais: Tutorial de Geoprocessamento*, INPE, in Portuguese. Available online < http://www.dpi.inpe.br/spring/portugues/tutorial/index.html >. Accessed on: 14 November 2015.

DUXBURY, A. C., DUXBURY, A. B., 1997, *An introduction to the world's oceans*, 5th ed. Wm. C. Brown Publishers, 504p., ISBN: 0-697-28273-2.

EL-DARYMLI, K., MCGUIRE, P., GILL, E., POWER, D., MOLONEY, C., 2014, "Understanding the significance of radiometric calibration for synthetic aperture radar imagery". In: *Proceedings of the 27th Canadian Conference on Electrical and Computer Engineering (CCECE), IEEE*, pp. 1-6, Toronto, ON, Canada, 4-7 May, doi: 10.1109/CCECE.2014.6901104.

ENGELHARDT, F. R., 1999, "Remote sensing for oil spill detection and response", *Pure Applied Chemistry: An issue of special reports reviewing oil spill countermeasures*, v. 71, n. 1, pp. 103-111.

EOE (The Encyclopedia of the Earth), 2010a, *BP Deepwater Horizon oil budget*. Available online: < http://www.eoearth.org/view/article/159470/ >. Accessed on: 14 November 2015.

EOE (The Encyclopedia of the Earth), 2010b, *Deepwater Horizon oil spill disaster: risk, recovery, and insurance implications*. Available online < http://www.eoearth.org/view/article/161922/ >. Accessed on: 14 November 2015.

EOE (The Encyclopedia of the Earth), 2010c, *Deepwater Horizon oil spill*. Available online: < http://www.eoearth.org/view/article/161185/ >. Accessed on: 15 November 2015.

EOE (The Encyclopedia of the Earth), 2010d, *Exxon Valdez oil spill*. Available online: < http://www.eoearth.org/view/article/152720/ >. Accessed on: 14 November 2015.

EPA (Environmental Protection Agency), 2008, *Cruise Ship Discharge Assessment Report*, *Section 4: Oily Bilge Water*, December 29, EPA 842-R-07-005, 22p. Available online: < http://water.epa.gov/polwaste/vwd/upload/2009_01_28_oceans_cruise_ships_section4_bilgewater.pdf >. Accessed on: 14 November 2015.

ESA (European Space Agency), 2014, Available online: < http://earth.eo.esa.int/polsarpro/ >. Accessed on: 14 November 2015.

ESAIAS, W., ABBOTT, M., BARTON, I., BROWN, O. B., CAMPBELL, J. W., CARDER, K. L., CLARK, D. K., EVANS, R. H., HOGE, F. E., GORDON, H. R., BALCH, W. M., LETELIER, R., MINNETT, P. J., 1998, “An overview of MODIS capabilities for ocean science observations”, *IEEE Transactions on Geoscience and Remote Sensing*, v. 36, n. 4, pp. 1250-1265.

ESPEDAL, H. A., 1998, *Detection of oil spill and natural film in the marine environment by spaceborne synthetic aperture radar*. Ph.D. Dissertation, Department of Physics, University of Bergen and Nansen Environmental and Remote Sensing Center (NERSC), Norway, 200p.

ESPEDAL, H. A., JOHANNESSEN, O. M., 2000, "Detection of oil spills near offshore installations using synthetic aperture radar (SAR)", Cover, *International Journal of Remote Sensing*, v. 21, n. 11, pp. 2141-2144.

ESPEDAL, H. A., JOHANNESSEN, O. M., JOHANNESSEN, J. A., DAN, E, LYZENGA, D. R., KNULST, J. C., 1998, "COASTWATCH'95: ERS 1/2 SAR detection of natural film on the ocean surface", *Journal of Geophysical Research*, v. 103, n. C11, pp. 24969-24982.

ESPEDAL, H. A., JOHANNESSEN, O. M., KNULST, J., 1996, "Satellite detection of natural films on the ocean surface", *Geophysical Research Letters*, v. 23, n. 22, pp. 3151-3154, doi: 10.1029/96GL03009.

ESPEDAL, H. A., WAHL, T., 1999, "Satellite SAR oil spill detection using wind history information", *International Journal of Remote Sensing*, v. 20, n. 1, pp. 49-65, doi: 10.1080/014311699213596.

ESPEDAL, H., 1999, "Detection of oil spill and natural film in the marine environment by spaceborne SAR" In: *Proceedings* of the International Geoscience and Remote Sensing Symposium (IGARSS '09), IEEE, pp. 1478-1480, Cape Town, South Africa, 12-17 July, v. 3, doi: 10.1109/IGARSS.1999.771993.

ESSA, S., HARAHSHEH, H., SHIOBARA, M., NISHIDAI, T., 2005, "Operational remote sensing for the detection and monitoring of oil pollution in the Arabian Gulf: case studies from the United Arab Emirates". In: Al-Azab, M., El-Shorbagy, W., Al-Ghais, S. (eds), *Oil Pollution and its Environmental Impact in the Arabian Gulf Region, Developments in Earth and Environmental Sciences*, v. 3, Chapter 3, pp. 31-48, Amsterdam, The Netherlands, Elsevier, doi: 10.1016/S1571-9197(05)80027-8.

ETOPO1 (Earth TOPOgraphy database at one-minute grid resolution), 2013, Available online: < http://www.ngdc.noaa.gov/mgg/gdas/gd_designagrid.html >. Accessed on: 14 November 2015.

EVANS, R. H., GORDON, H. R., 1994, "Coastal Zone Color Scanner 'system calibration': a retrospective examination", *Journal of Geophysical Research*, v. 99, pp. 7293-7307.

FALLAH, M. H., STARK, R. M., 1976, "Literature review: movement of spilled oil at sea", *Marine Technology Society Journal*, v. 10, pp. 3-18.

FARRIS, J. S., 1969, "On the cophenetic correlation coefficient", *Systematic Biology*, v. 18, n. 3, p.279-285, doi: 10.2307/2412324. Available online: < http://www.faculty.biol.ttu.edu/strauss/phylogenetics/Readings/Farris1969.pdf >. Accessed on: 14 November 2015.

FINGAS, M. F., BROWN, C. E., 2000, "Oil-spill remote sensing – an update", *Sea Technology*, v. 41, n. 10, pp. 21-26.

FINGAS, M. F., BROWN, C. E., 1997, "Review of oil spill remote sensing", *Spill Science and Technology Bulletin*, v. 4, n. 4, pp. 199-208.

FISCELLA, B., GIANCASPRO, A., NIRCHIO, F., PAVESE, P., TRIVERO, P., 2000, "Oil spill detection using marine SAR images", *International Journal of Remote Sensing*, v. 21, n. 18, pp. 3561-3566, doi: 10.1080/014311600750037589.

FISCELLA, B., GIANCASPRO, A., NIRCHIO, F., PAVESE, P., TRIVERO, P., 2010, "Oil spill monitoring in the Mediterranean Sea using ERS SAR data". In: *Proceedings of the Envisat Symposium, ESA,* 9p., Göteborg, Sweeden, 16-20 October.

FOX, P. A., JAMES, K., LUSCOMBE, A., 2003, "The RADARSAT-2 synthetic aperture radar diagnostics and calibration". In: *Proceedings of the IEEE International Symposium on Phased Array Systems and Technology*, pp. 253-258, Chicago, 14-17 October.

FOX, P. A., LUSCOMBE, A. P. THOMPSON, A. A., 2004, "RADARSAT-2 SAR modes development and utilization", *Canadian Journal of Remote Sensing*, v. 30, n. 3, pp. 258-264, doi: 10.5589/m04-014.

FREEMAN, A., 1992, "Radiometric calibration of SAR image data". In: *Proceedings of the XVII Congress for Photogrammetry and Remote Sensing (ISPRS)*, pp. 212-222. Available online: < http://www.isprs.org/proceedings/XXIX/congress/part1/212_XXIX-part1.pdf >. Accessed on: 14 November 2015.

FROST, V. S., STILES, J. A., SHANMUGAN, K. S., HOLTZMAN, J. C., 1982, "A model for radar images and its application to adaptive digital filtering of multiplicative noise", *IEEE Transactions on Pattern Analysis and Machine Intelligence*, v. 4, n. 2, pp. 157-166.

FWRI (Florida Wildlife Research Institute), 2002, *Red tides in Florida, 1954-2002: Harmful Algal Bloom Historical Database*, CD-ROM, Version 2.0.

GADE, M., ALPERS, W., 1999, "Using ERS-2 SAR images for routine observation of marine pollution in European coastal waters", *The Science of the Total Environment*, v. 237/238, pp. 441-448.

GADE, M., ALPERS, W., BAO, M., HUHNERFUSS, H., 1996, "Measurements of the radar backscattering over different oceanic surface films during the SIR-C/X-SAR campaigns". In: *Proceedings of the International Geoscience and Remote Sensing Symposium (IGARSS '96), IEEE,* v. 2, pp. 860-862, Lincoln, Nebraska, USA, 27-31 May, doi: 10.1109/IGARSS.1996.516501.

GADE, M., ALPERS, W., HUEHNERFUSS, H., MASUKO, H., KOBAYASHI, T., 1998a, "Imaging of biogenic and anthropogenic ocean surface films by the multi-frequency/multi-polarization SIR-C/X-SAR", *Journal of Geophysical Research*, v. 103, pp. 18851-18866.

GADE, M., ALPERS, W., HUHNERFUSS, H., WISMANN, V. R., LANGE, P. A., 1998b, "On the reduction of the radar backscatter by oceanic surface films: Scatterometer measurements and their theoretical interpretation", *Remote Sensing of Environment*, v. 66, n. 1, pp. 52-70.

GADE, M., REDONDO, J. M., 1999, "Marine pollution in European coastal waters monitored by the ERS-2 SAR: a comprehensive statistical analysis". In: *Proceedings of the Oceans '99, IEEE,* v. 3, pp. 1239-1243, doi: 10.1109/OCEANS.1999.800168.

GAMBARDELLA, A., GIACINTO, G., MIGLIACCIO, M., MONTALI, A., 2010, "One-class classification for oil spill detection", *Pattern Analysis and Applications*, v. 13, n. 3, pp. 349-366, doi: 10.1007/s10044-009-0164-z.

GAMBARDELLA, A., NUNZIATA, F., MIGLIACCIO, M., 2007, "Oil spill observation by means of Co-polar Phase Difference". In: *Proceedings of the 3rd International Workshop on Science and Applications of SAR Polarimetry and Polarimetric Interferometry (POLinSAR '07),* ESA, Frascati, Italy, 22-26 January. Available online: < http://earth.esa.int/workshops/polinsar2007/papers/49_gambardella.pdf >. Accessed on: 14 November 2015.

GARCIA-PINEDA, O., MACDONALD, I., ZIMMER, B., 2008, "Synthetic aperture radar image processing using the Supervised Textural-Neural Network Classification Algorithm". In: *Proceedings of the International Geoscience and Remote Sensing Symposium (IGARSS '08), IEEE,* v. 4, pp. IV-1265-IV-1268, Boston, Massachusetts, 8-11 July, doi: 10.1109/IGARSS.2008.4779960.

GARCIA-PINEDA, O., MACDONALD, I., ZIMMER, B., SHEDD, B., ROBERTS, H., 2010. "Remote-sensing evaluation of geophysical anomaly sites in the outer continental slope, northern Gulf of Mexico." *Deep-Sea Research Part II - Topical Studies in Oceanography*, v. 57, pp. 1859-1869.

GARCIA-PINEDA, O., ZIMMER, B., HOWARD, M., PICHEL, W., LI, X., MACDONALD, I. R., 2009, "Using SAR images to delineate ocean oil slicks with a texture classifying neural network algorithm (TCNNA)", *Canadian Journal of Remote Sensing*, v. 35, n. 5, 11p.

GARCIA, O., MACDONALD, I. R., ZIMMER, B., SHEDD, W., FRYE, M., 2009, "Satellite SAR inventory of Gulf of Mexico oil seeps and shallow gas hydrates", *Geophysical Research Abstracts, EGU-11633, General Assembly*, v. 11, 2p. Available online: < http://www.sarsea.org/natural_seapage.html >. Accessed on: 14 November 2015.

GATELY, D., 1986, "Lessons from the 1986 Oil Price Collapse", *Brookings Papers on Economic Activity*, n. 2, pp. 237-284. Available online: < http://www.brookings.edu/~/media/Projects/BPEA/1986-2/1986b_bpea_gately_adelman_griffin.PDF >. Accessed on: 14 November 2015.

GER, A., GONZALES, M., MAYBERRY, E., SHAMSZADEH, F., 2002, *Marine Hydrocarbon Seep Capture: Feasibility and potential impacts*, Santa Barbara, California, Master of environment science and management, Group project brief, 4p. Available online: < http://www2.bren.ucsb.edu/~seeps/Brief%204-17%20FINAL%20VERSION.pdf >. Accessed on: 14 November 2015.

GERGES, M. A., 1993, "On the impacts of the 1991 Gulf War on the environment of the region: General observations", *Marine Pollution Bulletin*, v. 27, pp. 305-314.

GERSHENSON, C., 2003, *Artificial neural networks for beginners*, Formal Computational Skills Teaching Package, 8p.

GILL, J. P. S., 2010, *RADARSAT-2: Data basics and processing*, University of Calgary. Available online: < http://www.ucalgary.ca/ccrg/system/files/radarsat-2-presentation_black.pdf >. Accessed on: 14 November 2015.

GIRARD-ARDHUIN, F., MERCIER, G., COLLARD, F., GARELLO, R., 2003, "Oil slick detection by SAR imagery: potential and limitation". In: *Proceedings of the Oceans '03, IEEE,* v. 1, pp. 164-169, doi. 10.1109/OCEANS.2003.178539.

GONZALEZ-SILVERA, A., SANTAMARIA-DEL-ANGELA, E., GARCIA, V. M. T., GARCIA, C. A. E., MILLAN-NUNEZ, R., MULLER-KARGER, F., 2004, "Biogeographical regions of the tropical and subtropical Atlantic Ocean off South America: classification based on pigment (CZCS) and chlorophyll-a (SeaWiFS) variability", *Continental Shelf Research*, n. 24, pp. 983-1000, doi: 10.1016/j.csr.2004.03.002.

GONZALEZ, N. M., MULLER-KARGER, F. E., ESTRADA, S. C., DE LOS REYES, R. P., DEL RIO, I. V., PEDEREZ, P. C., ARENAL, I.M., 2000, "Near-surface phytoplankton distribution in the western Intra-American Sea: The influence of El-niño and weather events", *Journal of Geophysical Research*, v. 105, n. C6, pp. 14029-14043.

GOODWALL, D. W., 1954, “Objective methods for the classification of vegetation, III. An essay in the use of factor analysis”, *Australian Journal of Botany*, v. 2, n. 3, pp. 304-324, doi: 10.1071/BT9540304.

GOWER, J. F. R., 2004, "In situ measurements of chlorophyll fluorescence and water optical properties as surface data for SeaWiFS, MODIS and MERIS", *International Journal of Remote Sensing*, v. 25, n. 7/8, pp. 1489-1493, doi: 10.1080/01431160310001592490.

GOWER, J. F. R., VACHON P. W., EDEL, H., 1993, "Ocean Applications of RADARSAT", *Canadian Journal of Remote Sensing*, v. 19, n. 4, pp. 372-383, doi: 10.1080/07038992.1993.10874572.

GOWER, J., HU, C., BORSTAD, G., KING, S., 2006, "Ocean color satellites show extensive lines of floating sargassum in the Gulf of Mexico", *IEEE Transactions on Geoscience and Remote Sensing*, v. 44, n. 12, pp. 3619-3625, doi: 10.1109/TGRS.2006.882258.

GREGG, W.W., CONKRIGHT, M.E., 2001, "Global seasonal climatologies of ocean chlorophyll: Blending in situ and satellite data for the Coastal Zone Color Scanner era", *Journal of Geophysical Research*, v. 106, n. C2, pp. 2499-2515.

GREGG, W.W., CONKRIGHT, M.E., 2002, "Decadal changes in global ocean chlorophyll", *Geophysical Research Letters*, v. 29, n. 15, 4p., doi: 0.1029/2002GL014689. Available online: <

http://gmao.gsfc.nasa.gov/research/oceanbiology/reprints/greggconkright_GRL2002.pdf >. Accessed on: 14 November 2015.

GUARNIERI, A. M., 2013, *Introduction to RADAR*, 1st ed., Politecnico di Milano, 136p. Available online: < http://home.deib.polimi.it/monti/ftp/srl/SAR_I.pdf >. Accessed on: 14 November 2015.

GUYON, I., ELISSEEFF, A., 2003, "An Introduction to Variable and Feature Selection", *Journal of Machine Learning Research*, v. 3, pp. 1157-1182. Available online: < http://jmlr.csail.mit.edu/papers/volume3/guyon03a/guyon03a.pdf >. Accessed on: 14 November 2015.

HAIR, J. F., ANSERSON, R. E., TATHAM, R. L., BLACK, W. C., 2005, Multivariate data analysis, 5th ed, Pearson Education, Prentice Hall, Translated to Portuguese by: Sant'Anna, A. S. and Chaves Neto, A., *Análise multivariada de dados*, Bookman, Porto Alegre, RS, Brazil, ISBN: 0-13-014406-7. Available online: < https://www.scribd.com/doc/242521055/187248100-Analise-Multivariada-de-Dados-Joseph-Hair-pdf >. Accessed on: 16 November 2015.

HALL, M. A., 1999, *Correlation-Based Feature Selection for machine learning*. D.Sc. Dissertation, The University of Waikato, Department of Computer Science, Hamilton, New Zealand, 178p. Available online: < http://www.cs.waikato.ac.nz/~mhall/thesis.pdf >. Accessed on: 14 November 2015.

HALL, M. A., SMITH, L. A., 1997, "Feature subset selection: a correlation based filter approach". In: *Proceedings of the 4th International Conference on Neural Information and Intelligent Information Systems,* pp. 855-858, Dunedin, New Zealand. Available online: < http://www.cs.waikato.ac.nz/ml/publications/1997/Hall-LSmith97.pdf >. Accessed on: 14 November 2015.

HALL, M. A., SMITH, L. A., 1999, "Feature selection for machine learning: comparing a correlation-based filter approach to the wrapper". In: *Proceedings of the 12th International FLAIRS Conference, Advancement of Artificial Intelligence (AAAI),* 5p. Available online: < http://www.aaai.org/Papers/FLAIRS/1999/FLAIRS99-042.pdf >. Accessed 14 November 2015.

HAMMER, Ø., 2015a, *PAST: Multivariate statistics*. Available online: < http://folk.uio.no/ohammer/past/multivar.html >. Accessed on: 15 November 2015.

HAMMER, Ø., 2015b, *PAST: PAleontological STatistics*, Reference manual, Version 3.06, University of Oslo, 225p. Available online: < http://folk.uio.no/ohammer/past/past3manual.pdf >. Accessed on: 29 April 2015.

HAMMER, Ø., HARPER, D. A. T., RYAN, P. D., 2001, "PAST: PAleontological STatistics software package for education and data analysis", *Palaeontologia Electronica*, v. 4, n. 1, 9p. Available online: < http://palaeo-electronica.org/2001_1/past/issue1_01.htm >. Accessed on: 16 November 2015.

HENDERSON, F. M., LEWIS, A. J., 1998, *Principles and applications of imaging radar, Manual of Remote Sensing*, 3rd ed, v. 2, Hoboken, New Jersey, USA, Wiley, 866p.

HOLECZ, F., MEIER, E., PIESBERGEN, J., NIIESCH, D., 1993, "Topographic effects on radar cross section". In: *Proceedings of the SAR Calibration Workshop, CEOS Calibration/Validation Working Group, SAR Calibration Sub-Group,* pp. 23-28, Estec, Noordwijk, Netherlands, 20-24 September. Available online: < https://earth.esa.int/documents/10174/1597298/SAR26.pdf >. Accessed on: 14 November 2015.

HOLT, B., 2004, "SAR imaging of the ocean surface", In: Jackson, C. R., Apel, J. R. (eds), *Synthetic Aperture Radar Marine User's Manual*, NOAA/NESDIS, Office of Research and Applications, Chapter 2, pp. 25-79. Washington, DC, USA. Available online: < http://www.sarusersmanual.com >. Accessed on: 14 November 2015.

HONG, X., CHANG, S. W., RAMAN, S., SHAY, L. K., HODUR, R., 2000, "The Interaction between Hurricane Opal (1995) and a Warm Core Ring in the Gulf of Mexico", *Monthly Weather Review*, v. 128, pp. 1347-1365, doi: 10.1175/1520-0493(2000)128<1347:TIBHOA>2.0.CO;2. Available online: < http://homepage.ntu.edu.tw/~iilin/courses/ARSDAA/references/gulf.pdf >. Accessed on: 14 November 2015.

HOOKER, S. B., ESAIAS, W. E., FELDMAN, G. C., GREGG, W. W., MCCLAIN, C. R., 1992, "An overview of SeaWiFS and ocean color". In: Hooker, S. B., Firestone, E. R. (eds), *NASA Technical Memorandum 104566*, v. 1, Greenbelt, Maryland, NASA Goddard Space Flight Center, pp. 25 plus color plates.

HOOKER, S. B., MCCLAIN, C. R., 2000, "The calibration and validation of SeaWiFS data", *Progress in Oceanography*, v. 45, pp. 427-465.

HORNAFIUS, J. S., QUIGLEY, D., LUYENDYK, B. P., 1999, "The world's most spectacular marine hydrocarbon seeps (Coal Oil Point, Santa Barbara Channel, California): Quantification of emissions", *Journal of Geophysical Research*, v. 104, n. C9, pp. 20703-20711.

HOSTETTLER, F. D., KVENVOLDEN, K .A., ROSENBAUER, R. J., AND SHORT, J. W., 1999, "Aspects of the Exxon Valdez oil spill – A forensic study and a toxics controversy". In: *U.S. Geological Survey Toxic Substances Hydrology Program* –

Proceedings of the Technical Meeting, Charleston, South Carolina, v. 2, pp. 135-144, 8-12 March.

HOTELLING, H., 1933, “Analysis of a complex of statistical variables into principal components”, *Journal of Educational Psychology*, v. 24, n. 6, pp. 417-441, doi: 10.1037/h0071325. Available online: < http://psycnet.apa.org/journals/edu/24/6/417/ >. Accessed on: 14 November 2015.

HOVIS, W. A., CLARK, D. K., ANDERSON, F., AUSTIN, R. W., WILSON, W. H., BAKER, E. T., BALL, D., GORDON, H. R., MUELLER, J. L., EL-SAYED, S. Z., STURM, B., WRIGLEY, R. C., YENTSCH, C. S., 1980, "Nimbus-7 Coastal Zone Color Scanner: System Description and Initial Imagery", *Science,* New Series, v. 210, n. 4465, pp. 60-63.

HOVLAND, H. A., JOHANNESSEN, J. A., DIGRANES, G., 1994, "Slick detection in SAR images". In: *Proceedings of the International Geoscience and Remote Sensing Symposium (IGARSS '94), IEEE*, v. 4, pp. 2038-2040, Pasadena, California, 8-12 August.

HU, C., CARDER, K. L., MULLER-KARGER, F. E., 2000, "How precise are SeaWiFS ocean color estimates? Implications of digitization-noise errors", *Remote Sensing of Environment*, v. 76, pp. 239- 249.

HU, C., LI, X., PICHEL, W. G., MULLER-KARGER, F. E., 2009, "Detection of natural oil slicks in the NW Gulf of Mexico using MODIS imagery", *Geophysical Research Letters*, v. 36, n. L01604, pp. 1-5, doi: 10.1029/2008GL036119.

HU, C., MULLER-KARGER, F. E., 2007, "Response of sea surface properties to Hurricane Dennis in the eastern Gulf of Mexico", *Geophysical Research Letters*, n. 34, v. L07606, doi: 10.1029/2006GL028935.

HU, C., MULLER- KARGER, F. E., TAYLOR, C. J., MYHRE, D., MURCH, B., ODRIOZOLA, A. L., GODOY, G., 2003, "MODIS detects oil spills in Lake Maracaibo, Venezuela”, *EOS Transactions American Geophysical Union*, v. 84, n. 33, pp. 313-319.

IMO (International Maritime Organization), 2010. Available online: < http://www.imo.org/blast/mainframe.asp?topic_id=109 >. Accessed on: 14 November 2015.

INNMAN, A., EASSON, G., ASPER, V. L., DIERCKS, A. R., 2010, "The Effectiveness of Using MODIS Products to Map Sea Surface Oil". In: *Proceedings of the Oceans '10, IEEE,* v. 1, pp. 1-5.

IOANNIDIS, C., VASSILAKI, D., 2008, "Combined use of Spaceborne Optical and SAR Data - Incompatible Data Sources or a Useful Procedure?, TS 1H -

Developments in Scanner and Sensor Technologies". In: *Proceedings of the Integrating Generations, FIG working week,* 17p., Stockholm, Sweden, 14-19 June. Available online: https://www.fig.net/pub/fig2008/papers/ts01h/ts01h_01_ioannidis_vassalaki_3022.pdf. Accessed on: 14 November 2015.

IPIECA (International Petroleum Industry Environmental Conservation Association), 2015, *Completed Products, Oil Spill Preparedness and Response: A Good Practice Framework*. Available online: < http://oilspillresponseproject.org/completed-products >. Accessed on: 14 November 2015.

IPIECA (International Petroleum Industry Environmental Conservation Association), 2012, *Sensitivity mapping for oil spill response*, 33p. Available online: < http://www.ogp.org.uk/pubs/477.pdf >. Accessed on: 14 November 2015.

ITOPF (International Tanker Owners Pollution Federation), 2015a, *Recent Case Studies*. Available online: < http://www.itopf.com/in-action/recent-case-studies/ >. Accessed on: 14 November 2015.

ITOPF (International Tanker Owners Pollution Federation), 2015b, *Fate of marine oil spills*, 12p. Available online: < http://www.itopf.com/fileadmin/data/Documents/TIPS%20TAPS/TIP2FateofMarineOilSpills.pdf >. Accessed on: 14 November 2015.

IVANOV, A. Y., ERMOSHKIN, I. S., FANG, M., HE, M. S., KROVOTYNTSEV, V. A., 2005, "Use of the wide-swath synthetic aperture radar images for mapping sea oil pollution", *Earth Exploration from Space*, n. 5, p. 78-95.

IVANOV, A. Y., GOLUBOV, B. N., ZATYAGALOVA, B. B., 2007, "On oil and gas seeps and underground fluid discharge in the Southern Caspian Based on space radar data", *Oil And Gas Radar, Publication 27 - Radar data for oil and gas seeps monitoring*, 24p. Available online: < http://www.scanex.ru/en/publications/pdf/publication27.pdf >. Accessed on: 15 November 2015.

IVANOV, A. Y., VOSTOKOV, S. V., ERMOSHKIN, I. S., 2004, "Mapping of oil slicks polluting sea surface based on space radar data (the Caspian Sea)", *Earth Exploration from Space*, n. 4, pp. 82-94.

IVANOV, A. Y., ZATYAGALOVA, V. V., 2008, "A GIS approach to mapping oil spills in a marine environment", *International Journal of Remote Sensing*, v. 29, n. 21, pp. 6297-6313, doi: 10.1080/01431160802175587.

IVANOV, A., HE, M.-X., FANG, M.-Q., 2002, "Oil spill detection with the RADARSAT SAR in the waters of the Yellow and East China Sea: A case study". In:

Proceedings of the 23rd Asian Conference on Remote Sensing (ACRS), 8p., Kathmandu, Nepal, 25-29 November.

IYYAPPAN, M., RAMAKRISHNAN, S. S., RAJU, K. S., 2014, Study of discrimination between plantation and dense scrub based on backscattering behavior of C band SAR data". In: *Proceedings of the International Archives of the Photogrammetry, Remote Sensing and Spatial Information Sciences, Volume XL-8, Technical Commission VIII Symposium, International Society for Photogrametry and Remote Sensing (ISPRS),* pp. 755-760, Hyderabad, India, 9-12 December, doi: 10.5194/isprsarchives-XL-8-755-2014.

JACKSON, D. A., 1993, "Stopping rules in principal components analysis: a comparison of heuristical and statistical approaches", *Ecology*, v. 74, n. 8, pp. 2204-2214. Available online: < http://labs.eeb.utoronto.ca/jackson/pca.pdf >. Accessed on: 15 November 2015.

JAIN, A., ZONGKER, D., 1997, "Feature Selection: Evaluation, Application, and Small Sample Performance", *IEEE Transactions on Pattern Analysis and Machine Intelligence*, v1. 9, n. 2, pp. 153-158. Available online: < http://homes.cs.bilkent.edu.tr/~saksoy/courses/cs551-Spring2009/papers/jain97_feature_selection.pdf >. Accessed on: 14 November 2015.

JAYASRI, P. V., 2014, "SAR data calibration". In: *Proceedings of the Pre symposium tutorials on polarimetric SAR data processing and applications, International Society for Photogrametry and Remote Sensing (ISPRS),* 41p., Hyderabad, India, 9-12 December. Available online: < http://www.nrsc.gov.in/isprs/pdf/3.%20SAR_calibration_ISPRS_pre_symp_Dec2014_Jayasri.pdf >. Accessed on 14 November 2015.

JAYASRI, P. V., USHA SUNDARI, H. S. V., SITA KUMARI, E. V. S., PRASAD, A. V. V., 2014, "Study of Oil spill in Norwegian area using Decomposition Techniques on RISAT-1 Hybrid Polarimetric Data". In: *Proceedings of the International Archives of the Photogrammetry, Remote Sensing and Spatial Information Sciences, Volume XL-8, Technical Commission VIII Symposium, International Society for Photogrametry and Remote Sensing (ISPRS)*, pp. 1043-1048, Hyderabad, India, 9-12 December, doi: 10.5194/isprsarchives-XL-8-1043-2014. Available online: < http://www.nrsc.gov.in/isprs/pdf/213.pdf >. Accessed on 14 November 2015.

JENSEN, J. R., HALLS, J. N., MICHEL, J., 1998, "A Systems Approach to Environmental Sensitivity Index (ESI) Mapping for Oil Spill Contingency Planning and Response", *Photogrammetric Engineering & Remote Sensing*, v. 64, n. 10,

pp. 1003-1014, Available online: < http://www.asprs.org/a/publications/pers/98journal/october/1998_oct_1003-1014.pdf >. Accessed on: 14 November 2015.

JERNELOV, A., 2010, "The threats from oil spills: Now, then, and in the future", *AMBIO*, n. 39, pp. 353-366, doi: 10.1007/s13280-010-0085-5.

JERNELOV, A., LINDEN, O., 1981a, "Ixtoc I: A case study of the world's largest oil spill", *AMBIO*, n. 10, n. 6, pp. 299-306.

JERNELOV, A., LINDEN, O., 1981b, "The effects of oil pollution on mangroves and fisheries in Ecuador-Colombia", In: Teas, H.J. (ed), Tasks for vegetation science, v. 8, Chapter 20, IVL Publ. B 610, ISBN: 978-90-481-8526-9.

JHA, M. N., LEVY, J., GAO, Y., 2008, "Review: Advances in remote sensing for oil spill disaster management: state-of-the-art sensors technology for oil spill surveillance", *Sensors*, v. 8, pp. 236-255.

JOHANNESSEN, O. M., ESPEDAL, H. A., JENKINS, A. J., KNULST, J., 1996, "SAR surveillance of ocean surface slicks". In: *Proceedings of the 2nd ERS Application Workshop*, pp. 187-192, London, UK, 6-8 December/1995.

JOHANNESSEN, O. M., KORSBAKKEN, E., SAMUEL, P., JENKINS, A. D., ESPEDAL, H. A., 1997, "COAST WATCH: Using SAR imagery in an operational system for monitoring coastal currents, wind, surfactants and oil spills". In: Stel, J.H., Behrens, H.W.A., Borst, J.C., Droppert, L.J., Meulen, J. v.d., *Operational Oceanography, The Challenge for European Co-operation*, Elsevier Science, pp. 234-242.

JOHANNESSEN, O. M., SANDVEN, S., JENKINS, A. D., DURAND, D., PETTERSSON, L. H., ESPEDAL, H., EVENSEN, G., HAMRE, T., 2000, "Satellite earth observation in operational oceanography", *Coastal Engineering*, v. 41, pp. 155-176.

JOLLIFF, J. K., WALSH, J. J., HE, R., WEISBERG, R., STOVALL-LEONARD, A., COBLE, P. G., CONMY, R., HEIL, C., NABABAN, B., ZHANG, H., HU, C., MULLER-KARGER, F. E., 2003, "Dispersal of the Suwannee River plume over the West Florida shelf: Simulation and observation of the optical and biochemical consequences of a flushing event", *Geophysical Research Letters*, v. 30, n. 13, p. 1709, doi: 10.1029/2003GL016964.

JOLLIFFE, I. T., 2002, *Principal component analysis*, 2nd ed, New York, USA, Springer-Verlag, 487p., ISBN: 0-387-95442-2. Available online: < http://cda.psych.uiuc.edu/statistical_learning_course/Jolliffe%20I.%20Principal%20Component%20Analysis%20(2ed.,%20Springer,%202002)(518s)_MVsa_.pdf >. Accessed on: 15 November 2015.

JONES, B., 2001, "A comparison of visual observations of surface oil with Synthetic Aperture Radar imagery of the Sea Empress oil spill", *International Journal of Remote Sensing*, v. 22, n. 9, pp. 1619-1638, doi: 10.1080/01431160010008564.

JONES, D. A., PLAZA, J., WATT, I., AL SANEI, M., 1998, "Long-term (1991-1995) monitoring of the intertidal biota of Saudi Arabia after the 1991 Gulf War oil spill", *Marine Pollution Bulletin*, v. 36, n. 6, pp. 472-489.

JURADO, M., MONTEMAYOR, M., 2005, Pido la palabra, 5º nivel, 5th Edition, Universidad Nacional Autónoma de Mexico (UNMA), ISBN: 978-968-36-1667-8, 255p.

KAISER, H. F., 1961, "A note on Guttman's lower bound for the number of common factors", *The British Journal of Statistical Psychology*, v. 14, n. 1, pp. 1-2, doi: 10.1111/j.2044-8317.1961.tb00061.x.

KELLEY, L. A., GARDNER, S. P., SUTCLIFFE, M. J., 1996, "An automated approach for clustering an ensemble of NMR-derived protein structures into conformationally related subfamilies", *Protein Engineering*, v. 9, n. 11, pp. 1063-1065. Available online: < http://www.sbg.bio.ic.ac.uk/people/kelley/pdfs/nmrclust.pdf >. Accessed on: 14 November 2015.

KLINKENBERG, B., 1994, "A review of methods used to determine the fractal dimension of linear features", *Mathematical Geology*, v. 26, n. 1, 46p. Available online: < http://ibis.geog.ubc.ca/~brian/publications/review_of_methods_fractals.pdf >. Accessed on: 14 November 2015.

KOSTIANOY, A. G., LITOVCHENKO, K. TS., LAVROVA, O., MITYAGINA, M. I., BOCHAROVA, T. Y., LEBEDEV, S. A., STANICHNY, S. V., SOLOVIEV, D. M., SIROTA, A. M., PICHUZHKINA, O. E., 2006, "Operational satellite monitoring of oil spill pollution in the southeastern Baltic Sea: 18 months experience", *Environmental Research, Engineering and Management*, v. 38, n. 4, pp. 70-77.

KUBAT, M., HOLTE, R. C., MATWIN, S., 1998, "Machine learning for the detection of oil spills in satellite radar images", *Machine Learning*, v. 30, pp. 195-215.

KULAWIAK, M., PROSPATHOPOULOS, A., PERIVOLIOTIS, L., LUBA, M., KIOROGLOU, S., STEPNOWSKI, A., 2010, "Interactive visualization of marine pollution monitoring and forecasting data via a Web-based GIS", *Computers & Geosciences*, n. 36, pp. 1069-1080, doi: 10.1016/j.cageo.2010.02.008

KUMARI, E. V. S. S., 2014, "SAR Remote Sensing Technology and Applications". In: *Proceedings of the Pre symposium tutorials on polarimetric SAR data processing and applications, International Society for Photogrametry and Remote Sensing*

(ISPRS), 47p., Hyderabad, India, 9-12 December. Available online: < http://www.nrsc.gov.in/isprs/pdf/1.%20ISPRS-SARRemoteSensing.pdf >. Accessed on: 14 November 2015.

KUSEK, K.M., VARGO, G., STEIDINGER, K., 1999, "Gymnodinium breve in the field, in the lab and in the newspaper – A scientific and journalistic analysis of Florida red tides", *Contributions in Marine Science*, v. 34, pp. 1-229.

KVENVOLDEN, K. A., COOPER, C. K., 2003, "Natural seepage of crude oil into the marine environment", *Geo-Marine Letters*, v. 23, pp. 140-146, doi: 10.1007/s00367-003-0135-0.

LAMMOGLIA, T., SOUZA FILHO, C. R., 2012, "Mapping and characterization of the API gravity of offshore hydrocarbon seepages using multispectral ASTER data", *Remote Sensing of Environment*, v. 123, pp. 381-389, ISSN 0034-4257, doi: 10.1016/j.rse.2012.03.026.

LANE, D. M., SCOTT, D., HEBL, M., GUERRA, R., OSHERSON, D., ZIEMER, H., 2015, *Introduction to Statistics*, Online Edition, 695p. Available online: < http://onlinestatbook.com/Online_Statistics_Education.pdf >. Accessed on: 14 November 2015.

LAUR, H., BALLY, P., MEADOWS, P., SANCHEZ, J., SCHAETTLER, B., LOPINTO, E., ESTEBAN, D., 1998, *Derivation of the Backscattering Coefficient Sigma-Nought in ESA ERS SAR PRI Products, ERS SAR Calibration*, Document No: ES-TN-RS-PM-HL09, 7 September 1998, n. 2, Rev. 5b, 51p.

LAVROVA, O. Y., KOSTIANOY, A. G., 2011, "Catastrophic Oil Spill in the Gulf of Mexico in April-May 2010". In: *Proceedings of the Izvestiya, Atmospheric and Oceanic Physics,* v. 47, n. 9, pp. 1114-1118, Original Russian Text, published in Issledovaniya Zemli iz Kosmosa, 2010, n. 6, pp. 67-72, doi: 10.1134/S0001433811090088.

LEDESMA, R. D., VALERO-MORA, P., 2007, “Determining the number of factors to retain in EFA: an easy-to-use computer program for carrying out Parallel Analysis”, *Practical Assessment, Research & Evaluation*, v. 12, n. 2, 11p. Available online: < http://pareonline.net/pdf/v12n2.pdf >. Accessed on: 15 November 2015.

LEE, M.-J., YUN, M. J., PARK, M.-S., CHA, S. H., KIM, M.-J., LEE, J. D., KIM, K. W., 2009, “Paraaortic lymph node metastasis in patients with intraabdominal malignancies: CT vs PET”, *World Journal of Gastroenterology*, v. 15, n. 35, pp. 4434-4438, doi: 10.3748/wjg.15.4434. Available online: < http://www.ncbi.nlm.nih.gov/pmc/articles/PMC2747065/pdf/WJG-15-4434.pdf >. Accessed on: 18 November 2015.

LEGENDRE, P., LEGENDRE, L., 2012, *Numerical ecology, 3rd English ed., Developments in Environmental Modelling,* Amsterdam, Elsevier Science B.V., 990p., ISBN: 978-0444538680.

LEIFER, I. KAMERLING, M. J., LUYENDYK, B. P., WILSON, D. S., 2010, "Geologic control of natural marine hydrocarbon seep emissions, Coal Oil Point seep field, California", *Geo-Marine Letters*, v. 30, pp. 331-338, doi: 10.1007/s00367-010-0188-9.

LEIFER, I., LEHR, W. J., SIMECEK-BEATTY, D., BRADLEY, E., CLARK, R., DENNISON, P., HU, Y., MATHESON, S., JONES, C. E., HOLT, B., REIF, M., ROBERTS, D. A., SVEJKOVSKY, J., SWAYZE, G., WOZENCRAFT, J., 2012, "Review – State of the art satellite and airborne marine oil spill remote sensing: Application to the BP Deepwater Horizon oil spill", *Remote Sensing of Environment*, v. 124, pp. 185-209, doi: 10.1016/j.rse.2012.03.024.

LEIFER, I., LUYENDYK, B., BRODERICK, K., 2006, "Tracking an oil slick from multiple natural sources, Coal Oil Point, California", *Marine and Petroleum Geology*, v. 23, n. 5, pp. 621-630, doi: 10.1016/j.marpetgeo.2006.05.001.

LEIFER, I., WILSON, K., 2004, "Quantified Oil Emissions with a video-monitored, oil seep-tent", *Marine Technology Society Journal, Underwater Pollution Threats to Our Nation's Marine Resources*, v. 38, n. 3, pp. 44-53.

LITOVCHENKO, K., IVANOV, A., 2008, "Monitoring of Oil Spills in the North Caspian Sea using SAR Imagery and Multi-Sensor Satellite Data". In: *Proceedings of the International Geoscience and Remote Sensing Symposium (IGARSS '08), IEEE,* v. 4, pp. IV-605-IV-608, Boston, Massachusetts, 8-11 July, doi: 10.1109/IGARSS.2008.4779794.

LITOVCHENKO, K., IVANOV, A., ERMAKOV, S., 1999, "Detection of oil slicks parameters from ALMAZ and ERS-1 SAR imagery". In: *Proceedings of the International Geoscience and Remote Sensing Symposium (IGARSS '99), IEEE,* pp. 1484-1486, Hamburgo, Germany, 28 June-02 July, doi: 10.1109/IGARSS.1999.771995.

LIU, P., LI, X., QU, J. J., WANGD, W., ZHAO, C., PICHEL, W., 2011, "Oil spill detection with fully polarimetric UAVSAR data", *Marine Pollution Bulletin*, v. 62, pp. 2611-2618, doi: 10.1016/j.marpolbul.2011.09.036.

LOHNINGER, H., 1999, *Teach/Me Data Analysis*, Text-Only Light Edition, Springer-Verlag, Berlin-New York-Tokyo. ISBN 3-540-14743-8. Available online: < http://www.vias.org/tmdatanaleng/cc_classif_intro.html >. Accessed on: 18 November 2015.

LONG, M. D. 2012, *Remote sensing for offshore marine oil spill emergency management, security and pollution control*, Bremerhaven, Germany, Development for The Americas, Optimare Senso Systeme, AG., 9p. Available online: < http://www.seadarq.com/lib/seadarq-bibliography/remote-sensing-for-offshore-marine-oil-spill-emergency-management-security-and-pollution-control-m.-d.-long >. Accessed on: 15 November 2015.

LUSCH, D. P., 1999a, Fundaments of GIS, Emphasizing GIS use for natural resource managements Center for Remote Sensing and GIS, Basic Science and Remote Sensing Initiative (BSRSI), Michigan State University, 84p.

LUSCH, D. P., 1999b, Introduction to environmental remote sensing, Center for Remote Sensing and GIS, Basic Science and Remote Sensing Initiative (BSRSI), Michigan State University, 247p.

LUSCH, D. P., 1999c, Introduction to microwave remote sensing, Center for Remote Sensing and GIS, Basic Science and Remote Sensing Initiative (BSRSI), Michigan State University, 84p.

LUSCOMBE, A. P., FERGUSON, I., SHEPHERD, N., ZIMCIK, D. G., NARAINE, P., 1993, "The RADARSAT Synthetic Aperture Radar development", *Canadian Journal of Remote Sensing*, v. 19, n. 4, pp. 298-310, doi: 10.1080/07038992.1993.10874565.

MACDONALD, I. R., 2010, "Deepwater disaster: how the oil spill estimates got it wrong", *Significance*, v. 7, n. 4, pp. 149-154.

MACDONALD, I. R., GUINASSO, N. L., ACKLESON, S. G., AMOS, J. F., DUCKWORTH, R., BROOKS, J. M., 1993, "Natural oil slicks in the Gulf of Mexico visible from space", *Journal of Geophysical Research*, v. 98, n. C9, pp. 16351-16364.

MACDONALD, I. R., LEIFER, I., SASSEN, R., STINE, P., MITCHELL, R., GUINASSO, N., 2002, "Transfer of hydrocarbons from natural seeps to the water column and atmosphere", *Geofluids*, v. 2, n. 2, pp. 95-107, doi: 10.1046/j.1468-8123.2002.00023.x.

MACDONALD, I. R., REILLY JR., J. F., BEST, S. E., VENKATARAMAIAH, R., SASSEN, R., AMOS, J., GUINASSO JR., N. L., 1996, "Remote sensing inventory of active oil seeps and chemosynthetic communities in the northern Gulf of Mexico". In: Schumacher, D., Abrams, M. A., *Hydrocarbon migration and its near-surface expression*, AAPG Memoir 66, Tulsa, Oklahoma, American Association of Petroleum Geologists, pp. 27-37.

MACDONALD, I. R., SMITH, M., HUFFER, F. W., 2010, "Community structure comparisons of lower slope hydrocarbon seeps, northern Gulf of Mexico", *Deep-Sea Research II*, n. 57, pp. 1904-1915.

MACDONALD, J. A., 1991, *Automatic classification of satellite images in the textural domains using semivariograms*. M.Sc. Thesis, University of Nevada, Reno, NV, 82p.

MAGAÑA, H. A., CONTRERAS, C., VILLAREAL, T. A., 2003, "A historical assessment of *Karenia brevis* in the western Gulf of Mexico", *Harmful Algae*, v. 2, pp. 163-171.

MAIMON, O., ROKACH, L., 2010, *Data Mining and Knowledge Discovery Handbook*, 2nd Edition, New York, Springer Science, 1,285p., doi: 10.1007/978-0-387-09823-4. Available online: < http://www.cs.bme.hu/nagyadat/Data_Mining_and_Knowledge_Discovery.pdf >. Accessed on: 18 November 2015.

MANO, M. F., BEISL, C. H., SIQUEIRA, C. Y. S., PEREIRA, J. S., 2014, "Evaluation of remote technologies applied to natural seep mapping and their impact in oil exploration". In: *Proceedings of the Rio Oil & Gas Expo and Conference*, 7p., 15-18 September, Rio de Janeiro, Brazil.

MANO, M. F., BEISL, C., LANDAU, L., 2011, "Identifying Oil Seep Areas at Seafloor Using Inverse Modeling. Extended Abstract." In: *Proceedings of the American Association of Petroleum Geologists International Conference & Exhibition, AAPG*, 3p., Milan.

MARGHANY, M., CRACKNELL, A. P., HASHIM, M., 2009, "Modification of fractal algorithm for oil spill detection from RADARSAT-1 SAR data", *International Journal of Applied Earth Observation and Geoinformation*, v. 11, pp. 96-102, doi: 10.1016/j.jag.2008.09.002.

MARTIN, S., 2004, *An introduction to ocean remote sensing*, 1st ed., Cambridge, Cambridge University Press, 426p., ISBN: 0-521-80280-6.

MASOOMI, A., HAMZEHYAN, R., SHIRAZI, N. C., 2012, "Speckle reduction approach for SAR image in satellite communication", *International Journal of Machine Learning and Computing*, v. 2, n. 1, pp. 62-70.

MASTERS, J., 2010, *Hurricane Karl: first major hurricane ever in the Bay of Campeche*, Weather Underground. Available online: < http://www.wunderground.com/blog/JeffMasters/comment.html?entrynum=1622&page=8 >. Accessed on: 14 November 2015.

MCCAFFERY, S. J., DAVIS, A., CRAIG, D., 2009, "Distinguishing between natural crude oil seepage and anthropogenic petroleum hydrocarbons in soils at a crude

oil processing facility, coastal California", *Environmental Forensics*, v. 10, pp. 162-174, doi: 10.1080/15275920902873459.

MCCANDLESS JR., S. W., JACKSON, C. R., 2004, “Principles of Synthetic Aperture Radar”, In: Jackson, C. R., Apel, J. R. (eds), *Synthetic Aperture Radar Marine User’s Manual,* NOAA/NESDIS, Office of Research and Applications, Chapter 1: pp. 1-23, Washington, DC, USA. Available online: < http://www.sarusersmanual.com >. Accessed on: 14 November 2015.

MCCANDLESS, S. W., JACKSON, C. R., 2004, "Principles of Synthetic Aperture Radar". In: Jackson, C. R., Apel, J. R. (eds), *Synthetic Aperture Radar Marine User’s Manual,* NOAA/NESDIS, Office of Research and Applications, Chapter 1, Washington, DC., USA, pp. 263-275. Available online: < http://www.sarusersmanual.com >. Accessed on: 14 November 2015.

MCCLAIN, C. R., FELDMAN, G. C., HOOKER, S. B., 2004, "An overview of the SeaWiFS project and strategies for producing a climate research quality global ocean bio-optical time series", *Deep-Sea Research II*, v. 51, pp. 5-42.

MCCLAIN, C. R., HOOKER, S. FELDMAN, G., BONTEMPI, P., 2006, "Satellite Data for Ocean Biology, Biogeochemistry, and Climate Research”, *EOS Transactions, American Geophysical Union*, v. 87, n. 34, pp. 337-343.

MCGARIGAL , K., MARKS, B. J., 1994, *FRAGSTATS: Spatial pattern analysis program for quantifying landscape structure*, USDA For. Serv. Gen. Tech. Rep. PNW-351, 134p. Available online: < http://www.umass.edu/landeco/pubs/mcgarigal.marks.1995.pdf >. Accessed on: 14 November 2015.

MCGREGOR, S. L. T., MURNANE, J. A., 2010, "Paradigm, methodology and method: Intellectual integrity in consumer scholarship", *International Journal of Consumer Studies*, v. 34, n. 4, pp. 419-427. Available online: < http://www.consultmcgregor.com/documents/research/Methodological-paper-2010-for-web.pdf >. Accessed on: 14 November 2015.

MCHUGH, S. L., 2009, *Satellite synthetic aperture radar in the prosecution of illegal oil discharges*. M.Sc. Thesis, Memorial University of Newfoundland, 122p. Available online: < http://collections.mun.ca/cdm4/document.php?CISOROOT=/theses4&CISOPTR=83576&REC=9 >. Accessed on: 14 November 2015.

MCLEROY-ETHERIDGE, S. L., ROESLER, C. S., 1999, "Are the inherent optical properties of phytoplankton responsible for the distinct ocean colors observed during harmful algal blooms?". In: *Proceedings of the Ocean Optics XIV, SPIE,* 7p., Kailua-Kona, Hawaii, 10-13 November.

MDA (MacDonald Dettwiler and Associates Ltd.), 2004, *RADARSAT-1 Product Description*. In: Technical Report RSI-GS-026, Issue/Revision: 3/0, 19 of August, 125p. Available online: < http://gs.mdacorporation.com/includes/documents/R1_PROD_SPEC.pdf >. Accessed on: 14 November 2015.

MDA (MacDonald, Dettwiler and Associates Ltd.), 2011, *RADARSAT-2 Product Format definition*. In: Technical Report RN-RP-51-2713, Issue/Revision: 1/10, 17 of August, Richmond, B.C., Canada, 83p. Available online: < http://gs.mdacorporation.com/includes/documents/RN-RP-51-2713%20RS-2%20Product%20Format%20Definition_1_10.pdf >. Accessed on: 14 November 2015.

MDA (MacDonald, Dettwiler and Associates Ltd.), 2014, *RADARSAT-2 Product Description*. In: Technical Report RN-SP-52-1238, Issue/Revision: 1/11, 5 of May, Richmond, B.C., Canada, 84p. Available online: < http://gs.mdacorporation.com/products/sensor/radarsat2/RS2_Product_Description.pdf >. Accessed on: 14 November 2015.

MENDOZA, A., MIRANDA, F., BANNERMAN, K., PEDROSO, E., HERRERA, M., 2004a, "Satellite Environmental Monitoring of Oil Spills in the South Gulf Of Mexico". In: *Proceedings of the Offshore Technology Conference, OCT 16410*, 7p., Houston, Texas.

MENDOZA, A., MIRANDA, F., PEDROSO, E., BANNERMAN, K., LOPEZ, O., 2004b, "Cantarell oil seep characterization using a satellite monitoring program in the South Gulf of Mexico". In: *Proceedings of the American Association of Petroleum Geologists International Conference, AAPG*, Cancun, Mexico, 24-27 October.

MERA, D., COTOS, J. M., VARELA-PET, J., GARCIA-PINEDA, O., 2012, "Adaptive thresholding algorithm based on SAR images and wind data to segment oil spills along the northwest coast of the Iberian Peninsula", *Marine Pollution Bulletin*, n. 64, pp. 2090-2096, doi: 10.1016/j.marpolbul.2012.07.018

MERA, D., COTOS, J. M., VARELA-PET, J., RODRÍGUEZ, P. G., CARO, A., 2014, "Automatic decision support system based on SAR data for oil spill detection", *Computers & Geosciences*, n. 72, pp. 184-191, doi: 10.1016/j.cageo.2014.07.015.

MERINO, M., 1997, "Upwelling on the Yucatan Shelf: hydrographic evidence", *Journal of Marine Systems*, n. 13, pp. 101-121.

MIGLIACCIO, M., GAMBARDELLA, A., NUNZIATA, F., SHIMADA, M., ISOGUCHI, O., 2009a, "The PALSAR polarimetric mode for sea oil slick observation, *IEEE*

Transactions on Geoscience and Remote Sensing, v. 47, n. 12, pp. 4032-4041, doi: 10.1109/TGRS.2009.2028737.

MIGLIACCIO, M., GAMBARDELLA, A., TRANFAGLIA, M., 2007, "SAR polarimetry to observe oil spills", *IEEE Transactions on Geoscience and Remote Sensing*, v. 45, n. 2, pp. 506-511, doi: 10.1109/TGRS.2006.888097.

MIGLIACCIO, M., NUNZIATA, F., BROWN, C. E., HOLT, B., LI, X., PICHEL, W., SHIMADA, M., 2012, "Polarimetric synthetic aperture radar utilized to track oil spills", *EOS Transactions, American Geophysical Union*, v. 93, n. 16, pp. 161-163. Available online: < http://onlinelibrary.wiley.com/doi/10.1029/2012EO160001/epdf >. Accessed on: 14 November 2015.

MIGLIACCIO, M., NUNZIATA, F., GAMBARDELLA, A., 2009b, "On the co-polarized phase difference for oil spill observation", *International Journal of Remote Sensing*, v. 30, n. 6, pp. 1587-1602, doi: 10.1080/01431160802520741.

MIGLIACCIO, M., NUNZIATA, F., MONTUORI, A., BROWN, C. E., 2011a, "Marine added-value products using RADARSAT-2 fine quad-polarization", *Canadian Journal of Remote Sensing*, v. 37, n. 5, pp. 443-451, doi: 10.5589/m11-054.

MIGLIACCIO, M., NUNZIATA, F., MONTUORI, A., LI, X., PICHEL, W. G., 2011b, "A multi-frequency polarimetric SAR processing chain to observe oil fields in the Gulf of Mexico", *IEEE Transactions on Geoscience and Remote Sensing*, v. 47, pp. 4729-4737.

MILLIE, D. F., SCHOFIELD, O. M., KIRKPATRICK, G. J., JOHNSEN, G., TESTER, P. A., VINYARD, B. T., 1997, "Detection of Harmful algal Bloom using photopigments and absorption signatures: A case study of the Florida red tide dinoflagellate, *Gymnodinium Breve"*, *Limnology and Oceanography*, v. 42, n. 5, part 2, pp. 1240-1251. Avaliable online: < http://www.aslo.org/lo/toc/vol_42/issue_5_part_2/1240.pdf >. Accessed on: 14 November 2015.

MILLIGAN, G. W., COOPER, M. C., 1988, "A study of standardization of variables in cluster analysis", *Journal of Classification*, v. 5, n. 2, pp. 181-204, doi: 10.1007/BF01897163.

MIRANDA, F. P., 1990, *Reconnaissance geologic mapping of a heavily-forested shield area (Guiana Shield, northwestern Brazil).* Ph.D. Dissertation, University of Nevada, Reno, 176p.

MIRANDA, F. P., BEISL, C. H., BENTZ, C. M., 1998, "Application of the Unsupervised Semivariogram Textural Classifier (USTC) for the detection of natural oil seeps

using RADARSAT-1 data obtained offshore the Amazon River mouth", *American Association of Petroleum Geology Bulletin*, n. 82, p. 1944.

MIRANDA, F. P., LANDAU, L., BENTZ, C. M., BEISL, C. H., PEDROSO, E. C., 2001, "Seepage slick detection in the Brazilian continental margin using RADARSAT-1 data". In: *Proceedings of the 20th International Conference on Offshore Mechanics and Arctic Engineering, OMAE '01*, v. 5, pp. 275-281, Rio de Janeiro, 3-8 June, doi: OMAE2001/OSU-5161.

MIRANDA, F. P., QUINTERO-MARMOL, A. M., PEDROSO, E. C., BEISL, C. H., WELGAN, P., MORALES, L. M., 2004, "Analysis of RADARSAT-1 data for offshore monitoring activities in the Cantarell Complex, Gulf of Mexico, using the unsupervised semivariogram textural classifier (USTC)", *Canadian Journal of Remote Sensing*, v. 30, n. 3, pp. 424-436, doi: 10.5589/m04-019.

MOITA NETO, J. M., MOITA, G. C., 1998, "Uma introdução à análise exploratória de dados multivariados", *Química Nova*, v. 21, n. 4, pp. 467-469, in Portuguese, doi: 10.1590/S0100-40421998000400016. Available online: < http://www.scielo.br/pdf/qn/v21n4/3193.pdf >. Accessed on: 14 November 2015.

MONSON, D. H., DOAK, D. F., BALLACHEY, B. E., JOHNSON, A., BODKIN, J. L., 2000, "Long-term impacts of the Exxon Valdez oil spill on sea otters, assessed through age-dependent mortality patterns". In: *Proceedings* of the National Academy of Sciences of the United States of America, v. 97, n. 12, pp. 6562–6567, doi: 10.1073/pnas.120163397

MONTAGNA, P. A., BAUER, J. E., PRIETO, M. C., HARDIN, D. H., SPIES, R. B., 1986, "Benthic metabolism in a natural coastal petroleum seep", *Marine Ecology Progress Series*, v. 34, p. 31-40.

MONTAGNA, P. A., BAUER, J. E., TOAL, J., HARDIN, D. H., SPIES, R. B., 1989, "Vertical distribution of meiofauna in the sediment of a natural hydrocarbon seep", *Journal of Marine Research*, v. 47 pp. 657-680.

MONTALI, A., GIANCITO, G., MIGLIACCIO, M., GAMBARDELLA, A., 2006, "Supervised pattern classification techniques for oil spill classification in SAR images: preliminary results". In: *Proceedings of the SEASAR '06 Workshop, ESA-ESRIN*, 6p., Frascati, Italy, 23-26 January.

MORENA, L. C., JAMES, K. V., BECK, J., 2004, "An introduction to the RADARSAT-2 mission", *Canadian Journal of Remote Sensing*, v. 30, n. 3, pp. 221-234, doi: 10.5589/m04-004.

MOROVIC, M., IVANOV, A., 2011, "Oil spill monitoring in the Croatian Adriatic waters: needs and possibilities", *Acta Adriatrica*, v. 52, n.1, pp. 45-56.

MPB (Marine Pollution Bulletin), 1993, *The 1991 Gulf War: Coastal and Marine Environmental Consequences,* Special issue examining the consequences of the 1991 Gulf War, Price, A.R.G., Robinson, J.H. (eds), v. 27, Available online: < http://www.sciencedirect.com/science/journal/0025326X/27/ >. Accessed on: 14 November 2015.

MULLER-KARGER, F. E., SMITH, J. P., WERNER, S., CHEN, R., ROFFER, M., LIU, Y., MUHLING, B., LINDO-ATICHATI, D., LAMKIN, J., CERDEIRA-ESTRADA, S., ENFIELD, D. B., 2015, "Natural variability of surface oceanographic conditions in the offshore Gulf of Mexico", *Progress in Oceanography*, n. 134, pp. 54-76, doi: 10.1016/j.pocean.2014.12.007.

MUTSVANGWA, T., DOUGLAS, T. S., 2007, "Morphometric analysis of facial landmark data to characterize the facial phenotype associated with fetal alcohol syndrome", *Journal of Anatomy*, v. 210, n. 2, pp. 209-220, doi: 10.1111/j.1469-7580.2006.00683.x. Available online: < http://www.ncbi.nlm.nih.gov/pmc/articles/PMC2100273/ >. Accessed on: 15 November 2015.

NAEHR, T. H., BIRGEL, D., BOHRMANN, G., MACDONALD, I. R., KASTEN, S., 2009, "Biogeochemical controls on authigenic carbonate formation at the Chapopote 'asphalt volcano', Bay of Campeche", *Chemical Geology*, v. 266, pp. 390-402, doi: 10.1016/j.chemgeo.2009.07.002

NCSS (Number Cruncher Statistical System), 2015, *Chapter 445: Hierarchical Clustering and Dendrograms*, NCSS Statistical Software, 15p., Available online: < http://ncss.wpengine.netdna-cdn.com/wp-content/themes/ncss/pdf/Procedures/NCSS/Hierarchical_Clustering-Dendrograms.pdf >. Accessed on: 14 November 2015.

NEUPARTH, T., MOREIRA, S. M., SANTOS, M. M., REIS-HENRIQUES, M. A., 2012, "Review of oil and HNS accidental spills in Europe: Identifying major environmental monitoring gaps and drawing priorities", *Marine Pollution Bulletin*, v. 64, n. 6, pp. 1085-1095, ISSN 0025-326X, doi: 10.1016/j.marpolbul.2012.03.016.

NHC (National Hurricane Center), 2015, *Hurricanes in History*, available online (last accessed on November 2015): http://www.nhc.noaa.gov/outreach/history/

NOAA (National Oceanic and Atmospheric Administration), 1980, *Proceedings of a Symposium on Prerliminary results from the September 1979 research/pierce Ixtoc-1 cruise,* Key Biscayne, Florida, June 9-10, U.S. Department of Commerce. Available online: < http://docs.lib.noaa.gov/noaa_documents/NOS/OMPA/IXTOC-I_cruise_1980.pdf >. Accessed on: 14 November 2015.

NOAA (National Oceanic and Atmospheric Administration), 1981, *The Ixtoc-1 oil spill: The Federal Scientific Response*, Hooper, C. H. (ed), Bolder, Colorado, USA, Department of Commerce. Available online: < http://docs.lib.noaa.gov/noaa_documents/NOS/OMPA/IXTOC_Special%20report.pdf >. Accessed on: 14 November 2015.

NOAA (National Oceanic and Atmospheric Administration), 2002, *Environmental Sensitivity Index Guidelines*, Version 3.0, NOAA Technical Memorandum NOS OR&R 11, Hazardous Materials Response Division, Office of Response and Restoration, NOAA Ocean Service, 89p. Available online: < http://response.restoration.noaa.gov/sites/default/files/ESI_Guidelines.pdf >. Accessed on: 14 November 2015.

NOAA (National Oceanic and Atmospheric Administration), 2013, *Mearns Rock: Watching Ecological Recovery from an Oil Spill*, Emergency Response Division, Office of Response and Restoration. Available online: < http://response.restoration.noaa.gov/mearns-rock-watching-ecological-recovery-oil-spill >. Accessed on: 15 November 2015.

NOVO, E. M. L. M., 1998, *Sensoriamento remoto, princípios e aplicações*, 2nd ed (3rd reprint), Editora Edgard Blucher Ltda, 308p.

NRCAN (Natural Resources Canada), 2014, *Fundamentals of Remote Sensing*. Available online: < http://www.nrcan.gc.ca/sites/www.nrcan.gc.ca/files/earthsciences/pdf/resource/tutor/fundam/pdf/fundamentals_e.pdf >. Accessed on: 14 November 2015.

NRCC (National Research Council Committee), 1985, *Oil in the Sea: Inputs, fates, and effects*, Washington, DC, The National Academies Press. Available online: < http://www.nap.edu/openbook.php?record_id=314 >. Accessed on: 14 November 2015.

NRCC (National Research Council Committee), 2003, *Oil in the sea III: Inputs, fates, and effects*, Washington, DC, The National Academies Press, ISBN: 9780309084383. Available online: < http://www.nap.edu/openbook.php?record_id=10388 >. Accessed on: 14 November 2015.

NUNZIATA, F., GAMBARDELLA, A., MIGLIACCIO, M., 2013, "On the degree of polarization for SAR sea oil slick observation", *Journal of Photogrammetry and Remote Sensing, International Society for Photogrametry and Remote Sensing (ISPRS)*, v. 78, pp. 41-49, doi: 10.1016/j.isprsjprs.2012.12.007.

NUNZIATA, F., MIGLIACCIO, M., 2015, "Oil spill monitoring and damage assessment via PolSAR measurements, International Oil Spill Response Technical Seminar", *Aquatic Procedia*, v. 3, pp. 95-102, doi: 10.1016/j.aqpro.2015.02.232.

NUSSMEIER, N. A., MIAO, Y., ROACH, G. W., WOLMAN, R. L., MORA-MANGANO, C., FOX, M., SZEKELY, A., TOMMASINO, C., SCHWANN, N.M., MANGANO, D.T., 2010, Predictive value of the National Institutes of Health Stroke Scale and the Mini-Mental State Examination for neurologic outcome after coronary artery bypass graft surgery, *Journal of Thoracic and Cardiovascular Surgery*, v. 139, n. 4, 12p., doi: 10.1016/j.jtcvs.2009.07.055.

OGC (Open Geospatial Consortium), 2015, *Oil Spill Response Common Operating Picture (COP)*. Available online: < http://www.opengeospatial.org/projects/initiatives/ogpoilspill >. Accessed on: 15 November 2015.

OKAMOTO, K., KOBAYASHI, T., MUSUKO, H., SHIMADA, M., 1994, "Artificial pollution detection experiments in the sea adjacent to Japan by the synthetic aperture radar on the European Remote Sensing satellite-1", *The Journal of Space Technology and Science, Special Issue on the Earth as Seen from Space, Japanese Rocket Society*, v. 10, n. 1, pp. 19-27, doi: 10.11230/jsts.10.1_19.

OLASCOAGA, M. J., BERON-VERA, F. J., BRAND, L. E., KOÇAK, H., 2008, "Tracing the early development of harmful algal blooms on the West Florida Shelf with the aid of Lagrangian coherent structures", *Journal of Geophysical Research*, v. 113, n. C12014, doi: 10.1029/2007JC004533.

OLITA, A., CUCCO, A., SIMEONE, S., RIBOTTI, A., FAZIOLI, L., SORGENTE, B., SORGENTE, R., 2012, "Oil spill hazard and risk assessment for the shorelines of a Mediterranean coastal archipelago", *Ocean & Coastal Management*, n. 57, pp. 44-52, doi: 10.1016/j.ocecoaman.2011.11.006.

ONSTOTT, R. G., SHUCHMAN, R. A., 2004, "SAR measurements of sea ice". In: Jackson, C. R., Apel, J. R. (eds), *Synthetic Aperture Radar Marine User's Manual*, NOAA/NESDIS, Office of Research and Applications, Chapter 3, pp. 263-275. Washington, DC, USA. Available online: < http://www.sarusersmanual.com >. Accessed on: 14 November 2015.

ORNITZ, B. E., CHAMP, M. A., 2002, *Oil Spills First Principles: Prevention and Best Response*, 1st ed., Kidlington, Oxford, Elsevier Science, 653p., ISBN 0080428142. Available online: < http://english.360elib.com/datu/T/EM298792.pdf >. Accessed on: 14 November 2015.

OZGOKMEN, T. M., BERON-VERA, F. J., BOGUCKI, D., CHEN, S., DAWSON, C., DEWAR, W., GRIFFA, A., HAUS, B. K., HAZA, A. C., HUNTLEY, H.,

ISKANDARANI, M., JACOBS, G., JAGERS, B., KIRWAN JR., A. D., LAXAGUE, N., LIPPHART JR., B., MACMAHAN, J., MARIANO, A. J., OLASCOAGA, J., NOVELLI, G., POJE, A. C., RENIERS, A. J. H. M., RESTREPO, J. M., ROSENHEIM, B., RYAN, E. H., SMITH, C., SOLOVIEV, A., VENKATARAMANI, S., ZHA, G., ZHU, P., 2014, "Research overview of the Sonsortium for Advanced Research on Transport of Hydrocarbon in the Environment (CARTHE)". In: *Proceedings of the International Oil Spill Conference,* v. 2014, n. 1, pp. 544-560, doi: 10.7901/2169-3358-2014.1.544. Available online: < http://ioscproceedings.org/doi/full/10.7901/2169-3358-2014.1.544 >. Accessed on 14 November 2015.

PADHYE, S. A., REGE, P. P., 2015, "Feature extraction from microwave data using backscatter coefficient". In: *Proceedings of the International Conference on Industrial Instrumentation and Control (ICIC),* pp. 789-794, College of Engineering Pune, India, 28-30 May.

PARASHAR, S., LANGHAM, E., MCNALLY, J., AHMED, S., 1993, "RADARSAT Mission Requirements and Concept", *Canadian Journal of Remote Sensing*, v. 19, n. 4, pp. 280-288, doi: 10.1080/07038992.1993.10874563.

PATTON, J. S., RIGLER, M. W., BOEHM, P. D., FIEST, D. L., 1981, "Ixtoc I oil spill: flaking of surface mousse in the Gulf of Mexico", *Nature*, v. 290 pp. 235-238.

PEARSON, K., 1901, “On lines and planes of closest fit to systems of points in space”, *Philosophical Magazine*, Series 6, v. 2, n. 11, pp. 559-572. Available online: < http://stat.smmu.edu.cn/history/pearson1901.pdf >. Accessed on: 14 November 2015.

PEDERSEN, J. P., SELJELEV, L. G., BAUNA, T., STROM, G. D., FOLLUM, O. A., ANDERSON, J. H., WAHL, T., SKOELV, A., 1996, "Towards an operational oil spill detection service in the Mediterranean? The Norwegian Experience: a pre-operational early warning detection service using ERS SAR Data", *Spill Science & Technology Bulletin*, v. 3, n. 1/2, pp. 41-46.

PEDROSO, E. C., 2009, *Ranking de exsudações de óleo como suporte à exploração petrolífera em águas ultra-profundas: estudo de caso no Golfo do México*. D.Sc. Dissertation, LABSAR, PEC, COPPE, UFRJ, Rio de Janeiro, 238p., in Portuguese. Available online: < http://www.coc.ufrj.br/index.php/teses-de-doutorado/153-2009/1174-enrico-campos-pedroso >. Accessed on: 14 November 2015.

PEDROSO, E. C., MIRANDA, F. P., BANNERMAN, K., BEISL, C. H., RODRÍGUEZ, M. H., CÁCERES, R. G., 2007, "A multi-sensor approach and ranking analysis procedure for oil seeps detection in marine environments". In: *Proceedings of the*

International Geoscience and Remote Sensing Symposium (IGARSS '07), IEEE, pp. 865-870, Barcelona, Spain, 23-28 July, doi: 10.1109/IGARSS.2007.4422934.

PEDROSO, E., HERRERA, M., MIRANDA, F. P., BANNERMAN, K., CACERES, R., BEISL, C., LANDAU, L., 2006, "Monitoring of the Cantarell oil seep in the Campeche Bay, southern Gulf of Mexico, using ENVISAT ASAR data". In: *Proceedings of the SEASAR '06 Workshop, ESA-ESRIN*, 1p., Frascati, Italy, 23-26 January. Available online: < https://earth.esa.int/workshops/seasar2006/proceedings/abstracts/272_pedroso.pdf >. Accessed on: 14 November 2015.

PEMEX (Petróleos Mexicanos), 2007, *Anuario Estadístico*. Available online: < http://www.pemex.com/files/content/Anuario2007.pdf >. Accessed on: 14 November 2015).

PEMEX (Petróleos Mexicanos), 2012a, *Anuario Estadístico*. Available online: < http://www.pemex.com/ri/Publicaciones/Anuario%20Estadistico%20Archivos/2012_ae_00_vc_e.pdf >. Accessed on: 14 November 2015.

PEMEX (Petróleos Mexicanos), 2012b, *Los reservas de Hidrocarburos de México, Los principales campos de petróleo y gas de México,* v2, Pemex Exploración Producción, México. Available online: < http://www.pemex.com/ri/Publicaciones/Reservas%20de%20hidrocarburos%20evaluaciones/120101_rh_00_vc_e.pdf >. Accessed on: 14 November 2015.

PEMEX (Petróleos Mexicanos), 2013a, *Historia de la exploracion petrolera en Mexico*. Available online: < http://www.ref.pemex.com/octanaje/23explo.htm >. Accessed on: 14 November 2015.

PEMEX (Petróleos Mexicanos), 2013b, available online (last accessed on June 2013): http://www.pemex.com/index.cfm?action=news&sectionID=118&catID=11391&contentID=20342

PERES-NETO, P. R., JACKSON, D. A., SOMERS, K. M., 2003. “Giving meaningful interpretation to ordination axes: assessing loading significance in principal component analysis”, *Ecology*, v. 84, pp. 2347-2363. Available online: < http://labs.eeb.utoronto.ca/jackson/ecology84.pdf >. Accessed on: 15 November 2015.

PERES-NETO, P. R., JACKSON, D. A., SOMERS, K. M., 2005, “How many principal components? Stopping rules for determining the number of non-trivial axes revisited”, *Computational Statistics & Data Analysis*, v. 49, pp. 974-997, doi: 10.1016/j.csda.2004.06.015.

PICKARD, G. L., EMERY, W. J., 1996, *Descriptive physical Oceanography: An introduction*, 5th ed. (2nd reprint), Oxford, Butterworth-Heinemann (BH), 320p., ISBN: 0-7506-2759-X.

PISANO, A., 2011, *Development of oil spill detection techniques for satellite optical sensors and their application to monitor oil spill discharge in the Mediterranean Sea*. Ph.D. Dissertation, Università di Bologna, 146p.

PLAZA, J., PÉREZ, R., PLAZA, A., MARTÍNEZ, P., VALENCIA, D., 2005, "Mapping oil spills on sea water using spectral mixture analysis of hyperspectral image data". In: *Proceedings of the Chemical and Biological Standoff Detection III, SPIE,* v. 5995, 8p., doi: 10.1117/12.631149. Available online: < http://www.umbc.edu/rssipl/people/aplaza/Papers/Conferences/2005.SPIE.Oilspills.pdf >. Accessed on: 14 November 2015.

POLYCHRONIS, K., VASSILIA, K., 2013, "Detection of oil spills and underwater natural oil outflow using multispectral satellite imagery", *International Journal of Remote Sensing Applications*, v. 3, n. 3, pp. 145-154.

PRANDLE, D., 2000, "Introduction: Operational Oceanography in coastal waters", *Coastal Engineering*, v. 41, pp. 3-12.

PREARO. L. C., GOUVÊA, M. A., ROMEIRO, M. C., 2012, "Avaliação da adequação da aplicação de técnicas multivariadas de dependência em teses e dissertações de algumas instituições de ensino superior", *Ensaios FEE*, v. 33, n. 1, pp. 267-296, in Portuguese.

PUS (Penn State University), 2015, *Applied multivariate statistical analysis*, STAT 505. Available online: < https://onlinecourses.science.psu.edu/stat505/node/89 >. Accessed on: 18 November 2015.

QUINTERO-MARMOL, A. M., MIRANDA, F. P., GOODMAN, R., BANNERMAN, K., PEDROSO, E. C., RODRÍGUEZ, M. H., 2005, "Emanacíon natural de Cantarell: laboratório natural para experimentos de derrames de petróleo". In: *Proceedings of the International Oil Spill Conference (IOSC),* v. 2005, n. 1, pp. 1039-1044, Miami, 15-17 May, doi: 10.7901/2169-3358-2005-1-1039.

QUINTERO-MARMOL, A. M., PEDROSO, E. C., BEISL, C. H., CACERES, R. G., MIRANDA, F. P., BANNERMAN, K., WELGAN, P., CASTILLO, O. L., 2003, "Operational applications of RADARSAT-1 for the monitoring of natural oil seeps in the South Gulf of Mexico". In: *Proceedings of the International Geoscience and Remote Sensing Symposium (IGARSS '03), IEEE,* v. 4, pp. 2744-2746, Toulouse, France, 21-25 July, doi: 10.1109/IGARSS.2003.1294571.

Quispe, N. R. P., 2003, *Técnicas e ferramentas para a extração inteligente e automática de conhecimento em banco de dados*, M.Sc. Thesis, UNICAMP, Campinas, SP, 95p., in Portuguese.

RAE (Rankings America Economia), 2010, Available online: < http://rankings.americaeconomia.com/2010/500/ranking-500-america-latina.php >. Accessed on: 14 November 2015.

RAO, C. R., 1964, "The use and interpretation of principal component analysis in applied research", *Sankhyã, The Indian Journal of Statistics, Series A*, v. 26, n. 4, pp. 329-358.

READMAN, J. W., FOWLER, S. W., VILLENEUVE, J. P., CATTININ, C., OREGIONI, B., MEE, L. D., 1992, "Oil and combustion-product contamination of the Gulf marine environment following the war", *Nature*, v. 358, pp. 662-664.

RICHARDSON, M., 2009, *Principal Component Analysis*, 23p. Available online: < http://people.maths.ox.ac.uk/richardsonm/SignalProcPCA.pdf >. Accessed on: 16 November 2015.

ROBERTS, E. S., 2008, *The Art & Science of Java, An Introduction to Computer Science, Pearson Education.* Boston, Pearson Education, 587p., ISBN: 978-0-321-48612-7.

ROBINSON, I. S., MITCHELSON, E. G., 1983, "Satellite observations of ocean colour [and discussion]", *Philosophical Transactions of the Royal Society of London, Series A, Mathematical and Physical Sciences,* v. 309, n. 1508, pp. 415-432. Available online: < http://rsta.royalsocietypublishing.org/content/309/1508/415.short >. Accessed on: 14 November 2015.

RODRIGUES, D. F., 2011, *Obtenção de campos de vento na superfície do mar no Golfo do México a partir de imagens de Radar de Abertura Sintética (SAR).* M.Sc. Thesis, LABSAR, PEC, COPPE, UFRJ, Rio de Janeiro, 78p., in Portuguese. Available online: < http://www.coc.ufrj.br/index.php/dissertacoes-de-mestrado/111-2011/1476-douglas-fraga-rodrigues >. Accessed on: 14 November 2015.

RODRIGUES, D. F., MIRANDA, F. P., TORRES JUNIOR, A. R., LANDAU, L., 2013, "Obtenção de campos de vento na superfície do mar no Golfo do México a partir de imagens de Radar de Abertura Sintética (SAR)". In: *Proceedings of the XI Brazilian Remote Sensing Symposium (SBSR),* pp. 8382-8389, INPE, Foz do Iguaçu, Brasil, 13-18 April, in Portuguese.

RODRÍGUEZ, M. H., BANNERMAN, K. CÁCERES, R. G., MIRANDA, F. P., PEDROSO, E. C., 2007, "Cantarell natural seep modelling using SAR derived

ocean surface wind and meteo- oceanographic buoy data". In: *Proceedings of the International Geoscience & Remote Sensing Symposium (IGARSS '07), IEEE,* pp. 3257-3260, Barcelona, Spain, 23-28 July, doi: 10.1109/IGARSS.2007.4423539.

ROKOSH, K., 2000, *Introduction to RADARSAT*, Reprinted courtesy of Canadian Space Agency, Compiled By Kevin Rokosh - IEEE, RADARSAT Ebook. Available online: < http://www.ieee.ca/millennium/radarsat/radarsat.pdf >. Accessed on: 14 November 2015.

RORIZ, C. E. D., 2006, *Detecção de exsudações de óleo utilizando imagens do satélite RADARSAT-1 na porção offshore do Delta do Niger*. M.Sc. Thesis, LABSAR, PEC, COPPE, UFRJ, Rio de Janeiro, 267p., in Portuguese. Available online: < http://www.coc.ufrj.br/index.php/dissertacoes-de-mestrado/106-2006/2036-carlos-eduardo-dias-roriz >. Accessed on: 14 November 2015.

RSI (RADARSAT International Inc.), 1997, *RADARSAT Data Products Specifications*. In: Technical Report RSI-GS-026, Issue/Revision: 2/0, 7 of November, Richmond, B.C., Canada. 148p. Available online: < http://www.ga.gov.au/image_cache/GA10292.pdf >. Accessed on: 14 November 2015.

RSI (RADARSAT International Inc.), 1998, *RADARSAT-1 Handbook: Guide to products and services*, 113p. Available online: < http://gs.mdacorporation.com/products/sensor/radarsat/rsiug98_499.pdf >. Accessed on: 14 November 2015.

SALOMONSON, V. V, BARNES, W. L., MAYMON, P. W., MONTGOMERY, H. E., OSTROW, H., 1989, “MODIS: Advanced Facility Instrument for Studies of the Earth as a System”, *IEEE Transactions on Geoscience and Remote Sensing*, v. 27, n. 2, pp. 145-153.

SANCHEZ, G., ROPER, W. E., GOMEZ, R., 2003, "Detection and monitoring of oil spills using hyperspectral imagery". In: *Proceedings of the Geo-Spatial and Temporal Image and Data Exploitation III,* SPIE v. 5097, pp. 233-240, doi: 10.1117/12.502593.

SARACLI, S., DOGAN, N., DOGAN, I., 2013, "Comparison of hierarchical cluster analysis methods by cophenetic correlation", *Journal of Inequalities and Applications*, 8p. Available online: < http://www.journalofinequalitiesandapplications.com/content/2013/1/203 >. Accessed on: 14 November 2015.

SARKAR, N., CHAUDHURI, B. B., 1994, “An efficient differential box-counting approach to compute fractal dimension of image”, *IEEE Transactions on*

Systems, Man, and Cybernetics, v. 24, n. 1, pp. 115-120, doi: 10.1109/21.259692.

SAUER, T. C., BROWN, J. S., BOEHM, P. D., AURAND, D. V., MICHEL, J., HAYES, M. O., 1993, "Hydrocarbon source identification and weathering characterization of intertidal and subtidal sediments along the Saudi Arabian coast after the Gulf War oil spill", *Marine Pollution Bulletin*, v. 27, pp. 117-134.

SCHOFIELD, O., GLENN, S., 2004, "Introduction to special section: Coastal Ocean Observatories", *Journal of Geophysical Research*, v. 109, n. C12S01, doi: 10.1029/2004JC002577.

SCHOFIELD, O., GRZYMSKI, J., BISSETT, W. P., KIRKPATRICK, G. J., MILLIE, D. F., MOLINE, M., ROESLER, C. S., 1999, "Optical monitoring and forecasting systems for harmful algal blooms: possibility or pipe dream?", *Journal of Psychology*, v. 35, pp. 1477-1496.

SCHOLZ, D. K., KUCKLICK, J. H., POND, R., WALKER, A. H., BOSTROM, A., FISHBECK, P., 1999, *Fate of Spilled Oil in Marine Waters: Where Does It Go? What Does It Do? How Do Dispersants Affect It?*: *An information booklet for decision makers*, Scientific and Environmental Associates Inc., Sea Consulting Group, 43p.

SENGUPTA, S., SAHA, K. K., 2008, "Use of satellite imageries to identify potential hydrocarbon microseepage in off-shore areas". In: *Proceedings of the 7th International Conference & Exposition on Petroleum Geophysics*, 7p.

SHAHEEN, M., SHAHBAZ, M., UR REHMAN, Z., GUERGACHI, A., 2011, "Data mining applications in hydrocarbon exploration", *Artificial Intelligence Review*, v. 35, pp. 1-18, doi: 10.1007/s10462-010-9180-z.

SHARMA, V., RAI S., DEV, A., 2012, "A comprehensive study of Artificial Neural Networks", *International Journal of Advanced Research in Computer Science and Software Engineering Research Paper*, v. 2, n. 10, ISSN: 2277.128X.

SHCHERBAK, S. S., LAVROVA, O. Y., MITYAGINA, M. I., BOCHAROVA, T. Y., KROVOTYNTSEV, V. A., OSTROVSKII, A. G., 2008, "Multisensor satellite monitoring of seawater state and oil pollution in the northeastern coastal zone of the Black Sea", *International Journal of Remote Sensing*, v. 29, n. 21, pp. 6331-6345, doi: 10.1080/01431160802175470.

SHEPHERD, N., 2000, *Extraction of beta nought and sigma nought from RADARSAT CDPF products*. In: Techical Report, n. AS97-5001, Revision 4, Altrix Systems, 28 April, 16p.

SHLENS, J., 2005, *A tutorial on Principal Component Analysis*, 13p. Available online: < http://www.brainmapping.org/NITP/PNA/Readings/pca.pdf >. Accessed on: 16 November 2015.

SILVA JUNIOR, C. L., MANO, M. F., HARGREAVES, F. M., CABRAL, A. P., MIRANDA, F. P., PEDROSO, E. C., BEISL, C. H., 2003, "Utilização de dados orbitais multisensores na caracterização de exsudações naturais de óleo no Golfo do México". In: *Proceedings of the XIV Brazilian Remote Sensing Symposium (SBSR),* pp. 929-936, INPE, Belo Horizonte, Brasil, 05-10 April, in Portuguese. Available online: < http://marte.dpi.inpe.br/rep/ltid.inpe.br/sbsr/2002/11.20.10.39 >. Accessed on 14 November 2015.

SILVA, A. R., DIAS, C. T. S., 2013, "A cophenetic correlation coefficient for Tocher's method", *Pesquisa Agropecuária Brasileira*, v. 48, n. 6, pp. 589-596, doi: 10.1590/S0100-204X2013000600003. Available online: < http://www.scielo.br/scielo.php?pid=S0100-204X2013000600003&script=sci_arttext >. Accessed on: 14 November 2015.

SILVA, G. M. A., EBECKEN, N. F. F., BEVILACQUA, L., BARROS, M. M., MIRANDA, F. P., 2013, "Target detection on offshore RADARSAT-1 images by dynamic fractal". In: *Proceedings of the Thirteenth PanAmerican Congress of Applied Mechanics PACAMXIII*, 9p., Houston, Texas, USA, May 22 a 24.

SILVEIRA, I. C. A., SCHMIDT, A. C. K., CAMPOS, E. J. D., GODOI, S. S., IKEDA Y., 2000, "The Brazil Current off the Eastern Brazilian Coast", *Revista Brasileira de Oceanografia*, v. 48, n. 2, pp. 171-183.

SINGHA, S., BELLERBY, T. J., TRIESCHMANN, O., 2013, "Satellite Oil Spill Detection Using Artificial Neural Networks", *IEEE Journal of Selected Topics in Applied Earth Observations and Remote Sensing*, n. 6, n. 6, pp. 2355-2363., doi: 10.1109/JSTARS.2013.2251864.

SIPELGAS, L., UIBOUPIN, R., 2007, "Elimination of oil spill like structures from radar image using MODIS data". In: *Proceedings of the International Geoscience and Remote Sensing Symposium (IGARSS '07), IEEE,* pp. 429-431, Barcelona, Spain, 23-28 July, doi: 10.1109/IGARSS.2007.4422822.

SMITH, L. I., 2002, "A Tutorial on Principal Components Analysis", 29p. Available online: < http://www.cs.otago.ac.nz/cosc453/student_tutorials/principal_components.pdf >. Accessed on: 15 November 2015.

SMYTH, T. J., SHUTLER, J. D., LAND, P. E., REEVES, T. R., CHEN, T., GROOM, S. B., 2003, "Near real time observations of ocean colour properties using NASA MODIS", *RSPSOC*, 4p.

SNEATH, P. H. A., SOKAL, R. R., 1973, *Numerical taxonomy – The principles and practice of numerical classification,* San Francisco, W. H. Freeman and Company, 573p., ISBN: 0-7167-0697-0. Available online: < http://www.brclasssoc.org.uk/books/Sneath/ >. Accessed on: 14 November 2015.

SOKAL, R. R., ROHLF, F. J., 1962, "The Comparison of dendrograms by objective methods", *Taxon*, v. 11, n. 2, pp. 33-40, doi: 10.2307/1217208.

SOLBERG, A. H. S., 2012, "Remote sensing of ocean oil-spill pollution". In: *Proceedings of the IEEE*, v. 100, n. 10, pp. 2931-2945, doi: 10.1109/JPROC.2012.2196250.

SOLBERG, A. H. S., STORVIK, G., SOLBERG, R., VOLDEN, E., 1999, "Automatic Detection of Oil Spills in ERS SAR Images", *IEEE Transactions on Geoscience and Remote Sensing*, v. 37, n. 4, pp. 1916-1944.

SOLBERG, A. H. S., VOLDEN, E., 1997, "Incorporation of prior knowledge in automatic classification of oil spills in ERS SAR images". In: *Proceedings of the International Geoscience and Remote Sensing Symposium (IGARSS '97), IEEE,* v. 1, pp. 157-159, Singapore, 3-8 August, doi: 10.1109/IGARSS.1997.615826.

SOLER, L. S., 2000, *Detecção de manchas de óleo na superfície do mar por meio de técnicas de classificação textural de imagens de radar de imagens de abertura sintética (RADARSAT-1).* M.Sc. Thesis, INPE, São José dos Campos, Brazil, INPE-8605-TDI/790, 167p.

SOLLACI, L. B., PEREIRA, M. G., 2004, "The introduction, methods, results, and discussion (IMRAD) structure: a fifty-year survey", *Journal of the Medical Library Association*, v. 92, n. 3, pp. 364-367. Available online: < http://www.ncbi.nlm.nih.gov/pmc/articles/PMC442179/ >. Accessed on: 14 November 2015.

SOUZA FILHO, P. W. M., PARADELLA, W. R., 2001, "Synthetic aperture radar for coastal erosion mapping and land-use assessment in the moist tropics: Bragança coastal plain case study". In: *Proceedings of the X Brazilian Remote Sensing Symposium (SBSR),* pp. 339-347, INPE, Foz do Iguaçu, Brasil, 21-26 April. Available online: < http://marte.sid.inpe.br/col/dpi.inpe.br/lise/2001/09.14.11.56/doc/0339.347.257.pdf >. Accessed on: 14 November 2015.

SOUZA, D. L., 2006, *Sistema inteligente para detecção de manchas de oleo na superfície marinha através de imagens de SAR*. M.Sc. Thesis, Universidade

Federal do Rio Grande Do Norte (UFRN), Natal, Brazil, PPgEE:M174, 105p., in Portuguese. Available online: < ftp://ftp.ufrn.br/pub/biblioteca/ext/bdtd/DaniloLS.pdf >. Accessed on: 14 November 2015.

SOUZA, R. B., 2005, "Satellite observations of eddies in the Southwestern Atlantic Ocean during 1993 and 1994". In: *Proceedings of the XIII Brazilian Remote Sensing Symposium (SBSR),* pp. 3687-3694, INPE, Goiânia, Brasil, 16-21 April. Available online: < http://marte.sid.inpe.br/col/ltid.inpe.br/sbsr/2004/10.05.09.42/doc/3687.pdf >. Accessed on: 14 November 2015.

SOUZA, R. B., 2009, *Oceanografia por satélites*, 2 ed., São Paulo, Oficina de Textos, 382p., ISBN: 978-85-86238-74-1.

SPIES, R. B., DAVIS, P. H., 1979, "The infaunal benthos of a natural oil seep in the Santa Barbara Channel", *Marine Biology*, v. 50, pp. 227-237.

SPIES, R. B., DESMARAIS, D. J., 1983, "Natural isotope study of trophic enrichment of marine benthic communities by petroleum seepage", *Marine Biology*, v. 73, n. 1, pp. 67-71.

STANKIEWICZ, B. A., 2003, "Integration of Geoscience and engineering in the oil industry – just a dream?", Insight commentary, *Nature*, v. 426, pp. 360-363.

STAPLES, G. C., HODGINS, D. O., 1998, "RADARSAT-1 emergency response for oil spill monitoring". In: *Proceedings of the 5th International Conference on Remote Sensing for Marine and Coastal Environments,* pp. 163-170, San Diego, California, Environmental Research Institute of Michigan (ERIM), 5-7 October.

STAPLES, G., RODRIGUES, D. R., 2013, "Maritime environmental surveillance with RADARSAT-2". In: *Proceedings of the XVI Brazilian Remote Sensing Symposium (SBSR),* pp. 8445-8452, INPE, Foz do Iguaçu, Brazil, 13-18 April. Available online: < http://www.dsr.inpe.br/sbsr2013/files/p1061.pdf >. Accessed on: 14 November 2015.

STEWART, C., LARSON, V., 2000, "Synthetic Aperture Radar Algorithms". In: Madisetti, V. K., Wollians, D. B. (eds), *The digital signal processing handbook*, CRCnetBase, Chapter 33, 15p. Available online: < http://www.dsp-book.narod.ru/DSPMW/33.PDF >. Accessed on: 14 November 2015.

STEWART, R. H., 2008, *Introduction to Physical Oceanography*, 2008 ed., Department of Oceanography, Texas A & M University, 345p. Available online: < http://oceanworld.tamu.edu/resources/ocng_textbook/PDF_files/book.pdf >. Accessed on: 14 November 2015.

STRINGER, W. J., AHLNÄS, K., ROYER, T. C., DEAN, K. E., GROVES, J. E., 1989, “Oil spill shows on satellite image”, *EOS Transactions, American Geophysical Union*, v. 70, n. 18, pp. 564-564, doi: 10.1029/89EO00143.

STUMPF, R. P., CULVER, M. E., TESTER, P. A., TOMLINSON, M., KIRKPATRICK, G. J., PEDERSON, B. A., TRUBY, E., RANSIBRAHMANAKUL, V., SORACCO, M., 2003, "Monitoring *Karenia brevis* blooms in the Gulf of Mexico using satellite ocean color imagery and other data", *Harmful Algae*, v. 2, pp. 147-160.

TAKAHASHI, W., KAWAMURA, H., 2005, “Detection method of the Kuroshio front using the satellite-derived chlorophyll-a images”, *Remote Sensing of Environment*, v. 97, pp. 83-91.

TALWANI, M., 2011, "The future of oil in Mexico", In: *Oil and gas in Mexico: Geology, production rates and reserves,* 34p., Houston, Rice University, James A. Baker III Institute for Public Policy. Available online: < https://bakerinstitute.org/media/files/Research/1274a8e6/EF-pub-TalwaniGeology-04292011.pdf >. Accessed on: 14 November 2015.

TETKO, I., BASKIN, I., VARNEK, A., 2008, *Tutorial on Machine Learning, Part 2: Descriptor Selection Bias*, 12p. Available online: < http://infochim.u-strasbg.fr/CS3/program/Tutorials/Tutorial2b.pdf >. Accessed on: 14 November 2015.

TEXEIRA, C. C., SIQUEIRA, C. Y. S., AQUINO NETO, F. R., MIRANDA, F. P., CERQUEIRA, J. R., VASCONCELOS, A. O., LANDAU, L., HERRERA, M., BANNERMAMAN, K., 2014, "Source identification of sea surface oil with geochemical data in Cantarell, Mexico", *Microchemical Journal*, v. 117, pp. 202-213, doi: 10.1016/j.microc.2014.06.025.

THAKUR, P. K., 2014, "SAR data processing to extract backscatter response from various features". In: *Proceedings of the In Proc. of the Pre symposium tutorials on polarimetric SAR data processing and applications, International Society for Photogrametry and Remote Sensing (ISPRS),* 94p., Hyderabad, India, 9-12 December. Available online: < http://www.nrsc.gov.in/isprs/pdf/4.%20SAR_Backscatter-Extraction_new.pdf >. Accessed on: 14 November 2015.

THERIAULT, C., SCHEIBLING, R., HATCHER, B., JONES, W., 2006, “Mapping the distribution of an invasive marine alga (Codium fragile spp. tomentosoides) in optically shallow coastal waters using the compact airborne spectrographic imager (CASI)”, *Canadian Journal of Remote Sensing Canadian Journal of Remote Sensing*, v. 32, n. 5, pp. 315-329, doi: 10.5589/m06-027.

THOMPSON, A. A., MCLEOD, I. H., 2004, "The RADARSAT-2 SAR processor", *Canadian Journal of Remote Sensing*, v. 30, n. 3, pp. 336–344, doi: 10.5589/m04-016.

THOMPSON, D. R., 2004, "Microwave scattering from the sea". In: Jackson, C. R., Apel, J. R. (eds), *Synthetic Aperture Radar Marine User's Manual*, NOAA/NESDIS, Office of Research and Applications, Chapter 4, pp. 117-138. Washington, DC, USA. Available online: < http://www.sarusersmanual.com >. Accessed on: 14 November 2015.

TISSOT, B. P., WELTE, D. H., 1984, "Coal and its relation to oil and gas". In: Petroleum formation and occurrence, Chapter 7, 2nd ed., Springer Berlin Heidelberg, pp. 202-224, doi: 10.1007/978-3-642-96446-6_12.

TOPOUZELIS, K., 2008, "Oil spill detection by SAR Images: dark formation detection, feature extraction and classification algorithms", *SENSORS*, v. 8, pp. 6642-6659, ISSN 1424-8220, doi: 10.3390/s8106642.

TOPOUZELIS, K., KARATHANASSI, V., PAVLAKIS, P., ROKOS, D., 2007. "Detection and discrimination between oil spills and look-alike phenomena through neural networks", *Journal of Photogrammetry and Remote Sensing, ISPRS*, v. 62, pp. 264-270, doi: 10.1016/j.isprsjprs.2007.05.003.

TOPOUZELIS, K., PSYLLOS, A., 2012, "Oil spill feature selection and classification using decision tree forest on SAR image data", *Journal of Photogrammetry and Remote Sensing, ISPRS*, v. 68, pp. 135-143, doi: 10.1016/j.isprsjprs.2012.01.005.

TOPOUZELIS, K., STATHAKIS, D., KARATHANASSI, V., 2009, "Investigation of genetic algorithms contribution to feature selection for oil spill detection", *International Journal of Remote Sensing*, v. 30, n. 3, pp. 611-625, doi: 10.1080/01431160802339456.

TOU, J. T., GONZALEZ, R. C., 1974, *Pattern recognition principals*, MA, Addison Wesley Reading, 377p.

TRASHER, J., FLEET, A. J., HAY, S. H., HOVLAND, M., DUPPENBACKER, S., 1996, *Understanding geodesy as the key to using seepage in exploration: spectrum of seepage stiles.* In: Schumacher, S., Abrams, M. A. (eds), *Hydrocarbon migration and its near-surface expression*, AAPG Memoir 66, Tulsa, Oklahoma, American Association of Petroleum Geologists, pp. 223-241.

TRIVERO, P., BIAMINO, W., 2010, "Observing marine pollution with Synthetic Aperture Radar". In: Impertore, P., Riccio, D., *Geoscience and remote sensing new achievements*, Chapter 21, In Tech, pp. 397-418.

TRIVERO, P., FISCELLA, B. GOMEZ, F., PAVESE, P., 1998, "SAR detection and characterization of sea surface slicks", *International Journal of Remote Sensing*, v. 19, n. 3, pp. 543-548, doi: 10.1080/014311698216161.

TUFTE, L., TRIESCHMANN, O., HUNSÄNGER, T., KRANZ, S., BARJENBRUCH, U., 2004, "Using air- and spaceborne remote sensing data for the operational oil spill monitoring of the German North Sea and Baltic Sea". In: *Proceedings of the Xth Photogrammetry and Remote Sensing Congress, ISPRS,* 5p., Istanbul, Turkey, 12-23 July.

USGS (United States Geological Survey), 2015, *Natural oil and gas seeps in California*. Available online: < http://walrus.wr.usgs.gov/seeps >. Accessed on: 14 November 2015.

VALENTIN, J. L., 2012, *Ecologia numérica – Uma introdução à análise multivariada de dados ecológicos*, 2nd ed., Rio de Janeiro, Editora Interciência, 153p., ISBN: 978-85-7193-230-2.

VAN DER SANDEN, J. J., 2004, "Anticipated applications potential of RADARSAT-2 data", *Canadian Journal of Remote Sensing*, v. 30, n. 3, pp. 369-379, doi: 10.5589/m04-001.

VELOTTO, D., MIGLIACCIO, M., NUNZIATA, F., LEHNER, S., 2010, "Oil-slick observation using single look complex TerraSAR-X dual-polarized data". In: *Proceedings of the International Geoscience and Remote Sensing Symposium (IGARSS '10), IEEE,* 4p., Honolulu, Hawaii, 25-30 July, doi: 10.1109/IGARSS.2010.5648883.

VELOTTO, D., MIGLIACCIO, M., NUNZIATA, F., LEHNER, S., 2011, "Dual-polarized TerraSAR-X data for oil-spill observation", *IEEE Transactions on Geoscience and Remote Sensing*, v. 49, n. 12, doi: 10.1109/TGRS.2011.2162960.

VILLALÓN, R. M., 1998, *Geoquímica de Reservatórios do Campo Taratunich da Área Marinha de Campeche, México*. M.Sc. Thesis, LABSAR, PEC, COPPE, UFRJ, Rio de Janeiro, 126p., in Portuguese. Available online: < http://www.coc.ufrj.br/index.php/dissertacoes-de-mestrado/98-1998/1622-rodrigo-maldonado-villalon >. Accessed on: 14 November 2015.

VN (Vice News), 2015, *Mexico finally opens auction for private oil exploration, but gets few takers*. Available online: < https://news.vice.com/article/mexico-finally-opens-auction-for-private-oil-exploration-but-gets-few-takers >. Accessed on: 15 November 2015.

VUKOVICH, F. M., 2004, "Preliminary Results of a Study to Develop a Climatology of Ocean Features in the Gulf of Mexico Using Satellite Remote Sensing Data". In: *Proceedings of the International Geoscience and Remote Sensing Symposium*

(IGARSS '04), IEEE, n. 5, pp. 3050-3053, Anchorage, Alaska, 20-24 September, doi: 10.1109/IGARSS.2004.1370463.

VUKOVICH, F. M., 2007, "Climatology of Ocean Features in the Gulf of Mexico Using Satellite Remote Sensing Data", *Journal of Physysical Oceanography*, n. 37, pp. 689-707, doi: 10.1175/JPO2989.1.

VUKOVICH, F.M., 2005, *Climatology of Ocean Features in the Gulf of Mexico: Final Report. U.S. Department of the Interior,* Minerals Management Service, Gulf of Mexico OCS Region, New Orleans, LA, OCS Study MMS 2005-031. 58p.

WAHL, T., SKØELV, A., PEDERSEN , J. P., SELJELV, L. G., ANDERSEN, J. H., FOLLUM, O. A., ANDERSSEN, T., STRØM, G. D., BERN, T.-I., ESPEDAL, H. H., HAMNES, H., SOLBERG, R., 1996, "Radar satellites: A new tool for pollution monitoring in coastal waters", *Coastal Management*, v. 24, n. 1, pp. 61-71, doi: 10.1080/08920759609362281.

WAND, M. P., 1997, "Data-Based Choice of Histogram Bin Width, Statistical computing and graphics", *The American Statistician*, v. 51, n. 1, pp. 59-64, doi: 10.1080/00031305.1997.10473591.

WENDT, C. J., CYPHERS, A., 2008, "How the Olmed used bitumen in ancient Mesoamerica", *Journal of Anthropological Archaeology*, v. 27, n. 2, pp. 175-191, doi: 10.1016/j.jaa.2008.03.001.

WHOI (Woods Hole Oceanographic Institution), 2015, *Natural Oil Seeps*. Available online: < http://www.whoi.edu/main/topic/natural-oil-seeps >. Accessed on: 25 December 2015.

WILT, C., THAYER J., RUML, W., 2010, "A Comparison of Greedy Search Algorithms". In: *Proceedings of the 3rd Annual Symposium on Combinatorial Search (SoCS-10), Advancement of Artificial Intelligence (AAAI),* pp. 129-136. Available online: < http://aaai.org/ocs/index.php/SOCS/SOCS10/paper/viewFile/2101/2515 >. Accessed on: 14 November 2015.

WISMANN, V., GADE, M., ALPERS, W., HUEHNERFUSS, H., 1993, "Radar signatures of mineral oil spills measured by an airborne multi-frequency multi-polarization microwave scatterometer". In: *Proceedings of the Oceans '99*, v. 2, pp. 348-353, Victoria, British Columbia, Canada, doi: 10.1109/OCEANS.1993.326118.

WISMANN, V., GADE, M., ALPERS, W., HUEHNERFUSS, H., 1998, "Radar signatures of marine mineral oil spills measured by an airborne multi-frequency multi-polarization microwave scatterometer", *International Journal of Remote Sensing*, v. 19, n. 18, pp. 3607-3623.

YING, L. I., GUO-XIN, L. A. N., JI-JUN, L. I., LONG, M. A., 2009, “Potential analysis of maritime oil spill monitoring based on MODIS thermal infrared data”, In: *Proceedings of the International Geoscience and Remote Sensing Symposium (IGARSS '09), IEEE*, v. 3, pp. 373-376, Cape Town, South Africa, 12-17 July, doi: 10.1109/IGARSS.2009.5417780.

YODER, J., A., KENNELLY M. A., 2006, "What have we learned about ocean variability from satellite ocean color images?", *Oceanography*, v. 19, n. 1, pp. 152-171.

APPENDIX 1

SCIENTIFIC PUBLICATIONS:

CARVALHO, G. A., LANDAU, L., MIRANDA, F. P., MINNET, P., MOREIRA, F., BEISL, C., 2015a, "The use of RADARSAT-derived information to investigate oil slick occurrence in Campeche Bay, Gulf of Mexico". *In: Proceedings of the XVII Brazilian Remote Sensing Symposium (SBSR), INPE*, pp. 1184-1191, João Pessoa-PB, Brasil, 25-29 April. Available online: < http://www.dsr.inpe.br/sbsr2015/files/p0217.pdf >. Accessed on: 5 January 2016.

CARVALHO, G. A., MINNETT, P. J., MIRANDA, F. P., LANDAU, L., MOREIRA, F., 2015b (Submitted), "The use of a RADARSAT-derived long-term dataset to investigate the sea surface expressions of human-related and naturally-occurring oil slicks in Campeche Bay, Gulf of Mexico", *Canadian Journal of Remote Sensing (Special Issue: Long-Term Satellite Data and Applications)*. Available online: < goo.gl/DlfL94 >. Accessed on: 5 January 2016.

CARVALHO, G. A., MINNETT, P. J., MIRANDA, F. P., LANDAU, L., PAES, E. T., 2015c (Submitted), "The use of Synthetic Aperture Radar measurements to distinguish natural oil seeps from human-related oil spills on the sea surface of Campeche Bay (Gulf of Mexico) using multivariate data analysis techniques, *Remote Sensing of Environment*. Available online: < goo.gl/DlfL94 >. Accessed on: 5 January 2016.

Anais XVII Simpósio Brasileiro de Sensoriamento Remoto - SBSR, João Pessoa-PB, Brasil, 25 a 29 de abril de 2015, INPE

The use of RADARSAT-derived information to investigate oil slick occurrence in Campeche Bay, Gulf of Mexico

Gustavo de Araujo Carvalho [1]
Luiz Landau [1]
Fernando Pellon de Miranda [1,2]
Peter Minnett [3]
Fabio Moreira [1]
Carlos Beisl [1]

[1] Universidade Federal do Rio de Janeiro - UFRJ
Instituto Alberto Luiz Coimbra de Pós-Graduação e Pesquisa de Engenharia - COPPE
Programa de Engenharia Civil - PEC
Laboratório de Métodos Computacionais em Engenharia - LAMCE
Laboratório de Sensoriamento Remoto por Radar Aplicado à Indústria do Petróleo - LabSAR
ggus.ocn@gmail.com
landau@lamce.coppe.ufrj.br
fmoreira@labsar.coppe.ufrj.br
beisl@labsar.coppe.ufrj.br

[2] Petróleo Brasileiro - PETROBRAS
Centro de Pesquisas e Desenvolvimento Leopoldo Américo Miguez de Mello – CENPES
fmiranda@petrobras.com.br

[3] University of Miami - UM
Rosenstiel School of Marine and Atmospheric Science - RSMAS
Department of Ocean Sciences - OCE
pminnett@rsmas.miami.edu

Abstract. The Mexican oil company (Pemex) has in Campeche Bay (Gulf of Mexico) a well-established activity engaged with the oil and gas exploration and production industry. Because of the associated risk of petroleum pollution in this region, an archive containing 14,210 oil slicks (i.e. man-made oil spills and natural oil seeps) observed between 2000 and 2012 has been produced using RADARSAT-derived information. This database is used in the current study to reach the objective of investigating the oil slick occurrence in Campeche Bay. The evidence of the considerable influence of oil naturally seeping out of the Cantarell Oil Seep is shown. Even though the total number of oil seeps (n=6,202; 43.6%) is smaller than the observed oil spills (n=7,456; 52.5%), the total superficial area coverage of all oil seeps (31,447 km^2; 67.4%) is larger than oil spills (14,352 km^2; 30.7%). Conversely, if the massive influence of the Cantarell Oil Seep is disregarded (19,743 km^2; 42.3%), oil seeps (11,704 km^2; 25.1%) cover less of the ocean surface than the oil spills (14,352 km^2; 30.7%). Most oil slicks have small (< 1 km^2) superficial area coverage (n=9,398; 66.2%). The average size of oil spills (1.9 km^2) is smaller than oil seeps (5.1 km^2). Oil spills usually tend to occur in water depths < 100 m, which correspond to the location of the Campeche Bay petroleum activity, whereas oil seeps in this region commonly occur in water depths > 1000 m.

Keywords: Oceanography, oil spill, oil seep. Oceanografia, derrame de óleo, exsudação de óleo.

1. Introduction

Oil released to the environment can result in serious ecosystem contamination, as it represents an imminent hazard capable of causing wild sea-life die-offs, major problems to seawater desalination systems and to different industry sectors such as tourism, fisheries, aquaculture, shellfish beds, etc. (NRCC, 2003). Throughout this manuscript, the oil floating at the sea surface is described with the following terminology:

Canadian Journal of Remote Sensing/ Journal canadien de Télédétection

Canadian Journal of Remote Sensing
Journal canadien de télédétection

The use of a RADARSAT-derived long-term dataset to investigate the sea surface expressions of human-related and naturally-occurring oil slicks in Campeche Bay, Gulf of Mexico.

Journal:	*Canadian Journal of Remote Sensing*
Manuscript ID	CJRS-15-0136
Manuscript Type:	Research Article
Date Submitted by the Author:	05-Nov-2015
Complete List of Authors:	Carvalho, Gustavo; Universidade Federal do Rio de Janeiro (UFRJ), Civil Engineer Minnett, Peter; University of Miami, Rosenstiel School of Marine and Atmospheric Science (RSMAS), Department of Ocean Sciences (OCE) de Miranda, Fernando; Universidade Federal do Rio de Janeiro (UFRJ), Civil Engineer Landau, Luiz; Universidade Federal do Rio de Janeiro (UFRJ), Civil Engineer Moreira, Fabio; Universidade Federal do Rio de Janeiro (UFRJ), Civil Engineer
Keyword:	SAR, image processing, classification, mapping, feature extraction, feature analysis, ocean surface processes, marine, coastal, radiometry

Research Paper

The use of a RADARSAT-derived long-term dataset to investigate the sea surface expressions of human-related and naturally-occurring oil slicks in Campeche Bay, Gulf of Mexico.

Gustavo de Araújo Carvalho[1,*], Peter J. Minnett[2], Fernando Pellon de Miranda[1], Luiz Landau[1], and Fabio Moreira[1].

[*] Corresponding author:

Email: ggus.ocn@gmail.com

Telephone: (55.21) 9.9838.0090

Fax: (55.21) 2556.0982

[1] Universidade Federal do Rio de Janeiro (UFRJ)

Instituto Alberto Luiz Coimbra de Pós-Graduação e Pesquisa de Engenharia (COPPE)

Programa de Engenharia Civil (PEC)

Laboratório de Métodos Computacionais em Engenharia (LAMCE)

Laboratório de Sensoriamento Remoto por Radar Aplicado à Indústria do Petróleo (LabSAR)

Centro de Tecnologia - Bloco i - Sala 214, Av. Athos da Silveira Ramos, 149, Cidade Universitária, Rio de Janeiro, RJ, Brazil, 21941-909.

[2] University of Miami (UM)

Rosenstiel School of Marine and Atmospheric Science (RSMAS)

Department of Ocean Sciences (OCE)

4600 Rickenbacker Causeway, Miami, FL, USA, 33149-1098.

=====> Abstract:

Campeche Bay, located in the Gulf of Mexico, is a well-established fossil fuel producing region, with numerous oilrigs exploring oil and natural gas. In an effort to reduce negative impacts on marine ecosystems, Pemex continuously monitors Campeche Bay for oil slicks – i.e. naturally occurring oil seeps and man-made oil spills. A long-term dataset (2000-2012) of synthetic aperture radar measurements from RADARSAT satellites (n=766) is leveraged to investigate the spatio-temporal distribution of oil slicks (n=14,210) in this region. The present study has a threefold goal: 1) Describe the monitoring strategy completed by Pemex and the information produced during such monitoring; 2) Investigate the spatio-temporal distribution of the oil slick observed in Campeche Bay, centering on aspects related to their occurrence; and 3) Demonstrate the usefulness of RADARSAT-derived information in the execution of effective long-term environmental applications to locate seeps and spills on the sea surface. The observations corroborate previous findings about the massive oil input contribution of the Cantarell Oil Seep to the Campeche Bay. Oil spills (96%) usually occur in water depths shallower than 100m, whereas oil seeps (63%) commonly occur in waters deeper than 1000m. The successful long-term application of RADARSAT-derived information has been shown.

Elsevier Editorial System(tm) for Remote Sensing of Environment

Manuscript Draft

Manuscript Number:

Title: The use of Synthetic Aperture Radar measurements to distinguish natural oil seeps from human-related oil spills on the sea surface of Campeche Bay (Gulf of Mexico) using multivariate data analysis techniques

Article Type: Research Paper

Keywords: Oceanography, Remote Sensing, Satellite, Synthetic Aperture Radar, SAR, Environmental Monitoring, Campeche Bay, Gulf of Mexico, Oil Slicks, Oil Seeps, Oil Spills, Multivariate Data Analysis, Discriminant Function, Principal Components Analysis.

Corresponding Author: Mr. Gustavo de Araújo Carvalho, Ph.D.

Corresponding Author's Institution: Federal University of Rio de Janeiro - UFRJ

First Author: Gustavo de Araújo Carvalho, Ph.D.

Order of Authors: Gustavo de Araújo Carvalho, Ph.D.; Peter J Minnett, Ph.D.; Fernando P de Miranda, Ph.D.; Luiz Landau, Ph.D.; Eduardo T Paes, Ph.D.

The use of Synthetic Aperture Radar measurements to distinguish natural oil seeps from human-related oil spills on the sea surface of Campeche Bay (Gulf of Mexico) using multivariate data analysis techniques

Gustavo de Araújo Carvalho[1,*], Peter J. Minnett[2], Fernando Pellon de Miranda[1], Luiz Landau[1], and Eduardo Tavares Paes[3].

[*] Corresponding author:
Email: ggus.ocn@gmail.com
Telephone: (55.21) 9.9838.0090
Fax: (55.21) 2556.0982

[1] Universidade Federal do Rio de Janeiro (UFRJ)
Instituto Alberto Luiz Coimbra de Pós-Graduação e Pesquisa de Engenharia (COPPE)
Programa de Engenharia Civil (PEC)
Laboratório de Métodos Computacionais em Engenharia (LAMCE)
Laboratório de Sensoriamento Remoto por Radar Aplicado à Indústria do Petróleo (LabSAR)

[2] University of Miami (UM)
Rosenstiel School of Marine and Atmospheric Science (RSMAS)
Department of Ocean Sciences (OCE)
4600 Rickenbacker Causeway, Miami, FL, USA, 33149-1098.

[3] Universidade Federal Rural da Amazônia (UFRA)
Instituto Socioambiental e dos Recursos Hídricos (ISARH)
Laboratório de Ecologia Marinha e Oceanografia Pesqueira da Amazônia (LEMOPA)

Abstract: The present research uses Synthetic Aperture Radar (SAR) measurements to discriminate between two oil slick types: naturally-occurring oil seeps and human-related oil spills. The use of satellite remote sensors for this task is still poorly documented. Herein, a multi-year dataset (2008-2012) of RADARSAT-derived measurements is leveraged to investigate the oil slicks on the surface of the ocean in Campeche Bay (Gulf of Mexico). After a Data Treatment practice (log transformation, ranging standardization, etc.), multivariate data analysis techniques, such as Correlation (R-mode), Principal Components Analysis (PCA), and Discriminant Function, have been explored to design a simple classification algorithm to distinguish the oil slick type. The proposed analysis promotes a novel idea bridging geochemistry and remote sensing research to express geophysical differences between seeped and spilled oil. SAR-derived backscatter coefficients, i.e. sigma-naught (σ^o), beta-naught (β^o), and gamma-naught (γ^o), are combined with various attributes referring to the geometry, shape, and dimension that describe oil slicks (referred to as size information). Results indicate that the synergy of combining these several characteristics with the application of the multivariate data analysis techniques is capable of distinguishing the oil slick type. Nevertheless, the sole, and simple use of the oil slick size information is also capable of distinguishing oil seeps from oil spills observed on the sea surface to a useful accuracy for systematic use: 70% of Overall Accuracy.

Keywords: Oceanography, Remote Sensing, Satellite, Synthetic Aperture Radar, SAR, Environmental Monitoring , Campeche Bay, Gulf of Mexico, Oil Slicks, Oil Seeps, Oil Spills, Multivariate Data Analysis, Discriminant Function, Principal Components Analysis.

APPENDIX 2

TYPICAL VALUES OF BASIC QUALITATIVE-QUANTITATIVE STATISTICS: 3RD ATTRIBUTE TYPE (TABLE 5-4: GEOMETRY, SHAPE, AND DIMENSION – SIZE INFORMATION)

Table 6-13a: Typical values (i.e. basic qualitative-quantitative statistics: minimum, maximum, average, and standard deviation) characterizing, per class, the geometry, shape, and dimension characteristics (Table 5-4: 3rd Attribute Type) of the oil seeps within the Campeche Bay Oil Slick Modified Database (CBOS-DScMod).

Cantarell (n=238)	Minimum	Maximum	Average	Standard Deviation	Sum (km^2)
LEN *	353.0	823,850.0	46,767.2	97,892.5	
Area (km^2)	0.0100	436.1525	27.1550	51.8702	6,462.9
Per (km)	0.3	2484.8	296.9	416.2	
AtoP (km)	0.0143	0.2821	0.0761	0.0445	
PtoA (km^{-1})	3.5451	69.6899	17.8632	10.4614	
PtoA.nor **	0.8463	46.1191	15.6376	9.6568	
COMPLEX.ind **	9.0	26,728.3	4,239.8	5,408.2	
COMPACT.ind **	0.0005	1.3963	0.0180	0.0917	
SHAPE.ind (km^{-1})	0.75	40.87	13.86	8.56	
FRAC.ind **	-2,353.2	383.1	-7.9	157.7	
Clusters (n=1,200)	**Minimum**	**Maximum**	**Average**	**Standard Deviation**	**Sum (km^2)**
LEN *	36.0	142,611.0	3,652.7	8,044.5	
Area (km^2)	0.0200	89.1600	2.1612	4.9010	2,593.5
Per (km)	1.1	588.3	33.1	46.8	
AtoP (km)	0.0036	0.2796	0.0512	0.0290	
PtoA (km^{-1})	3.5766	280.0000	25.5519	16.7575	
PtoA.nor **	1.3877	29.5263	6.5196	3.1654	
COMPLEX.ind **	24.2	10955.4	659.9	758.9	
COMPACT.ind **	0.0011	0.5193	0.0459	0.0521	
SHAPE.ind (km^{-1})	1.23	26.17	5.78	2.81	
FRAC.ind **	-402.3	426,242.8	1,746.2	24,946.7	
Orphan Seeps (n=583)	**Minimum**	**Maximum**	**Average**	**Standard Deviation**	**Sum (km^2)**
LEN *	13.0	43,024.0	1,961.0	3,989.8	
Area (km^2)	0.0200	26.8900	1.1741	2.4503	684.5
Per (km)	0.8	414.5	19.4	28.4	
AtoP (km)	0.0061	0.3978	0.0490	0.0325	
PtoA (km^{-1})	2.5139	164.4444	26.1165	13.5966	
PtoA.nor **	1.3877	32.9604	5.1738	2.8655	
COMPLEX.ind **	24.2	13,652.0	439.4	720.7	
COMPACT.ind **	0.0009	0.5193	0.0800	0.0885	
SHAPE.ind (km^{-1})	1.23	29.21	4.59	2.54	
FRAC.ind **	-267.2	1,660.6	1.8	74.3	

* Number of pixels within the oil slicks.

** Dimensionless quantity.

Table 6-13b: Typical values (i.e. basic qualitative-quantitative statistics: minimum, maximum, average, and standard deviation) characterizing, per class, the geometry, shape, and dimension characteristics (Table 5-4: 3rd Attribute Type) of the oil spills within the Campeche Bay Oil Slick Modified Database (CBOS-DScMod).

Brightspots (n=1,050)	Minimum	Maximum	Average	Standard Deviation	Sum (km^2)
LEN *	3.0	443,948.0	2,698.1	18,535.9	
Area (km^2)	0.0100	277.4900	1.6847	11.5151	1,769.0
Per (km)	0.6	772.3	18.0	48.6	
AtoP (km)	0.0080	0.6311	0.0444	0.0412	
PtoA (km^{-1})	1.5846	125.0000	30.5618	14.7221	
PtoA.nor **	1.1968	37.5652	4.5878	2.9400	
COMPLEX.ind **	18.0	17,732.9	373.0	895.4	
COMPACT.ind **	0.0007	0.6981	0.0982	0.1012	
SHAPE.ind (km^{-1})	1.06	33.29	4.07	2.61	
FRAC.ind **	-487.9	251.4	-2.2	32.0	
Ship Spills (n=159)	**Minimum**	**Maximum**	**Average**	**Standard Deviation**	**Sum (km^2)**
LEN *	9.0	10,272.0	885.3	1,668.0	
Area (km^2)	0.0100	6.4200	0.5699	1.0558	90.6
Per (km)	0.6	106.5	11.3	17.0	
AtoP (km)	0.0125	0.1558	0.0436	0.0234	
PtoA (km^{-1})	6.4172	80.0000	28.8082	13.4818	
PtoA.nor **	1.2616	16.2815	4.0281	2.5582	
COMPLEX.ind **	20.0	3,331.2	285.6	468.1	
COMPACT.ind **	0.0038	0.6283	0.1343	0.1321	
SHAPE.ind (km^{-1})	1.12	14.43	3.57	2.27	
FRAC.ind **	-110.6	364,103.6	2,289.8	28,875.3	
Orphan Spills (n=580)	**Minimum**	**Maximum**	**Average**	**Standard Deviation**	**Sum (km^2)**
LEN *	6.0	138,888.0	2,245.1	9,284.8	
Area (km^2)	0.0025	86.8100	1.2751	4.9817	739.6
Per (km)	0.2	504.3	15.6	36.7	
AtoP (km)	0.0093	0.3880	0.0537	0.0403	
PtoA (km^{-1})	2.5772	107.5000	25.0434	12.6311	
PtoA.nor **	1.1283	34.7857	4.0632	2.8377	
COMPLEX.ind **	16.0	15,205.9	308.5	773.1	
COMPACT.ind **	0.0008	0.7855	0.1310	0.1219	
SHAPE.ind (km^{-1})	1.00	30.83	3.60	2.51	
FRAC.ind **	-58.3	330,692.6	571.3	13,731.2	

* Number of pixels within the oil slicks.

** Dimensionless quantity.

Table 6-13c: Typical values (i.e. basic qualitative-quantitative statistics: minimum, maximum, average, and standard deviation) characterizing, per class, the geometry, shape, and dimension characteristics (Table 5-4: 3rd Attribute Type) of the oil spills within the Campeche Bay Oil Slick Modified Database (CBOS-DScMod).

Bright-1 (n=575)	Minimum	Maximum	Average	Standard Deviation	Sum (km^2)
LEN *	3.0	66,268.0	1,352.0	4,830.4	
Area (km^2)	0.0100	78.1300	0.9150	4.2674	526.1
Per (km)	0.4	451.3	13.8	30.0	
AtoP (km)	0.0036	0.6582	0.0396	0.0347	
PtoA (km^{-1})	1.5193	280.0000	33.6563	20.3851	
PtoA.nor **	1.1284	19.7813	4.4930	2.5151	
COMPLEX.ind **	16.0	4,917.2	333.0	473.7	
COMPACT.ind **	0.0026	0.7854	0.0973	0.0971	
SHAPE.ind (km^{-1})	1.00	17.53	3.98	2.23	
FRAC.ind **	-85.5	278.6	-0.1	16.8	
Bright-2 (n=276)	**Minimum**	**Maximum**	**Average**	**Standard Deviation**	**Sum (km^2)**
LEN *	4.0	20,516.0	613.8	1,411.2	
Area (km^2)	0.0100	12.8200	0.3867	0.8686	106.7
Per (km)	0.6	197.5	9.0	14.6	
AtoP (km)	0.0033	0.2099	0.0381	0.0210	
PtoA (km^{-1})	4.7642	300.0000	33.0007	21.5291	
PtoA.nor **	1.3029	15.5611	4.0231	2.0526	
COMPLEX.ind **	21.3	3,042.9	256.1	335.2	
COMPACT.ind **	0.0041	0.5890	0.1098	0.0979	
SHAPE.ind (km^{-1})	1.15	13.79	3.57	1.82	
FRAC.ind **	-322.3	251.8	-1.5	27.2	
Bright-3 (n=255)	**Minimum**	**Maximum**	**Average**	**Standard Deviation**	**Sum (km^2)**
LEN *	4.0	106,696.0	2,254.4	9,037.1	
Area (km^2)	0.0076	66.6900	1.4264	5.6466	363.7
Per (km)	0.4	468.1	19.2	50.1	
AtoP (km)	0.0060	0.2148	0.0427	0.0268	
PtoA (km^{-1})	4.6564	168.0000	30.6835	17.0164	
PtoA.nor **	1.3029	19.4004	4.6806	2.8041	
COMPLEX.ind **	21.3	4,729.7	373.7	577.2	
COMPACT.ind **	0.0027	0.5891	0.0950	0.0974	
SHAPE.ind (km^{-1})	1.15	17.19	4.15	2.49	
FRAC.ind **	-41.0	395,511.4	1,550.3	24,767.9	

* Number of pixels within the oil slicks.

** Dimensionless quantity.

APPENDIX 3

TYPICAL VALUES OF BASIC QUALITATIVE-QUANTITATIVE STATISTICS: 4TH ATTRIBUTE TYPE (TABLE 5-5: SAR BACKSCATTER SIGNATURE)

Average (*AVG*) SAR backscatter signature (**Sigma-naught: σ^o**)

for incidence angles ranging from **≥19.5° to <28.5°**.

Sigma-naught (σ^o)	*SIG.amp.AVG*	*SIG.amp.FF.AVG*	*SIG.dB.AVG*	*SIG.dB.FF.AVG*
Oil Slicks (n=1,482)	**Amplitude without Frost**	**Amplitude with Frost**	**Decibels without Frost**	**Decibels with Frost**
Minimum	0.001800	0.001911	-56.258023	9.552999
Maximum	0.660908	0.635781	-8.801640	56.383544
Average	0.069069	0.074136	-28.664991	28.980375
Standard Deviation	0.065365	0.069391	7.510521	7.410171
Oil Spills (n=806)	**Amplitude without Frost**	**Amplitude with Frost**	**Decibels without Frost**	**Decibels with Frost**
Minimum	0.003775	0.004039	-50.216029	11.133664
Maximum	0.660908	0.635781	-9.089579	50.179703
Average	0.068910	0.073930	-29.033849	29.349085
Standard Deviation	0.074542	0.079005	7.622256	7.495145
Oil Seeps (n=676)	**Amplitude without Frost**	**Amplitude with Frost**	**Decibels without Frost**	**Decibels with Frost**
Minimum	0.001800	0.001911	-56.258023	9.552999
Maximum	0.447408	0.474392	-8.801640	56.383544
Average	0.069259	0.074381	-28.225200	28.540758
Standard Deviation	0.052418	0.055864	7.356548	7.288733

Average (*AVG*) SAR backscatter signature (**Sigma-naught: σ^o**)

for incidence angles ranging from **≥28.5° to <37.5°**.

Sigma-naught (σ^o)	*SIG.amp.AVG*	*SIG.amp.FF.AVG*	*SIG.dB.AVG*	*SIG.dB.FF.AVG*
Oil Slicks (n=2,094)	**Amplitude without Frost**	**Amplitude with Frost**	**Decibels without Frost**	**Decibels with Frost**
Minimum	0.001800	0.001911	-56.258023	9.552999
Maximum	0.447408	0.474392	-8.801640	56.383544
Average	0.069259	0.074381	-28.225200	28.540758
Standard Deviation	0.052418	0.055864	7.356548	7.288733
Oil Spills (n=1,082)	**Amplitude without Frost**	**Amplitude with Frost**	**Decibels without Frost**	**Decibels with Frost**
Minimum	0.002349	0.002593	-55.011272	24.770263
Maximum	0.109381	0.121003	-24.620990	55.154226
Average	0.013510	0.014591	-41.620440	41.786712
Standard Deviation	0.011114	0.011860	5.596447	5.530816
Oil Seeps (n=1,012)	**Amplitude without Frost**	**Amplitude with Frost**	**Decibels without Frost**	**Decibels with Frost**
Minimum	0.001372	0.001481	-59.230428	26.677456
Maximum	0.060255	0.062095	-26.242518	59.259544
Average	0.010128	0.010983	-44.193368	44.214445
Standard Deviation	0.007940	0.008411	6.356980	6.249099

Average (*AVG*) SAR backscatter signature (**Sigma-naught: σ^o**)

for incidence angles ranging from **≥37.5^o to ≤46.6^o**.

Sigma-naught (σ^o)	*SIG.amp.AVG*	*SIG.amp.FF.AVG*	*SIG.dB.AVG*	*SIG.dB.FF.AVG*
Oil Slicks (n=1,340)	**Amplitude without Frost**	**Amplitude with Frost**	**Decibels without Frost**	**Decibels with Frost**
Minimum	0.000907	0.000995	-62.195921	35.431792
Maximum	0.107952	0.114450	-35.080355	62.054795
Average	0.004213	0.004594	-51.265255	51.304869
Standard Deviation	0.005099	0.005513	4.549087	4.502321
Oil Spills (n=1,007)	**Amplitude without Frost**	**Amplitude with Frost**	**Decibels without Frost**	**Decibels with Frost**
Minimum	0.001060	0.001135	-61.211937	35.431792
Maximum	0.097043	0.107837	-35.080355	61.200692
Average	0.004171	0.004550	-51.320413	51.368698
Standard Deviation	0.004688	0.005118	4.402869	4.348059
Oil Seeps (n=333)	**Amplitude without Frost**	**Amplitude with Frost**	**Decibels without Frost**	**Decibels with Frost**
Minimum	0.000907	0.000995	-62.195921	37.106547
Maximum	0.107952	0.114450	-37.027594	62.054795
Average	0.004338	0.004726	-51.098454	51.111850
Standard Deviation	0.006182	0.006571	4.968460	4.941576

Average (*AVG*) SAR backscatter signature (**Beta-naught: β°**)

for incidence angles ranging from **≥19.5° to <28.5°**.

Beta-naught (β°)	*BET.amp.AVG*	*BET.amp.FF.AVG*	*BET.dB.AVG*	*BET.dB.FF.AVG*
Oil Slicks (n=1,482)	**Amplitude without Frost**	**Amplitude with Frost**	**Decibels without Frost**	**Decibels with Frost**
Minimum	0.003796	0.004030	-49.777594	5.101585
Maximum	1.882817	1.811290	0.216535	49.921560
Average	0.180189	0.193434	-21.012211	21.528420
Standard Deviation	0.188861	0.200736	8.219440	7.931229
Oil Spills (n=806)	**Amplitude without Frost**	**Amplitude with Frost**	**Decibels without Frost**	**Decibels with Frost**
Minimum	0.008022	0.008584	-43.460739	5.101585
Maximum	1.882817	1.811290	0.216535	43.445126
Average	0.179628	0.192768	-21.593993	22.130951
Standard Deviation	0.215877	0.229090	8.460319	8.091849
Oil Seeps (n=676)	Amplitude without Frost	Amplitude with Frost	Decibels without Frost	Decibels with Frost
Minimum	0.003796	0.004030	-49.777594	5.267341
Maximum	1.254385	1.329995	0.059730	49.921560
Average	0.180858	0.194229	-20.318549	20.810018
Standard Deviation	0.150597	0.160682	7.872841	7.679709

Average (*AVG*) SAR backscatter signature (**Beta-naught: β°**)

for incidence angles ranging from **≥28.5° to <37.5°**.

Beta-naught (β°)	*BET.amp.AVG*	*BET.amp.FF.AVG*	*BET.dB.AVG*	*BET.dB.FF.AVG*
Oil Slicks (n=2,094)	**Amplitude without Frost**	**Amplitude with Frost**	**Decibels without Frost**	**Decibels with Frost**
Minimum	0.002264	0.002458	-54.899231	18.618650
Maximum	0.228484	0.252758	-18.388067	54.884913
Average	0.022448	0.024268	-37.673371	37.805972
Standard Deviation	0.020322	0.021637	6.520048	6.409090
Oil Spills (n=1,082)	**Amplitude without Frost**	**Amplitude with Frost**	**Decibels without Frost**	**Decibels with Frost**
Minimum	0.004023	0.004441	-50.165700	18.618650
Maximum	0.228484	0.252758	-18.388067	50.327430
Average	0.025842	0.027889	-36.341631	36.547895
Standard Deviation	0.023227	0.024770	6.053569	5.978531
Oil Seeps (n=1,012)	Amplitude without Frost	Amplitude with Frost	Decibels without Frost	Decibels with Frost
Minimum	0.002264	0.002458	-54.899231	20.442622
Maximum	0.119225	0.125898	-19.923015	54.884913
Average	0.018820	0.020396	-39.097228	39.151070
Standard Deviation	0.015892	0.016858	6.700525	6.581411

Average (*AVG*) SAR backscatter signature (**Beta-naught: β^o**)

for incidence angles ranging from **≥37.5^o to ≤46.6^o**.

Beta-naught (β^o)	*BET.amp.AVG*	*BET.amp.FF.AVG*	*BET.dB.AVG*	*BET.dB.FF.AVG*
Oil Slicks (n=1,340)	**Amplitude without Frost**	**Amplitude with Frost**	**Decibels without Frost**	**Decibels with Frost**
Minimum	0.001282	0.001407	-59.187699	31.783421
Maximum	0.163773	0.173632	-31.356205	59.053293
Average	0.006366	0.006943	-47.775754	47.832512
Standard Deviation	0.007804	0.008440	4.721009	4.675939
Oil Spills (n=1,007)	**Amplitude without Frost**	**Amplitude with Frost**	**Decibels without Frost**	**Decibels with Frost**
Minimum	0.001493	0.001598	-58.418408	31.783421
Maximum	0.149751	0.166409	-31.356205	58.403050
Average	0.006256	0.006825	-47.906358	47.971852
Standard Deviation	0.007189	0.007850	4.583830	4.530868
Oil Seeps (n=333)	Amplitude without Frost	Amplitude with Frost	Decibels without Frost	Decibels with Frost
Minimum	0.001282	0.001407	-59.187699	33.389689
Maximum	0.163773	0.173632	-33.280177	59.053293
Average	0.006697	0.007299	-47.380804	47.411142
Standard Deviation	0.009425	0.010022	5.100451	5.073501

Average (*AVG*) SAR backscatter signature (**Gamma-naught: γ^o**)

for incidence angles ranging from **≥19.5° to <28.5°**.

Gamma-naught (γ^o)	*GAM.amp.AVG*	*GAM.amp.FF.AVG*	*GAM.dB.AVG*	*GAM.dB.FF.AVG*
Oil Slicks (n=1,482)	**Amplitude without Frost**	**Amplitude with Frost**	**Decibels without Frost**	**Decibels with Frost**
Minimum	0.002044	0.002170	-55.151609	9.016371
Maximum	0.705821	0.682226	-8.194344	55.279979
Average	0.075074	0.080579	-27.822521	28.149132
Standard Deviation	0.069702	0.073976	7.377056	7.273076
Oil Spills (n=806)	Amplitude without Frost	Amplitude with Frost	Decibels without Frost	Decibels with Frost
Minimum	0.004278	0.004578	-49.186249	10.757918
Maximum	0.705821	0.682226	-8.547585	49.152696
Average	0.075018	0.080479	-28.140251	28.467647
Standard Deviation	0.079497	0.084233	7.461274	7.328244
Oil Seeps (n=676)	Amplitude without Frost	Amplitude with Frost	Decibels without Frost	Decibels with Frost
Minimum	0.002044	0.002170	-55.151609	9.016371
Maximum	0.479105	0.508002	-8.194344	55.279979
Average	0.075142	0.080699	-27.443689	27.769363
Standard Deviation	0.055882	0.059542	7.262711	7.193730

Average (*AVG*) SAR backscatter signature (**Gamma-naught: γ^o**)

for incidence angles ranging from **≥28.5° to <37.5°**.

Gamma-naught (γ^o)	*GAM.amp.AVG*	*GAM.amp.FF.AVG*	*GAM.dB.AVG*	*GAM.dB.FF.AVG*
Oil Slicks (n=2,094)	**Amplitude without Frost**	**Amplitude with Frost**	**Decibels without Frost**	**Decibels with Frost**
Minimum	0.002044	0.002170	-55.151609	9.016371
Maximum	0.479105	0.508002	-8.194344	55.279979
Average	0.075142	0.080699	-27.443689	27.769363
Standard Deviation	0.055882	0.059542	7.262711	7.193730
Oil Spills (n=1,082)	Amplitude without Frost	Amplitude with Frost	Decibels without Frost	Decibels with Frost
Minimum	0.002894	0.003194	-53.287052	23.602221
Maximum	0.124585	0.137823	-23.440131	53.436325
Average	0.015929	0.017210	-40.073678	40.250320
Standard Deviation	0.012661	0.013518	5.433290	5.367734
Oil Seeps (n=1,012)	Amplitude without Frost	Amplitude with Frost	Decibels without Frost	Decibels with Frost
Minimum	0.001719	0.001856	-57.244287	25.536313
Maximum	0.070785	0.072946	-24.844529	57.305490
Average	0.012062	0.013084	-42.565411	42.595729
Standard Deviation	0.009176	0.009716	6.217107	6.109007

Average (*AVG*) SAR backscatter signature (**Gamma-naught: γ^o**)

for incidence angles ranging from **≥37.5° to ≤46.6°**.

Gamma-naught (γ^o)	*GAM.amp.AVG*	*GAM.amp.FF.AVG*	*GAM.dB.AVG*	*GAM.dB.FF.AVG*
Oil Slicks (n=1,340)	**Amplitude without Frost**	**Amplitude with Frost**	**Decibels without Frost**	**Decibels with Frost**
Minimum	0.001282	0.001407	-59.183525	33.079375
Maximum	0.143551	0.152193	-32.682959	59.193962
Average	0.005649	0.006160	-48.661963	48.713941
Standard Deviation	0.006753	0.007300	4.438928	4.386220
Oil Spills (n=1,007)	Amplitude without Frost	Amplitude with Frost	Decibels without Frost	Decibels with Frost
Minimum	0.001467	0.001571	-59.162005	33.079375
Maximum	0.127417	0.141589	-32.682959	58.769908
Average	0.005625	0.006136	-48.661442	48.722687
Standard Deviation	0.006205	0.006773	4.282075	4.222131
Oil Seeps (n=333)	Amplitude without Frost	Amplitude with Frost	Decibels without Frost	Decibels with Frost
Minimum	0.001282	0.001407	-59.183525	34.744858
Maximum	0.143551	0.152193	-34.647164	59.193962
Average	0.005721	0.006232	-48.663539	48.687495
Standard Deviation	0.008201	0.008715	4.889619	4.855522

APPENDIX 4

ROOTED-TREE DENDROGRAMS BASED ON THE UPGMA (UNWEIGHTED PAIR GROUP METHOD WITH ARITHMETIC MEAN) IMPLEMENTATION PER DATA SUB-DIVISION

Rooted-tree dendrograms based on the UPGMA implementation: **all SAR backscatter signature variables (n=423: σ^o, β^o, and γ^o) analyzed together with the attributes of geometry, shape, and dimension (n=10)**. In the bottom panel, the two horizontal red lines correspond to the Cophenetic Correlation Coefficient (CCC=0.8227) and similarity of 0.5, respectively (top and bottom lines). Same information plotted in the upper and middle panels: respectively for 0.8227 and 0.5.

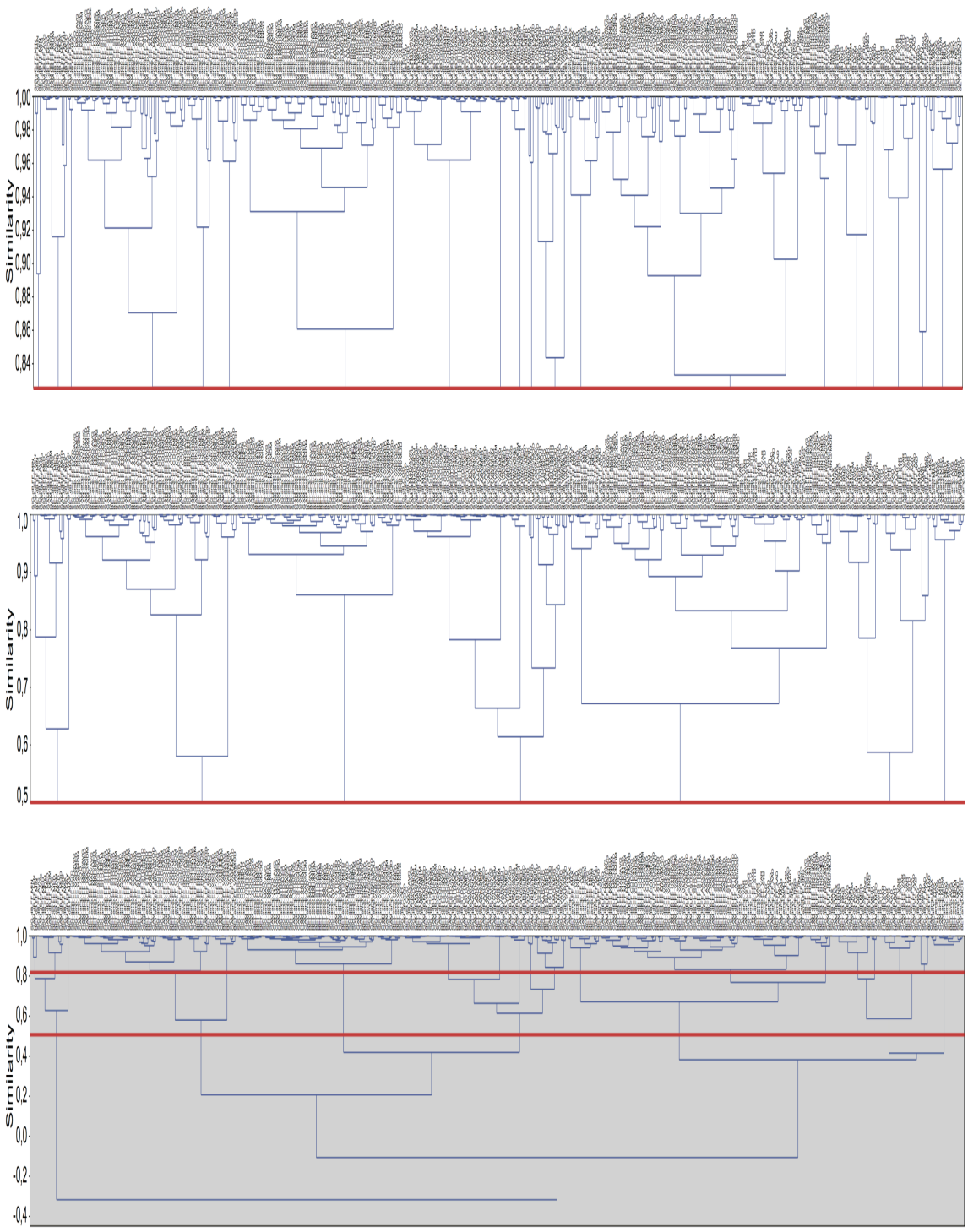

Rooted-tree dendrograms based on the UPGMA implementation: **all SAR backscatter signature variables only (n=423: σ^o, β^o, and γ^o)**. In the bottom panel, the two horizontal red lines correspond to the Cophenetic Correlation Coefficient (CCC=0.8253) and similarity of 0.5, respectively (top and bottom lines). Same information plotted in the upper and middle panels: respectively for 0.8253 and 0.5.

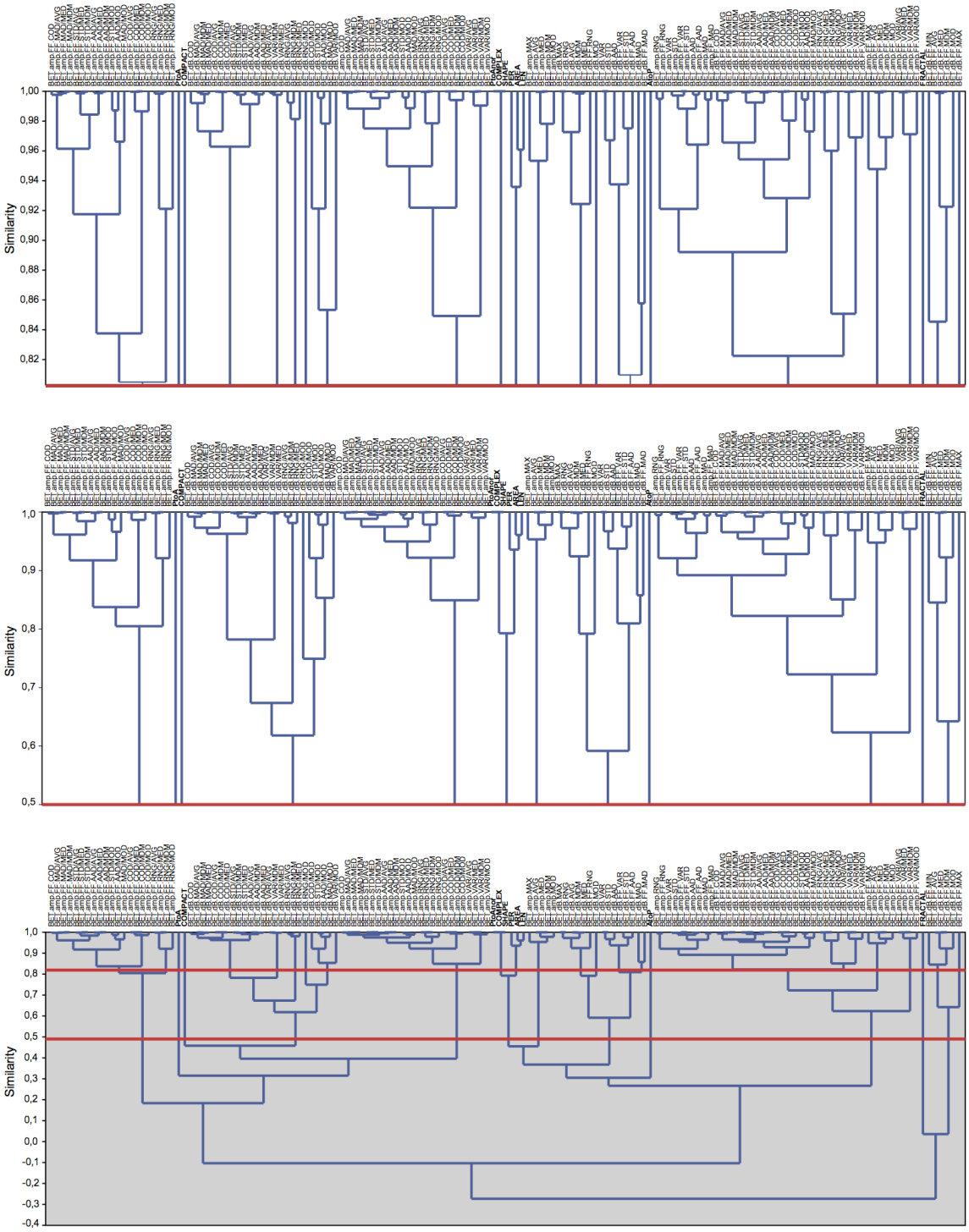

Rooted-tree dendrograms based on the UPGMA implementation: **beta-naught (β^o) variables (n=141) together with the attributes of geometry, shape, and dimension (n=10)**. In the lower panel, the two horizontal red lines correspond to the Cophenetic Correlation Coefficient (CCC=0.8031) and similarity of 0.5, respectively (top and bottom lines). Same information plotted in the upper and middle panels: respectively for 0.8031 and 0.5.

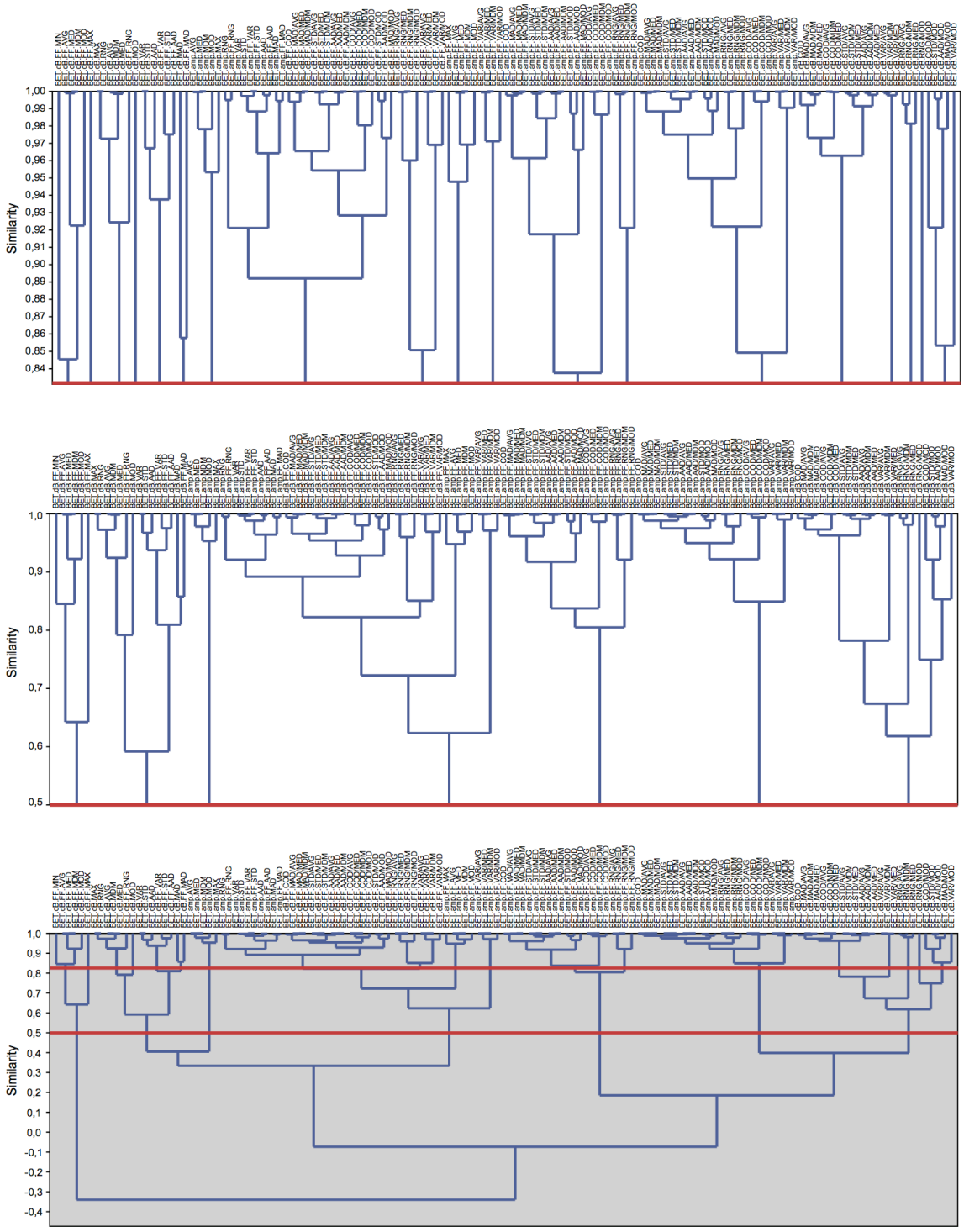

Rooted-tree dendrograms based on the UPGMA implementation: **beta-naught (β^o) variables only (n=141)**. In the lower panel, the two horizontal red lines correspond to the Cophenetic Correlation Coefficient (CCC=0.8130) and similarity of 0.5, respectively (top and bottom lines). Same information plotted in the upper and middle panels: respectively for 0.8130 and 0.5.

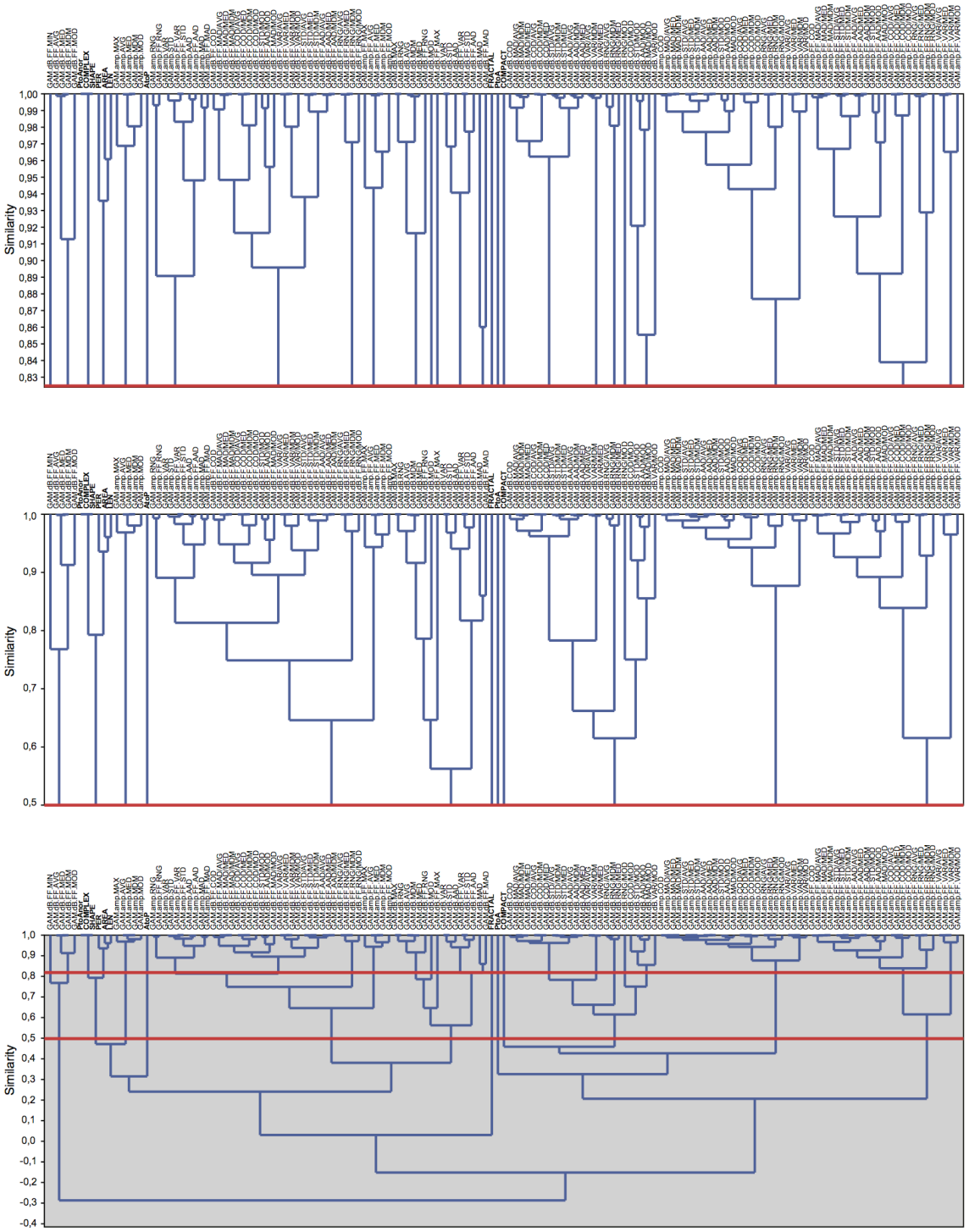

Rooted-tree dendrograms based on the UPGMA implementation: **gamma-naught (γ^o) variables (n=141) together with the attributes of geometry, shape, and dimension (n=10)**. In the lower panel, the two horizontal red lines correspond to the Cophenetic Correlation Coefficient (CCC=0.8240) and similarity of 0.5, respectively (top and bottom lines). Same information plotted in the upper and middle panels: respectively for 0.8240 and 0.5.

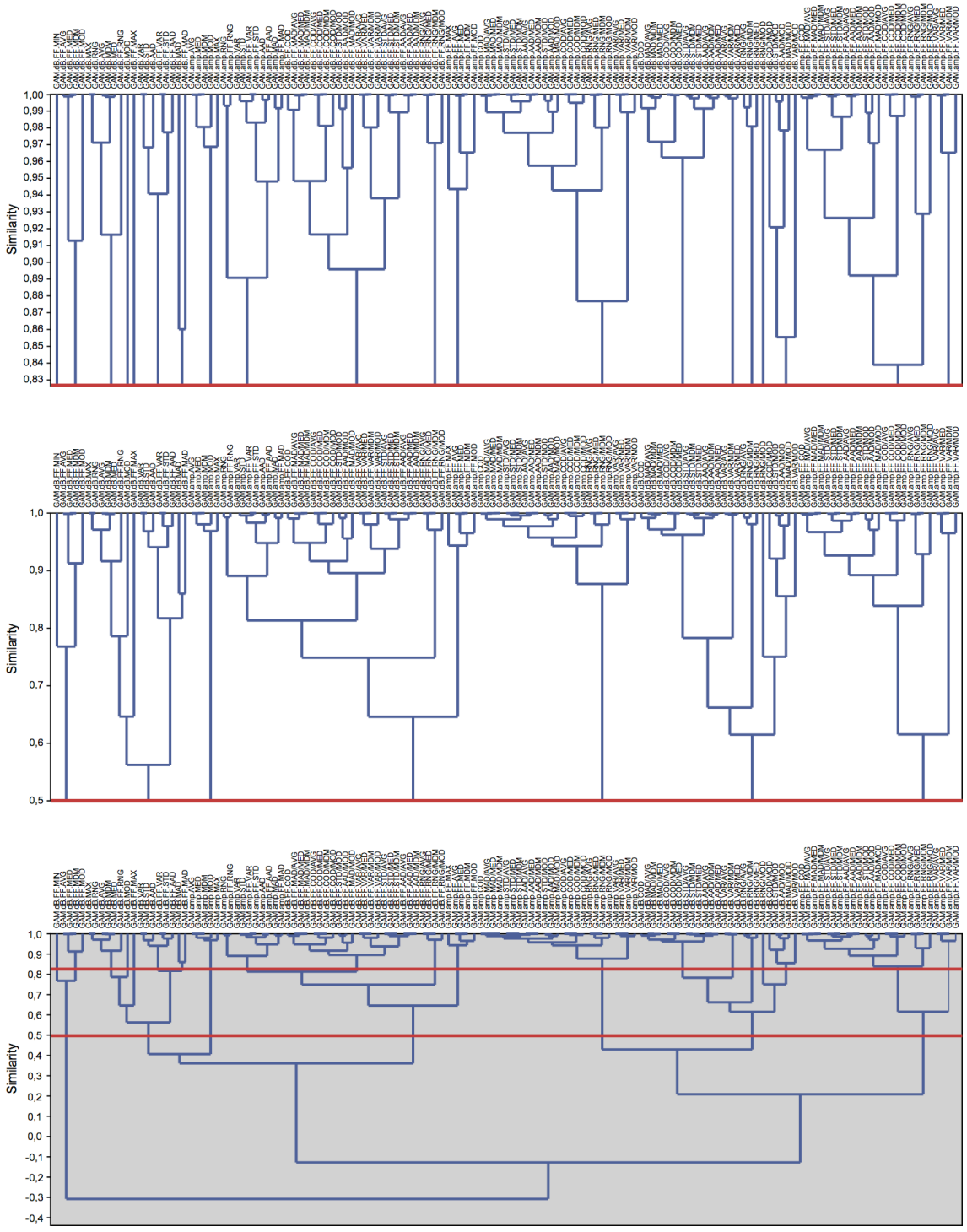

Rooted-tree dendrograms based on the UPGMA implementation: **gamma-naught (γ^o) variables only (n=141)**. In the lower panel, the two horizontal red lines correspond to the Cophenetic Correlation Coefficient (CCC=0.8260) and similarity of 0.5, respectively (top and bottom lines). Same information plotted in the upper and middle panels: respectively for 0.8260 and 0.5.

APPENDIX 5

CONSTANT OFFSETS (C_{OFF}) OF THE DISCRIMINANT FUNCTIONS

Constant offset (C_{off}) per data sub-divisions (Figure 5-3).

No PCA: See Table 6-31 for the number of variables.	**Original Sets**	**UPGMA (CCC)**	**UPGMA (0.5)**	**CFS**
Complete Exploration of the CBOS-DScMod	20.70810	26.75160	22.38290	§
All SAR Backscatter Signature ¥ with Size*	4.73703	†	†	5.89046
Only all SAR Backscatter Signature ¥	5.94918	††	††	-0.97017
Size* and Sigma-naught (σ^o)	14.62320	16.69950	17.70760	4.34108
Size* and Beta-naught (β^o)	9.60851	15.46650	17.28380	5.39505
Size* and Gamma-naught (γ^o)	13.70120	14.81050	16.47300	7.24409
Only Size*	3.85919	4.18807	3.96403	3.70246
Only Sigma-naught (σ^o)	17.54930	15.09050	8.16940	1.19049
Only Beta-naught (β^o)	11.17600	14.15150	10.18060	1.68465
Only Gamma-naught (γ^o)	16.42570	14.23110	7.02485	-10.40370
Only Digital Numbers (DN's)	2.87075	1.76280	1.26008	3.42718
With PCA: See Table 6-33 for the selected PC's.	**Original Set**	**UPGMA (CCC)**	**UPGMA (0.5)**	**CFS**
Complete Exploration of the CBOS-DScMod	1.2740100	6.6779200	7.0276700	§
All SAR Backscatter Signature ¥ with Size*	0.0795821	†	†	0.0780176
Only all SAR Backscatter Signature ¥	0.0447324	††	††	0.0472360
Size* and Sigma-naught (σ^o)	0.0665499	0.0839193	0.0574982	0.0796083
Size* and Beta-naught (β^o)	0.0678715	0.0821239	0.0576795	0.0826254
Size* and Gamma-naught (γ^o)	0.0644667	0.0833115	0.0562702	0.0768122
Only Size*	0.0772492	0.0795265	0.0811427	0.0811096
Only Sigma-naught (σ^o)	0.0443751	0.0440276	0.0334348	0.0478720
Only Beta-naught (β^o)	0.0436300	0.0346945	0.0325406	0.0457521
Only Gamma-naught (γ^o)	0.0432606	0.0429225	0.0322825	0.0453125
Only Digital Numbers (DN's)	0.0103062	0.0121737	0.0103375	0.0157960

§ Discriminant Function not performed (see Table 6-23).

* Attributes of geometry, shape, and dimension.

¥ See: Table 5-1 and Table 5-5.

σ^o *SIG.amp*, *SIG.amp.FF*, *SIG.dB*, and *SIG.dB.FF*.

β^o *BET.amp*, *BET.amp.FF*, *BET.dB*, and *BET.dB.FF*.

γ^o *GAM.amp*, *GAM.amp.FF*, *GAM.dB*, and *GAM.dB.FF*.

† Same as Size* and Sigma-naught (σ^o).

†† Same as only Sigma-naught (σ^o).

APPENDIX 6

CONFIGURATION OF THE TWO DESIGNED CLASSIFICATION ALGORITHMS PROPOSED ON PHASE 10 (SECTIONS 5.10 AND 6.10)

Configuration of the first proposed algorithm showing how the accuracy depicted on Table 6-42 is achieved using known and unknown samples.

Known sample	Sigma + Size	Beta + Size	Gamma + Size	Algorithm
Seep	Seep	Seep	Seep	**Seep**
Seep	Seep	Seep	Spill	**Seep**
Seep	Seep	Spill	Spill	**Spill**
Seep	Spill	Spill	Spill	**Spill**
Spill	Spill	Spill	Spill	**Spill**
Spill	Spill	Spill	Seep	**Spill**
Spill	Spill	Seep	Seep	**Seep**
Spill	Seep	Seep	Seep	**Seep**
Unknown sample		**First Proposed Algorithm**		
?	Seep	Seep	Seep	**Seep**
?	Seep	Seep	Spill	**Seep**
?	Seep	Spill	Spill	**Spill**
?	Spill	Spill	Spill	**Spill**

Configuration of the second proposed algorithm showing how the accuracy depicted on Table 6-43 is achieved using known and unknown samples.

Known sample	Size	Sigma	Beta	Gamma	Algorithm
Seep	Seep	Seep	Seep	Seep	**Seep**
Seep	Seep	Seep	Seep	Spill	**Seep**
Seep	Seep	Seep	Spill	Spill	**Seep ***
Seep	Seep	Spill	Spill	Spill	**Spill**
Seep	Spill	Spill	Spill	Spill	**Spill**
Spill	Spill	Spill	Spill	Spill	**Spill**
Spill	Spill	Spill	Spill	Seep	**Spill**
Spill	Spill	Spill	Seep	Seep	**Spill ***
Spill	Spill	Seep	Seep	Seep	**Seep**
Spill	Seep	Seep	Seep	Seep	**Seep**
Unknown sample	**1st Mode of the Second Proposed Algorithm**				
?	Seep	Seep	Seep	Seep	**Seep**
?	Seep	Seep	Seep	Spill	**Seep**
?	Seep	Seep	Spill	Spill	**Spill**
?	Seep	Spill	Spill	Spill	**Spill**
?	Spill	Spill	Spill	Spill	**Spill**
Unknown sample	**2nd Mode of the Second Proposed Algorithm**				
?	Spill	Spill	Spill	Spill	**Spill**
?	Spill	Spill	Spill	Seep	**Spill**
?	Spill	Spill	Seep	Seep	**? ***
?	Spill	Seep	Seep	Seep	**Seep**
?	Seep	Seep	Seep	Seep	**Seep**
Unknown sample	**3rd Mode of the Second Proposed Algorithm**				
?	Spill	Spill	Spill	Spill	**Spill**
?	Spill	Spill	Spill	Seep	**Spill**
?	Spill	Spill	Seep	Seep	**Seep**
?	Spill	Seep	Seep	Seep	**Seep**
?	Seep	Seep	Seep	Seep	**Seep**

* Not considered on the 2nd Mode.